ABSTRACT

Title of Document: QUANTITATIVE MODELING OF MANTLE HETEROGENEITY AND STRUCTURE.

Ricardo David Arevalo Jr., Ph.D. Geology, 2010

Directed By: Professor William F. McDonough, Department of Geology

Mantle-derived rocks, particularly mid-ocean ridge basalts (MORB) and intraplate ocean island basalts (OIB), provide insights into the compositional heterogeneity and first-order structural make-up of the modern mantle; laser ablation (LA-) ICP-MS analysis provides the ideal analytical tool for the *in situ* chemical characterization of these materials. The silicate Earth, as defined by the MORB and OIB source regions plus the continental crust, is determined to have a representative W/U and K/U ratio of 0.65 ± 0.45 (2σ) and 13,800 ± 2600 (2σ), respectively, equating to 13 ± 10 ng/g W and 280 ± 120 μg/g K in the silicate Earth. Although both the isotopic composition of W and the constancy of the terrestrial W/U ratio may serve as tracers of putative core-mantle interactions, both of these proxies are sensitive to the chemical composition of the mantle source and have yet to resolve a core signal in Hawaiian picrites. The abundance of K in the silicate Earth indicates a current convective Urey ratio of ~0.34 and mantle cooling rate of 70–130 $K \cdot Gyr^{-1}$, after taking into account potential heat flux across the core-mantle boundary. The Earth's balance of radiogenic heat and

budget of ^{40}Ar necessitate a lower mantle reservoir enriched in radioactive elements. The bulk Earth Pb/U ratio, determined here to be ~85, suggests ~1200 ng/g Pb in the bulk Earth and ≥3300 ng/g Pb in the core.

A compositional model of MORB, which is derived from a suite of sample measurements augmented by a critically compiled data set, shows that Atlantic, Pacific and Indian MORB can be distinguished based on both trace element abundances and ratios. The geochemical signatures associated with global MORB are not entirely complementary to the continental crust, and require an under-sampled reservoir enriched in Ti, Nb and Ta. A compositional model of OIB, which is based on the inferred chemical composition of OIB parental melts from Hawaiian shield volcanoes as well as the Austral-Cook islands, indicates that the OIB source region may only be ≥1.0x as enriched in incompatible elements as the unfractionated silicate Earth, and constitute up to ≤50% of the modern mantle mass.

QUANTITATIVE MODELING OF MANTLE HETEROGENEITY AND STRUCTURE.

By

Ricardo David Arevalo Jr.

Dissertation submitted to the Faculty of the Graduate School of the
University of Maryland, College Park, in partial fulfillment
of the requirements for the degree of
Doctor of Philosophy
2010

Advisory Committee:
Professor William F. McDonough, Chair
Professor Richard J. Walker
Associate Research Scientist Philip M. Piccoli
Assistant Professor Saswata Hier-Majumder
Faculty Research Assistant Richard D. Ash
Dean's Representative Professor Elizabeth J. Beise

Preface

A significant portion of the research and data reported in this thesis was previously published and/or submitted in the form of peer-reviewed journal articles. These contributions reflect not only my own work, but also that of my co-authors and our insightful reviewers and editors. Chapters 1, 2 (section 2.1), 7 (section 7.8), and 8 represent original work first submitted here; the references for the remaining chapters and sections are provided on the first page of each chapter (though all published/submitted material has been modified from its original format).

Dedication

This work is dedicated to my family, who has encouraged me from the beginning. In particular, I dedicate this dissertation to my wife, Paula, who has been with me through it all, including both the highs and the lows of my academic career. I owe her more than anyone, and I am ever thankful for her angelic presence in my life. She is my greatest blessing.

I also owe a great deal of debt and gratitude to my mom, who always supported me in my studies, even as I changed my major from pre-medicine to the geological sciences. She and my dad have supported me throughout the course of my studies, from grade school up to the present, and without their unwavering support I would not be here today. As for my sister, Sharon, she has been a best friend to me. Her love and sympathy helped me endure. I also appreciate all of the comfort provided to me by my mildly obese cat, Gaul.

"*I know that I've been given more than beyond measure. I come alive when I see beyond my fears. I know that I've been given more than earthly treasure. I come alive when I've broken down and given You control.*"

- Jeremy Camp (*Beyond Measure*)

Acknowledgements

First and foremost, I must acknowledge all of the time and energy that my advisor, Bill McDonough, has poured out on my behalf during my graduate studies. Despite Bill's cliché jokes and flamboyant ties, he has been an integral part of my professional development and maturation as an Earth scientist. I have enjoyed, more than anything, our regular (and sometimes intense) scientific discussions, though I will not necessarily miss his lectures on counting significant figures or memorizing all of the stable mono-isotopes (n = 21!). I also owe a great deal of gratitude to Rich Walker and Phil Piccoli, both of whom served as my collaborators, co-authors and friends. I thank Sash Hier-Majumder for providing me with intuitive insights into my research, and Richard Ash for teaching me the subtle (and not-so-subtle) nuances of laser ablation and mass spectrometry. I would also like to thank the Dean's Representative, Betsy Beise, for taking interest in my research and joining my committee.

As for my friends and colleagues, Tom Ireland gets the first acknowledgement for knowing me the longest, serving as a groomsman in my wedding and being a great co-author. Barry Reno acted as a statistical consult on much of this work, and also served as my running partner whenever I needed a break. Lin Qiu and Jeremy Bellucci both provided positive outlets for any frustrations I encountered during my studies. I also appreciate the great friendships I developed with (in alphabetical order by last name): Madalyn Blondes, James Day, Nick Gava, Nick Geboy, Brian Harms, John-Luke Henriquez, Ryan Kerrigan, Katya Klochko, Jingao Liu, Adam Mansur, Michael Mengason, Kristen and Jessica Miller, Brian Mumaw, Kate Scheiderich,

Emily Seldomridge, Sarah Sillin, Brian and Becca Tattitch, Fang-Zhen Teng, Lisa and Ben Walsh, and the rest of the department.

I would like to extend a personal thanks to the support staff of the Geology department, especially Sandy Romeo for her perpetual support and smiles, Jeanne Martin for her constant encouragement, Todd Karwoski for fixing my computer issues, Dorothy Brown, and Suzanne Martin.

I would also like to acknowledge Leslie Hale, Sorena Sorenson, Timothy O'Hearn, the late Jim Luhr, and the Division of Petrology and Volcanology, Department of Mineral Sciences, Smithsonian Institute, as well as Michael Garcia, Emily Klein, Charles Langmuir, Gaby Loock, Yaoling Niu, Marc Norman, and Michael Perfit for sample donations. This study was funded by NSF grants #0337621 and #0739006.

Table of Contents

List of Tables

Chapter 7

List of Figures

Chapter 1: Introduction[1]

[1] The text, tables and figures in this chapter were created/written by R. Arevalo Jr.

1.1 The modern mantle

The modern mantle, which constitutes the entire silicate portion of the Earth minus the continental crust, represents more than ⅔ of the planet by mass and >80% by volume (*e.g.*, Yoder, 1995). Geophysical and geochemical studies of the Earth's mantle indicate that it is both structurally and compositionally complex. Beginning in the late 1960's and early-to-mid 1970's, he results of geochemical studies were used to infer a layered mantle structure (Fig. 1.1A) based on chemical differences between mid-ocean ridge basalts (MORB) and intraplate ocean island basalts (OIB). These early studies and subsequent works have demonstrated that MORB are derived from an upper mantle source (*i.e.*, ≤200 km depth; *e.g.*, Forsyth *et al.,* 1998) that is largely depleted in incompatible elements ($D_i^{sol/liq} < 1$, where D is approximated by the concentration ratio of element i in the *solid* to the *liquid*) relative to the unfractionated silicate Earth (or "primitive mantle"); OIB, which are commonly attributed to intraplate "hotspots" or "plumes" that originate from lower mantle source regions (*i.e.*, >660 km depth; *e.g.*, Montelli *et al.,* 2004), are less depleted or even enriched in incompatible elements relative to the silicate Earth.

The observation of seismic-velocity discontinuities at depths of 410 and 660 km within the Earth provided geophysical support for the layered mantle hypothesis. However, the development of 3-dimensional mantle tomographic models has served to illustrate: i) the subduction of down-going slabs across the 660 km discontinuity

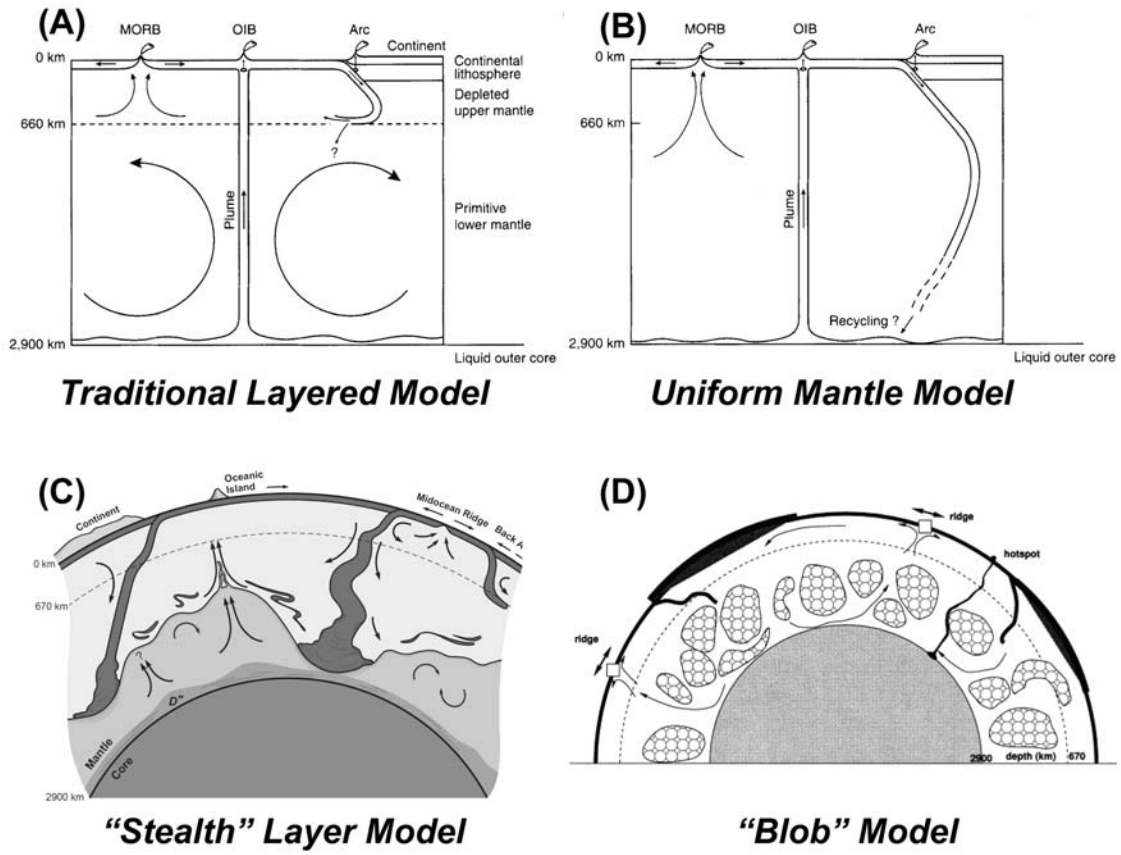

Fig. 1.1. Examples of proposed paradigms of mantle structure found in the literature. Models (A) and (B) represent the traditional layered and non-layered perspectives of mantle structure, respectively (from Hofmann, 1997). Model (C) illustrates the "stealth" layer model proposed by Kellogg *et al.,* (1999), in which an undulating chemical stratification exists at depth in the mantle, and (D) shows the "blob" model of Becker *et al.,* (1999), in which discrete blobs of unmelted, undepleted materials have remained preserved in the mantle since the planet's accretion and differentiation.

and into the depths of the mid- to lower mantle (*e.g.*, van der Hilst *et al.,* 1991; Grand *et al.,* 1997; Li *et al.,* 2008; Fig. 1.2A); and, ii) the extension of plume conduits across the transition zone and into lower mantle depths (*e.g.*, Zhao, 2001; Montelli *et al.,* 2004; Li *et al.,* 2008; Fig. 1.2B). Thus, 3-D seismic tomography, coupled with geochemical arguments based on upper mantle heterogeneity and the mass balance of incompatible element abundances in the silicate Earth (*e.g.*, Hofmann, 2003 and references therein), suggest significant communication between the upper and lower mantles. Moreover, studies in both the geochemical and geophysical communities have demonstrated the highly variable composition of mantle-derived materials; in particular, the distinct geochemical and isotopic signatures associated with MORB derived from the Atlantic, Pacific and Indian Ocean basins as well as the different OIB extreme isotopic "end-members," together provide evidence against a chemically uniform mantle. The spectrum of elemental and isotopic signatures observed in both MORB and OIB have served as fodder for a variety of alternative mantle models, ranging from models of whole-mantle convection with no substantive chemical layering (Fig. 1.1B) to hybrid models that incorporate an undulating "stealth" layer at depth (*e.g.*, Kellogg *et al.,* 1999; van der Hilst and Kárason, 1999; Fig. 1.1C) or essentially represent a mantle matrix with interspersed heterogeneities existing as strips or veins (*e.g.*, Allègre and Turcotte, 1986), "plums" (Morgan and Morgan, 1999) or "blobs" (*e.g.*, Allègre *et al.,* 1984; Becker *et al.,* 1999; Fig. 1.1D).

1.1.1 Major mantle domains: MORB and OIB source regions

The (long-term) compositional heterogeneity of the mantle is manifest as the range of elemental and isotopic compositions observed in oceanic basalts (*e.g.*, Gast *et al.,*

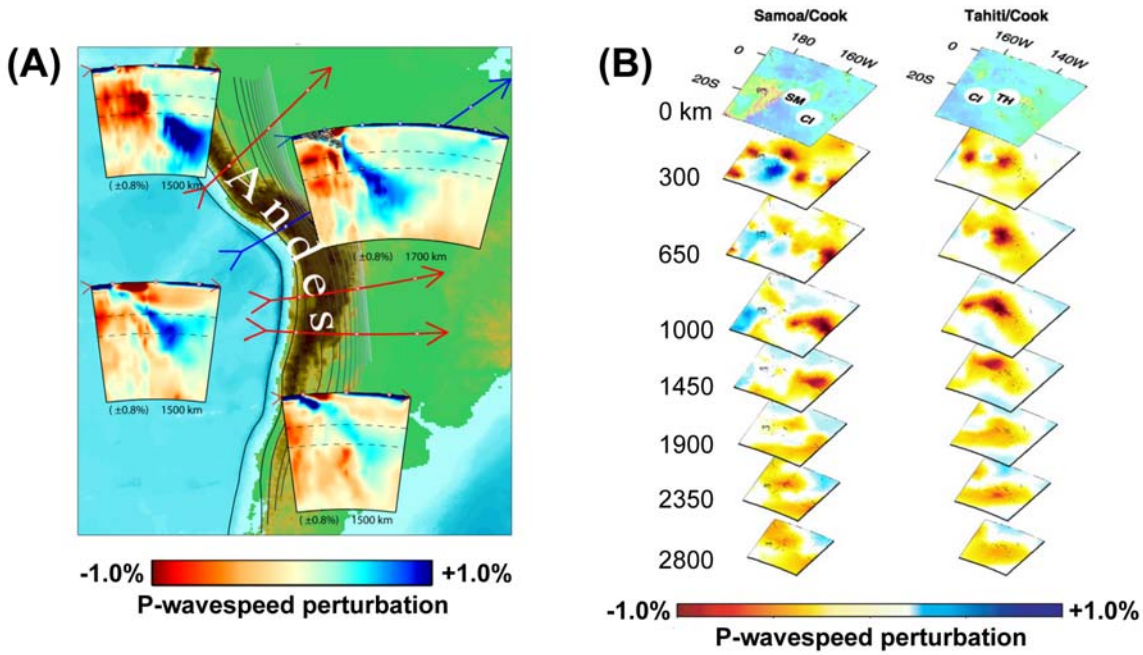

Fig. 1.2. Mantle tomographic models illustrating the subduction of down-going slabs and the extension of deep mantle plumes across the transition zone and into the lower mantle. (A) Four cross-sections of P-wave speed variations through the Andean subduction zone under South America indicating the persistence of the Pacific plate as deep as >1500 km (from Li *et al.*, 2008); the dashed lines represent the 410 km and 660 km discontinuities. (B) Three-dimensional view of P-wave speed variations through the plume conduits that feed the Samoan, Cook and Tahitian ocean island chains (from Montelli *et al.*, 2004); both 3-D profiles shown, which each represent an area 40° in latitude by 40° in longitude, reveal the continuation of at least one cohesive mantle plume down to (near) the core-mantle boundary.

1964; Schilling, 1973; DePaolo and Wasserburg, 1976; Dupré and Allègre, 1983; Zindler and Hart, 1986; Ito *et al.,* 1987; Sun and McDonough, 1989; Hofmann, 1997, 2003; Arevalo *et al.,* 2009; Arevalo and McDonough, 2010), olivine-hosted melt inclusions (*e.g.*, Saal *et al.,* 1998; Shimizu and Layne, 2003; Maclennan, 2008), abyssal mantle peridotites (*e.g.*, Workman and Hart, 2005; Warren *et al.,* 2009), and oceanic seamounts (*e.g.*, Zindler *et al.,* 1984; Niu and Batiza, 1997). Mid-ocean ridge basalts, which are predominantly tholeiitic in composition (*e.g.*, Engel *et al.,* 1965; Melson *et al.,* 1976), provide an ideal case study of the heterogeneity of the upper portion of the mantle as these samples: i) originate from large upper mantle melt zones that can extend several hundred kilometers laterally and to depths of ≤200 km (*e.g.*, Forsyth *et al.,* 1998); ii) represent adiabatic upwelling and decompression of the ambient upper mantle (*e.g.*, McKenzie and O'Nions, 1991), and therefore exemplify a relatively simple melting history with a limited opportunity for crustal contamination; and, iii) are accessible (the global mid-ocean ridge system extends >60,000 km) and abundant (the average global rate of magma emplacement is between about 26 and 34 $km^3 \cdot yr^{-1}$, of which 75% is generated by mid-ocean ridge volcanism; Crisp, 1984).

The MORB source region, commonly referred to as the depleted MORB mantle (or DMM), is largely depleted in incompatible trace elements relative to the unfractionated silicate Earth; this geochemical signature has long been identified as a complementary signature to that of the incompatible element-enriched continental crust (*e.g.*, Hofmann, 1988; Sun and McDonough, 1989), with several notable exceptions (*e.g.*, Ti, Nb and Ta; McDonough, 1991; Rudnick *et al.,* 2000; Arevalo and McDonough, 2010). Although MORB were originally considered to represent a

relatively homogeneous mantle domain, subsequent studies have demonstrated that MORB show a spectrum of geochemical signatures, ranging from depleted to enriched in incompatible element abundances (Fig. 1.3A), and exhibiting a range of radiogenic isotopic compositions (Fig. 1.3B). The geochemical variability observed in MORB reflects the heterogeneity of the MORB source region and has been interpreted to represent mixing between two or more distinct mantle components (*e.g.*, Hofmann, 2003 and references therein).

Historically, MORB have been subdivided into two distinct classes, termed "normal-type" and "enriched-type," based on one or more chemical criteria (Schilling, 1973). Normal-type MORB, or N-MORB, represent the majority of global MORB samples and are characterized by depletions in highly incompatible elements (*e.g.*, large-ion lithophile elements, LILE, high-field strength elements, HFSE, and light rare-earth elements, LREE) relative to less incompatible elements (*e.g.*, Hofmann, 2003 and references therein), resulting in diagnostic trace element ratios (*e.g.*, $(La/Sm)_N < 1$) and isotopic compositions (*e.g.*, high $^{143}Nd/^{144}Nd$ and low $^{87}Sr/^{86}Sr$). In contrast, enriched-type MORB, or E-MORB, represent a subsidiary component of global MORB and are anomalously enriched in highly incompatible elements; these samples are typically characterized by trace element ratios and isotopic compositions (*e.g.*, $(La/Sm)_N \geq 1$, low $^{143}Nd/^{144}Nd$ and high $^{87}Sr/^{86}Sr$) distinct from more common N-MORB.

As previously described, OIB are typically characterized by enrichments in incompatible elements (Figs. 1.4A), diverse radiogenic isotopes (Fig. 1.4B) and significantly higher proportions of primordial gases (Fig. 1.4C); such geochemical

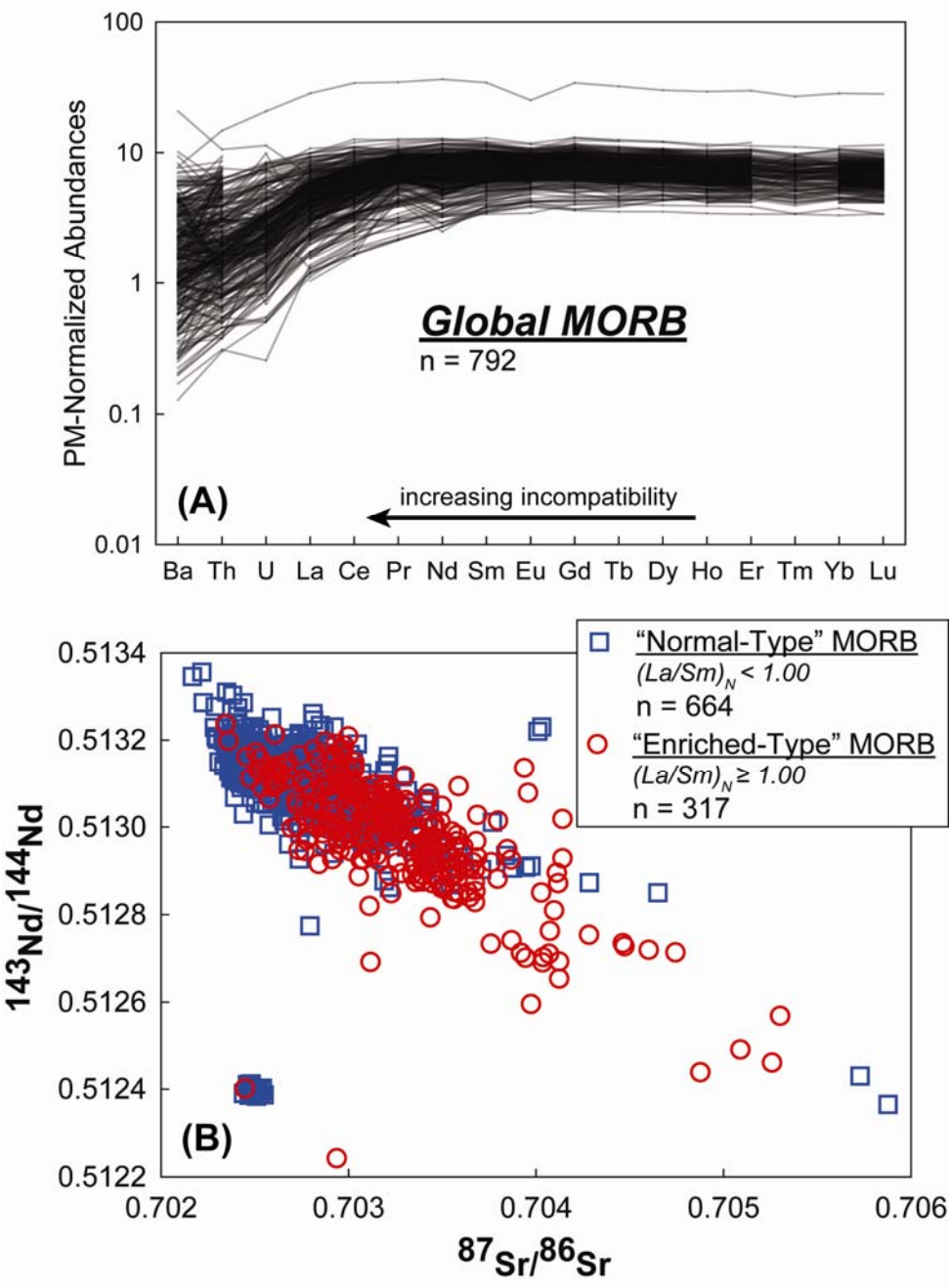

Fig. 1.3. Geochemical variability exhibited by global MORB. (A) Trace element variations observed in MORB range from extremely depleted in incompatible elements abundances to undepleted or even enriched in anomalous samples (data from Arevalo and McDonough, 2010). (B) Depleted, "normal-type" and enriched MORB, defined by their respective La/Sm ratios, show similar ranges in isotopic compositions (data downloaded from the PetDB database; http://www.petdb.org/).

signatures are opposite to those associated with MORB, which are primarily derived from a depleted and largely degassed peridotitic source region in the upper mantle. Further, numerous geochemical and geophysical studies have suggested that at least some OIB sources are derived from the lower mantle, perhaps as deep as the core-mantle boundary (*e.g.*, Russell *et al.,* 1998; Brandon *et al.,* 1999; Zhao, 2001; Courtillot *et al.,* 2003; Humayun *et al.,* 2004; Montelli *et al.,* 2004). As a result, the OIB source region has commonly been ascribed to an enriched, lower mantle reservoir that is both heterogeneous and chemically distinct from the DMM. However, whether or not a chemical boundary between the OIB and MORB source regions exists as discrete mantle domains (such as enriched veins, blobs or plums in a depleted matrix mantle) or as a stratified layer remains unresolved.

1.1.2 Potential chemical layering in the modern mantle

The dominant mode of convection in the modern mantle has been a hotly debated topic for decades. Whereas geophysical observations intimate significant material transfer throughout the entire mantle (*e.g.*, Creager and Jordan, 1984; van der Hilst *et al.,* 1991; Grand, 1994; Grand *et al.,* 1997; van der Hilst *et al.,* 1997; Zhao, 2001; Montelli, 2004; Li *et al.,* 2008), geochemical arguments based on chemical and isotopic differences between MORB and OIB (*e.g.*, Schilling, 1973; Zindler and Hart, 1986; Sun and McDonough, 1989; Hofmann 1997, 2003; Arevalo *et al.,* 2009), rare gas systematics (Kurz *et al.,* 1982; O'Nions and Oxburgh, 1983, Allègre *et al.,* 1983, 1987, 1996), isotope and trace element variations between continental and oceanic crust (*e.g.*, DePaolo and Wasserburg, 1976; O'Nions *et al.,* 1979; Arevalo and McDonough, 2010), and the Earth's radiogenic heat budget (Albarède and van der

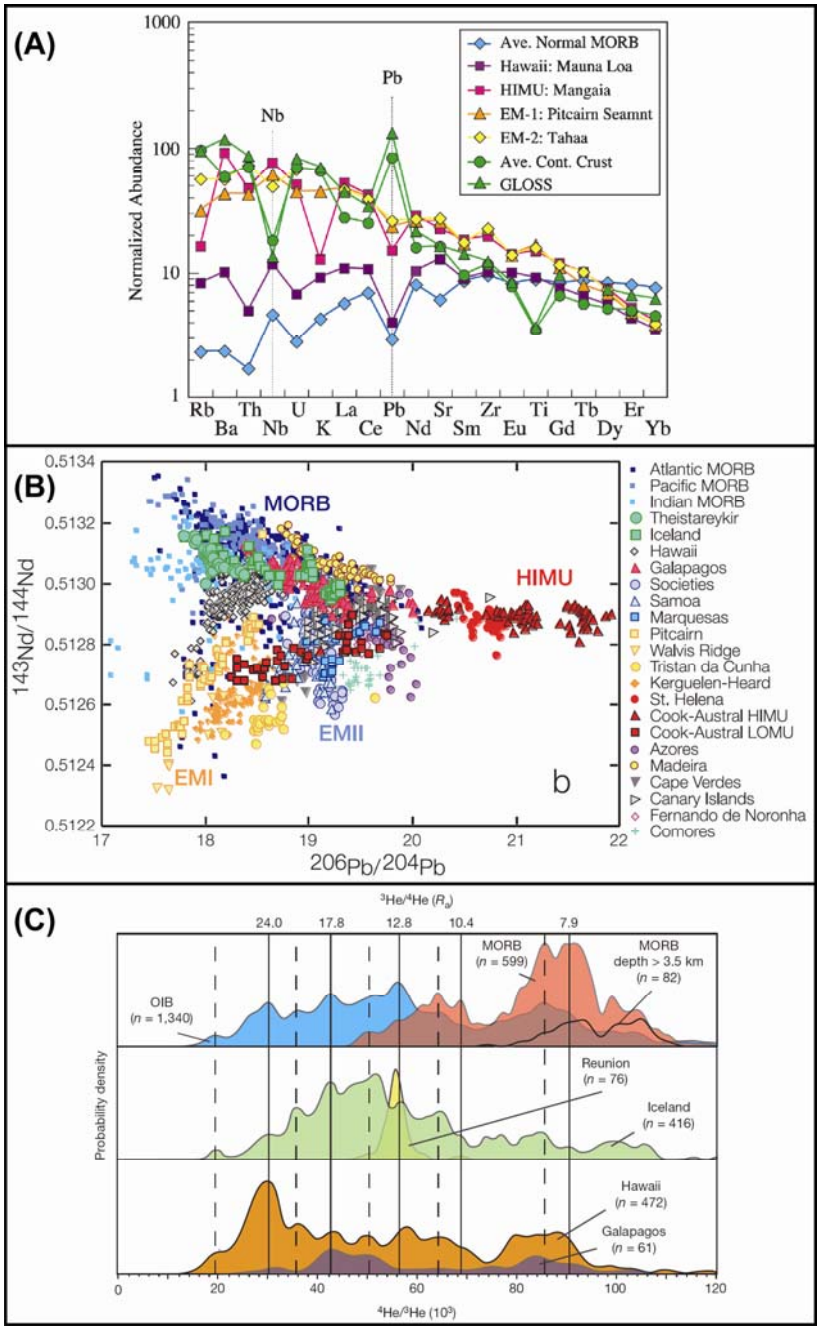

Fig. 1.4. Geochemical heterogeneity of the modern mantle and chemical distinctions between MORB and OIB. (A) Primitive-mantle normalized trace element abundances for model compositions of common N-MORB, continental crust, global loess (GLOSS), and several OIB end-members (from Hofmann, 2003). (B) Range of isotopic signatures exhibited by OIB compared to MORB (from Stracke *et al.*, 2003). (C) Probability density of helium isotopes observed in various OIB and MORB (from Parman, 2007).

Hilst, 2002; van Keken *et al.,* 2002; Arevalo *et al.,* 2009) require a multi-component mantle structure consisting of at least two independent reservoirs: a depleted upper mantle (as sampled by normal MORB) and a chemically enriched lower mantle or D″ layer at the core-mantle boundary (as sampled by OIB and potentially enriched-type MORB).

Although geochemical studies have established that the modern mantle is chemically heterogeneous and warrant the possibility of a stratified mantle structure, any potential layering must reside below the 660-km discontinuity in order to satisfy geophysical observations of mass transport across the transition zone as well as a simple mass balance of incompatible element abundances. The thin, basal D″ layer at the core-mantle boundary has commonly been interpreted to be a chemically-distinct dense layer that could explain the high $^{3}He/^{4}He$ observed in some OIB end-members (Albarède, 1998; Anderson, 1998; Coltice and Ricard, 1999), account for primordial solar-like helium, neon and xenon in the mantle (Tolstikhin and Hofmann, 2005; Tolstikhin *et al.,* 2006), satisfy the planet's budget of element abundances (*e.g.*, Ti, Nb and Ta; McDonough, 1991; Rudnick *et al.,* 2000; Arevalo and McDonough, 2010), and serve as the "hidden reservoir" called upon by ^{146}Sm-^{142}Nd and ^{147}Sm-^{143}Nd systematics of the sampled silicate Earth (Lassiter, 2004; Boyet and Carlson, 2005, 2006). Other studies have proposed that a deep dense boundary layer may exist at mid-mantle depths, potentially in the form of an undulating but globally continuous ~1000 km thick layered reservoir (Kellogg *et al.,* 1999; van der Hilst and Kárason, 1999; Arevalo *et al.,* 2009) or in the form of isolated thermochemical "piles" of material that may extend up to ~1500 km into the mid-mantle (*e.g.*, Tackley, 1998;

McNamara and Zhong, 2005) and correspond to the seismically imaged "superplumes" underlying southern Africa and the central Pacific (*e.g.*, Dziewonski, 1984; Su *et al.,* 1994; Li and Romanowicz, 1996; Romanowicz and Gung, 2002; Wang and Wen, 2004).

The lack of geophysical evidence for a mid-mantle thermochemical boundary layer (*e.g.*, Masters *et al.,* 2000; Vidale *et al.,* 2001; Wen *et al.,* 2001; Ni *et al.,* 2002; Wang and Wen, 2004) may reflect the insufficient resolution of current seismic models (*i.e.*, the boundary layer is not sharp enough to see seismically), or that the layer is so uneven it does not produce a clear reflection of seismic waves. Additionally, while some subducted slabs are observed to sink as deep as the core-mantle boundary, the loss of resolution of downwelling materials in tomographic studies (*e.g.*, van der Hilst *et al.,* 1997), three-dimensional models of heat transport across mid-mantle depths (Forte and Woodward, 1997), and the identification of ubiquitous chemical heterogeneities in the lowermost 1000 km of the mantle (*e.g.*, van der Hilst and Kárason, 1999; Garnero, 2000; Trampert *et al.,* 2004), suggest reduced mass transfer across mid-mantle depths, potentially corroborating a complex stratification scheme at depth in the modern mantle.

Many laboratory experiments and geodynamical models have been performed to understand the dynamical consequences of a dense layer in the Earth's deep mantle (*e.g.*, Tackley, 1998; Davaille, 1999a, 1999b; Davaille *et al.,* 2002; Tackley, 2002; Jellinek and Manga, 2002, 2004; McNamara and Zhong, 2004a,b, 2005), but relatively few of these studies have investigated the three-dimensional morphology of such a layer or the viability of a chemical layering at mid-mantle depths. Extensive

laboratory studies of thermochemical convection within fluids that are stratified in both viscosity and density indicate that at high buoyancy ratios (the ratio of the stabilizing chemical density anomaly to the destabilizing thermal density anomaly) convection remains stratified and fixed, and long-lived thermochemical plumes are generated at the interface; but at low buoyancy ratios, hot domes oscillate vertically while thin tubular plumes can rise from their upper surfaces (Davaille, 1999a, 1999b; Davaille *et al.,* 2002). A dense layer at the bottom of the mantle could induce lateral variations in temperature and viscosity that could, in turn, determine the location and dynamics of long-lived, spatially-fixed mantle plumes (Jellinek and Manga, 2002, 2004). Applied to the Earth's mantle, these observations (although oversimplified) indicate that thermochemical convection in a stratified mantle could theoretically explain long-lived, fixed intraplate ocean islands, the superplume features beneath Africa and the Pacific, and the survival of distinct geochemical reservoirs in the deep mantle over geologic time.

1.1.3 Enriched mantle components observed in OIB and MORB

The characteristic chemical enrichments observed in OIB and anomalous E-MORB have been a subject of intense study since the concept of fixed mantle plumes was first introduced (Wilson, 1963; Morgan, 1971). The source(s) of mantle hotspots, which give rise to intraplate OIB localities and are likely responsible for a significant fraction of E-MORB genesis, was first deemed to be undepleted, or "primitive," based largely on arguments for an undegassed mantle reservoir (*e.g.*, Kurz *et al.,* 1982; Allègre *et al.,* 1987; O'Nions, 1987; Honda *et al.,* 1991; Poreda and Farley, 1992). However, it was later realized that an unprocessed mantle reservoir was

unlikely, as OIB (and E-MORB) are highly variable in composition and show evidence for multiple enriched mantle end-members that are geologically old and defined by elevated U/Pb, Th/Pb and Rb/Sr, and depleted Sm/Nd and U/Th ratios relative to the depleted upper mantle source of common N-MORB (*e.g.*, Anderson, 1981; Hofmann and White 1982; Zindler and Hart, 1986). Additionally, almost all OIB have: i) more highly radiogenic Pb than primitive mantle (*e.g.*, Allègre, 1969); ii) supra-primitive Nb/U and Ce/Pb relative to primitive mantle (*e.g.*, Hofmann *et al.,* 1986); and, iii) abundances of incompatible elements that are too enriched to be accounted for by conventional melting of a primitive source without requiring unrealistically small degrees of partial melting. Therefore, OIB and enriched MORB cannot be derived from a chemically uniform, primitive source.

To account for the range of geochemical signatures observed in the global OIB spectrum (as described above), Hofmann and White (1982) suggested that the source enrichment observed in OIB originated from subducted oceanic crust, which may pile up at the core-mantle boundary and reach thicknesses of 100 km or more. Radiogenic heat produced within the stored oceanic crust, coupled with heat transfer from the core, would eventually cause the temperature to rise in this "slab graveyard" until the recycled layer became unstable, with diapirs developing and ascending into the upper mantle; the hot ascending materials would thus also serve to enrich the ambient depleted upper mantle, potentially contributing to the genesis of E-MORB while also functioning as the source for OIB. Although recycling of oceanic crust has garnered much support and has served for nearly 30 years as the dominant paradigm for creating mantle heterogeneities, recent studies offer a number of alternative

hypotheses, most notably a crust-free, metasomatic model of enrichment (*e.g.*, Sun and McDonough, 1989; Kelemen *et al.,* 1992; McKenzie and O'Nions, 1995; Niu and O'Hara, 2003; Pilet *et al.,* 2005, 2008).

1.1.4 Sources of mantle enrichment: A case study of Hawaii

The Hawaiian ocean island chain, which represents the surface manifestation of a mantle hotspot with the highest buoyancy flux (Davies, 1988; Sleep, 1990) and hottest mantle potential temperature (Putirka, 2008) of any modern hotspot, serves as a quintessential expression of intraplate volcanism and provides a unique perspective into the composition and lithology of the OIB and enriched MORB source regions. Both geophysical and geochemical studies suggest that the Hawaiian source region extends into the lower mantle, potentially as low as the core-mantle boundary (*e.g.*, Russell *et al.,* 1998; Brandon *et al.,* 1999; Zhao, 2001; Courtillot *et al.,* 2003; Montelli *et al.,* 2004; Li, 2008), and thus likely samples a lower mantle domain distinct from that of common N-MORB.

The shield volcanoes of the Hawaiian islands, which fall along two sub-parallel curvilinear trends, define two distinct compositional end-members (Fig. 1.5): Loa-trend volcanic centers (*e.g.*, Mauna Loa, Hualalai and Kahoolawe) are characterized by relatively high SiO_2, Al_2O_3, La/Nb, Sr/Nb, $^{87}Sr/^{86}Sr$, $^{187}Os^{188}Os$, $\delta^{18}O$ and low TiO_2, CaO, total iron, $^{143}Nd/^{144}Nd$, $^{176}Hf/^{177}Hf$, and $^{206}Pb/^{204}Pb$ (*e.g.*, Frey and Rhodes, 1993; Frey *et al.,* 1994; Roden *et al.,* 1994; Eiler *et al.,* 1996; Lassiter and Hauri, 1998; Blichert-Toft *et al.,* 1999), whereas Kea-trend volcanic centers (*e.g.*, Mauna Kea, Haleakala and Kilauea) exhibit opposite geochemical signatures. Additionally, lavas from the Koolau shield on Oahu define an anomalous,

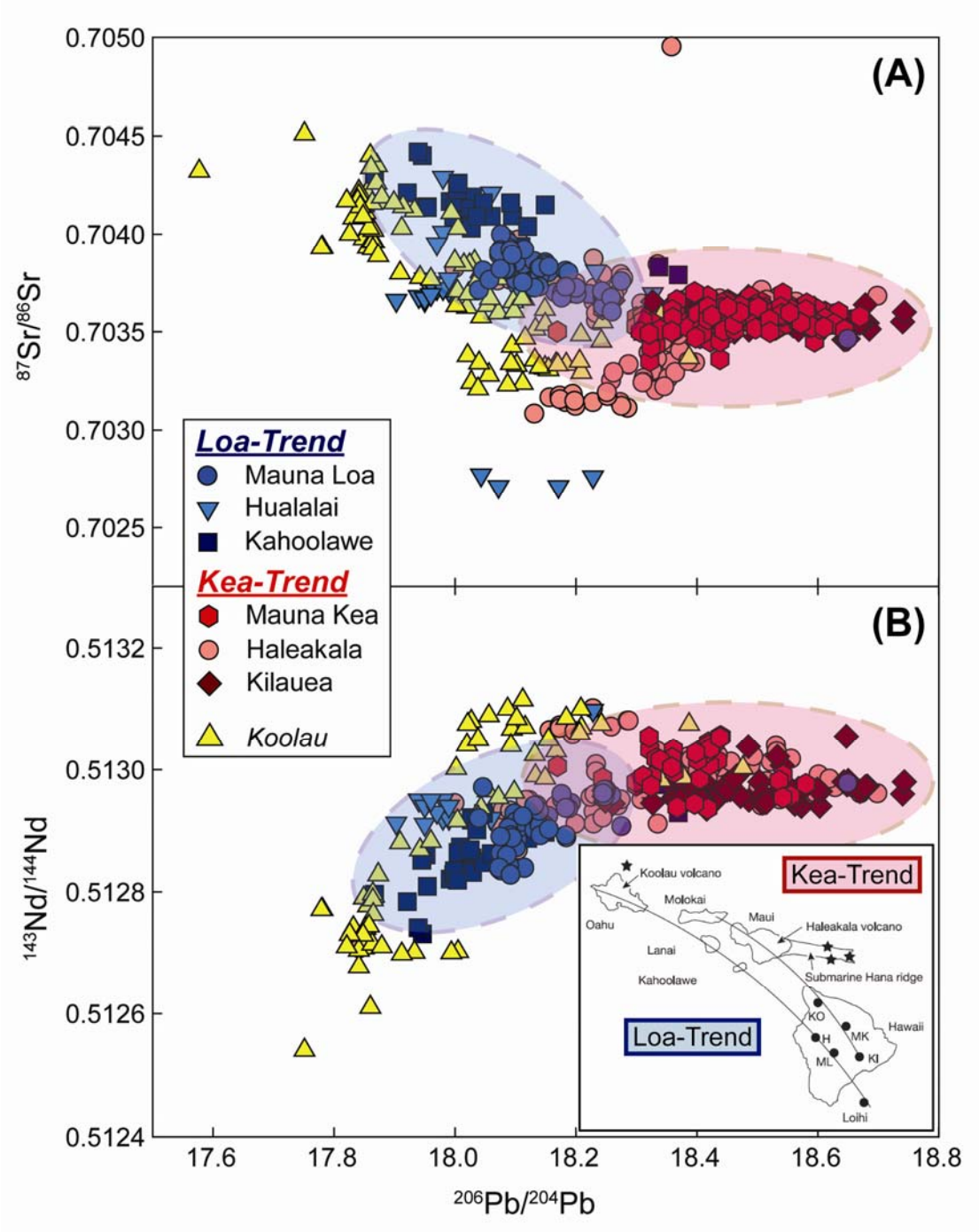

Fig. 1.5. Isotopic distinctions between Loa- and Kea-tend volcanic centers. Koolau lavas represent an extreme component of the Loa-trend signatures. (Data downloaded from the GEOROC database; http://georoc.mpch-mainz.gwdg.de/georoc/).

extreme end-member projected along the Loa-volcano trend (*e.g.*, Frey et al, 1994; Roden *et al.,* 1994; Lassiter and Hauri, 1998). Although some of the geochemical differences between different Hawaiian volcanic centers may be related to melting processes, there is a general consensus that the source for the Hawaiian shield volcanoes is chemically heterogeneous (*e.g.*, Hauri, 1996; Huang *et al.,* 2005; Frey *et al.,* 2005; Ren *et al.,* 2005). Moreover, geochemical observations and binary mixing arrays, coupled with principal component analyses, have indicated that the isotopic variations recorded by Hawaiian lavas require anywhere from two (Bennett *et al.,* 1996; Lassiter and Hauri, 1998; Blichert-Toft *et al.,* 1999) to three (Eiler *et al.,* 1996; Hauri, 1996; Eiler *et al.,* 1998; Blichert-Toft and Albarède, 2009) to four (Abouchami *et al.,* 2000; Eisele *et al.,* 2003) distinct mantle components in the Hawaiian source. Thus, lavas derived from the Hawaiian shield volcanoes, which represent mixing of several distinct source end-members, provide an ideal case study for the origin(s) of enrichment and potential role of recycled oceanic crust in the OIB (and potentially E-MORB) source regions.

1.2 Incompatible elements as tracers of MORB and OIB source characteristics

Elemental abundances and isotopic compositions of mantle melts are controlled by a number of processes, including: i) the degree of partial melting; ii) fractional crystallization; iii) crustal contamination/assimilation; iv) olivine (+ other minerals on the liquidus) addition/removal; v) tectonic provenance; vi) source lithology; and, vii) bulk source composition. Whereas major elements (defined by abundances of >1.0 wt.%) are largely buffered during mantle melting and, thus, primarily reflect the

petrology (*i.e.*, lithology and mineralogy) of the source, trace elements (defined by abundances of <0.1 wt.%) can vary by orders of magnitude in concentration and are sensitive to melting and crystallization processes (*e.g.*, fractional versus equilibrium melting/crystallization), tectonic conditions (*e.g.*, pressure, temperature, oxygen fugacity, etc.), metasomatism and/or crustal contamination, and potential post-eruptive alteration in addition to the source petrology. Highly incompatible elements (*e.g.*, HFSE, LILE and LREE), those which preferentially partition into the melt phase (*e.g.*, basaltic melt) over the residual solid (*e.g.*, mantle peridotite), are particularly likely to reflect source characteristics, as these elements are effectively removed from their respective source(s) after only a minor degree of partial melting.

In contrast to the enriched geochemical signatures characteristic of OIB and the continental crust, MORB are largely depleted in highly incompatible trace elements ($D_i^{sol/liq} << 1$; *e.g.*, K, Th, U, W, etc.), where $D_i^{sol/liq}$ is defined by the activity (a_i) of element *i* in the bulk *solid* and *liquid* phases at constant pressure and temperature:

$$D_{i(P,T)}^{sol/liq} = \frac{a_i^{sol}}{a_i^{liq}} = \frac{X_i^{sol}\gamma_i^{sol}}{X_i^{liq}\gamma_i^{liq}} \approx \frac{C_i^{sol}}{C_i^{liq}} \quad (1).$$

Following Henry's Law, the activity (a_i) may be related to the molar concentration (X_i) by an activity coefficient (γ_i) which approaches unity in dilute or low concentrations, such as those of trace elements in terrestrial sources (Shaw, 2006). As a result, the bulk partition coefficient may be approximated by the ratio of the concentration (C_i; by mass) of element *i* in the bulk *solid* to *liquid* phase.

In a mantle melt, pairs of highly incompatible elements ($D_{i,j}^{sol/liq} << 1$) are likely to record homogeneous source ratios and/or the weighted average ratio of all

the components in a heterogeneous source (Stracke and Bourdon, 2009), as these elements are concentrated in mantle melts over their respective source region. Concentration ratios of similarly incompatible trace elements (*i.e.*, $D_i^{sol/liq} \approx D_j^{sol/liq}$) also provide reliable insights into the trace element composition of the source. Concentration ratios that are relatively constant in oceanic basalts, including both MORB and OIB, and are independent of the absolute concentrations of the elements involved likely represent the mantle (*e.g.*, Hofmann *et al.,* 1986; Newsom *et al.,* 1986; Sun and McDonough, 1989). Such concentration ratios must be interpreted with caution, however, because unlike isotope ratios they may be fractionated as a function of varying melting/crystallization conditions.

"Canonical" trace element ratios (*c.f.*, Sims and DePaolo, 1997; Workman and Hart, 2005), such as Ti/Eu, Ba/Th, Nb/U, Zr/Hf, Ce/Pb, Nb/Ta, Sr/Nd, and Th/U, have been documented to remain relatively constant in oceanic basalts over a large range in incompatible element concentrations and MgO contents, and have consequently been summoned by geochemical studies to constrain terrestrial source compositions, including the MORB source (*e.g.*, Salters and Stracke, 2004; Workman and Hart, 2005; Boyet and Carlson, 2006), continental crust (*e.g.*, McLennan *et al.,* 1980; Taylor and McLennan, 1985; Sims *et al.,* 1990; Plank and Langmuir, 1998; Rudnick and Gao, 2003), bulk silicate Earth (BSE; *e.g.*, Hofmann, 1988; Sun and McDonough, 1989; McDonough and Sun, 1995; Palme and O'Neill, 2003), and core (*e.g.*, McDonough, 2003). However, several recent studies have taken a closer look into the systematics of canonical ratios and found that some of them are actually *not* conserved during mantle melting and/or vary between samples from different

geographical provenances, particularly Nb/U and Ce/Pb (Sims and DePaolo, 1997; Niu *et al.,* 1999; Stracke *et al.,* 2003; Willbold and Stracke, 2006; Pfänder *et al.,* 2007; Sun *et al.,* 2008; Arevalo and McDonough, 2010), and K/U (Arevalo *et al.,* 2009). Consequently, the true constancy of and systematic variations in canonical trace element ratios (as observed in samples derived from distinct global localities) need to be quantitatively examined to confidently establish the legitimacy of using such proxies as a guide to determining mantle source compositions.

Historically, the constancy of a canonical trace element ratio was demonstrated by a lack of correlation between the ratio *i/j* and the concentration of the elements involved (*i* or *j*). However, such comparisons are not statistically robust, as the two variables (*e.g.*, *i/j* vs. *i*) are not mathematically independent (Sims and DePaolo, 1997); hence, errors in the concentration measurement of *i* appear in both the x- and y-values, resulting in the unequal weight in their relative uncertainties. Additionally, variations in *i/j* are relatively small compared to those in *i* (or *j*) for any trace element pair with similar partitioning behavior, thus variations in the ratio (typically <10) are relatively small in comparison to the variations seen in concentration (typically 10–10^3; Arevalo and McDonough, 2008, 2010 and references therein). An alternative representation that provides a statistically robust analysis of the relative incompatibilities of two or more trace elements is a log-log covariation diagram (*e.g.*, log *i* vs. log *j*; Sims and DePaolo, 1997; Hofmann, 2003; Willbold and Stracke, 2006; Pfänder *et al.,* 2007; Arevalo and McDonough, 2008; Sun *et al.,* 2008; Arevalo *et al.,* 2009; Arevalo and McDonough, 2010). This type of diagram plots statistically independent variables that are dispersed across a wider distribution and a

similar order of magnitude along both axes. In this way, the data and their associated errors are weighted uniformly across the range of values.

The potential for partial melting processes to fractionate "canonical" ratios can be (and has been) evaluated through log-log covariation assessments of the trace element variability seen in MORB, which is presumed to reflect both the heterogeneity of the source as well as different degrees of partial melting and/or fractional crystallization. In a log-log covariation diagram (Fig. 1.6), a slope (m) equal to unity ($m = 1.0$) indicates an equally incompatible trace element pair, whereas a slope that is statistically distinct from unity ($m \neq 1.0$) represents a trace element pair with dissimilar geochemical behavior during MORB genesis; more specifically, a slope of greater than unity ($m > 1.0$) indicates a more incompatible element along the ordinate axis, whereas a slope of less than unity ($m < 1.0$) indicates a more incompatible element along the abscissa. In this way, the incompatibility of trace elements may be statistically assessed, and the true constancy and variability of canonical trace element ratios evaluated.

1.3 The scope of this study

The focus of this dissertation involves evaluating the dominant paradigms of the mantle (*e.g.*, layered vs. non-layered structure) through a global geochemical assay of both MORB and OIB, including an assessment of the relative chemical enrichment and potential volume of the MORB and bulk OIB source regions. The primary tools with which this geochemical investigation will rely are precise measurements of trace element abundances, particularly highly incompatible trace elements, in a global suite

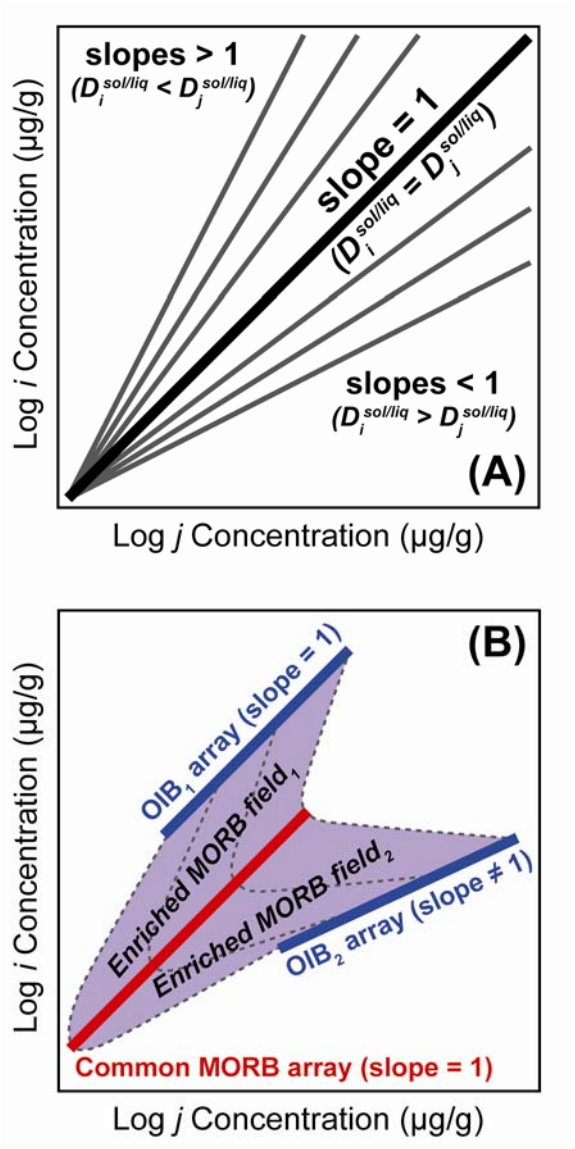

Fig. 1.6. Schematic representations of log-log covariation diagrams. (A) In these types of graphical depictions, a slope equal to unity ($m = 1.0$) indicates an equally incompatible pair of elements; a slope greater than unity ($m > 1.0$) signifies a more incompatible element along the ordinate (y-) axis, whereas a slope of less than unity ($m < 1.0$) signifies a more incompatible element along the abscissa (x-axis). (B) The utility of a log-log covariation diagram may be compromised due to the effects of source mixing; two equally incompatible elements may appear to behave dissimilarly due to mixing between two source components with distinct ratios, regardless if the two elements involved behave equally in both source components. Revised from Arevalo *et al.*, (2009).

of MORB and OIB. Of particular importance to this study are the abundances of: i) tungsten (W), which exhibits dual behavior as both a siderophile (iron-loving) and highly incompatible lithophile (oxygen-loving) element, and may serve as a sensitive tracer of putative core-mantle interactions; ii) potassium (K), which provides a measure of the radiogenic heat budget and volatile element depletion of the Earth; iii) uranium (U), which behaves similarly to both W and K during silicate differentiation and also serves as a radiogenic heat source; and, iv) thorium (Th), which contributes the greatest amount of radiogenic heat to the planet's contemporary heat budget and also represents one of the most incompatible elements that is not significantly affected by fluid fluxes (and thus is conserved during subduction zone processes and arc magmatism). By examining the geochemical behavior/affinities of these elements, and establishing a model composition for both the MORB and OIB source reservoirs, the chemical structure of the mantle (including the ubiquity and scale of mantle heterogeneities) may be qualitatively *and* quantitatively established.

1.3.1 W in mantle-derived materials: Evidence for putative core-mantle exchange?

Tungsten is a refractory trace element whose initial abundance in the silicate Earth can be calculated from chondritic relative abundances without a volatility correction. Difficulties in determining the abundance of W in the silicate Earth stem from the binary behavior of the element: under reducing conditions (low oxygen fugacity), such as during of core formation, W has behaved as a moderately siderophile element and thus preferentially partitioned into metallic phases over silicates; under more oxidizing conditions, such as during present-day mantle melting and the evolution of the continental crust, W behaves as a highly incompatible lithophile element and thus

preferentially partitions into silicate melts over silicate residua. Consequently, the dual behavior of W has left the modern mantle largely depleted in this element (Fig. 1.7); >90% of the Earth's store of W has been extracted into the planet's metallic core, with approximately ⅖ of the remaining <10% sequestered in the continental crust. Although the depleted composition of mantle-derived melts (particularly MORB) makes the measurement of W a difficult analytical feat, the depletion of W in mantle source regions may allow for putative core-mantle interactions to be detected by the abundance and isotopic composition of this element in deep mantle-derived materials.

In addition to the binary geochemical behavior displayed by W under varying redox conditions, W boasts another exceptional characteristic: some fraction of isotope ^{182}W is the daughter product of the short-lived ^{182}Hf radionuclide, which undergoes double beta-decay with a half-life of 8.90 ± 0.09 Ma (2σ; Vockenhuber *et al.,* 2004). Because of the short-lived nature of the $^{182}Hf \rightarrow {}^{182}W$ radiogenic system, any existing W isotopic heterogeneities within the Earth must have been inherited during the first ~50 Ma of solar system history (the functional lifetime of ^{182}Hf). Similar to W, Hf is also a refractory trace element during accretion, and thus its initial concentration may too be determined through chondritic relative abundances without a volatile correction. However, Hf and W differ in their geochemical affinities; under the reducing conditions of core formation, Hf acted as a lithophile element, and thus preferred to remain in silicate phases, whereas W behaved as a moderately siderophile element. Consequently, the Earth's metallic core has a Hf/W ratio of ~0,

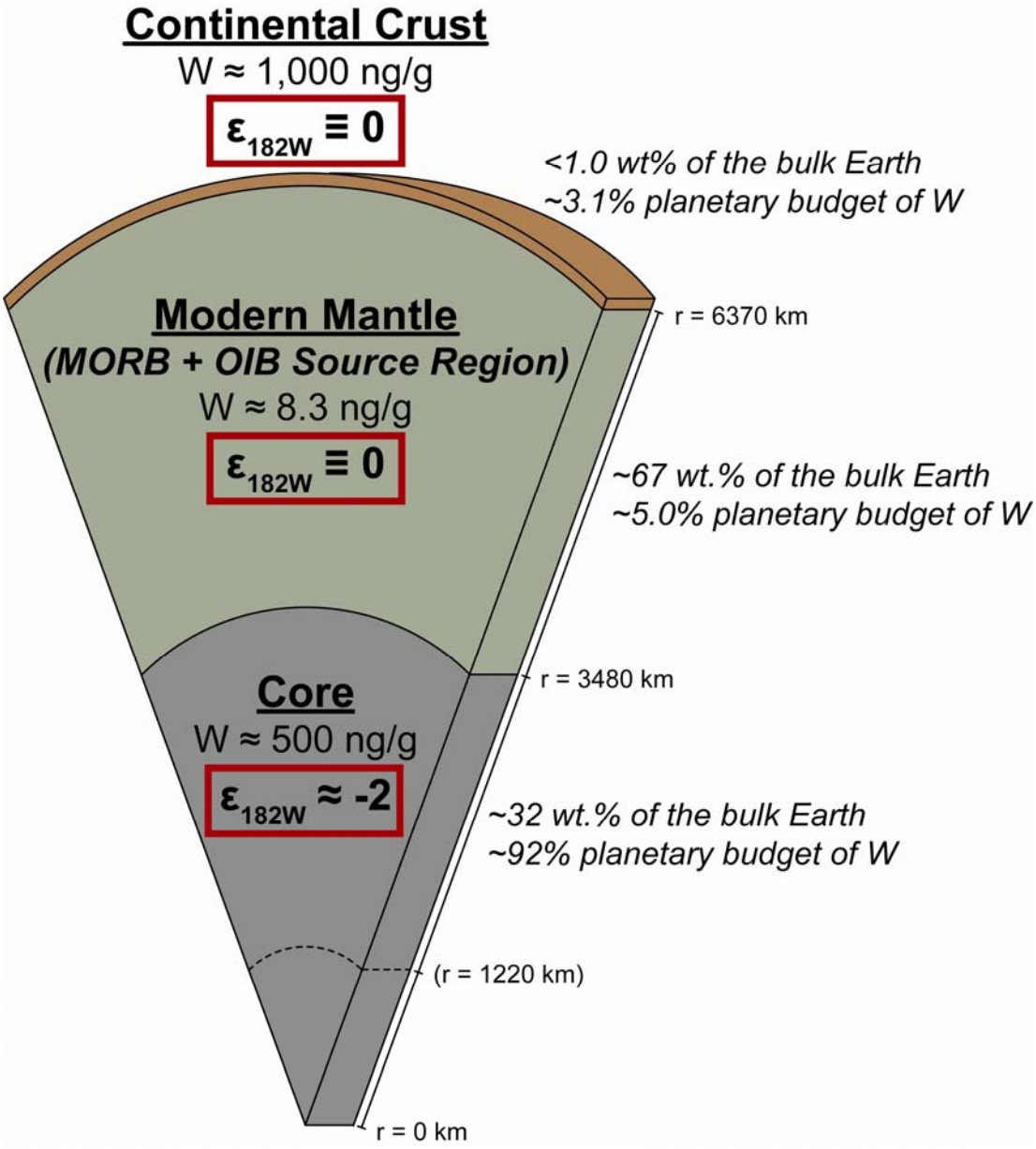

Fig. 1.7. Elemental abundance and isotopic composition of W in the Earth's major reservoirs, namely the silicate Earth (modern mantle + continental crust) and core. The modern mantle, as represented by both the MORB and OIB source regions, is >50x depleted in W relative to the core and >100x depleted relative to the continental crust. The silicate Earth, as represented by both the modern mantle and continental crust, is defined by $\varepsilon_{182W} = 0$, requiring the core to be characterized by $\varepsilon_{182W} = -2.2 – -2.4$ in order to reconcile the W isotopic composition of the bulk Earth with that of chondritic meteorites.

and therefore a W isotopic composition that was inherited from the effective time of core-mantle separation (≤30 Ma after t_0; Jacobsen, 2005 and references therein).

In 2002, three independent research groups showed that chondrites, stony meteorites that originated from an asteroidal parent body that was too small to have been affected by melting and/or differentiation processes and are therefore thought to represent the composition of the bulk Earth, were 2 parts-per-10,000, or 2 ε-units, depleted in ^{182}W relative to the silicate Earth (Kleine *et al.,* 2002; Schoenberg *et al.,* 2002; Yin *et al.,* 2002). Therefore, assuming the W isotopic composition of the bulk Earth matches that of chondrites, the Earth's core must have an ε_{182W} of -2.2 – -2.4 relative to the silicate portion of the Earth ($\varepsilon_{182W} \equiv 0$). Consequently, mantle materials derived from deep source regions near the core-mantle boundary may record putative core-mantle interactions through small depletions in ^{182}W and/or enrichments in W abundances (as W is concentrated in the core) relative to a lithophile element with similar geochemical behavior (*e.g.*, Ba, Th and/or U). Although initial studies found that no such geochemical signature could be distinguished in Hawaiian picrites (Scherstén *et al.,* 2004), which had previously been suggested to record a core signature based on ^{186}Os-^{187}Os isotope systematics (Brandon *et al.,* 1999), the abundance of W in the silicate Earth (modern mantle + continental crust) and core must be better constrained before core-mantle exchange can be adequately modeled by W isotopes or relative abundances. The results and conclusions of this study regarding these topics are reported in Chapter 4.

1.3.2 K/U in the silicate Earth: A measure of the terrestrial radiogenic heat budget and volatile element depletion of the bulk planet

The abundance of potassium (K) in the silicate Earth provides control on the composition of the modern mantle, the planet's radiogenic heat budget and the volatile depletion of the Earth. The distribution of K in the Earth's major silicate reservoirs (*i.e.*, the MORB and OIB mantle source regions + the continental crust) is also an important variable for understanding the dominant mode of convection in the mantle, the thermal evolution of the planet and the concentration of Pb in the planet's core. Potassium is a moderately volatile element (Fig. 1.8), and thus its initial abundance in the silicate Earth cannot be established by chondritic relative abundances without a volatile correction. As a result, the terrestrial abundance of K provides a measure as to the volatile element depletion of the Earth relative to other planetary bodies and chondritic meteorites. Potassium also behaves as a highly incompatible element during mantle melting, and thus discerning the abundance of K in the MORB and OIB source regions provides a perspective into the mass fraction of each of these reservoirs. As K is one of the three primary heat-producing elements in the Earth (Th and U being the other two) and at present produces some 4 TW of radiogenic heat (~10% of the planet's total global heat flux), the terrestrial K/U ratio also relays information regarding the heat budget of the Earth, including the Urey ratio (Ur), which serves to relate the radiogenic heat production within a body to its total heat output and serves as a proxy to the mode of convection in the modern mantle.

Determining the K content of the silicate Earth has traditionally hinged on establishing the ratio of K to a refractory, lithophile element that behaves similarly

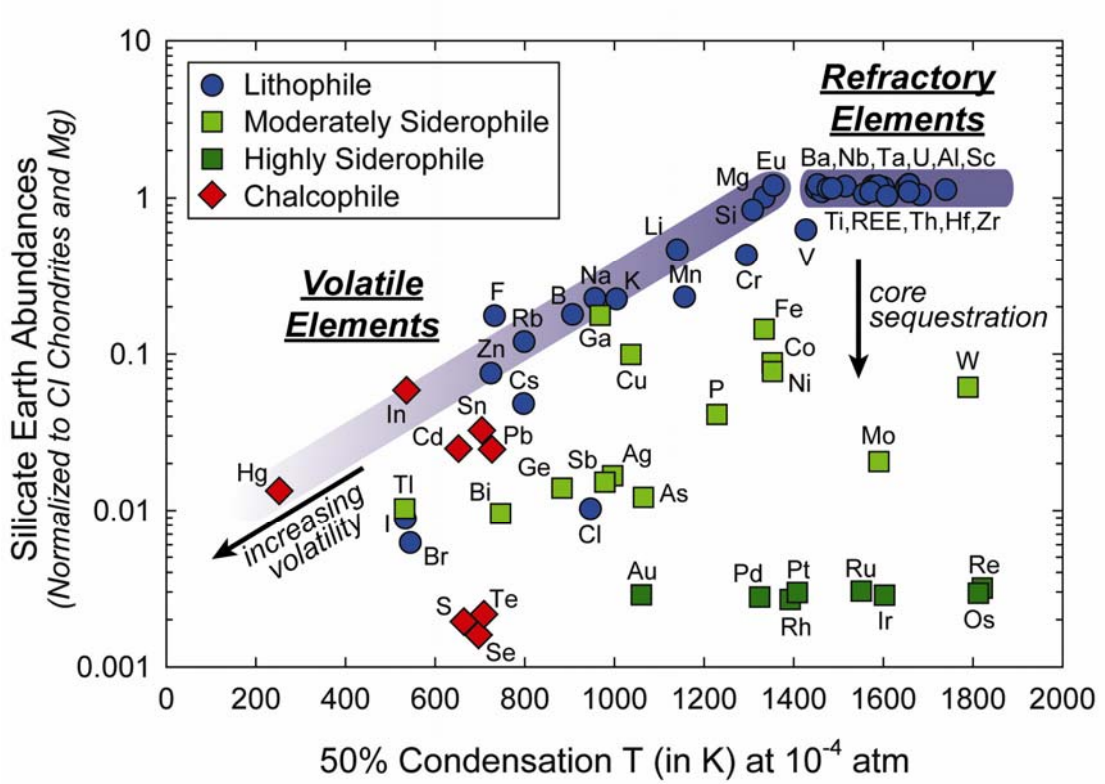

Fig. 1.8. Elemental abundances in the silicate Earth (normalized to CI carbonaceous chondrites and Mg) plotted relative to 50% condensation temperatures at 10^{-4} atm pressure (a commonly used proxy for the nebular condensation sequence). Potassium plots near the volatility trend line with a 50% condensation temperature around 1000 K. Siderophile and chalcophile elements generally plot below the refractory and volatility trend lines due to sequestration into the core. Data for condensation temperatures and the composition of CI chondrites are from Lodders (2003); the composition of the silicate Earth is primarily from McDonough and Sun (1995), with updated values for W and K from Arevalo and McDonough (2008) and Arevalo *et al.*, (2009), respectively.

during silicate differentiation, namely U. However, for over 25 years the dominant model for the K/U ratio of the silicate Earth has hinged on a relatively small dataset of MORB (n = 22; Jochum *et al.,* 1983). The geochemical similarities between K and U and can be used to confidently establish the K/U ratio of the silicate Earth. Thus, a comprehensive examination of mantle-derived samples, including MORB, OIB and continental flood basalts, needs to be examined in concert with the composition of samples derived from the continental crust. Only by considering all major inventories of K can the K/U ratio of the entire silicate portion of the Earth be adequately determined. The results and conclusions of this study regarding these topics are reported in Chapter 5.

1.3.3 A compositional model of MORB

Historically, it has been assumed that the modern mantle comprises two major silicate reservoirs: the MORB and OIB source regions. As previously mentioned, MORB are typically abundant (75% of the planet's annual magmatic output), accessible (the mid-ocean ridge system spans >60,000 km in length) and representative of a relatively simple melting history (decompression melting). Geochemical models of MORB composition have generally only considered depleted samples (*e.g.*, Hofmann, 1988; Sun and McDonough, 1989), thereby underestimating the degree of heterogeneity and range of incompatible element enrichments observed in these samples. As a result, the true variability observed in MORB, and a representative model that adequately describes the characteristic composition of global MORB samples, have yet to be adequately established.

In order to determine a representative trace element composition for MORB, and by extension the MORB source, a global distribution of both depleted and enriched samples needs to be considered. However, the frequency distribution of trace elements, particularly highly incompatible trace elements, show skewed geometries in both continental crustal and mantle samples (*e.g.*, Ahrens, 1954; McDonough, 1990). As a result, the arithmetic mean of the population does not provide an adequate description of the representative composition. Taking the logarithm of the concentrations of trace elements, though, normalizes the data into a more Gaussian distribution, thus allowing for a traditional statistical treatment of the data. A comprehensive model of MORB composition would serve as the first step for quantitatively modeling mantle heterogeneity, by beginning to quantify the chemical distinctions between the mantle's major reservoirs: the MORB and OIB source regions. The results and conclusions of this study regarding these topics are reported in Chapter 6.

1.3.4 W, Th and U abundances in primary OIB melts: Inferences into the enrichment and mass fraction of the OIB source region

Ocean island basalts show even greater trace element and isotopic variability than the spectrum observed for global MORB. Further, different OIB localities commonly reflect varying degrees of partial melting, different contributions of pyroxenite in their sources, and different phase assemblages on the solidus and liquidus. In order to deconvolve the effects of all of these processes and attempt to characterize the common source component observed in various OIB, the compositions of the parental melts from multiple volcanic centers need to be established. By definition, parental

melts represent the most primitive, undifferentiated melts of the source region. To establish the geochemical composition of a parental melt, suites of cogenetic OIB need to be analyzed to identify systematic geochemical trends in trace element abundances as a function of a magmatic processing and evolution (for which MgO can serve as a proxy). Once a parental melt composition has been determined, a melting model can be used to estimate the source composition.

A representative model composition for global MORB and its source allow inferences to be drawn regarding the OIB source region, assuming the modern mantle is comprised mainly of these two source regions (presuming a negligible mass fraction for a "hidden" reservoir, despite geochemical evidence for an under-sampled silicate reservoir at depth; *e.g.*, McDonough, 1991; Rudnick *et al.,* 2000; Boyet and Carlson, 2005; Tolstikhin and Hofmann, 2005; Boyet and Carlson, 2006; Tolstikhin *et al.,* 2006; Arevalo and McDonough, 2010). Following an appropriate melting model, the composition of the MORB source region (DMM) may be inferred based on a model composition for global MORB. This model composition for the MORB source, in turn, allows us to infer the relationship between the representative composition of the common OIB source region as a function of the mass fraction of this reservoir (Fig. 1.9). A study of OIB parental melts, and by implication OIB source compositions, will allow for the identification of the average OIB source enrichment, and thus provide an estimate of the mass fraction of the OIB source region. In this way, we may begin to shed light, quantitatively, on the scale of heterogeneity and dominant chemical structure of the mantle. The results and conclusions of this study regarding these topics are reported in Chapters 6 and 7.

1.3.5 Summary and conclusions

This dissertation focuses on characterizing the chemical composition of the modern mantle, including both the MORB and OIB source regions, and quantitatively evaluating the degree of heterogeneity and the dominant structure of this volume. To facilitate these goals, an analysis of the trace element chemistry of a comprehensive, global distribution of mantle-derived materials has been performed. Trace element abundances provide insights into both magmatic processes as well as source characteristics, and thus are the ideal tool for evaluating the chemical structure of the modern mantle. The conclusions of this study, including a review of future work considerations, are supplied in Chapter 8.

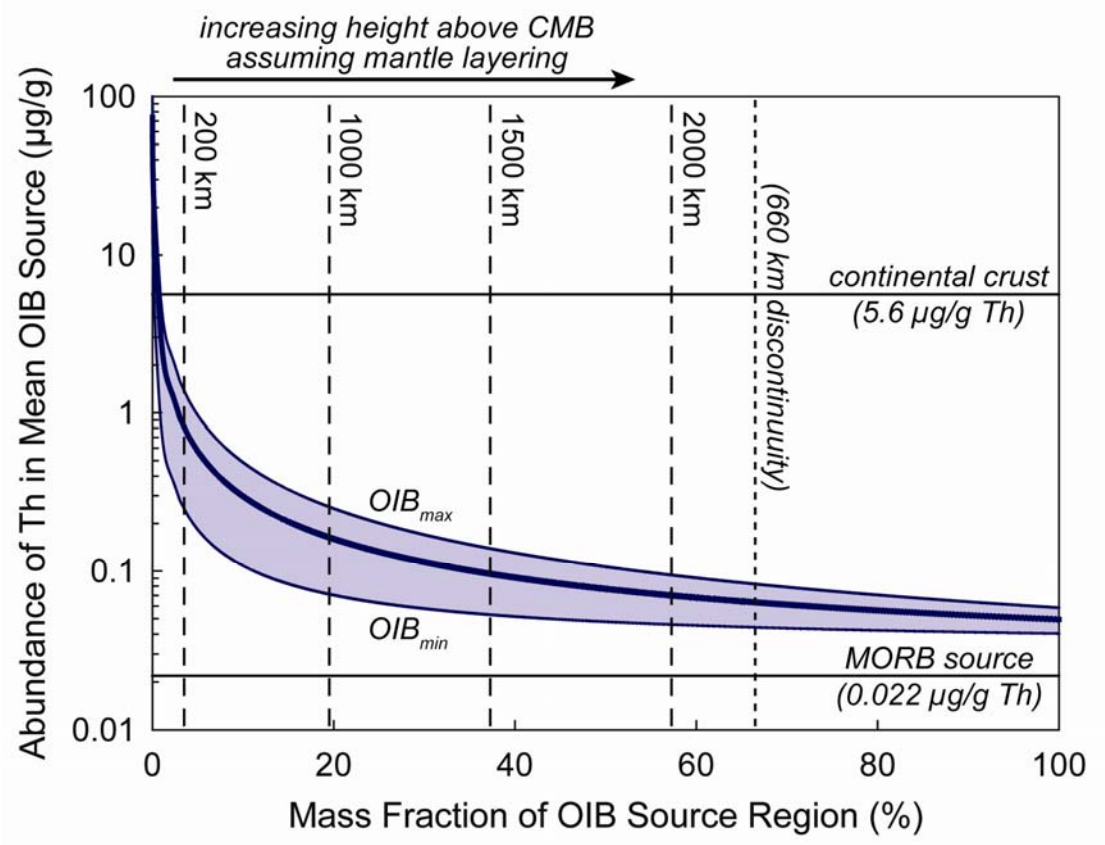

Fig. 1.9. Tradeoff between the relative enrichment and size of the mean OIB source region according to the mass balance of Th in the silicate Earth. The curves for OIB_{max} and OIB_{min} represent the upper and lower bounds of the propagated uncertainties in the model compositions of the continental crust (Rudnick and Gao, 2003) and MORB source (Arevalo and McDonough, 2010). The mass balance calculation assumes a two-box model of mantle structure and follows the simple formula: $C_{Th}^{SE} = C_{Th}^{CC} X^{CC} + C_{Th}^{DMM} X^{DMM} + C_{Th}^{EM} X^{EM}$, where X represents the mass fraction of continental crust (CC), depleted MORB mantle (DMM) and enriched mantle source of OIB (EM), and C_{Th} represents the concentration of Th in the silicate Earth (SE) and its constituent reservoirs. The lack of overlap between the composition of the MORB source and a mantle that is 100% composed f the OIB source indicates that the MORB source and continental crust are not completely complementary in their trace element budgets, according to mass balance.

Chapter 2: Analytical Methods[1,2,3,4,5]

[1] R. Arevalo Jr. created/wrote all the materials in Sections 2.1 through 2.3.

[2] Section 2.2 has been published as Supplemental Materials for:
Arevalo Jr., R. and McDonough, W.F., 2008. Tungsten geochemistry and implications for understanding the Earth's interior. *Earth and Planetary Science Letters* (272), 656-665, doi:10.1016/j.epsl.2008.05.031.

[3] Section 2.3 has been published as Supplemental Materials for:
Arevalo Jr., R., McDonough, W.F., and Luong, M., 2009. The K/U ratio of the silicate Earth: Insights into mantle composition, structure and thermal evolution. *Earth and Planetary Science Letters* (278), 361-369, doi:10.1016/j.epsl.2008.12.023.

[4] R. Arevalo Jr. developed the medium-resolution LA-ICP-MS analytical method and measured the trace element chemistry of all the samples and standards reported in Section 2.4. Electron probe microanalysis of these samples was performed chiefly by P.M. Piccoli with the assistance of R. Arevalo Jr. Both R. Arevalo Jr. and W.F. McDonough contributed to the interpretation of the data. The text, tables and figures of Section 2.4 were written/created by R. Arevalo Jr.

[5] Section 2.4 has been submitted for publication and is currently in revision as:
Arevalo Jr., R., McDonough, W.F., and Piccoli, P.M., in revision. *In situ* determination of first-row transition metal, Ga and Ge abundances in geological materials via medium-resolution LA-ICP-MS. *Geostandards and Geoanalytical Research*.

2.1 Laser ablation principles and instrumentation: A review

In situ methods of chemical analysis provide an ideal way to analyze precious sample specimens from both the geological and non-geological realm without introducing potential contaminants or interferences via wet chemical procedures. In particular, laser ablation (LA-) inductively-coupled plasma mass spectrometry (ICP-MS) allows for: i) bulk and/or spatially-resolved, ng/g-level (multi-)element measurements of micrometer-scale sample specimens; ii) negligible sample processing (which is time-consuming, costly and can introduce impurities and/or isobaric interferences); iii)

minimal analytical blanks; iv) low limits of detection; v) limited oxide production and spectral matrix effects; and, vi) the ability to avoid surface and grain-boundary contamination. Additionally, laser ablation methods provide rapid data acquisition over a wide mass range, require smaller quantities of sample (≤μg) compared to traditional solution analyses (≥mg), and allow the implementation of either internal and external calibration techniques, each of which has been demonstrated to yield reproducible data (commonly ≤3% precision at the 2σ-level) that are consistent with isotope dilution and high-precision standard addition measurements within 95% confidence limits (*e.g.*, Jochum *et al.,* 2005a; Jochum *et al.,* 2007; Arevalo and McDonough, 2008; Arevalo *et al.,* 2009). Data acquired through LA-ICP-MS processing have also consistently been shown to correlate with measurements from comparative bulk (*e.g.*, instrumental neutron activation analysis, INAA, x-ray fluorescence, XRF, and spark source mass spectrometry, SS-MS) and microanalytical (*e.g.*, electron probe microanalysis, EPMA, secondary ion mass spectrometry, SIMS, and proton induced x-ray emission, PIXE) methods of chemical analysis (*e.g.*, Ludden *et al.,* 1995; Pearce *et al.,* 1997; Norman *et al.,* 1998; Jochum *et al.,* 2000; Gao *et al.,* 2002; Jochum *et al.,* 2005a, 2006, 2007). The primary drawbacks to LA-ICP-MS are the destructive nature of laser ablation processing, the limited ion transmission (typically 0.1-0.3%) associated with the method, and the inability to chemically separate the targeted elements from potential isobaric interferences.

2.1.1 Spectral absorption and photon-substrate coupling

During laser ablation processing, the interaction (or coupling) between the incident laser radiation and the surface of the substrate, such as a geological sample, depends

on the parameters of the laser beam, including the incident irradiance, wavelength of light, spatial and temporal coherence, and pulse duration, as well as the optical (*i.e.*, transparency), physical (*i.e.*, microstructure) and chemical properties (*i.e.*, elemental composition) of the target material and gas atmosphere (*e.g.*, Russo, 1995; Bäuerle, 1996; Durrant, 1999 and references therein). The incident laser light may be attenuated by one of three primary mechanisms: i) transmission; ii) reflection; or, iii) absorption (see Fig. 2.1). The spectral transmittance (τ), or the ratio of radiation intensity that is transmitted (I_t) to the incident intensity (I_i) at a given wavelength (λ), provides a measure as to the transparency of the substrate and is given by:

$$\tau(\lambda) = \frac{I_t(\lambda)}{I_i(\lambda)} \qquad (2\text{-}1).$$

The spectral reflectance (R), or the ratio of the total reflected intensity (I_R) to the incident intensity (I_i), may be defined as:

$$R(\lambda) = \frac{I_R(\lambda)}{I_i(\lambda)} \qquad (2\text{-}2).$$

The spectral absorbance (α), or the intensity that is absorbed (I_a) by the substrate at a given wavelength, may be defined as:

$$\alpha(\lambda) = \frac{I_a(\lambda)}{I_i(\lambda)} = I_i - I_t - I_r \qquad (2\text{-}3),$$

and decreases exponentially as a function of penetration depth (x), such that:

$$I_a(x) = e^{-a(\lambda)x} \qquad (2\text{-}4).$$

The absorption coefficient, $a(\lambda)$, characterizes the absorption characteristics of the substrate material.

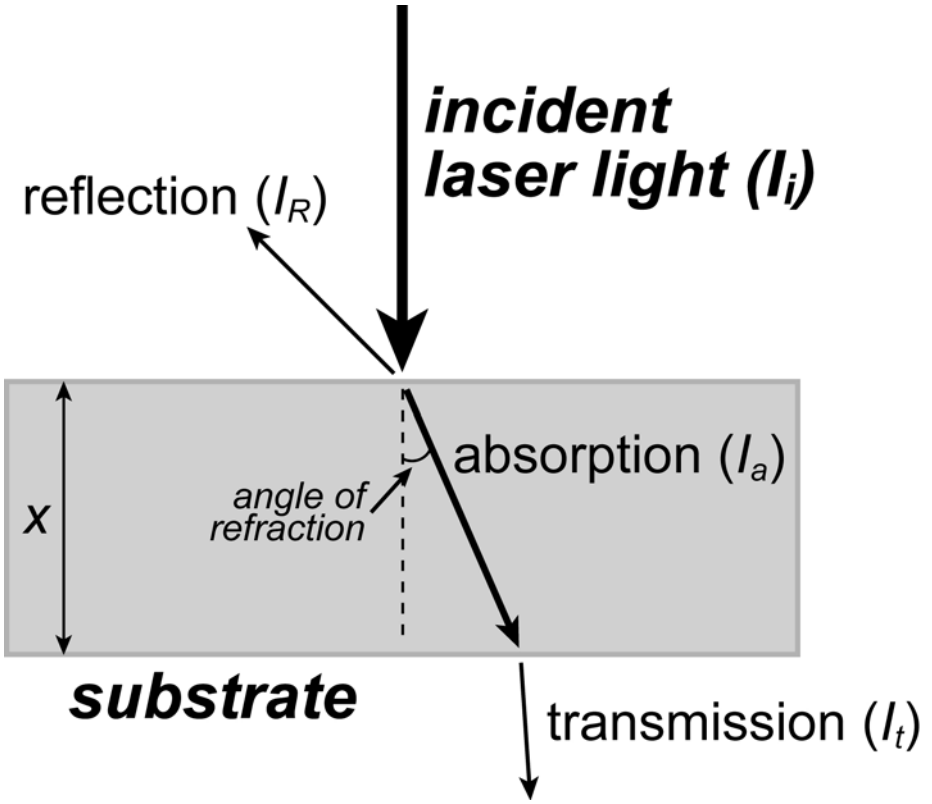

Fig. 2.1. Schematic representation of spectral transmittance (I_t), reflectance (I_R) and absorbance (I_a) of electromagnetic radiation (I_i) incident on a substrate of thickness *x*.

The incident radiation intensity (I_i; typically in W, or $J \cdot s^{-1}$), which effectively represents the incident radiant flux when the radiation is directed perpendicular to the substrate surface, represents the radiant energy (in J) transported per unit time (in s) by the electromagnetic waves produced by the laser system. Alternatively, the irradiance (E_i; in $W \cdot cm^{-2}$) is defined as the radiant flux incident on an effective target area. The total irradiation (in $J \cdot cm^{-2}$) experienced by the substrate surface during laser ablation analysis is determined by the incident irradiance integrated over a given time interval (*e.g.*, the pulse duration, or dwell time of each laser pulse). For a more thorough review of optics and the physics behind photometrics, the reader is referred to the Handbook of Physics (2006).

2.1.2 Thermal and non-thermal processes induced during laser ablation analysis

Laser ablation is the process of removing substrate material, most commonly in a solid sample, by irradiating the surface of the sample with an intensive beam of coherent (*i.e.*, low divergence), collimated (*i.e.*, parallel directionality) and monochromatic (*i.e.*, single wavelength) radiation. The term laser is an acronym for light amplification by stimulated emission of radiation, where light may be defined by any electromagnetic radiation and is not limited to the visible spectrum (*i.e.*, approximately 400-700 nm in wavelength). Incident photons that are absorbed by the substrate may induce thermal or non-thermal (*i.e.*, photo-chemical and photo-mechanical) processes, depending primarily on the intensity, wavelength and duration of the laser radiation in addition to the optical and physical properties of the substrate.

Thermal processes, which ultimately result in the heating, melting and/or vaporization of the substrate, primarily occur at low radiation intensities as electrons

in the substrate surface absorb incident photons and transfer the energy into the lattice, typically as vibrational, rotational or translational kinetic energy. Thermal processes dominate when the incident radiation intensity (I_i) is below a critical threshold for ablation (I_c), which may be written as $I_i < I_c$, but also occur if the duration of irradiance, or laser pulse duration, significantly exceeds the phonon relaxation time of the substrate material. Because most solids have a range of phonon relaxation rates on the order of 10^{-6} to 10^{-12} seconds (*e.g.*, Bäuerle, 1996), only lasers that can produce high irradiance (*e.g.*, $\geq 10^9$ W·cm^{-2}) and have short pulse durations (*e.g.*, ≤10 ns) can adequately serve to generate stoichiometric ablation of most solid materials (*e.g.*, Ready, 1965; Russo, 1995; Bäuerle, 1996; Young *et al.,* 1998; Jackson, 2001; Russo *et al.,* 2002; Excimer Laser Technology, 2005).

Above the critical ablation threshold (*i.e.*, $I_i > I_c$), the incident photon energy is higher than the bonding energy between neighboring atoms in the substrate, thus allowing the radiation to directly break the atomic lattice and induce a number of phenomena, including: an explosive ejection of atomic, ionic, molecular, and particulate species; shock waves; plasma initiation and expansion; and, (ideally) limited fractional vaporization and/or melting (*e.g.*, Ready, 1965; Russo, 1995; Bäuerle, 1996; Mao *et al.,* 2000 a,b,c; Russo *et al.,* 2002; Excimer Laser Technology, 2005). The critical ablation thresholds of most inorganic insulators and semi-conductors, such as silicate minerals and glasses, have been experimentally investigated and generally found to be $\geq 10^9$ W·cm^{-2} (*e.g.*, Ready, 1965; Russo, 1995; Bäuerle 1996; Figg *et al.,* 1998; Jeong *et al.,* 1999), equal to ≥1 J·cm^{-2} for a standard

ultraviolet (UV) wavelength laser system with a nanosecond pulse duration (*e.g.*, most solid-state laser systems).

During stoichiometric laser ablation, the surface temperature of the irradiated substrate is instantaneously heated past its vaporization temperature through linear single-photon absorption, nonlinear multi-photon absorption, dielectric breakdown, and additional mechanisms (*e.g.*, Ready, 1965; Bloembergen, 1979; Russo, 1995; Bäuerle, 1996; Young *et al.,* 1998). Before the surface layer can completely volatilize, however, layers of the substrate underneath the surface become superheated and reach their vaporization temperature, resulting in an explosive expulsion of substrate atoms, ions, molecules and solid particles/fragments (Fig. 2.2). These ablated species, which continue to be irradiated by the laser pulse, are the root cause of plasma shielding, which is described below in Section 2.1.3.

Electronic transitions, such as interband and intraband promotions of electrons across the bandgap, excitation of phonons (quantized modes of vibration), formation of excitons (localized electron-hole pairs), and electron transitions within defect/impurity absorption centers are primarily responsible for the absorption of laser photons with energies near or above the ablation threshold during laser ablation processing (*e.g.*, Bäuerle, 1996; Young *et al.,* 1998). Bandgap energies of geologically relevant materials, which ultimately provide an estimation of the binding energy required to dissociate/remove an atom from the substrate lattice, are on the order of ≥4.0 eV, generally greater than the photon energy from infrared laser systems, but comparable to the energy of photons generated by standard UV-wavelength systems (*i.e.*, 5.8 eV and 6.4 eV for 213 nm and 193 nm wavelength

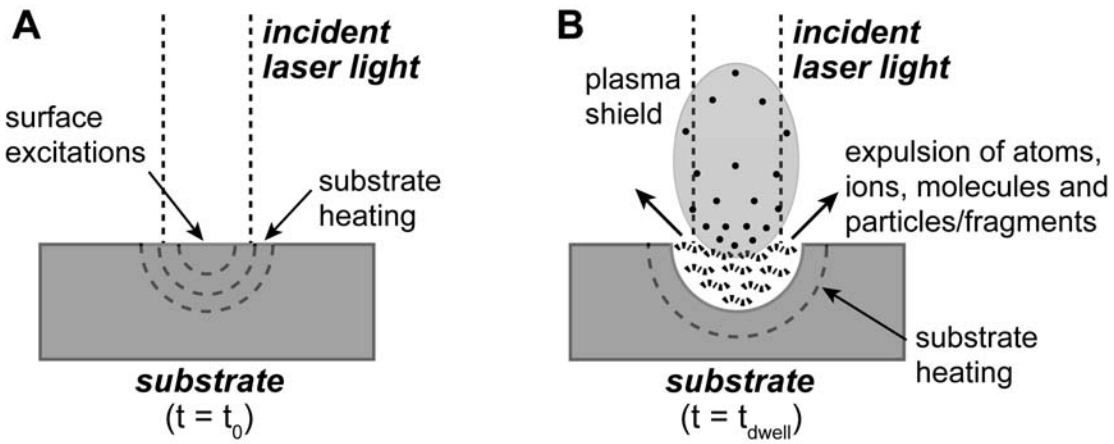

Fig. 2.2. Schematic representation of laser ablation processing.

radiation, respectively, given: $E = hc/\lambda$). However, even infrared laser systems may produce some ablation effects, largely due to the occurrence of lattice defects and impurities, which are present in all solid materials (and are further generated during each laser pulse) and can serve as incubation centers until a threshold density of point heating is crossed, resulting in the mechanical failure and dissociation of the substrate lattice (*e.g.*, Wiechert and Hoefs, 1995; Bäuerle, 1996; Young *et al.,* 1998).

2.1.3 Plasma shielding and the rate of ablation

As described above in Section 2.1.2, the mass of sample ablated per laser pulse (or rate of ablation), which is dependent on the optical energy provided by the incident photons and the absorption properties of the substrate, is primarily a function of the energy density, beam diameter, pulse duration, frequency, and spatial/temporal coherence of the incident laser radiation. At radiation intensities below the critical ablation threshold ($I_i < I_c$), the incident laser light induces changes in surface morphology and microstructure, such as the generation of defects, the depletion of volatile components and potentially some surface melting/vaporization (*e.g.*, Ready, 1965, 1971; Russo, 1995; Bäuerle, 1996). Above the critical ablation threshold ($I_i > I_c$), the incident photon energy is absorbed by electronic mechanisms, leading to stoichiometric ablation through a variety of largely non-thermal, electronic transitions that promote the explosive release of atomic, ionic and particulate species from the uppermost layers of the substrate.

Typically, greater radiation intensities result in a larger ablated mass, and hence greater signal to the mass spectrometer. Photon-substrate coupling is inhibited at excessive energy densities, however, due to the formation of a plasma plume over

the irradiated sample surface, a process that serves to absorb and/or reflect the incident laser radiation and thus depresses the ablation efficiency (Ready, 1965, 1971; von Allmen, 1986; Phipps and Dreyfuss, 1993; Russo, 1995; Bäuerle, 1996; Mao *et al.,* 1996; Liu *et al.,* 1999; Russo *et al.,* 2002; Bogaerts and Chen, 2005). The initiation and maintenance of a plasma plume at the sample surface is dependent on the laser beam properties and physical properties of the substrate and surrounding gas environment. The plasma, which can reach temperatures of $>10^5$ K and electron densities of $>10^{19}$ cm^{-3} (Liu *et al.,* 1999; Borchert *et al.,* 2005), is generated and sustained by the inverse bremsstrahlung process, whereby ambient gas atoms and ablated substrate ions/atoms/molecules/ particles undergo collisions as they expand into the gas atmosphere and absorb photons from the incident laser beam above the ablated substrate surface, resulting in an avalanche ionization of the ablated substrate species and formation of a plasma plume at the laser-substrate interface (*e.g.*, Chiao *et al.,* 1964; Ready, 1965, 1971; Kelley, 1965; Fabbro *et al.,* 1982; Phipps and Dreyfuss, 1993; Russo, 1995; Bäuerle, 1996; Mao *et al.,* 1996; Liu *et al.,* 1999). The plasma plume serves to scatter and/or absorb incident laser light and shield irradiation of the substrate, ultimately depressing the efficiency of ablation, in a process termed "plasma shielding."

Laser-substrate interactions can involve complex, nonlinear processes that are difficult to model or predict and are not entirely understood. Of the many factors that impact the coupling between the incident laser light and the surface of the substrate, the irradiance of the substrate is one of the most important with regard to controlling the effects of plasma shielding (Liu *et al.,* 1999). Experimental studies have

determined that, regardless of the chemical, physical or optical properties of the substrate material, laser-induced plasma plumes can be generated at radiation intensities as low as ≥0.1 $GW \cdot cm^{-2}$ (equal to an irradiation of ≥0.1 $J \cdot cm^{-2}$ from a nanosecond pulse) using a UV laser system (*e.g.*, Mao *et al.,* 1996; Shannon *et al.,* 1995; Fernandez *et al.,* 1995; Rieger *et al.,* 2003; Bogaerts and Chen, 2005), similar to the instrumentation employed for this dissertation. With increasing irradiance, although the absorption of the substrate and thus the ablation rate increases, the plasma plume expands and the temperature, degree of ionization and electron density in the vapor also increase, resulting in progressive absorption of the incident radiation, shielding of the substrate surface and fractionation effects associated with ablation (Liu *et al.,* 1999; Bogaerts & Chen, 2005; Borchert *et al.,* 2005). The implementation of lower radiation intensities has been demonstrated to produce smaller plasma plumes that cool more quickly and thus absorb less incident energy (Rieger *et al.,* 2003).

Assuming a constant irradiance, short pulse durations (*i.e.*, picosecond and/or femtosecond pulses) are associated with hotter temperatures, higher electron densities and increased expansion velocities (Borchert *et al.,* 2005). However, plasma shielding is generally more prevalent during longer pulses (*i.e.*, nanosecond pulses) largely due to longer plasma plume decay times (Mao *et al.,* 1998a,b; Drogoff *et al.,* 2004; Bochert *et al.,* 2005). Longer (*i.e.*, infrared) wavelengths contribute to lower rates of ablation and reduced ablation efficiency compared to shorter (*i.e.*, UV) wavelengths, principally due to increases reflectivity and decreased absorption at higher wavelengths, resulting in stronger plasma shielding but lower plasma temperatures,

degrees of ionization and electron densities (*e.g.*, Fabbro *et al.,* 1982; Mao *et al.,* 1998a,b; Bogaerts *et al.,* 2005). Additionally, the use of He as a carrier gas over ambient air helps to reduce the electron density of the plasma plume (Detalle *et al.,* 2003), likely due to the higher ionization potential of He compared to other potential carrier gases (*e.g.*, Ar or Kr), and improves the transmission rate of ablated species (Eggins *et al.,* 1998b; Mao *et al.,* 1998a; Günther and Heinrich, 1999a).

2.1.4 Fractionation effects and the benefits of UV wavelengths

Laser-induced elemental fractionation (LIEF), or the time-dependent change in elemental response ratios during analysis, is an inevitable result of laser ablation processing. Generally, the critical energy (E_c) required to raise one mole of mass from a solid phase into vapor is given by:

$$E_c = C_p T_s + L_v \qquad (2\text{-}5),$$

where C_p represents the heat capacity of the material, T_s the surface temperature and L_v the latent heat of vaporization (*e.g.*, Liu *et al.,* 1999). The time required to raise the substrate material to its vaporization temperature may be defined as (Durrant, 1999):

$$t_v = \frac{\pi K \rho C_p (T_v - T_0)^2}{4P^2} \qquad (2\text{-}6),$$

where K is the thermal conductivity, ρ the mass density of the sample, T_0 the initial temperature, T_v the vaporization temperature of the sample, and P the laser power density. As K, C and T_v depend on the composition of the sample, t_v is sensitive to variations in the chemical compositions of different substrates. Due to the distinct latent heat of vaporization (L_v) for each element and the sensitivity of t_v to the composition of the substrate, thermal effects during laser ablation can induce

significant elemental fractionation effects; thus, limiting the non-thermal mechanisms of ablation during LA-ICP-MS analysis is critical.

Laser-induced elemental fractionation of geological materials has been experimentally determined to be of significant effect at both low (*e.g.*, ≤0.3 GW·cm^{-2}; Borisov *et al.,* 2000) and high radiation intensities, but only of nominal importance in between 1 – 10 GW·cm^{-2}, the typical range of irradiances employed for LA-ICP-MS analysis. Because many geological materials, including rock-forming minerals and glasses, are optically transparent or translucent, these materials absorb a higher proportion of incident laser light at shorter wavelengths (*e.g.*, < 250 nm); these higher-energy photons are more efficient at non-thermal bond-breaking and ionization of the substrate compared to longer wavelengths. The early work of Jeffries *et al.,* (1995b) first revealed the potential advantages of employing UV-wavelength laser light (*i.e.*, 10 – 400 nm) versus infrared wavelengths (*i.e.*, 700 nm – 300 μm), particularly with regard to limiting LIEF, which essentially represents the sum of the non-stoichiometric effects that occur during the ablation, transport and ionization processes (*e.g.*, Fryer *et al.,* 1995; Figg *et al.,* 1998; Borisov *et al.,* 2000; Guillong and Günther, 2002; Guillong *et al.,* 2003). Consequently, studies employing UV-wavelength laser systems, particularly frequency-quintupled 213 nm Nd:YAG and/or 193 nm ArF excimer lasers, have found a reduction in elemental fractionation compared to longer wavelengths (*e.g.*, Jeffries *et al.,* 1998; Pettit and Ediger, 1996; Guillong *et al.,* 2003), largely due to more stable power outputs (and thus laser irradiance), smaller particle size distributions, and lower penetration depths. These developments have resulted in reduced LIEF and improved signal stability, sensitivity

and reproducibility (Mao *et al.,* 1998a,b; Figg and Kahr, 1997; Günther and Heinrich, 1999; Liu *et al.,* 2000; Russo *et al.,* 2000; Guillong *et al.,* 2003; Bogaerts and Chen, 2005). Internal and external calibrations with matrix-matched standard reference materials can account for LIEF, and both methods have been demonstrated to generate reproducible results that agree with other methods of analysis (*e.g.*, Jeffries *et al.,* 1995a; Pearce *et al.,* 1997; Eggins *et al.,* 1998a; Norman *et al.,* 1998; Rocholl 1998; Gao *et al.,* 2002; Kent *et al.,* 2004; Jochum *et al.,* 2005; Willbold and Jochum 2005; Jochum *et al.,* 2006, 2007; Arevalo and McDonough 2008; Arevalo *et al.,* 2009).

2.1.5 Optimized parameters for LA-ICP-MS

The overall proficiency of the ablation process, which is defined by Arrowsmith and Hughes (1988) as the fraction of ablated species that are ionized and subsequently measured in the mass spectrometer (also termed the transmission efficiency), is sensitive to a range of physical parameters, including: i) the amount of sample mass removed per laser pulse (or rate of ablation), which is in turn is governed by the irradiance, beam diameter, wavelength, pulse duration, plasma shielding, and physical/chemical/optical characteristics of the substrate material; ii) the distribution of particle sizes generated during irradiation; iii) the entrainment and transport of atomic, ionic, molecular, and particulate species through the sample chamber, transport tubing and mass spectrometer; iv) the atomization and ionization efficiency of both the laser system and inductively-coupled plasma source; and, v) the response function, or sensitivity, of the mass spectrometer (*e.g.*, Ready, 1965; Fryer *et al.,* 1995; Russo, 1995; Bäuerle, 1996; Mao *et al.,* 1998a,b; Durrant, 1999; Jackson,

2001; Russo *et al.,* 2002 and references therein). In order to minimize the potential for elemental fractionation during laser ablation processing for this study, various analytical protocols were enforced to effectively maintain an efficient ablation rate and limit inconsistent laser-induced fractionation effects, including: the use of non-transparent calibrating reference materials (*e.g.*, Gaboardi and Humayun 2009); active focusing (*e.g.*, Hirata and Nesbitt, 1995); slow traverse speeds (*e.g.*, Guillong and Günther, 2002); high carrier gas flow rates (*e.g.*, Jeong *et al.,* 1999); low repetition rates (*e.g.*, Norman *et al.,* 1996; Günther *et al.,* 1997; Jackson, 2001); large beam diameters (*e.g.*, Fernandez *et al.,* 1995; Jeong *et al.,*1999; Mank and Mason 1999; Jochum *et al.,* 2007JAAS); incident irradiances surpassing the critical ablation threshold but below the threshold of mass ablation roll-off due to plasma shielding (*i.e.*, between 0.1 – 1.0 GW/cm^2; *e.g.*, Russo 1995; Bäuerle 1996; Mao *et al.,* 1996; Figg *et al.,* 1998; Jeong *et al.,* 1999; Bogaerts and Chen 2005); ablation lines and/or rasters rather than spots, and thus low depth-to-diameter pit aspect ratios, which prevent the loss of signal intensity associated with deepening crater geometries (*e.g.*, Perkins *et al.,* 1997; Eggins *et al.,* 1998b; Günther and Heinrich 1999a; Mank and Mason 1999; Borisov *et al.,* 2000; Horn *et al.,* 2000; Russo *et al.,* 2000; Ruf *et al.,* 2001; Morishita *et al.,* 2005); and, the use of UV-wavelength light (*i.e.*, 213 nm) and constant energy densities (*i.e.*, 1.2 – 1.3 J/cm^2), which contribute to a smaller and more constant particle size distribution (*e.g.*, Fernandez *et al.,* 1995; Jeffries *et al.,* 1995b; Figg and Kahr 1997; Günther and Heinrich 1999b; Figg *et al.,* 1998; Guillong and Günther 2002; Guillong *et al.,* 2003; Bogaerts and Chen 2005). Because helium has a higher ionization potential and smaller ionization cross-section compared to

argon, it is the preferred carrier gas for laser ablation mass spectrometry (von Allmen, 1986; Russo, 1995) and has been shown to improve signal sensitivity, stability and reproducibility by minimizing the deposition of ablation products and improving sample transport efficiency during UV-wavelength laser ablation (Eggins *et al.,* 1998b; Mao *et al.,* 1998a; Günther and Heinrich, 1999a); therefore, He was used as the carrier gas for this study.

The following sections of this chapter are dedicated to the development of specific analytical methods and procedures that have been employed for the various individual studies that constitute this dissertation. Emphasis has been placed on maximizing precision and accuracy and minimizing interferences, including both spectral (isobaric) and non-spectral types. These sections have either been published as supplementary materials in a peer-reviewed journal article, or are currently under review.

2.2 *In situ* measurements of highly incompatible Ba, W, Th, and U abundances in oceanic basalts via LA-ICP-MS

This study examined the major, minor and trace element composition of an inclusive suite of oceanic basalts (n = 86; Fig. 2.3), including a global distribution of MORB (n = 52) as well as several smaller suites of intraplate basalts (including both OIB and intraplate continental volcanics), back-arc basin basalts (BABB), and convergent margin volcanics (including island arc basalts, IAB, and continental arc basalts, CAB). Most of the rocks were glasses or fine-grained scoria and exhibited a range in major and trace element chemistry. The chemical make-up of these samples

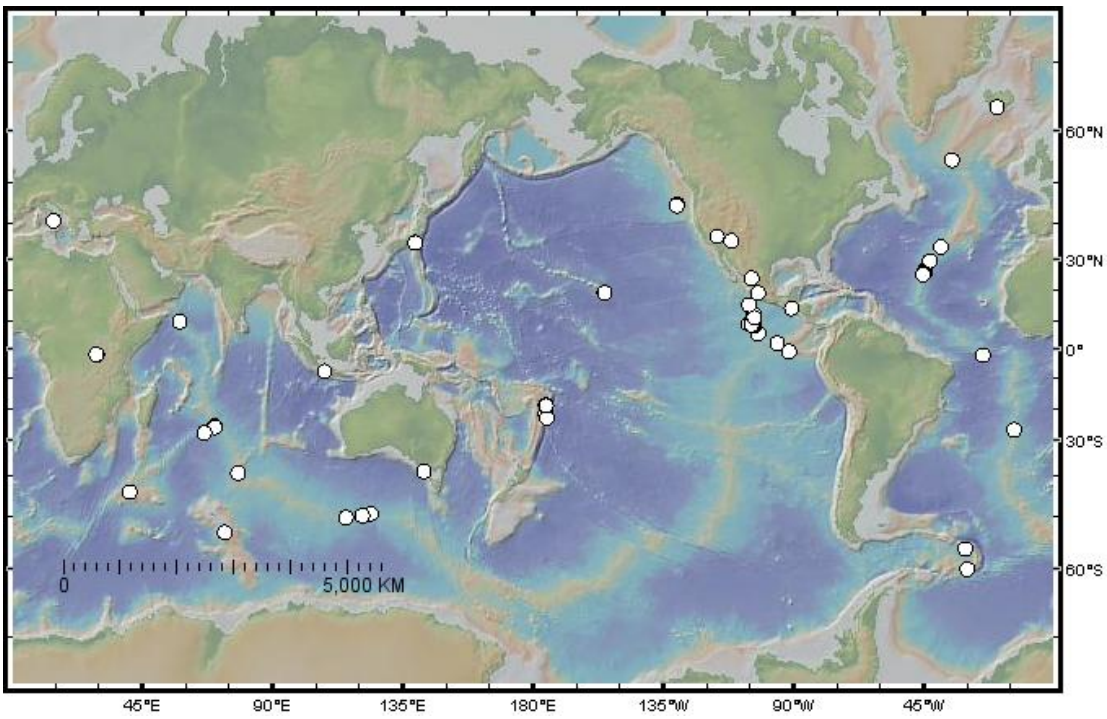

Fig. 2.3. Sample localities of basaltic samples analyzed in this study.

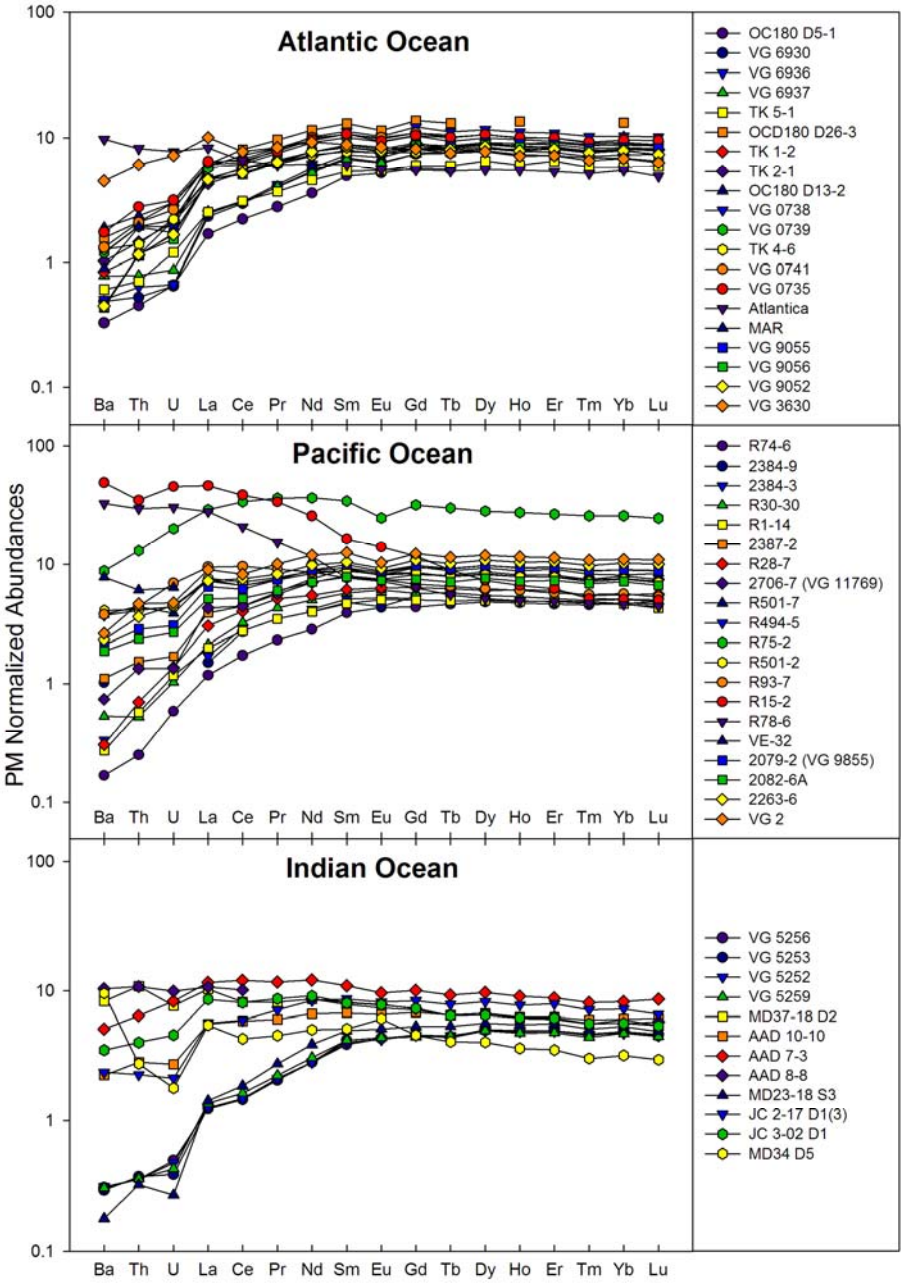

Fig. 2.4. Trace element variation diagrams of MORB examined in this study, grouped according to oceanic province. The elements listed along the x-axis are arranged in order of relative compatibility as determined by Sun and McDonough (1989); from left to right the elements become more compatible in basaltic melts. Element concentrations are normalized to the Primitive Mantle values of McDonough and Sun (1995).

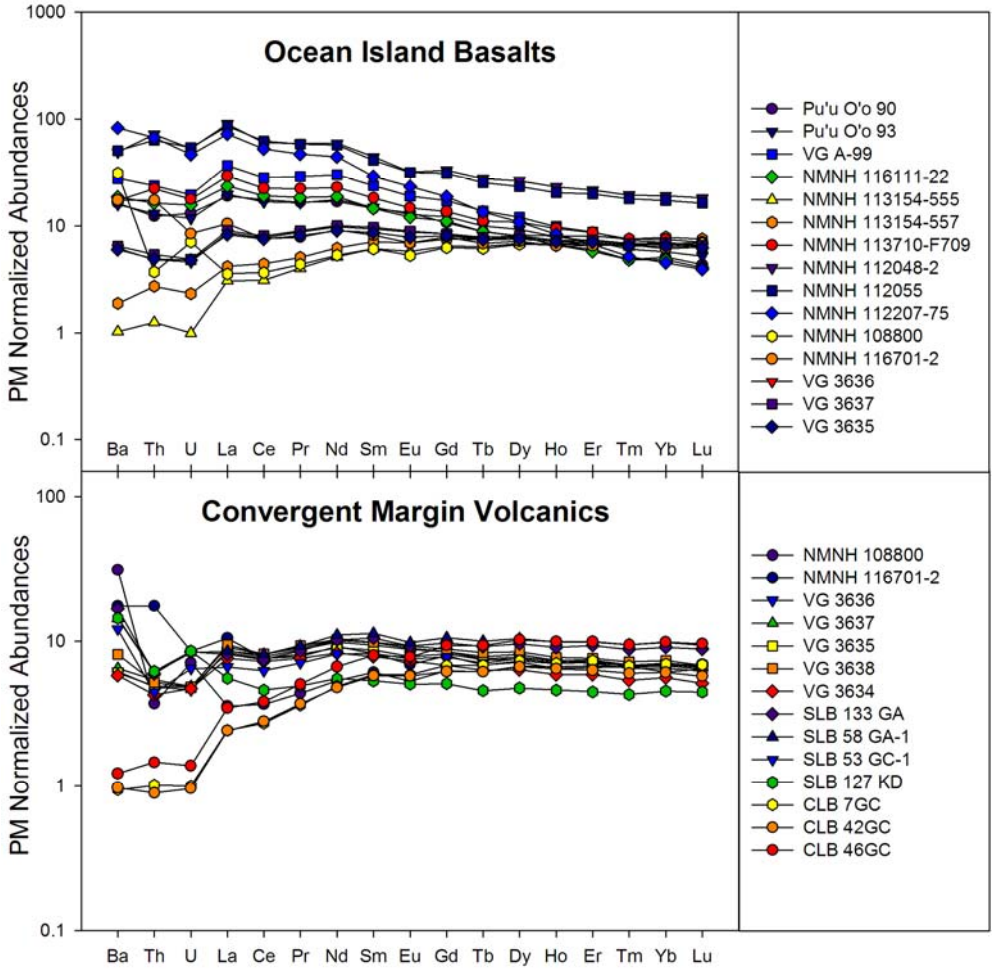

Fig. 2.5. Trace element variation diagrams of intraplate and convergent margin samples. Note how the central Lau Basin samples (CLB) are depleted in the light rare-earth and highly incompatible elements; these samples appear to tap a source that contains a MORB-like component.

represents a broad spectrum of basaltic compositions (Figs. 2.4 and 2.5), from very depleted (10^{-1} x Primitive Mantle) to extremely enriched (10^{2} x Primitive Mantle) in incompatible trace elements; thus, a wide-range of magma types, from primitive to significantly differentiated and enriched, are represented by this sample set.

The samples analyzed in this study represent products of varying degrees of melting and crystallization, from pristine glasses to microcrystalline textures. Although hand-picking the freshest glass specimens and carefully preparing/polishing the laser mounts essentially eliminates the presence of alteration zones, minor silicate phenocrysts, as well as <5 μm Fe-S(-O) and oxide phases, do exist in a number of these samples (Fig. 2.6). In order to quantify the concentrations of trace elements (including rare-earth elements, REE, and highly incompatible Ba, W, Th, and U) in the matrix, which most precisely represents the composition of the magma source, avoiding these phases during laser ablation analysis is integral. Silicate phenocrysts, most commonly found to be plagioclase and olivine, are easy to circumvent as their crystals are easily seen under the laser camera system. Oxide and Fe-S(-O) phases, on the other hand, are commonly too small to be identified during laser analysis but can be recognized and isolated from sample spectra, as seen in Fig. 2.7. Such precautions are necessary in order to appropriately characterize the composition of the melt.

Fresh glass chips or fine-grained scoria fragments (~1-5 millimeters in diameter) from each sample were separated and arranged on one-inch epoxy mounts which were subsequently polished to a flat surface. The polished mounts were sonicated in ethanol and milli-Q water in order to remove any surface contamination. Samples not previously evaluated for major element chemistry were analyzed using a

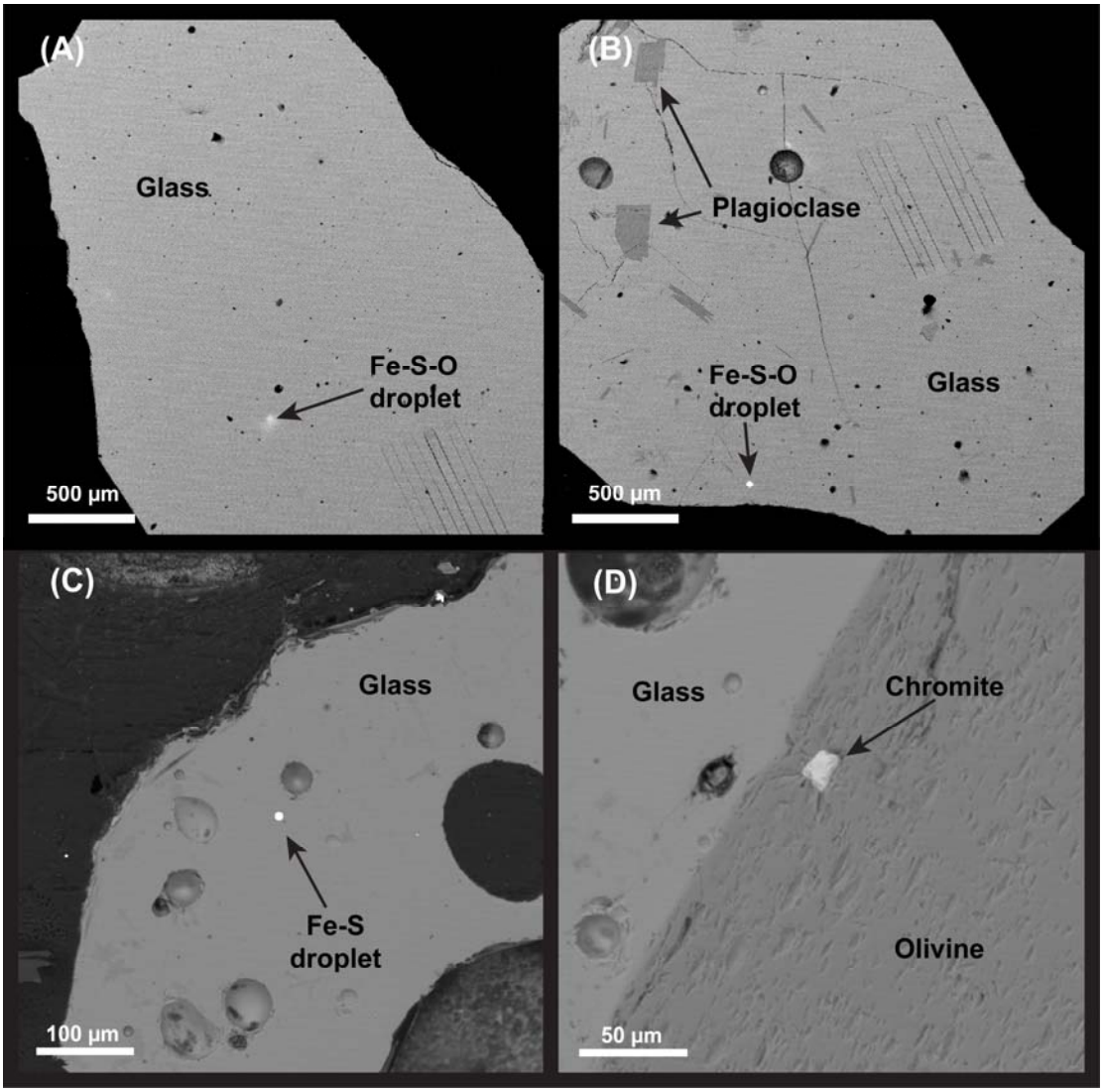

Fig. 2.6. Back-scattered electron images of four basaltic samples. Phases with heavier atomic compositions appear as lighter features in these images. Each sample specimen shows evidence for a minor heavy phase: (A) and (B), both MORB, contain several ≤10µm Fe-S-O globules. (C), a vesiculated OIB, reveals a similarly-sized Fe-S droplet, and (D), a BABB, shows a chromite crystal included within a massive olivine grain. *In situ* determinations of each phase were performed via energy-dispersive spectroscopy (EDS). The track marks in (B) represent laser ablation paths from prior trace element analyses.

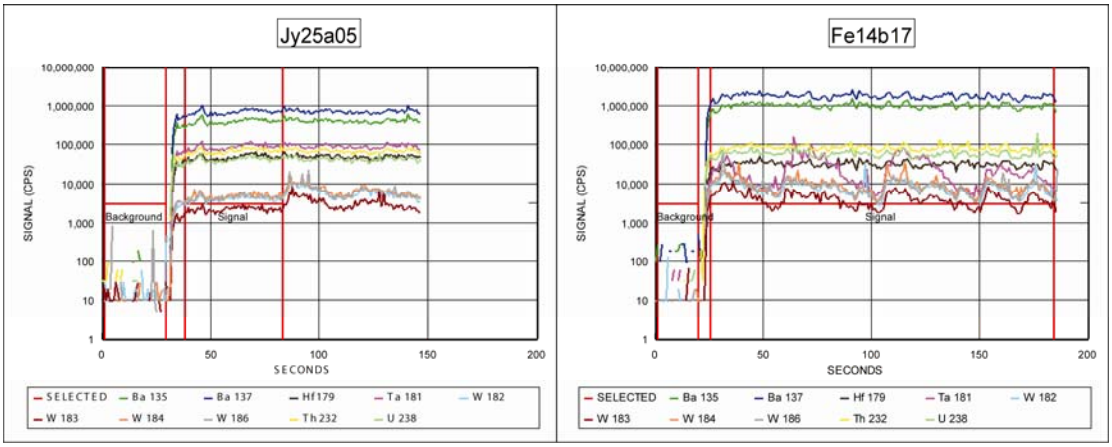

Fig. 2.7. Time-resolved spectra for two basaltic samples. The Jy25a05 sample is the OIB from Fig. 2.6 (C; NMNH 16111-22, with 228 ng/g W) that contains a phase with approximately an order of magnitude more W than the matrix; the phase is likely an Fe-S(-O) inclusion. The Fe14b17 sample is the BABB from Fig. 2.6 (D; SLB127KD, with 72 ng/g W) comprising several phases enriched in both W and Ta, likely a series of chromites.

JEOL JXA-8900 SuperProbe electron probe microanalyzer (EPMA) with a ZAF correction program at the University of Maryland. Analytical conditions were: 15 kV accelerating voltage, 10 nA beam current and a 10 μm beam diameter. Counting times were 20 s for SiO_2, Al_2O_3 and P_2O_5, 40 s for MgO and K_2O, 90 s for FeO_{total} and TiO^2, 120 s for Na_2O and MnO, and 180 s for CaO (Na was analyzed early in the sequence to avoid diffusive loss). Oxides are reported as weight percent and represent the average of 5-10 analytical spots normalized to multiple standards, including Indian Ocean Basalt (NMNH 113716), Kakanui Hornblende (NMNH 143965), Durango Apatite (NMNH 104021-3), and Broken Hill Rhodonite (USGS PXBH). The major element compositions and longitude/latitude coordinates of each sample are provided in Appendix A.

2.2.1 Laser ablation methodology

Trace element concentrations (including W) of these glassy specimens were determined via LA-ICP-MS using a frequency-quintupled New Wave Nd-YAG laser (213 nm light) coupled to a Thermo Finnigan Element2 single-collector ICP-MS at the University of Maryland. Prior to sample analysis, the mass spectrometer was tuned to maximize signal (based on ^{43}Ca and ^{232}Th spectra) and minimize oxide production ($^{232}Th^{16}O/^{232}Th < 0.20\%$) while ablating NIST SRM 612. NIST SRM 612 also served as the standard reference material in our laser ablation analyses, as this synthetic glass has been extensively characterized (*e.g.*, Norman, 1996; Pearce *et al.,* 1997; Eggins *et al.,* 1998a; Kane, 1998a,b), established to be homogeneous with regard to Ba, Th, U, and W (Eggins and Shelley, 2002), and shown to yield precise

and reproducible results using ultra-violet light with a Nd:YAG laser system (*e.g.*, Jochum *et al.,* 2005, 2006, 2007).

Before each sample ablation, the laser system was permitted to warm-up for at least 120 seconds to stabilize the output power of the laser pulse, and a standard five minute washout period between ablation signals was instituted in order to allow adequate time for cleaning of the sample-injection tubing, thus limiting memory effects. The parameters for each ablation path (lines were preferred over spots in order to better represent the matrix of the entire glass specimen) varied according to the concentrations of the targeted trace elements in the sample and the sensitivity of the mass spectrometer. The parameters for the ablation lines for NIST SRM 612 were most commonly selected as: 45% output power, 55 - 75 μm spot diameter, and 8 Hz repetition rate, resulting in approximately 0.7 - 2.0 J/cm^2 focused on the glass. The ablation lines for the basaltic samples demanded a larger range in parameters, shown in Table 2.1, but were ultimately fashioned to produce similar photon fluences between 0.7 - 3.0 J/cm^2. Blank count rates were measured for 20 – 30 s prior to each ablation, and a total ablation signal of 80 s during the analysis of REE + Ba, and 150 s during the analysis of W, Th and U, was implemented. All ablations occurred in a helium (He) atmosphere due to the advantages of this gas transporting ablated species (von Allmen, 1986; Eggins *et al.,* 1998b; Mao *et al.,* 1998a; Günther and Heinrich, 1999).

Ablated materials, including both samples and standard reference glasses, were analyzed with an Element2 single-collector ICP-MS, which has a reverse Nier-Johnson geometry. Ion intensities were measured in the low mass resolution mode

(m/Δm = 300) with a mass window of 10%, search window of 150% and integration window of 80%. Measurements were performed using the electrical scan mode (E-scan) and counting mode of detection. The detection parameters included a dwell time of 10 ms for REE and ^{135,137}Ba, 30 ms for ^{232}Th and ^{238}U, and 100 ms for ^{182,183,184,186}W in order to accumulate adequate counting statistics to evaluate and constrain isobaric interferences, thus increasing analytical precision. One sample per peak was utilized as it yielded superior signal-to-noise ratios compared to spectra with 10 samples per peak. The operational parameters employed during our measurements are listed in Table 2.1.

Table 2.1. LA-ICP-MS operating conditions for measuring highly incompatible Ba, W, Th, and U abundances in basaltic glasses.

Laser Ablation Parameters	
Ablation Pattern	Line
Scan Speed	10 μm/s
Spot Size (Diameter)	45-350 μm
Repetition Rate	8-20 Hz
Energy Density*	0.7-3.0 J/cm^2
Mass Spectrometer Parameters	
Forward Power	1250W
HV	10 kV
Scan Optimization	Speed
Number of Pre-Scans	1
Active Dead Time	25 ns
Cool Gas Flow	16 L/min
Auxiliary Gas Flow	1.5 L/min
Sample Gas Flow	0.7 L/min
Carrier (He) Gas Flow	1.1 L/min
Cones	Ni-alloy

*Laser parameters were programmed to produce ideal photon fluences between 1-2 J/cm^2

As an additional consideration, we tested the effect of running our analyses under "cool" plasma conditions (with a forward power of 900W, rather than the typical 1250W). Our assessment indicated a twenty-fold drop in signal under these conditions. Furthermore, the guard electrode (GE) function of the mass spectrometer was found to diminish the signal-to-noise ratio of our analyses, and thus was not applied during our measurements. Data reduction and quantification was conducted using LAMTRACE, a Lotus 123 macro-based spreadsheet package developed by Simon E. Jackson of the Macquerie University, Australia (Achterbergh *et al.,* 2001).

2.2.2 Matrix effects

The photon absorption behavior of an analyte, and thus the absolute amount of material ablated during each analysis, is dependent on the chemical composition of the analyte matrix. Matrix effects can be divided into two principal species: spectral (isobaric) and non-spectral types. Spectral matrix effects include elemental isobaric mass interferences, such as ^{186}Os at ^{186}W, and molecular interferences, such as ^{170}Er^{16}O at ^{186}W. Non-spectral effects (*e.g.*, photon-matrix coupling) are largely associated with changes in the sensitivity of an analyte relative to a standard due to compositional differences (*c.f.*, Albarède and Beard, 2004).

In this study, the only potential elemental isobaric interference is ^{186}Os at ^{186}W. Fortunately, the concentration of Os in basaltic melts is too low to present a problem. As a safeguard, however, we monitored the amount of Os in several samples during solution ICP-MS analysis and found no ^{189}Os counts above the blank or milli-Q water. A potentially more problematic source of isobaric interferences is diatomic oxides. The issue of oxide mass interferences inevitably arises when discussing mass

spectrometry, particularly laser ablation mass spectrometry since no chemical separations/purifications have been performed on the samples before analysis. First, it should be noted that our analytical protocol measures the concentration of W by monitoring four isotope mass stations: ^{182}W, ^{183}W, ^{184}W, and ^{186}W. Any potential oxide interferences on these masses would be expected to yield discordant results between isotope ratios, but no systematic variances were detected (Fig. 2.8).

Further, we conducted an experiment in which we analyzed a synthetic basaltic glass doped with 500 μg/g of the heavy rare-earth elements (HREE). Employing the analytical parameters described above, HREE-oxide production rates (*i.e.*, YbO/Yb and TmO/Tm) were measured to be 10^{-6}, with a lower limit of $\sim10^{-7}$ and an upper limit of $\sim10^{-4.5}$ for a "poorly-tuned" plasma (*i.e.*, tuned to $^{232}Th^{16}O/^{232}Th$ = 1.2%). Accordingly, HREE-oxides do not present significant isobaric interferences to even the most depleted W concentrations in our natural samples. The independence of our data to oxide interferences is verified in the terrestrial W isotopic compositions of our samples, shown in Fig. 2.8.

Because the sensitivity of the analyte fluctuates as a function of the mass-to-charge ratio of the matrix, non-spectral matrix effects in concentration measurements acquired through LA-ICP-MS can result from differences in chemical compositions between the analyte and the standard reference material. Although NIST SRM 612 (the standard reference material utilized for our measurements) has been well characterized and found to be homogeneous with respect to Ba, Th, U, and W, this glass represents a more enriched composition (with approximately 40 μg/g of each of these elements) than oceanic basalts, which can be far more depleted, particularly

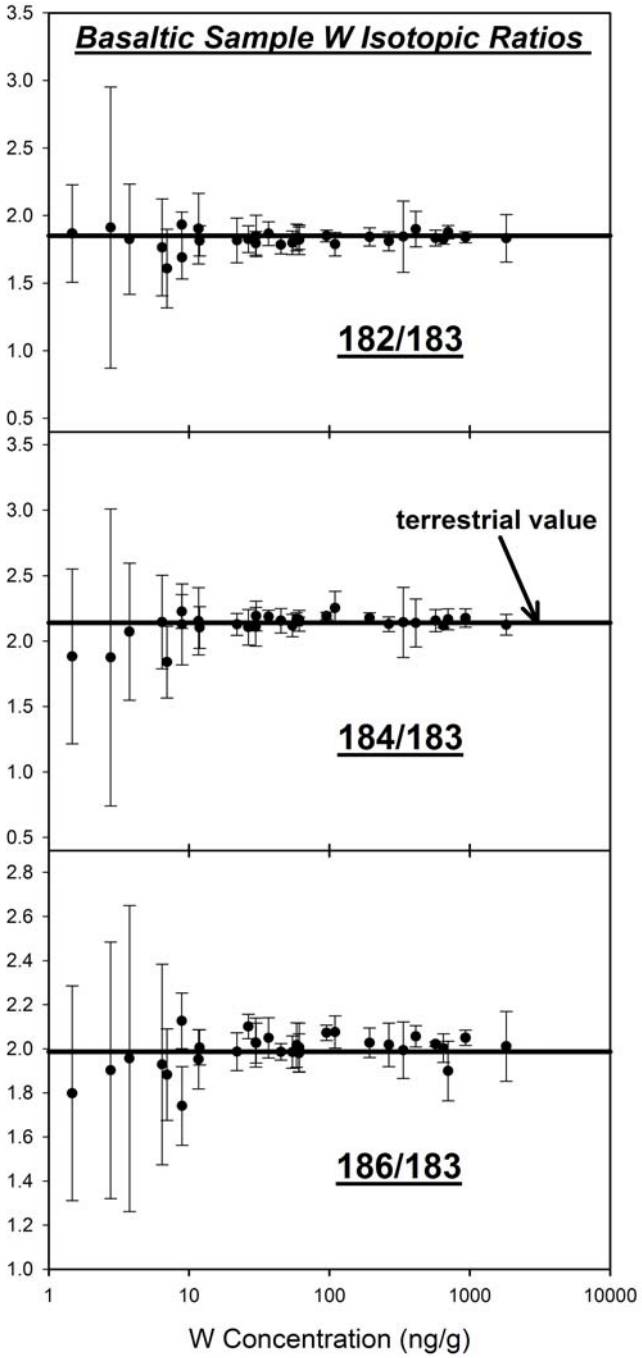

Fig. 2.8. Tungsten isotopic compositions of various samples, including the most depleted and enriched in W, compared to the accepted terrestrial values of Jacobsen (2005). The error bars, which represent 2σ uncertainties, reflect both the analytical reproducibility of the measurements as well as the heterogeneity of the samples.

with regard to Th, U, and W. In order to account for this discrepancy, which could potentially lead to analytical biases (*e.g.*, Hinton, 1995), we have calibrated our measurements to a suite of rocks analyzed via solution ICP-MS, including both isotope dilution and high-precision standard addition analyses.

Since the Ba content of our samples (~1 – 1000 μg/g) is on the same order as NIST SRM 612 (39.7 μg/g Ba; Jochum *et al.,* 2005), we maintained this synthetic glass as our internal calibrating standard and found our Ba measurements to be statistically within 2% of previously published high-precision solution measurements (see Fig. 4.1). However, the concentrations of Th and U in our samples are far more depleted (from 10 ng/g to 10 μg/g) and thus were externally calibrated to a ten point curve comprising ten samples (between 15 ng/g and 5 μg/g of Th and U) previously analyzed via isotope dilution mass spectrometry by White (1993); the resulting laser calibration resulted in our measurements being within 1% of previously published analyses for Th and 2% for U. Unfortunately, W represents an even more depleted incompatible element, and very few high-precision W measurements have been previously published on oceanic basalts or geologic glass standards. In order to account for this problem, we analyzed a number of our own samples, as well as several prominent basaltic glass standards, for their W abundances via isotope dilution and/or standard addition mass spectrometry. By calibrating our laser measurements to two samples that we also analyzed by both solution methods, namely CLB42GC and Pu'u O'o 93, we found that our laser values are within 3% of our solution measurements. The 3% deviation likely represents a relict of the

uncertainty of our measurements, which typically ranged from 2-5% ($2\sigma_m$) on the laser and 10-30% (2σ) via solution.

2.2.3 Isotope dilution and standard addition ICP-MS analytical procedures

The accuracy of our W measurements is manifest by the correlation of our laser data with those acquired through two modes of solution analysis: isotope dilution and standard addition ICP-MS. A comparison between these methods is provided in Figure 4.1, which examines three geologic glass standards (BIR-1g, BHVO-2g and BCR-2g) and two basaltic samples (2384-9 and JdF MORB).

For isotope dilution analyses, 10-100 mg of sample powders were digested on a hotplate at 120°C for 48-60 hours in ~5 mL of concentrated Teflon-distilled HNO_3 + concentrated Seastar HF (3:2) and a few drops of concentrated Teflon-distilled HCl. The solutions were subsequently dried down in a laminar flow hood and re-dissolved in ~2 mL of 1 M HCl plus a drop of concentrated HF. Anion column chromatography was then performed according to the separation procedures detailed in Table 2.2. After the W collection step, the solutions were again dried down and finally taken up again in ~5 mL of 5% HNO_3 and centrifuged; the supernatant fluid of each sample solution was analyzed in the Element2 ICP-MS. The analytical blank of this procedure ranged from 0.5 to 2.5 ng W, instigating the more stringent cleaning protocols implemented in subsequent standard addition measurements. The analytical uncertainties of the most depleted analyte measurements (typically 20-30%, 2σ external reproducibility) were primarily controlled by the high blanks, whereas the uncertainties of the more enriched analytes (10-15%) are an artifact of small heterogeneities in the glass.

For standard addition analysis, approximately 100 mg of each sample powder was digested in 1-2 mL of concentrated HF-HNO_3 (3:1) on a hotplate at 150°C for 60 hours. Sample digestions were carried out in new 15 mL Savillex Teflon vessels, which were pre-cleaned according to the protocol of Kleine *et al.,* (2002, 2004). After being dried down, these solutions were taken up again in 6 M HCl + 0.06 M HF. Following the procedures of Bellucci *et al.,* (2007), aliquots of the standard addition

Table 2.2. Single Bio-rad disposable column separation procedures for W concentration analysis via ID-ICP-MS.

Step	Volume (mL)	Acid and/or Solution
Loading/Cleaning Resin		
Load Resin	2	AG 1X8 (100-200 mesh) anion exchange resin
Cleaning	5	1M HCL + a few drops conc. HF
Cleaning	10	9M HCL + a few drops conc. HF
Equilibrate Resin	10	1M HCl + a few drops conc. HF
Eluting Sample		
Load sample	~2	1M HCl (+ HF) sample solution
Rinse Matrix	6	1M HCl + a few drops conc. HF
Rinse Matrix	1	9M HCl + a few drops conc. HF
Collect W	6	9M HCl + a few drops conc. HF

sample solutions were added to varying amounts of a W standard (100-1000 µL of NIST SRM3163, diluted to 2.5 ng/g in 6.2% HNO_3 and 0.8% HF) plus a Ta drift correction agent (1000 µL of ASSURANCE Lot#12-170TA, diluted to 2.5 ng/g in 0.8% HF). The matrix of the final standard addition mixtures were 0.56 M HNO_3 + 0.24 M HF, similar to the solution chemistry of Kleine *et al.,* (2002, 2004). Analysis on the Element2 ICP-MS, which was performed while using a sapphire torch and Teflon nebulizer and spray chamber, indicated a total procedural blank of ≤480 pg W.

2.3 Measuring K in oceanic basalts via medium-resolution LA-ICP-MS

In this study, we have examined the concentrations of K (and U) in 93 fresh oceanic basalts from the Atlantic, Pacific and Indian oceans, including a suite of MORB, ranging from depleted (La/Sm < 1.00, n =42) to enriched (La/Sm ≥ 1.00, n = 33) in composition, as well representative suites of BABB (n = 12) and OIB (n = 6). Vitric fragments of each sample were mounted in epoxy and polished to a flat surface. Prior to analysis, the mounted samples were sonicated in ethanol and milli-Q water to remove potential surface contamination. All samples had been previously analyzed for major element chemistry by Melson (2003) or Arevalo Jr. and McDonough (2008).

2.3.1 Acquisition of high-precision K concentration data via LA-ICP-MS

Whereas the concentration of U in our basaltic samples was determined via the protocol established by Arevalo Jr. and McDonough (2008), the analysis of K required more stringent analytical methods. The concentration of K in each sample was determined via LA-ICP-MS at the University of Maryland using a New Wave UP-213 laser system (213 nm light) coupled to a Thermo-Finnigan Element2 ICP-MS. We measured K by monitoring isotope ^{39}K, which competes with the mass peaks for $^{23}Na^{16}O$, $^{38}Ar^{1}H$ and the tail end of ^{40}Ar. In order to effectively separate the mass peak of ^{39}K from these potential isobaric mass interferences, we performed our analyses under medium-resolution detection mode ($m/\Delta m = 4000$).

The element menu we used included ^{39}K, ^{42}Ca and ^{43}Ca, with ^{43}Ca serving as the internal standard element. Six samples per peak were measured for all isotopes. The sampling times were 50 ms for ^{39}K, 10 ms for ^{42}Ca and 20 ms for ^{43}Ca, thus

optimizing counting statistics within a reasonable analysis time. Analyses were conducted using medium-resolution detection ($m/\Delta m = 4000$) and "mass accuracy" mode of the ICP-MS. The guard electrode was turned off so as to optimize signal-to-noise ratio of ^{39}K. For all analyses, data was acquired for 20-25 seconds with the laser firing but shutter closed to collect a background signal and allow the laser pulse to reach a stable energy density. Between ablations, the sample cell and transport tubing were flushed with He gas for ~3 minutes to limit any memory effects.

Laser parameters varied for samples and standards according to the K concentrations of the glasses and the sensitivity of the instrument (*i.e.*, condition of the sample/skimmer cones). The parameters for BIR-1G typically included a 200-250 μm spot, 20 Hz repetition rate, and a power output of approximately 50%, resulting in ~1.0 to 1.5 J/cm² energy density on the glass. For BCR-2G, the parameters included a 100 μm spot, 10 Hz repetition rate, and a power output of ~45%, which resulted in an energy density of 1.0 to 2.0 J/cm². The laser settings utilized for our sample analyses are described in Table 2.3.

Samples and standards were ablated in and transported by He gas before mixing with the ICP-MS "sample" Ar gas supply prior to injection into the plasma. The mass spectrometer was initially tuned to maximize ^{43}Ca and ^{232}Th signals while minimizing oxide production ($^{232}Th/^{232}Th^{16}O < 0.20\%$) in low-resolution mode ($m/\Delta m = 300$). Subsequently, a two-stage mass calibration (low-resolution followed by medium-resolution) was carried out while ablating NIST SRM 612. Following this calibration, the mass spectrometer was again tuned, this time in medium-resolution ($m/\Delta m = 4000$), to maximize the sensitivity and sharpen the peak shapes of ^{43}Ca,

^{139}La and ^{178}Hf. The mass spectrometer specifications used for our K measurements can be found in Table 2.3.

Table 2.3. LA-ICP-MS operating conditions employed for collecting K concentration data.

Laser Ablation Parameters[a]	
Ablation Pattern	Line
Scan Speed	10 μm/s
Spot Size (Diameter)	45-350 μm
Repetition Rate	8-20 Hz
Energy Density*	0.7-3.0 J/cm2
Mass Spectrometer Parameters	
Forward Power	1250W
HV	10 kV
Scan Optimization	Mass Accuracy
Number of Pre-Scans	1
Active Dead Time	25 ns
Cool Gas Flow	16 L/min
Auxiliary Gas Flow	1.5 L/min
Sample Gas Flow	0.7 L/min
Carrier (He) Gas Flow	1.1 L/min
Cones	Ni-alloy

[a] Laser parameters were programmed to produce ideal photon fluences between 1-2 J/cm^2

Two well-characterized USGS standard reference glasses, BIR-1G and BCR-2G, bracketed each set of sample analyses; approximately 12 sample ablations were performed between sets of four standard measurements, two for each reference glass. As seen in Fig. 2.9, measurements calibrated internally with BIR-1G produced results within 1% of previously measured isotope dilution values, whereas calibration to BCR-2G resulted in a 7% deviation. This discrepancy suggested a non-spectral matrix effect between BCR-2G and our basaltic samples, as BCR-2G represents a chemical composition more enriched in K (~15,000 μg/g K) than any of the oceanic basalts

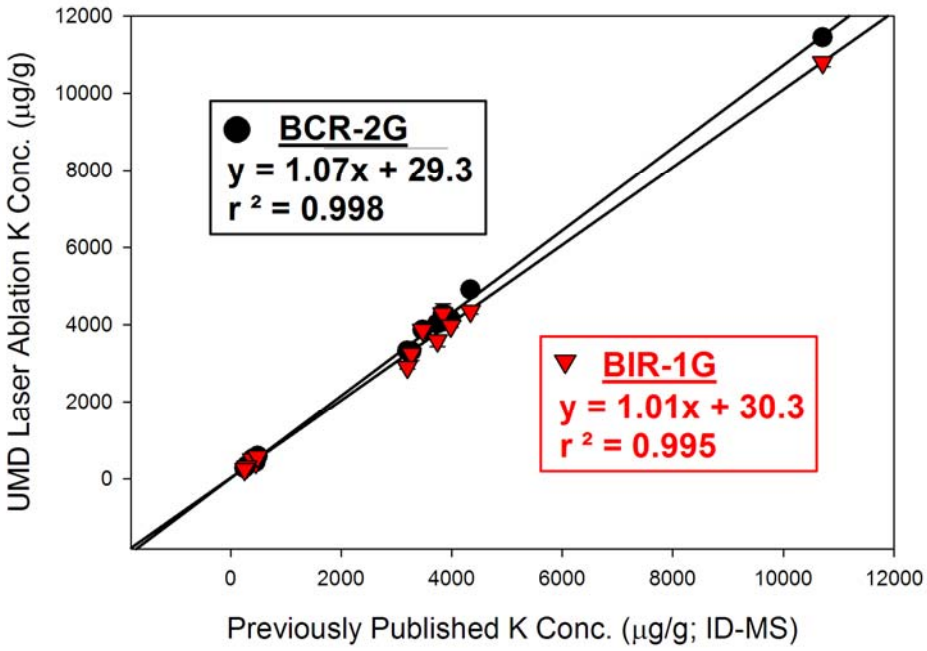

Fig. 2.9. Accuracy of K concentration measurements made via medium-resolution (m/Δm = 4000) LA-ICP-MS using internal standardization with BCR-2G and BIR-1G. The deviation of the values obtained through BCR-2G standardization and previously published isotope dilution measurements likely represents a non-spectral matrix effect due to the enriched composition of BCR-2G relative to oceanic glasses. Accordingly, BIR-1G was utilized as the internal calibrant for our measurements, providing us with data that plot within ~1% of previously published, high-precision isotope dilution data (Loock *et al.,* 1990; Raczek *et al.,* 2005; Jochum *et al.,* 2006).

investigated here, including the most enriched OIB (*i.e.*, VG-A99 with <6000 μg/g K) or E-MORB (*i.e.*, VG1223 with ~12,000 μg/g K). BIR-1G (~200 μg/g K), on the other hand, represents a less enriched chemical composition that is more consistent with the makeup of typical oceanic basalts. Accordingly, BIR-1G was instituted as the internal calibration standard for our sample K measurements.

As illustrated in Figure 2.9, our laser ablation K data, which span over 2 orders of magnitude in concentration, coincide within 1% of previously published isotope dilution measurements (with BIR-1G as the internal standard). The typical uncertainties of our K measurements were ± ≤3% (2σ). The concentrations of K and U and associated uncertainties for each of our samples are reported in Appendix B.

2.3.2 Discrepancy with the low MORB K/U from Jochum et al., (1983)

Our MORB dataset, as described further in Chapter 4, illustrates that depleted "normal-type" MORB (N-MORB; defined by La/Sm < 1.00) with and average K/U = 20,000 ± 2300 (2σ), and anomalous "enriched-type" MORB (E-MORB; La/Sm ≥ 1.00) with an average K/U = 15,700 ± 3100 (2σ), are both characterized by higher K/U ratios than the previous MORB measurements made by Jochum *et al.,* (1983; average K/U = 12,700 ± 400, 2σ). Our data are also in agreement with high-precision data (ICP-MS, isotope dilution and TIMS methods) from the PetDB database which suggest a K/U_{MORB} > 22,000 (data available for download from author or doi:10.1016/j.epsl.2008.12.023). The discrepancy with the Jochum *et al.,* (1983) study is likely due to an analytical bias. For example, the spark source (SS-) mass spectrometry (MS) U data of Jochum *et al.,* (1983), when compared with high-precision ID-MS measurements of the same samples by White (1993), appear to be

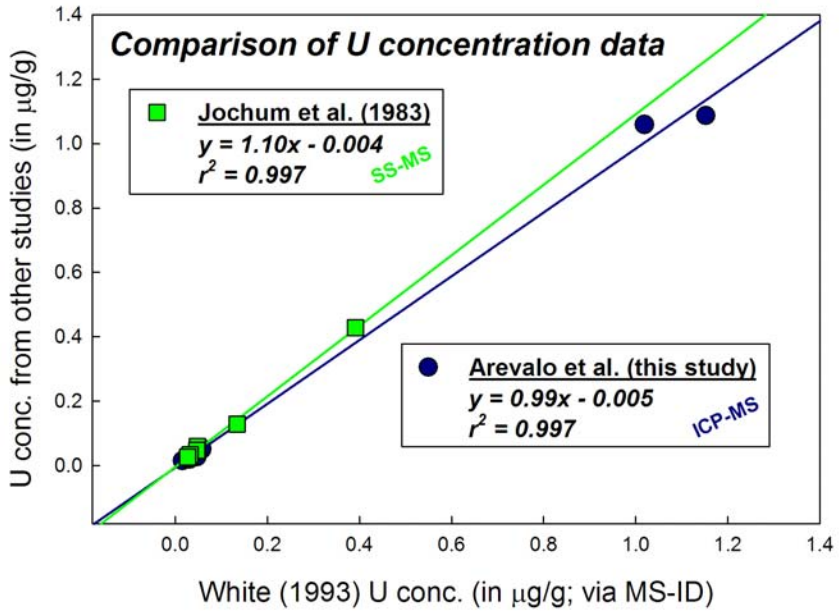

Fig. 2.10. Comparison of Jochum *et al.*, (1983) and Arevalo *et al.*, (this study) U data versus high-precision isotope dilution data from White (1993). Note that the Jochum *et al.*, (1983) data are systematically 10% higher than the White (1993) data, whereas our measurements plot within 1% of White (1993).

~10% high (Fig. 2.10). In comparison, our data plot to within 1% of White (1993). Accordingly, we propose that the low K/U data from Jochum *et al.,* (1983) represents an analytical bias.

2.4 *In situ* determination of first-row transition metal, Ga and Ge abundances in geological materials via medium-resolution LA-ICP-MS

2.4.1 Abstract

An *in situ*, medium-resolution (MR-) LA-ICP-MS method has been developed to measure the abundances of the first-row transition metals, Ga and Ge in a suite of geological materials, namely the MPI-DING reference glasses. The analytical protocol established here hinges on maximizing the ablation rate of the UV laser system and the sensitivity of the ICP-MS, as well minimizing the production of diatomic oxides and argides, which serve as the dominant sources of isobaric interferences. Non-spectral matrix effects are accounted for by using multiple external calibrants, including NIST SRM610 and the USGS basaltic glasses BHVO-2G, BIR-1G and BCR-2G, and utilizing ^{43}Ca as an internal standard. Analyses of the MPI-DING reference glasses, which represent geological matrices ranging from basaltic to rhyolitic in composition, included measurements of concentrations as low as $<10^0$ μg/g and as high as $>10^4$ μg/g. The new data reported here were found to statistically correlate with the preferred values for these materials at the 95% confidence-level, though with significantly better precision, typically on the order of ≤3% ($2\sigma_m$). This analytical method may be extended to any matrix-matched geological sample, particularly oceanic basalts.

2.4.2 Introduction: The role of transition metals, Ga and Ge in characterizing mantle source lithologies

In geological materials, the first-row transition metals (*i.e.*, Sc, Ti, V, Cr, Mn, Fe, Co, Ni, Cu, and Zn), Ga and Ge represent a collection of major (defined by abundances >1.0 wt.%), minor (0.1 – 1.0 wt.%) and trace (<0.1 wt.%) elements that are related by a common [Ar]4s electron orbital base configuration. Because these elements are only mildly incompatible during mantle melting (*i.e.*, $D_i^{sol/liq} < 1$, where D is approximated by the concentration ratio of element i in the *solid* to the *liquid*), their abundances reflect the composition and mineralogy/lithology of the mantle source region in addition to the conditions of melting and/or crystallization. Recently, the concentrations of Cr, Mn, Fe, Co, and Ni in olivine phenocrysts from basaltic lavas (Sobolev *et al.,* 2005, 2007) and TiO_2 in ocean island basalts (Prytulak and Elliott 2007) have been implicated as potential tracers of hybrid pyroxenite in the source regions of ocean islands (*e.g.*, Hawaii), large igneous provinces (*e.g.*, Siberian Traps), komatiites (*e.g.*, Gorgona island) and mid-ocean ridge basalts. However, in addition to the mineralogy/lithology of the source, the behavior of the first-row transition metals in the upper mantle is also sensitive to a range of physical and environmental factors, including: melting temperature; pressure; oxygen fugacity; and, melt composition/polymerization (*e.g.*, Hart and Davis 1978; Kinzler *et al.,* 1990; Ehlers *et al.,* 1992; Hirschmann and Ghiorso 1994; Taura *et al.,* 1998; O'Neill and Eggins 2002; Li *et al.,* 2003; Wang and Gaetani 2008). As a result, discerning the effects of source mineralogy/lithology versus the conditions under which the melting occurs is complicated at best.

Additionally, V, Cr, Mn, Fe, Co, Ni, Cu, Ga, and Ge all behave as moderately siderophile elements under reducing conditions and are depleted in the silicate portion of the Earth relative to chondrites; thus, a significant proportion of these elements has been inferred to reside in the core (*e.g.*, Jagoutz *et al.,* 1979; Arculus and Delano 1981; Brett 1984; McDonough 2003 and references therein). Consequently, these elements have been implicated in studies of core-mantle segregation during the planet's accretion (*e.g.*, Righter *et al.,* 1997; Jana and Walker 1997a, b; Gaetani and Grove 1997; Righter and Drake 2000; Liu and Fleet 2001; Righter 2003 and references therein). Further, Fe/Mn ratios have recently been implicated as a tracer of excess iron in the source regions of ocean island basalts (Humayun *et al.,* 2004; Huang *et al.,* 2007), which has been postulated to result from putative core-mantle interactions, and V/Sc ratios have been shown to act as a sensitive proxy of oxygen fugacity in the upper mantle (Li and Lee 2004; Lee *et al.,* 2005). Consequently, precise and accurate determinations of the first-row transition metals, Ga and Ge are integral to the study and understanding of mantle sources, upper mantle melting processes and potentially core-mantle dynamics.

Concentrations of the first-row transition metals have traditionally been determined via comparative surface and bulk methods of chemical analysis (*e.g.*, electron probe microanalysis, EPMA; instrumental neutron activation analysis, INAA; and, x-ray fluorescence, XRF), but no comprehensive geochemical dataset, covering Sc to Ge, has been produced on global suite of oceanic basalts, which represent primitive mantle-derived materials. Published Ga and Ge concentrations in geological materials are particularly scarce in the scientific literature; in fact, only 11

basalt samples in the entire Lamont–Doherty PetDB Database of Oceanic Basalts (http://www.petdb.org/) currently have reported Ge concentration data. Although *in situ* laser ablation techniques are commonly associated with complications from isobaric interferences, particularly diatomic oxides and argides (*e.g.*, $^{54}Fe^{16}O^{+}$ and $^{30}Si^{40}Ar^{+}$ interferences on mass ^{70}Ge), medium-resolution (MR; $m/\Delta m = 4000$) laser ablation (LA-) inductively-coupled plasma mass spectrometry (ICP-MS) can resolve most spectral interferences while also allowing for: i) bulk and/or spatially-resolved, ng/g-level multi-element measurements of micrometer-scale sample specimens; ii) negligible sample processing (which is time-consuming, costly and can introduce impurities and/or isobaric interferences); iii) low analytical blanks and limits of detection; iv) limited oxide production and spectral matrix effects; and, v) the ability to avoid surface and grain-boundary contamination. Additionally, laser ablation methods provide rapid data acquisition over a wide mass range, require smaller quantities of sample ($\leq$ μg) compared to traditional solution analyses ($\geq$ mg), allow the implementation of either internal or external calibration techniques, and have been validated through numerous analytical studies of geological materials and standard reference materials (*e.g.*, Jeffries *et al.,* 1995a; Pearce *et al.,* 1997; Eggins *et al.,* 1998a; Norman *et al.,* 1998; Rocholl 1998; Gao *et al.,* 2002; Kent *et al.,* 2004; Jochum *et al.,* 2005; Willbold and Jochum 2005; Jochum *et al.,* 2006, 2007; Arevalo and McDonough 2008; Arevalo *et al.,* 2009). Consequently, MR-LA-ICP-MS provides a potentially effective way to measure the abundances of the first-row transition metals, Ga and Ge in geological materials, such as oceanic basalts.

We have established an analytical method to determine accurately the abundances of the first-row transition metals, Ga and Ge in geological reference glasses via MR-LA-ICP-MS. Typically, our concentration measurements are associated with quantitative uncertainties of <3% ($2s_m$, external reproducibility) and are concordant with the reference values of the materials examined here, namely the MPI-DING reference glasses (*i.e.*, ATHO-G, StHs6/80-G, T1-G, ML3B-G, KL2-G, GOR132-G, GOR128-G, and BM90/21-G; Jochum *et al.,* 2000, 2006).

2.4.3 Instrumentation and operating conditions

Elemental concentrations were determined using a Thermo Finnigan Element2 single-collector ICP-MS coupled to a New Wave frequency-quintupled Nd:YAG laser system (213 nm wavelength light) in the Department of Geology, Plasma Laboratory at the University of Maryland. All LA-ICP-MS measurements were conducted while implementing: i) medium-resolution mass discrimination ($m/\Delta m = 4000$) in order to distinguish mono-isotopic masses from most potential molecular isobaric interferences; ii) "mass accuracy" peak-jumping mode, as opposed to the traditional "speed" setting typically used during low-resolution laser ablation analysis; and, iii) a maximum laser spot size and power output, with the goal of maximizing count rates and improving counting statistics. Table 2.4 provides a detailed list of laser and mass spectrometer parameters employed for this study.

Prior to analysis, the ionic lenses and the position of the torch of the ICP-MS were tuned to maximize signal (based on ^{43}Ca and ^{232}Th spectra) and minimize oxide production ($^{232}Th^{16}O/^{232}Th \leq 0.12\%$) in low-resolution ($m/\Delta m = 300$) in order to improve sensitivity and reduce isobaric interferences mostly resulting from diatomic

Table 2.4. Laser system and mass spectrometer operating conditions implemented for the measurement of 1st row transition metals, Ga and Ge.

New Wave Nd:YAG Laser Parameters	
Ablation Pattern	Line
Scan Speed	10 μm/s
Spot Size (Diameter)	250 μm
Wavelength	213 nm @ 5th harmonic
Repetition Rate	12 Hz
Pulse duration	5 ns
Energy Density[a]	1.2-1.3 J/cm^2

Thermo Finnigan Element2 ICP-MS Parameters	
Forward Power	1250W
HV	10 kV
Scan Optimization	Mass Accuracy
Number of Pre-Scans	1
Active Dead Time	25 ns
Guard electrode	Disabled
Mass resolution (m/Δm)	4000
Mass window	5%
Dwell time (per isotope)[b]	10 - 50 ms
Samples per peak	1
Search window	100%
Integration window	80%
Scan type	Escan
Detection mode[c]	Both
Runs and passes	200 x 1
Sampler cone[d]	1.0 mm Ni-alloy
Skimmer cone[d]	0.4 mm Ni-alloy
Cool gas flow	16 L/min Ar
Auxiliary gas flow	1.5 L/min Ar
Sample gas flow	0.7 L/min Ar
Carrier gas flow	1.1 L/min He

[a] Employing a maximum laser spot size of 250 μm and 100% power output results in a maximum fluence of 1.2-1.3 J/cm^2.
[b] All isotope mass stations measured with a sample time of 10 ms with the exceptions of ^{71}Ga and ^{72,73,74}Ge (50 ms).
[c] All isotope mass stations measured via the counting mode of detection with the exception of ^{56}Fe (analog).
[d] Analytical testing revealed that Al cones increased elemental fractionation between the standard and samples (see text).

oxides. A three-stage mass calibration (low-resolution → medium-resolution with a wide search window → medium-resolution with a narrow search window) was then performed to properly calibrate the magnet and electrostatic analyzer and center/sharpen the peak shapes of various isotope mass stations, spanning from ^{7}Li up to ^{232}Th^{16}O.

The element menu employed, which measured multiple isotopes of the same element when available in order to monitor spectral matrix effects, included the following mass stations: ^{43}Ca, ^{45}Sc, ^{47,49}Ti, ^{51}V, ^{52,53}Cr, ^{55}Mn, ^{56,57}Fe, ^{59}Co, ^{60,62}Ni, ^{63,65}Cu, ^{66,67,68}Zn, ^{69,71}Ga, ^{72,73,74}Ge, ^{75}As, and ^{77}Se, with ^{43}Ca serving as the internal standard. The essential detection parameters included a dwell time of 10 ms for all isotope mass stations, with the exceptions of ^{71}Ga and ^{72,73,74}Ge (50 ms each), as the concentrations of these two elements are generally more depleted than the first-row transition metals in most geological materials, thus requiring longer counting times for statistical purposes. The guard electrode was disabled and a "hot" plasma (*i.e.*, 1250W forward power) was employed as these settings have been found to improve signal-to-noise ratios during trace element analysis via LA-ICP-MS (Arevalo and McDonough 2008; Arevalo *et al.,* 2009).

For each sample and standard analysis, a blank signal was collected for 20-30 seconds (Fig. 2.11) with the laser firing but the shutter closed so as to collect an adequate background signal as well as allow the laser pulse to reach a stable energy density. Because helium (He) has a higher ionization potential and smaller ionization cross-section compared to argon (Ar), it is a superior carrier gas for laser ablation mass spectrometry (Russo, 1995; Leung *et al.,* 1998) and has been shown to improve

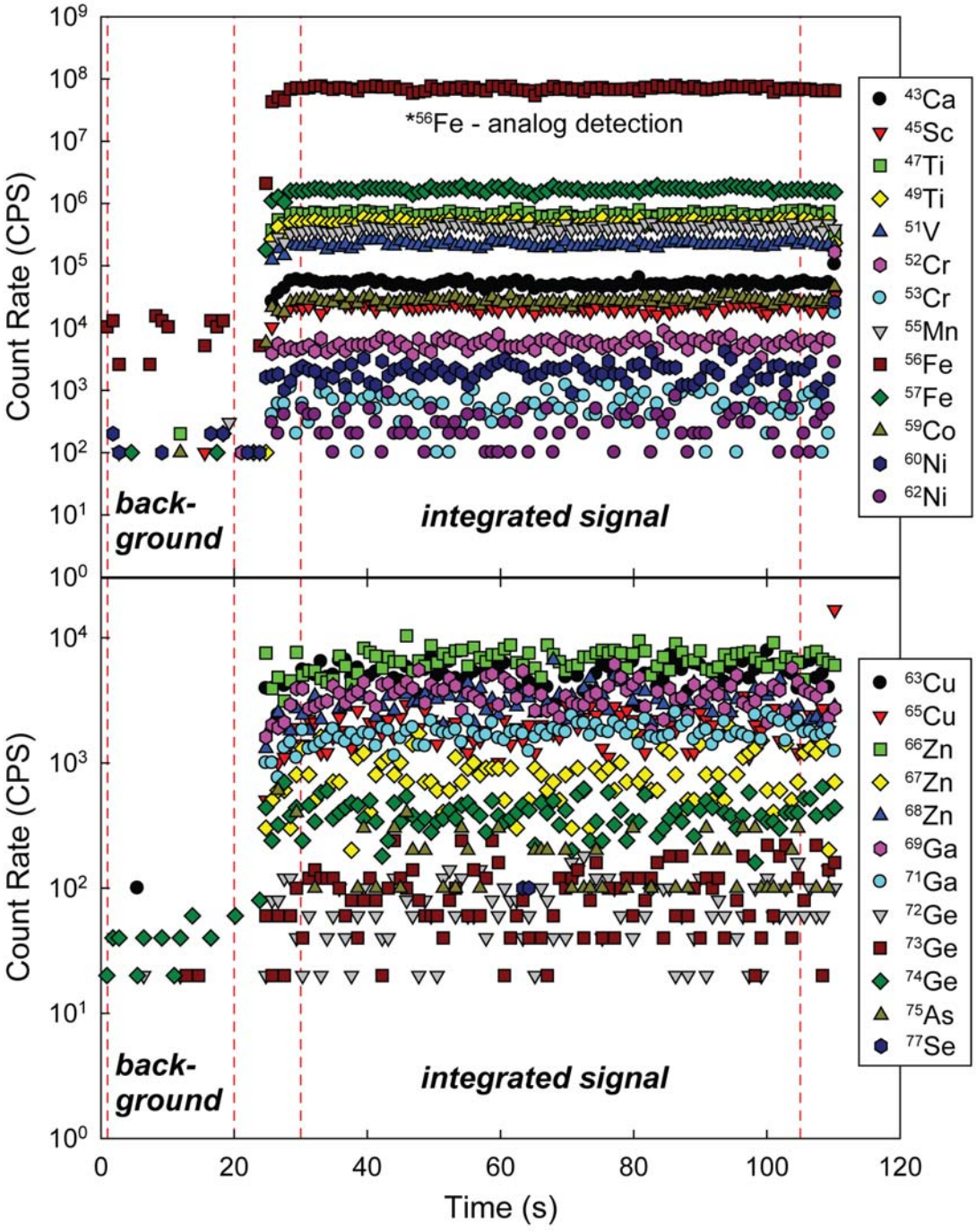

Fig. 2.11. Time-resolved medium-resolution (MR-) LA-ICP-MS spectra from the analysis of the USGS standard reference glass BCR-2G.

signal sensitivity, stability and reproducibility by minimizing the deposition of ablation products and improving sample transport efficiency during ultraviolet (UV) wavelength laser ablation (Eggins *et al.,* 1998b; Mao *et al.,* 1998; Günther and Heinrich 1999a,b); therefore, all ablations in this study occurred in an He atmosphere. Between each sample/standard ablation, the ablation cell and transport tubing were flushed with He gas for 2 minutes to minimize any memory effects.

2.4.4 Samples and standard reference materials

The samples and standards analyzed here represent various reference materials, ranging from ultramafic to highly silicic in composition (Fig. 2.12); included in this suite is the NIST SRM610 calcium-sodium aluminosilicate wafer, three basaltic USGS reference glasses (BHVO-2G, BIR-1G and BCR-2G), and eight MPI-DING glasses with geological matrices, comprising two tholeiitic basalts (KL2-G and ML3B-G), two basaltic komatiites (GOR128-G and GOR132-G), a peridotite (BM90/21-G), andesitic quartz-diorite (T1-G), dacite (StHs6/80-G), and rhyolite (ATHO-G). The chemical compositions and homogeneity of these samples/standards have been extensively characterized through various analytical means, including EPMA, INAA, XRF, ICP-MS, secondary ion mass spectrometry (SIMS), proton induced x-ray emission (PIXE), isotope dilution mass spectrometry (ID-MS), and laser ablation methods (*e.g.*, Pearce *et al.,* 1997; Eggins *et al.,* 1998a; Norman *et al.,* 1998; Rocholl 1998; Jochum *et al.,* 2000; Gao *et al.,* 2002; Kent *et al.,* 2004; Jochum *et al.,* 2005; Willbold and Jochum 2005; Jochum *et al.,* 2006, 2007; Arevalo and McDonough 2008; Arevalo *et al.,* 2009).

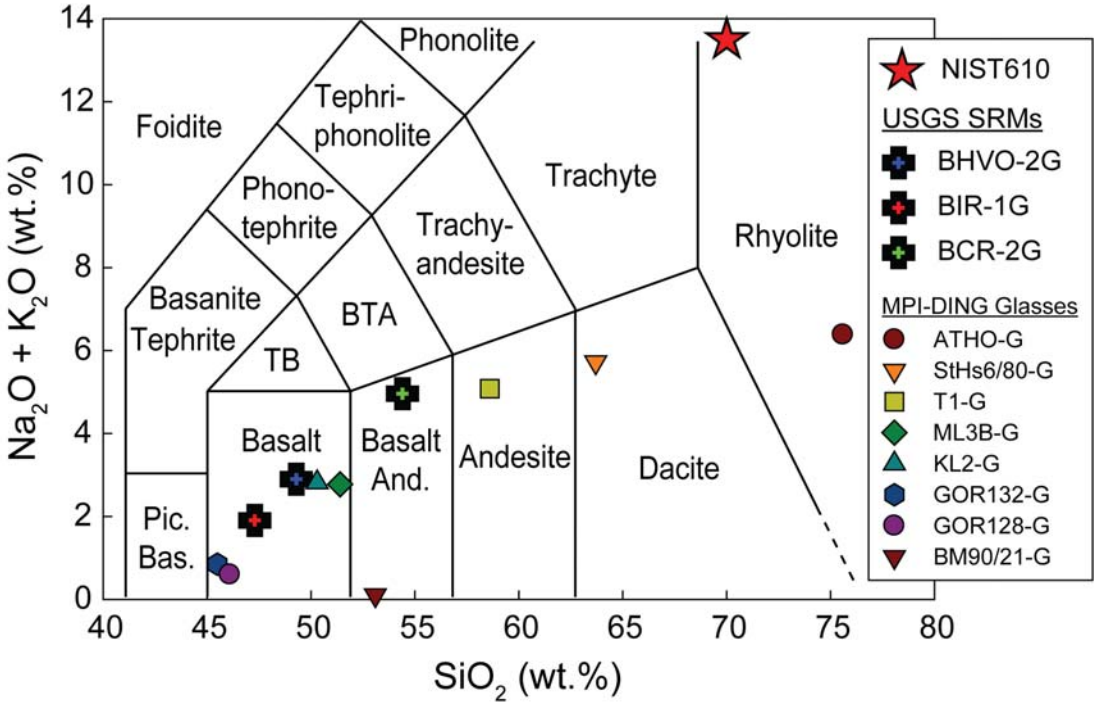

Fig. 2.12. IUGS classification of the USGS and NIST calibrating standard reference materials and MPI-DING glasses analyzed here. The USGS reference glasses BHVO-2G, BIR-1G and BCR-2G, along with the MPI-DING glasses KL2-G, ML3B-G, GOR128-G, and GOR132-G are all basaltic in composition. The MPI-DING glasses also include an andesitic (T1-G), dacitic (StHs6/80-G), rhyolitic (ATHO-G), and peridotitic (BM90/21-G) specimen.

2.4.5 Spectral (Isobaric) matrix effects

Matrix effects can be effectively divided into two principal species: spectral (isobaric) and non-spectral types (Albarède and Beard 2004). Spectral matrix effects, which occur when two or more atomic and/or molecular species have overlapping mass-to-charge ratios that cannot be resolved via mass spectrometry, primarily occur as: elemental isobaric mass interferences, such as $^{70}Zn^{+}$ at mass station $^{70}Ge^{+}$; double-charged interferences, such as $^{140}Ce^{++}$ at $^{70}Ge^{+}$; diatomic oxides, such as $^{54}Fe^{16}O^{+}$ and $^{54}Cr^{16}O^{+}$ at $^{70}Ge^{+}$; and, diatomic argides, such as $^{30}Si^{40}Ar^{+}$ at $^{70}Ge^{+}$. Non-spectral matrix effects, which generally occur as disproportionate laser-induced elemental fractionation during LA-ICP-MS, are the result of asymmetrical photon-substrate coupling between the external standard reference material and the sample unknowns.

Table 2.5 lists all of the pertinent atomic and molecular isobaric interferences that can not be resolved via medium-resolution ICP-MS ($m/\Delta m = 4000$). The majority of potential spectral interferences in this study are diatomic metal oxides (*i.e.*, MO^{+}, where M = Ti, V, Cr, Mn, Fe, or Ni) and diatomic non-metal argides (*i.e.*, ArX^{+}, where X = Si, P, S, Cl, or Ar), which are formed in the plasma due to a positive plasma potential induced by capacitive coupling with the load coil, behind the sampling cone due to the effects of a secondary discharge, and potentially at the substrate surface due to photon bombardment during laser processing (*e.g.*, Rohlfing *et al.,* 1984; Nonose *et al.,* 1994; Sakata and Kawabata 1994); with the exception of $^{74}Se^{+}$ on mass $^{74}Ge^{+}$, all elemental isobaric interferences (single-charged species) are resolvable under medium-resolution detection.

Table 2.5. Irresolvable isobaric interferences concerning the first-row transition metals, Ga and Ge at medium-resolution (m/Δm = 4000) mass discrimination.

Isotope	Abundance	Interfering Species	m/Δm[a]
^{43}Ca	0.14%	$^{86}Sr^{++}$, $^{86}Kr^{++}$	12400
^{45}Sc	100%	$^{90}Zr^{++}$	12700
^{47}Ti	7.30%	$^{94}Mo^{++}$, $^{94}Zr^{++}$	59400
^{49}Ti	5.50%	$^{98}Ru^{++}$, $^{98}Mo^{++}$	10200
^{51}V	99.8%	$^{102}Ru^{++}$, $^{102}Pd^{++}$	6210
^{52}Cr	83.8%	$^{104}Pd^{++}$, $^{104}Ru^{++}$	4520
^{53}Cr	9.50%	$^{106}Pd^{++}$, $^{106}Cd^{++}$	4770
^{55}Mn	100%	$^{110}Cd^{++}$	4080
^{56}Fe	91.7%	none	N/A
^{57}Fe	2.20%	none	N/A
^{59}Co	100%	none	N/A
^{60}Ni	26.1%	none	N/A
^{62}Ni	3.59%	none	N/A
^{63}Cu	69.2%	none	N/A
^{65}Cu	30.8%	$^{49}Ti^{16}O^{+}$	4330
^{66}Zn	27.9%	$^{28}Si^{38}Ar^{+}$, $^{50}Ti^{16}O^{+}$, $^{50}Cr^{16}O^{+}$, $^{30}Si^{36}Ar^{+}$, $^{50}V^{16}O^{+}$	4840
^{67}Zn	4.10%	$^{51}V^{16}O^{+}$, $^{29}Si^{38}Ar^{+}$, $^{31}P^{36}Ar^{+}$	5750
^{68}Zn	18.8%	$^{52}Cr^{16}O^{+}$, $^{30}Si^{38}Ar^{+}$, $^{28}Si^{40}Ar^{+}$, $^{32}S^{36}Ar^{+}$	6430
^{69}Ga	60.1%	$^{53}Cr^{16}O^{+}$, $^{31}P^{38}Ar^{+}$, $^{29}Si^{40}Ar^{+}$, $^{33}S^{36}Ar^{+}$, $^{52}Cr^{17}O^{+}$	6910
^{71}Ga	39.9%	$^{55}Mn^{16}O^{+}$, $^{31}P^{40}Ar^{+}$, $^{35}Cl^{36}Ar^{+}$, $^{53}Cr^{18}O^{+}$	8590
^{72}Ge	27.4%	$^{56}Fe^{16}O^{+}$, $^{34}S^{38}Ar^{+}$, $^{32}S^{40}Ar^{+}$, $^{36}Ar^{36}Ar^{+}$, $^{55}Mn^{17}O^{+}$, $^{54}Fe^{18}O^{+}$	9260
^{73}Ge	7.80%	$^{57}Fe^{16}O^{+}$, $^{35}Cl^{38}Ar^{+}$, $^{37}Cl^{36}Ar^{+}$, $^{33}S^{40}Ar^{+}$, $^{56}Fe^{17}O^{+}$, $^{55}Mn^{18}O^{+}$	10600
^{74}Ge	36.5%	$^{74}Se^{+}$, $^{58}Fe^{16}O^{+}$, $^{34}S^{40}Ar^{+}$, $^{58}Ni^{16}O^{+}$, $^{36}Ar^{38}Ar^{+}$, $^{56}Fe^{18}O^{+}$	56900

[a] Minimum resolution required to resolve all isobaric interferences.

The relative production of diatomic metal oxides (*i.e.*, MO+/M+) has been found to correlate with bond strengths (or bond dissociation energies) in studies of molecular ion formation during ICP-MS analysis (*e.g.*, Michiels and Gijbels 1984; Becker and Dietze 1995; Becker *et al.,* 1996; Becker and Dietze 2000). The rare-earth elements (REE; *i.e.*, La through Lu) generally have lower first ionization potentials, and more importantly, higher diatomic oxide bond strengths compared to the first-row transition metals, as reported in Table 2.6. Thus, the REE may be inferred to be more prone to oxide formation than the first-row transition metals; by comparison, Th has the highest diatomic oxide bond strength (878.6 kJ/mol) and has been shown to be the

Table 2.6. Atomic numbers, first ionization potentials and bond strengths of irresolvable interferences at medium resolution (m/Δm = 4000) mass discrimination.

Z	Element	1st Ionization Potential (eV)[a]	Diatomic Interference(s)	Diatomic Bond Strength ($D°_{298}$/kJ mol^{-1})[a]	Targeted Analyte(s)
13	Al	5.9858	Al-O	511.0	reference
			Al-Ar	5.18	reference
14	Si	8.1517	Si-Ar	unknown	Zn, Ga
			$^{28}Si^{38}Ar^+$		^{66}Zn
			$^{29}Si^{38}Ar^+$		^{67}Zn
			$^{30}Si^{38}Ar^+$, $^{28}Si^{40}Ar^+$		^{68}Zn
			$^{29}Si^{40}Ar^+$		^{69}Ga
15	P	10.487	P-Ar	unknown	Zn, Ga
			$^{31}P^{36}Ar^+$		^{67}Zn
			$^{31}P^{38}Ar^+$		^{69}Ga
			$^{31}P^{40}Ar^+$		^{71}Ga
16	S	10.360	S-Ar	unknown	Zn, Ga, Ge
			$^{32}S^{36}Ar^+$		^{68}Zn
			$^{33}S^{36}Ar^+$		^{69}Ga
			$^{34}S^{38}Ar^+$, $^{32}S^{40}Ar^+$		^{72}Ge
			$^{33}S^{40}Ar^+$		^{73}Ge
			$^{34}S^{40}Ar^+$		^{74}Ge
17	Cl	12.968	Cl-Ar	unknown	Ga, Ge
			$^{35}Cl^{36}Ar^+$		^{71}Ga
			$^{35}Cl^{38}Ar^+$, $^{37}Cl^{36}Ar^+$		^{73}Ge
18	Ar	15.760	Ar-Ar	4.73	Ge
			$^{36}Ar^{36}Ar^+$		^{72}Ge
			$^{36}Ar^{38}Ar^+$		^{74}Ge
19	K	4.3407	K-O	277.8	reference
			K-Ar	4.20	reference
22	Ti	6.8281	Ti-O	672.4	Cu, Zn
			$^{49}Ti^{16}O^+$		^{65}Cu
			$^{50}Ti^{16}O^+$		^{66}Zn
23	V	6.7463	V-O	626.8	Zn, Ga
			$^{50}V^{16}O^+$		^{66}Zn
			$^{51}V^{16}O^+$		^{67}Zn
24	Cr	6.7665	Cr-O	461.0	Zn, Ga
			$^{50}Cr^{16}O^+$		^{66}Zn
			$^{52}Cr^{16}O^+$		^{68}Zn
			$^{53}Cr^{16}O^+$, $^{52}Cr^{17}O^+$		^{69}Ga
			$^{53}Cr^{18}O^+$		^{71}Ga
25	Mn	7.4340	Mn-O	402.9	Ga, Ge
			$^{55}Mn^{16}O^+$		^{71}Ga
			$^{55}Mn^{17}O^+$		^{72}Ge
			$^{55}Mn^{18}O^+$		^{73}Ge
26	Fe	7.9024	Fe-O	390.4	Ge
			$^{56}Fe^{16}O^+$, $^{54}Fe^{18}O^+$		^{72}Ge
			$^{57}Fe^{16}O^+$, $^{56}Fe^{17}O^+$		^{73}Ge
			$^{58}Fe^{16}O^+$, $^{56}Fe^{18}O^+$		^{74}Ge
27	Ni	7.6398	Ni-O	382.0	Ge
			$^{58}Ni^{16}O^+$		^{74}Ge
57	La	5.5770	La-O	799.0	reference
58	Ce		Ce-O		reference
71	Lu	5.4259	Lu-O	678.0	reference
90	Th	6.3067	Th-O	878.6	reference
92	U	6.1941	U-O	759.4	reference

[a] Source: CRC Handbook of Chemistry and Physics, 82nd Edition 2001.

most prevalent oxide during ICP-MS analysis (*e.g.*, Lichte *et al.,* 1987; Becker and Dietze, 2000). The analytical method developed here to measure the abundances of the first-row transition metals, Ga and Ge in geological samples emphasizes the minimization of oxide formation by selectively tuning to a $^{232}Th^{16}O/^{232}Th$ production rate of ≤0.12%, which has been shown to result in typical REE-oxide production rates of $<10^{-6}$ (Arevalo and McDonough 2008).

The production of diatomic argides has also been found to correlate with bond strengths (*e.g.*, Barshik *et al.,* 1995; Becker and Dietze 1997), and also with diatomic oxide production in a study of REE molecular ion formation during ICP-MS analysis, albeit with MAr^+/MO^+ on the order of $<10^{-3}$ (Becker *et al.,* 1996). The lower abundance of diatomic argide species relative to diatomic oxides likely represents the lower stability of these molecules, as argides are typically defined by bond strengths >100 times lower than diatomic oxides (see Al and K in Table 2.6). Thus, by limiting the production of oxides by minimizing $^{232}Th^{16}O/^{232}Th$ through our tuning procedures, we are not only capping the production of oxide species, but also argides. Consequently, diatomic oxides and argides do not serve as a significant source of interferences in this study.

Some double-charged species, particularly double-ionized second-row transition metals (*e.g.*, Zr^{++} and Mo^{++}), are irresolvable from the spectra of ^{43}Ca (our internal standard) and the lightest first-row transition metals (*i.e.*, Sc, Ti, V, Cr, and Mn) with medium-resolution detection parameters. For this reason, we investigated the production of double-charged species by looking at the ionization of all isotopes of Zr (2^{nd} ionization potential of 13.1 eV) and Mo (2^{nd} ionization potential of 16.2

eV) during LA-ICP-MS while applying the same analytical protocol described here. The production of double-charged species of Zr, measured during the analysis of the zircon standard 91500, was determined to be $^{XX}Zr^{++}/^{XX}Zr^{+} < 0.01\%$ for all isotopes. The production of Mo^{++}, measured during the analysis of a molybdenite from Kouenda, Korea, was determined to be $^{XX}Mo^{++}/^{XX}Mo^{+} < 0.004\%$ for all isotopes (see Supplemental Materials for details). The limited efficiency of double-ionization of both Zr and Mo, which exemplify potential isobaric interferences (*i.e.*, $^{90}Zr^{++}$ on mass $^{45}Sc^{+}$, $^{94}Zr^{++}$ and $^{94}Mo^{++}$ on $^{47}Ti^{+}$, and $^{98}Mo^{++}$ on $^{49}Ti^{+}$), suggests that double-charged elemental species do not pose a significant source of isobaric interferences for this study. However, as an additional safeguard against all spectral matrix effects, we monitored multiple isotope mass stations of several targeted elements in our search menu (*e.g.*, $^{47,49}Ti$, $^{52,53}Cr$, etc.) in order to identify potential isobaric interferences, including diatomic oxides, argides and double-charged species; no systematic variances diagnostic of spectral matrix effects were detected.

2.4.6 Non-spectral matrix effects and calibration techniques

During laser ablation processing, the interaction (or coupling) between the incident laser radiation and the surface of the substrate, such as a geological sample or standard reference material, depends on the parameters of the laser beam, including: the incident irradiance (*i.e.*, radiant flux incident on a defined area of the substrate, E_i; typically in $W \cdot cm^{-2}$); wavelength of light; spatial and temporal coherence of the beam; and, pulse duration. However, in addition to the properties of the laser light, photon-substrate coupling is also contingent on the optical (*i.e.*, reflectivity, transmissivity, absorptivity, and dielectric permissivity), physical (*i.e.*,

microstructure) and chemical (*i.e.*, elemental composition) properties of the target material (*e.g.*, Russo 1995; Bäuerle 1996; Durrant 1999 and references therein). When the parameters of the laser system are held constant, as during LA-ICP-MS, the photon absorption behavior of different substrate materials is primarily dependent on the chemical composition of the substrate matrix. Discrepancies between the matrix of a calibrating standard reference material and the matrix of a geological sample can result in disproportionate ablation efficiency and asymmetrical laser-induced elemental fractionation (*e.g.*, Fryer *et al.,* 1995; Ludden *et al.,* 1995; Stix *et al.,* 1995; Durrant 1999).

Although NIST SRM610 and SRM612 have both been extensively characterized (*e.g.*, Norman *et al.,* 1996; Pearce *et al.,* 1997; Kane 1998; Eggins and Shelley 2002; Kent *et al.,* 2004; Hu *et al.,* 2008a,b), these materials represent synthetic calcium-sodium aluminosilicate glasses doped with a range of trace elements (from $_{3}$Li up to $_{92}$U) at concentrations of approximately 400 μg/g and 40 μg/g, respectively. Because we are interested in developing an analytical method for measuring transition metals with the highest precision and accuracy in geological materials, such as oceanic basalts, the NIST SRM glasses do not provide a matrix-matched calibrant and may not be ideally suited for the analysis of natural materials. Consequently, we also implemented the use of the USGS basaltic reference glasses BHVO-2G, BIR-1G and BCR-2G as external calibrating standards for this study.

In order to minimize further the potential for elemental fractionation during laser ablation processing, we enforced various analytical protocols that have been shown to effectively maintain an efficient ablation rate and limit inconsistent laser-

induced fractionation effects, including the use of: non-transparent calibrating reference materials (*e.g.*, Gaboardi and Humayun 2009); active focusing (*e.g.*, Hirata and Nesbitt, 1995); slow traverse speeds (*e.g.*, Guillong and Günther, 2002); high carrier gas flow rates (*e.g.*, Jeong *et al.,* 1999); low repetition rates (*e.g.*, Norman *et al.,* 1996; Günther *et al.,* 1997); large spot diameters (*e.g.*, Fernandez *et al.,* 1995; Jeong *et al.,*1999; Mank and Mason 1999); incident irradiances surpassing the critical ablation threshold but below the threshold of mass ablation roll-off due to plasma shielding (*i.e.*, between 0.1 – 1.0 GW/cm^2; *e.g.*, Russo 1995; Bäuerle 1996; Mao *et al.,* 1996; Figg *et al.,* 1998; Jeong *et al.,* 1999; Bogaerts and Chen 2005); ablation lines and/or rasters rather than spots, and thus low depth-to-diameter pit aspect ratios (*e.g.*, Perkins *et al.,* 1997; Eggins *et al.,* 1998b; Günther and Heinrich 1999b; Mank and Mason 1999; Borisov *et al.,* 2000; Horn *et al.,* 2000; Russo *et al.,* 2000; Ruf *et al.,* 2001; Morishita *et al.,* 2005); and, the use of ultraviolet-wavelength light (*i.e.*, 213 nm) and constant energy densities (*i.e.*, 1.2 – 1.3 J/cm^2), which contribute to a smaller and more constant particle size distribution (*e.g.*, Fernandez *et al.,* 1995; Jeffries *et al.,* 1995b; Figg and Kahr 1997; Günther and Heinrich 1999b; Figg *et al.,* 1998; Guillong and Günther 2002; Guillong *et al.,* 2003; Bogaerts and Chen 2005). As an additional consideration, we tested the viability of using Al cones in place of the Ni-alloy cones generally preferred during ICP-MS, as Al cones have been reported to improve signal-to-noise ratios (Latkoczy and Günther, 2002). However, our results found that these parameters failed to significantly decrease background count rates, which were nominal with Ni-alloy cones using medium-resolution mass discrimination (generally <100 counts per second, with the exception of ^{56}Fe in

analog detection mode), nor the sensitivity, oxide production, and/or precision of our measurements. Furthermore, the use of Al cones actually served to increase the elemental fractionation observed between the external calibrating materials and samples (see Supplemental Materials), and thus were not used during this study.

2.4.7 Determination of calibrant compositions

As justified above, in addition to NIST SRM610, the USGS reference glasses BHVO-2G, BIR-1G and BCR-2G were employed as supplemental external calibrating standards in the quantification of our dataset due to their matrix-matched composition relative to geological samples, such as the MPI-DING reference glasses analyzed here. However, rather than depending on published measurements of the USGS glasses, which yield discordant compositional estimates ranging over a factor of two for some elements and frequently include analyses based on LA-ICP-MS methods using NIST SRM610/612 as external calibrants (*e.g.*, GeoReM Database; http://georem.mpch-mainz.gwdg.de/), for our calibrations we independently assessed the composition of these standard reference materials by various in-house methods of analysis.

Concentrations of Sc, V, Co, Ni, Cu, Zn, Ga, and Ge in the USGS reference glasses were determined for BHVO-2G and BIR-1G via high-precision standard addition ICP-MS using a multi-element dopant created in-house, an analytical method that does not rely on sample-standard bracketing and thus is immune to matrix effects. Alternatively, these elements were determined in BCR-2G via traditional solution ICP-MS analysis using standard-sample bracketing with BHVO-2G and BIR-1G. Powdered aliquots of these standard reference materials were digested in 15

mL Savillex Teflon vials at 180°C for 24 hours in a concentrated acid solution of HF:HNO_3 (3:1). Subsequently, the sample solutions were dried down and two doses of 350 mL of concentrated $HClO_4$ were applied and allowed to dry in order to oxidize the trace metals (*e.g.*, Lichtin, 1930) and breakdown any insoluble fluorides and (*e.g.*, Yokoyama 1999). The digested samples were taken up in 2% HNO3 and then split five ways for standard addition analysis or prepped for traditional solution ICP-MS analysis (see Supplemental Materials).

Although Cr was also analyzed via standard addition for both BHVO-2G and BIR-1G, a significant fraction (~10%) was found to be lost during the wet digestion of the sample powders, potentially due to incomplete acid decomposition (*e.g.*, Matusiewicz *et al.,* 1991; Liu *et al.,* 1996), the persistence of chromite and/or Cr-bearing silicate phases (*e.g.*, Bond *et al.,* 1970; Thompson and Wood 1982) and/or insoluble fluorides (*e.g.*, Thompson and Walsh 1988), or loss by evaporation of volatile species (*e.g.*, CrO_2Cl_2; Portmann 1964; Wang *et al.,* 1999). Consequently, Cr, together with V and the major elements Ti, Mn and Fe, was determined in these standard materials using a JEOL JXA-8900 electron probe microanalyzer at the University of Maryland. A combination of NIST SRM 610 (Pearce *et al.,* 1997) and Corning 95IRW/95IRX (Carpenter *et al.,* 2002) glasses were used to determine appropriate peak and background positions, and to evaluate peak overlaps. Slow speed, high-resolution WDS scans were performed in the regions around Mn, Cr, V and Ti peaks. Once positions were determined, SCA (Single-Channel Pulse-Height Analyzer) settings were adjusted to maximize count rates and to minimize the probability of higher order overlaps. During analysis, absorbed current was monitored

continuously in order to evaluate sample and/or carbon coat degradation. Raw intensities were corrected using a ZAF algorithm. Due to the low concentrations of V and Cr (approximately 300 – 400 μg/g) and Mn (<1500 μg/g) in the USGS glasses, the sensitivity of the microprobe had to be maximized and the peak shapes of potential spectral overlaps (*e.g.*, Ti$K\beta_1$ on V$K\alpha_{1,2}$) had to be located, counted and recorded.

In order to reach adequate counting statistics, the following specifications were employed: 15 kV accelerating voltage; 200 nA current; 30 μm beam diameter; and, 90 s count times for each element peak and 45 s for each background position. Because the abundances of Ti and Fe in the USGS glasses are on the order of wt.%, these concentrations were also determined via EPMA, though more customary specifications were employed in order to avoid diffusive loss of Na, including: 15 kV accelerating voltage; 10 nA current; 30 μm electron beam diameter; and, 30 s count times for each element signal and background. All EPMA measurements represent the average composition of a 25-point raster of the glass surface. A comparison of our in-house chemical analyses of the USGS reference glasses BHVO-2g, BIR-1G and BCR-2G, including standard addition, traditional solution ICP-MS, and EPMA measurements, versus other published values is given in Table 2.7.

2.4.8 Data precision and accuracy

Abundances of the first-row transition metals, Ga and Ge for the eight MPI-DING glasses analyzed in this study range from the sub-μg/g level (*e.g.*, Ge) up to several wt.% (*e.g.*, Ti and Fe), but with most concentrations on the order of several hundred μg/g. The typical uncertainty of our measurements is on the order of ±3% ($2\sigma_m$) or

Table 2.7. Comparison of concentration values (in µg/g) for the NIST standard reference material SRM610 and the USGS basaltic standards BIR-1(G), BHVO-2(G) and BCR-2(G).

NIST SRM610

Element	Preferred Value	Reference	NIST Cert. Value[a]	GeoReM Pref. Glass Value[b]	Pearce *et al.* (1997) Value[c]
Ca	*82200 ± 2900 (2σ)*	*c*		*82200 ± 2900*	*82200 ± 2900*
Sc	441 ± 20	c		441 ± 20	441 ± 20
Ti	434 ± 30	c		434 ± 30	434 ± 30
V	442 ± 86	c		442 ± 86	442 ± 86
Cr	405 ± 64	c		405 ± 64	405 ± 64
Mn	485 ± 10	a	485 ± 10	485 ± 10	433 ± 62
Fe	458 ± 9	a	458 ± 9	458 ± 9	457 ± 44
Co	405 ± 46	c		405 ± 46	405 ± 46
Ni	459 ± 4	a	459 ± 4	459 ± 4	444 ± 48
Cu	430 ± 48	c		430 ± 48	430 ± 48
Zn	456 ± 38	c		456 ± 38	456 ± 38
Ga	438 ± 22	c		438 ± 22	438 ± 22
Ge	426 ± 20	c		426 ± 20	426 ± 20

USGS BHVO-2(G)

Element	In-House Value[d]	In-House Method[e]	USGS Cert. Powder Value[f]	GeoReM Pref. Glass Value[b]	GeoReM Pref. Powder Value[b]
Ca	*81500 ± 1400 (2σ)*	*N/A*	*81700 ± 2400*	*81500 ± 1400*	*81500 ± 2900*
Sc	31.0 ± 0.3	1	32 ± 2	33 ± 4	32 ± 2
Ti	16500 ± 100	2	16400 ± 400	16300 ± 1800	16300 ± 4000
V	274 ± 12	1,3	317 ± 22	308 ± 38	317 ± 22
Cr	332 ± 8	3	280 ± 38	293 ± 24	280 ± 38
Mn	1290 ± 10	3	1290 ± 80	1320 ± 460	1320 ± 80
Fe	85100 ± 900	2	86000 ± 2800	87800 ± 1500	86000 ± 2800
Co	47.1 ± 0.7	1	45 ± 6	44 ± 4	45 ± 6
Ni	127 ± 3	1	119 ± 14	116 ± 14	119 ± 14
Cu	129 ± 3	1	127 ± 14	127 ± 22	127 ± 14
Zn	102 ± 1	1	103 ± 12	102 ± 12	103 ± 12
Ga	21.9 ± 0.2	1	21.7 ± 1.8	22 ± 6	22 ± 4
Ge	1.61 ± 0.02	1		1.6 ± 0.2	1.6 ± 0.2

USGS BIR-1(G)

Element	In-House Value[d]	In-House Method[e]	USGS Cert. Powder Value[f]	GeoReM Pref. Glass Value[b]	GeoReM Pref. Powder Value[b]
Ca	*95800 ± 2900 (2σ)*	*N/A*	*95100 ± 1700*	*95100 ± 2900*	*95800 ± 2900*
Sc	40.6 ± 0.8	1	44 ± 2	43 ± 6	43 ± 4
Ti	5680 ± 60	2	5750 ± 120	5400 ± 400	5600 ± 1000
V	282 ± 6	1,3	310 ± 22	326 ± 64	319 ± 36
Cr	428 ± 12	3	370 ± 16	392 ± 48	391 ± 30
Mn	1330 ± 10	3	1360 ± 50	1470 ± 150	1360 ± 120
Fe	78800 ± 1000	2	79000 ± 1700	80800 ± 1600	79000 ± 1700
Co	52.8 ± 1.4	1	52 ± 4	52 ± 10	52 ± 6
Ni	169 ± 3	1	170 ± 12	178 ± 36	166 ± 14
Cu	115 ± 4	1	125 ± 8	119 ± 24	119 ± 16
Zn	60.8 ± 4.4	1	70 ± 18	78 ± 34	72 ± 36
Ga	15.7 ± 0.3	1		15 ± 4	15.3 ± 1.6
Ge	1.43 ± 0.03	1		1.2 ± 0.2	1.4 ± 0.4

USGS BCR-2(G)

Element	In-House Value[d]	In-House Method[e]	USGS Cert. Powder Value[f]	GeoReM Pref. Glass Value[b]	GeoReM Pref. Powder Value[b]
Ca	*51600 ± 2900 (2σ)*	*N/A*	*50900 ± 1600*	*50500 ± 1600*	*50900 ± 1600*
Sc	32.8 ± 2.0	4	33 ± 4	33 ± 4	33 ± 4
Ti		N/A	13500 ± 600	13600 ± 500	13500 ± 600
V	374 ± 9	4	416 ± 28	425 ± 36	416 ± 28
Cr	17.4 ± 1.7	4	18 ± 4	17 ± 4	18 ± 4
Mn		N/A	1520 ± 120	1550 ± 140	1520 ± 120
Fe		N/A	96600 ± 3000	96400 ± 2300	96600 ± 3000
Co	36.4 ± 1.2	4	37 ± 6	38 ± 4	37 ± 6
Ni	11.3 ± 0.4	4		13 ± 4	18 ± 2
Cu	15.2 ± 0.6	4	19 ± 4	21 ± 10	21 ± 2
Zn	115 ± 6	4	127 ± 18	125 ± 10	127 ± 18
Ga	22.3 ± 0.7	4	23 ± 4	23 ± 2	23 ± 4
Ge	1.54 ± 0.15	4		1.5 ± 0.2	

[a] NIST Standard Reference Materials: http://ts.nist.gov/measurementservices/referencematerials/index.cfm.

[b] GeoReM Database: http://georem.mpch-mainz.gwdg.de/.

[c] N.J.G. Pearce, et al. (1997). A compilation of new and published major and trace element data for NIST SRM 610 and NIST SRM 612 glass reference materials. Geostandards Newsletter: The Journal of Geostandards and Geoanalysis, 21, 115-144.

[d] Precision of in-house measurements reported as $2\sigma_m$ external reproducibilities.

[e] 1: standard addition ICP-MS; 2: major element EPMA; 3: high-sensitivity EPMA; 4: solution ICP-MS.

[f] USGS Geochemical Reference Materials and Certificates: http://minerals.cr.usgs.gov/geo_chem_stand/.

better, based on the reproducibility of 2 – 4 measurements of one or more isotope mass stations per element. In general, Ge yielded the highest uncertainties, ranging from 3.8% (T-1G) up to 16.8% (ML3B-G), due to the lowest concentrations (and thus lowest count rates) measured, between 0.480 μg/g (BM90/21-G) and 1.93 μg/g (ATHO-G). The only significant discrepancy between concentration data acquired through multiple isotope mass stations was observed between ^{56}Fe and ^{57}Fe. However, we believe this to be a function of a detection bias between the counting mode of detection used for mass ^{57}Fe and the analog mode used for mass ^{56}Fe, rather than representing an isobaric interference on either one of these mass stations. Consequently, we only consider the data acquired through the measurement of isotope mass station ^{57}Fe, as negligible background was observed at this station and all other mass stations were also measured via the counting mode of detection.

Rather than relying on just one external standard reference material to calibrate our measurements, such as typically performed during laser ablation analysis (usually with NIST SRM610 or SRM612), we independently considered four different external calibrants (*i.e.*, NIST SRM610, BHVO-2G, BIR-1G and BCR-2G) in order to minimize non-spectral matrix effects and a compromise in accuracy. An element-by-element comparison of the data acquired by using each of these calibrating standards is given in Table 2.8. Overall, BHVO-2G provides the best external calibration for the analysis of the first-row transition metals, Ga and Ge in geological materials, as represented by the MPI-DING reference glasses. However, NIST SRM 610 provides the best calibration for measuring V, and BIR-1G is ideally suited for measuring Cr, Mn and Co abundances. Although BCR-2G also provides

Table 2.8. Correlations between our LA-ICP-MS data acquired with different external calibrating materials and the preferred GeoReM values for the MPI-DING silicate glasses[a].

	Sc	Ti	V	Cr	Mn	Fe	Co	Ni	Cu	Zn	Ga	Ge
NIST SRM610												
slope	**0.97**	0.90	**0.98**	**0.92**	**1.07**	0.87	0.93	0.88	0.88	**1.25**	**0.96**	**1.00**
± *(95% confidence)*	***0.11***	*0.01*	***0.04***	***0.08***	***0.30***	*0.10*	*0.06*	*0.05*	*0.10*	***0.54***	***0.13***	***0.39***
y-intercept	**-2.2**	2.0	**-0.08**	**-2.2**	**-8.0**	4200	-0.3	-0.1	2.3	**-15**	**0.0**	**0.02**
± *(95% confidence)*	***2.6***	*31*	***0.51***	***2.7***	***280***	*5400*	*1.0*	*2.5*	*3.4*	***41***	***1.9***	***0.38***
USGS BHVO-2G												
slope	**1.01**	0.96	0.86	**1.07**	**0.95**	**0.94**	1.08	**1.02**	**1.04**	**1.03**	**1.07**	**1.10**
± *(95% confidence)*	***0.11***	*0.02*	*0.04*	***0.09***	***0.26***	***0.11***	*0.07*	***0.06***	***0.12***	***0.44***	***0.15***	***0.42***
y-intercept	**-2.3**	2.0	-0.07	**-2.5**	**-7.0**	**4600**	-0.3	**-0.1**	**2.7**	**-12**	**0.0**	**0.02**
± *(95% confidence)*	***2.7***	*33*	*0.45*	***3.1***	***250***	***5900***	*1.1*	***2.9***	***4.1***	***34***	***2.1***	***0.42***
USGS BIR-1G												
slope	**0.98**	0.94	0.85	**1.02**	**0.98**	**0.91**	**0.96**	0.85	0.87	**0.79**	0.85	**0.91**
± *(95% confidence)*	***0.11***	*0.02*	*0.04*	***0.09***	***0.27***	***0.10***	***0.07***	*0.05*	*0.10*	***0.34***	*0.12*	***0.35***
y-intercept	**-2.2**	2.0	-0.07	**-2.4**	**-7.0**	**4448**	**-0.3**	-0.1	2.3	**-9.0**	0.0	**0.02**
± *(95% confidence)*	***2.7***	*33*	*0.44*	***3.0***	***250***	***5700***	***1.0***	*2.4*	*3.4*	***26***	*1.7*	***0.35***
USGS BCR-2G												
slope	**0.97**	N/A	0.82	**1.00**	N/A	N/A	0.90	0.74	0.77	**0.83**	0.86	**0.84**
± *(95% confidence)*	***0.11***	*N/A*	*0.04*	***0.09***	*N/A*	*N/A*	*0.06*	*0.05*	*0.09*	***0.36***	*0.12*	***0.33***
y-intercept	**-2.2**	N/A	-0.07	**-2.4**	N/A	N/A	-0.2	-0.1	2.0	**-10**	0.0	**0.02**
± *(95% confidence)*	***2.7***	*N/A*	*0.42*	***2.9***	*N/A*	*N/A*	*1.0*	*2.1*	*3.0*	***27***	*1.7*	***0.32***

[a] Standard reference materials that produce a calibration curve with a slope staistically indistinguishable from one and an are indicated by bold statistics.

[b] The preferred calibrating standard for each elemental determination is indicated by boxed statistics and takes into account: i) the best correlations with the preferred values, manifest as slopes (Figs. 1 and 2) and net discrepancies (Figs. 3 and 4),; and, ii) the confidence in the calibrant composition.

reliable data for many of the targeted elements, the standard reference materials listed above represent the preferred calibrants in this study. As a result, the use of multiple standard reference materials is recommended for *in situ* laser ablation methods that attempt multi-element measurements of first-row transition metal, Ga and Ge abundances in geological materials. Table 2.9 provides the abundances of these elements in the MPI-DING glasses, as determined here by MR-LA-ICP-MS.

Figures 2.13 and 2.14 illustrate the precision and agreement of our calibrated measurements of the MPI-DING geological glasses relative to the "preferred" reference values from Jochum *et al.,* (2006), which represent a compilation of independent measurements from a variety of institutions, laboratories and analytical methods, including measurements based on EPMA, ICP-MS, INAA, secondary ionization mass spectrometry (SIMS), spark-source mass spectrometry (SS-MS), and XRF techniques. Utilizing the analytical protocols summarized here and employing BHVO-2G, BIR-1G and/or NIST SRM610 as our external calibrants, our MR-LA-ICP-MS method is shown to produce data for the MPI-DING glasses that are both reproducible and statistically indistinguishable (at the ≥95% confidence-level, with the exception of Ti) from the reference values for these samples, as demonstrated by slopes of unity and y-intercepts of zero (within the uncertainty of the linear regression statistics), but with improved precision of ≤3% ($2\sigma_m$) for most analyses. The discrepancy between our MR-LA-ICP-MS data for Ti and the reference values likely reflects an overestimation of TiO_2 by Jochum *et al.,* (2006) based on their artificially elevated concentrations determined by laser ablation versus the other methods reported in that study (see Supplemental Materials).

Table 2.9. First-row transition metal, Ga and Ge concentrations in the MPI-DING glasses as determined here by medium-resolution LA-ICP-MS.

	Sc	Ti	V	Cr	Mn	Fe	Co	Ni	Cu	Zn	Ga	Ge
ATHO-G (µg/g)	4.70	1520	3.31	6.19	881	30400	1.68	6.92	24.7	158	26.5	2.11
$2\sigma_m$ (%)	*7.2%*	*3.7%*	*3.5%*	*14.4%*	*5.6%*	*5.6%*	*7.6%*	*13%*	*6.7%*	*5.3%*	*4.9%*	*9.2%*
StHs6/80-G	9.35	4080	73.3	12.6	543	35700	14.7	23.9	43.4	57.0	24.0	1.23
$2\sigma_m$ (%)	*2.6%*	*0.9%*	*0.7%*	*3.8%*	*1.6%*	*1.0%*	*1.7%*	*5.7%*	*2.4%*	*3.0%*	*2.1%*	*8.5%*
T1-G	24.6	4330	165	17.5	986	53900	21.7	11.6	21.4	66.1	21.3	1.26
$2\sigma_m$ (%)	*0.7%*	*1.0%*	*1.2%*	*3.3%*	*1.3%*	*1.6%*	*3.4%*	*4.7%*	*2.4%*	*3.0%*	*1.5%*	*3.8%*
ML3B-G	29.7	11900	231	166	1070	81700	42.9	107	115	75.9	18.3	1.05
$2\sigma_m$ (%)	*1.3%*	*1.3%*	*2.4%*	*3.0%*	*3.9%*	*2.2%*	*4.5%*	*1.8%*	*3.2%*	*6.3%*	*6.1%*	*17%*
KL2-G	31.3	14700	253	296	1060	79700	42.7	108	88.8	78.9	19.3	1.25
$2\sigma_m$ (%)	*1.2%*	*0.5%*	*1.2%*	*1.9%*	*1.2%*	*1.0%*	*0.9%*	*3.3%*	*1.3%*	*5.2%*	*3.3%*	*8.3%*
GOR132-G	31.0	1750	199	2840	1160	82500	102	1260	234	62.5	11.9	0.899
$2\sigma_m$ (%)	*2.0%*	*1.0%*	*2.3%*	*1.5%*	*1.9%*	*1.4%*	*1.8%*	*1.2%*	*0.8%*	*2.2%*	*2.3%*	*5.6%*
GOR128-G	30.8	1650	164	2500	1330	78300	95.3	1140	67.5	69.5	9.34	1.33
$2\sigma_m$ (%)	*2.0%*	*1.1%*	*1.4%*	*1.8%*	*2.5%*	*2.8%*	*1.8%*	*2.1%*	*1.9%*	*4.0%*	*1.6%*	*5.5%*
BM90/21-G	11.3	351	49.2	2360	744	52400	96.0	1840	36.0	33.6	2.03	0.522
$2\sigma_m$ (%)	*2.5%*	*1.3%*	*2.6%*	*1.5%*	*1.1%*	*0.9%*	*0.9%*	*0.9%*	*1.8%*	*10.2%*	*9.2%*	*8.6%*

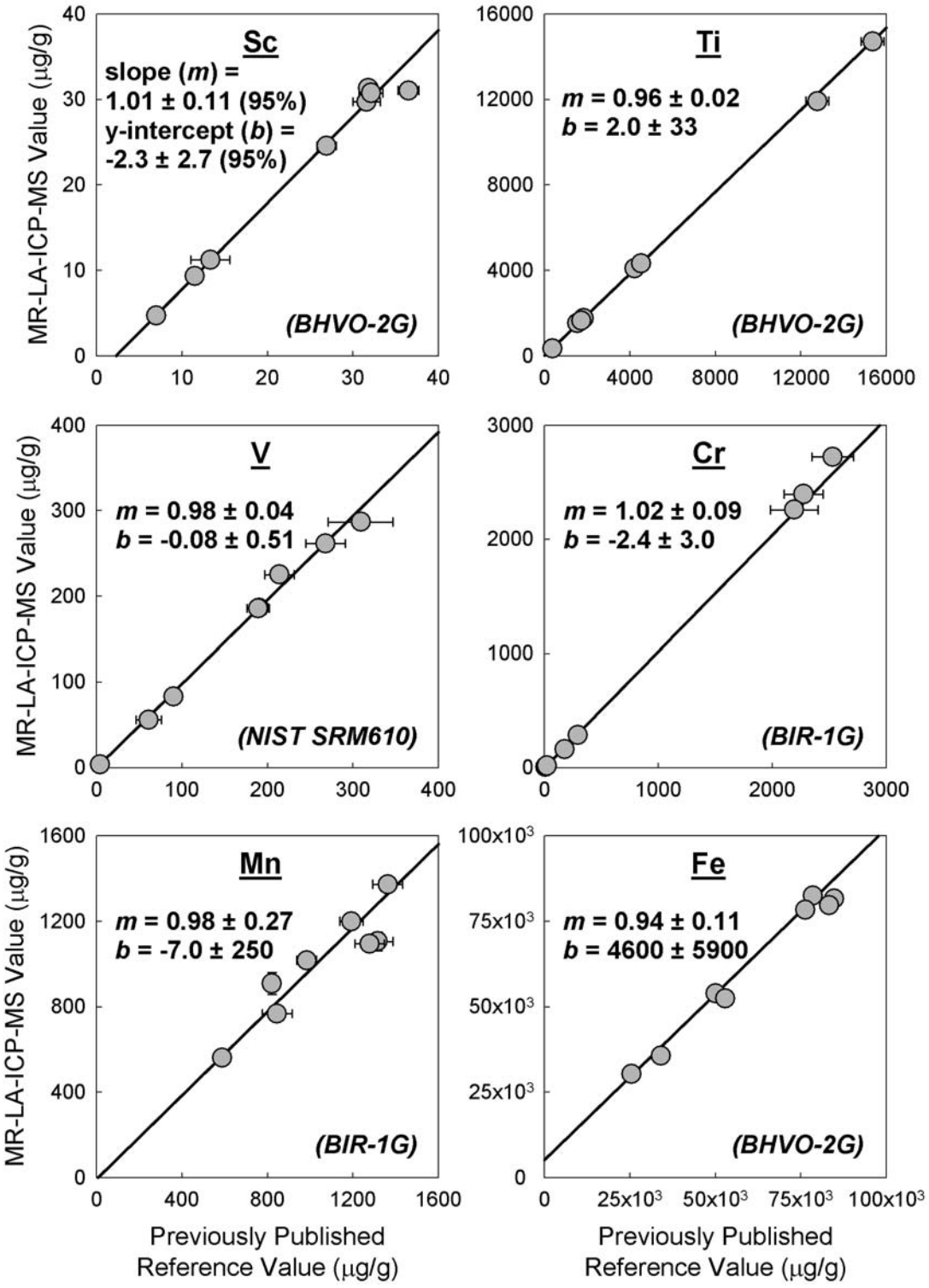

Fig. 2.13. Correlation of our externally calibrated MR-LA-ICP-MS measurements (for elements Sc to Fe) with the preferred values of Jochum *et al.*, (2006) for the MPI-DING glasses. The best-fit bivariate linear regression, which

accounts for the uncertainties in both x- and y-coordinates (as opposed to conventional univariate least-squares methods; see Appendix C for a discussion of linear regression statistics), is represented by the solid line in each panel. In these types of graphical comparisons, a linear regression with a slope equal to 1.00 indicates statistical equity between two distinct data sets. As would be expected, the origin is encompassed by the 95% confidence envelope for each linear regression. The preferred external calibrating reference material for each elemental determination is given in parentheses.

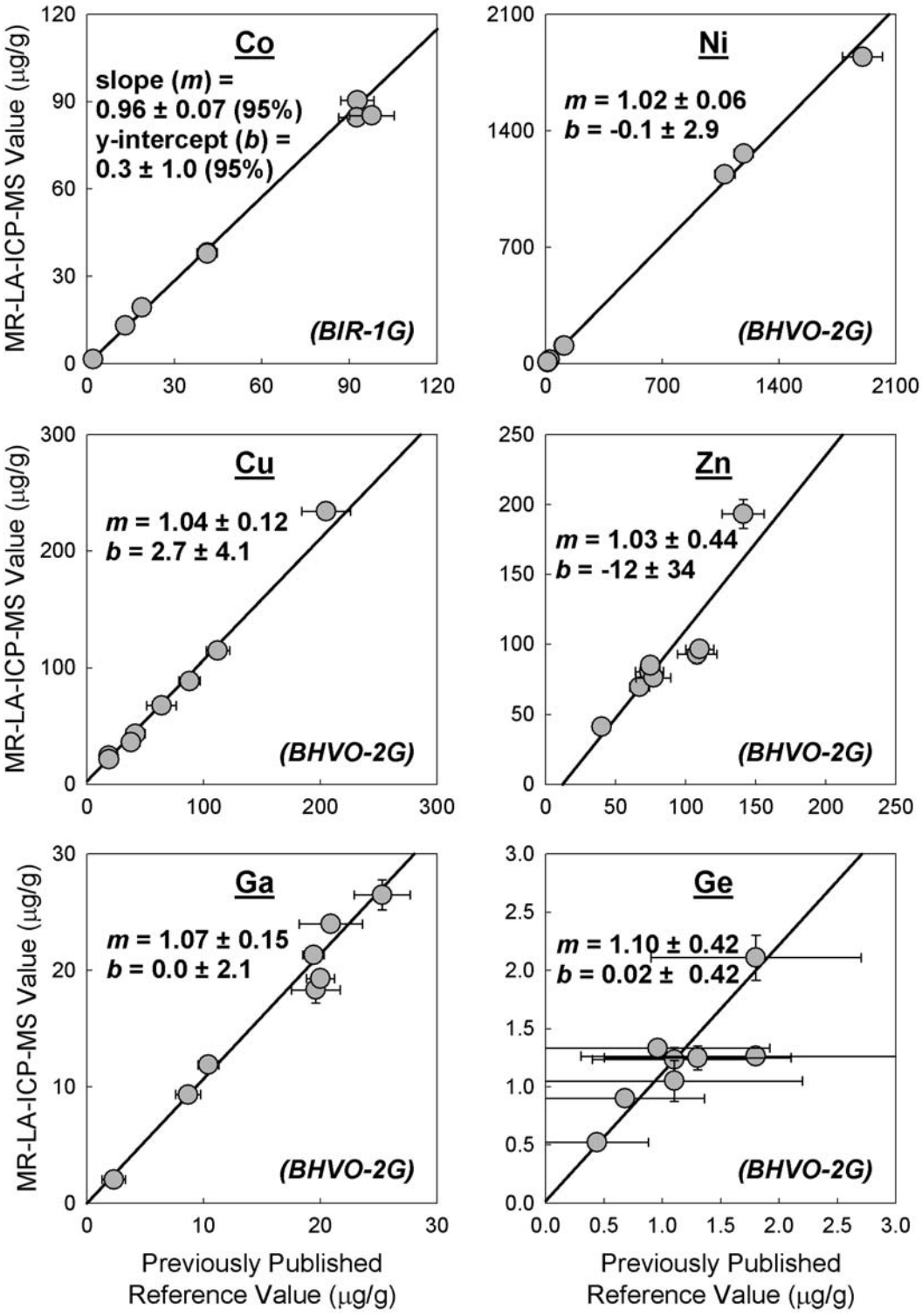

Fig. 2.14. Correlation of our externally calibrated MR-LA-ICP-MS measurements (for elements Co to Ge) with the preferred values of Jochum *et al.*, (2006) for the MPI-DING glasses.

The slopes and y-intercepts determined here, which are given in Figs. 2.13 and 2.14 and Table 2.8, were calculated based on a bivariate least-squares method, which accounts for the uncertainty in both x- and y-coordinates (as opposed to conventional univariate least-squares methods, which are used in commercial software programs such as Microsoft Excel and Systat SigmaPlot, and assume only errors in the y-coordinates). Thus, the linear functions derived here are based on minimizing the sum of squares of the distances perpendicular to the best-fit line, or perpendicular residuals, following the protocol established in York (1966) but also accounting for the uncertainty in both the laser ablation measurements reported here and the "preferred" reference values from Jochum *et al.,* (2006; see Appendix C for a description of linear regression statistics).

Figs. 2.15 and 2.16 show the overlap between our concentration data and the preferred values of Jochum *et al.,* (2006). For nearly all elemental analyses of all the MPI-DING glasses, our measurements agree with the reference values within the uncertainties of the measurements. Only the analysis of Sc for several of the MPI-DING glasses, namely ATHO-G. StHs6/80-G and GOR132-G, provides statistically distinct values between our medium-resolution laser ablation data and the compilation of Jochum *et al.,* (2006), despite an agreement in the overall slope and y-intercept of all the MPI-DING values between these two studies. This discrepancy may potentially represent: i) an overestimation of Sc by Jochum *et al.,* (2006) due to inter-laboratory biases, which is supported by the disparate range of values obtained through different means of analysis reported by this study (*e.g.*, from 4.9 μg/g Sc determined by ICP-MS to 7.6 μg/g Sc determined by laser ablation in ATHO-G); ii)

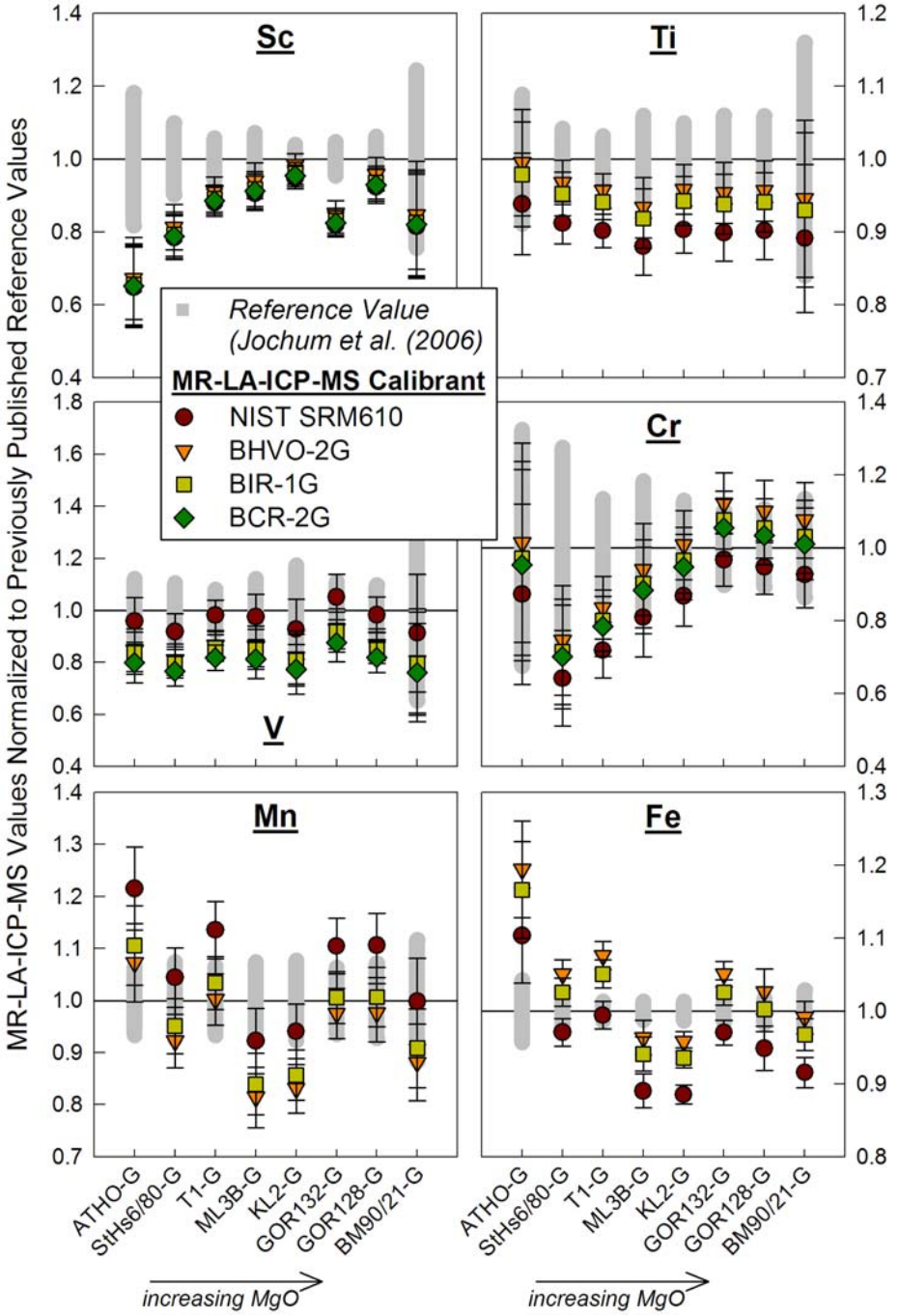

Fig. 2.15. Our new MR-LA-ICP-MS concentration data (for elements Sc to Fe) for the MPI-DING glasses normalized to the preferred values from Jochum *et al.*, (2006). Our data agree with the preferred values, within the uncertainty of the measurements, for nearly all elemental analyses of all samples with the exception of Sc in ATHO-G, StHs6/80-G and GOR132-G, which is briefly discussed in the text.

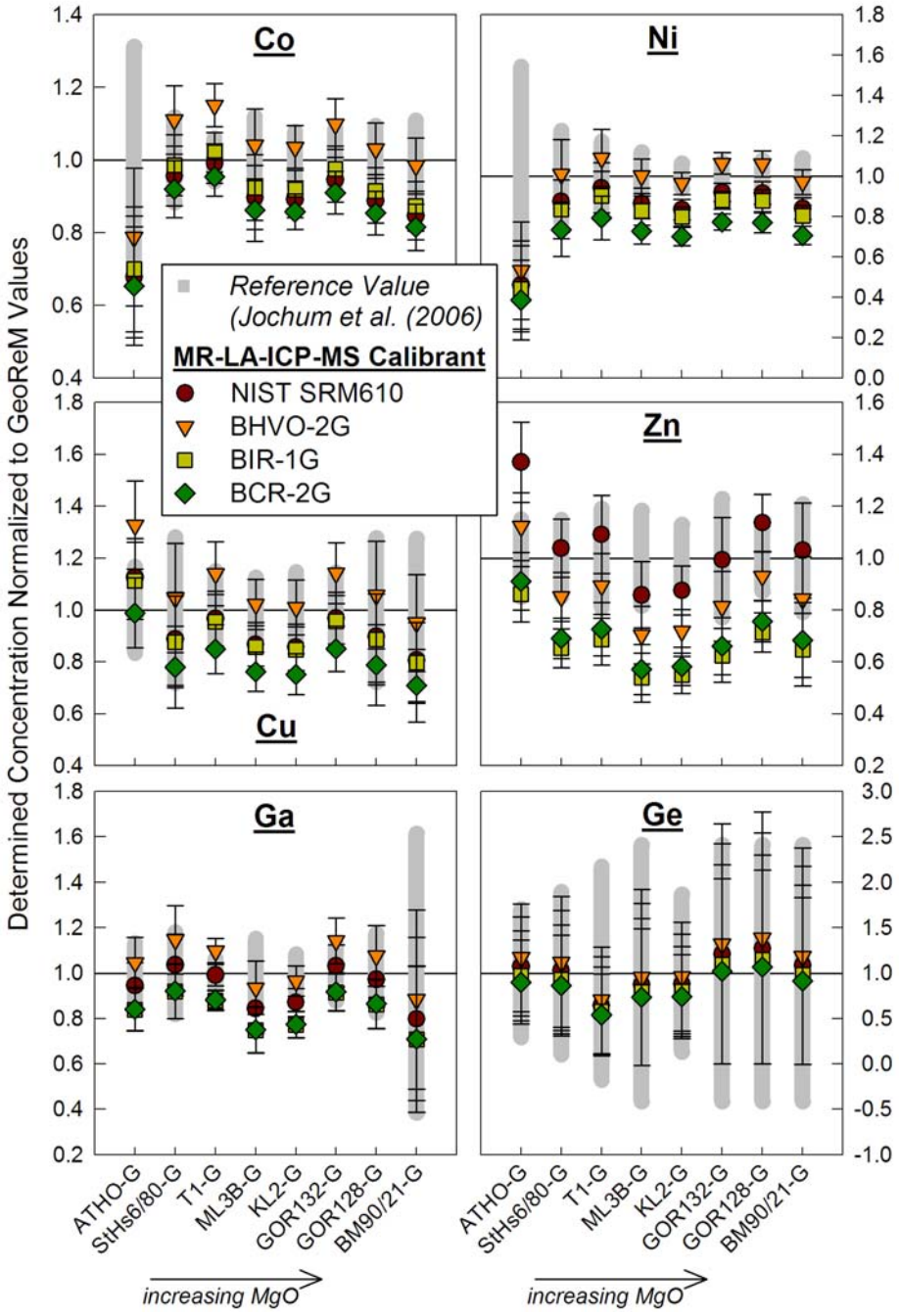

Fig. 2.16. Our new MR-LA-ICP-MS concentration data (for elements Co to Ge) for the MPI-DING glasses normalized to the preferred values from Jochum *et al.*, (2006).

an underestimation of Sc in these three samples as analyzed here; and/or, iii) an underestimation in the uncertainty of the preferred Sc values from Jochum *et al.,* (2006) and/or the new Sc data reported here.

2.4.9 Conclusions

In situ LA-ICP-MS provides an ideal way to analyze the chemical composition of geological materials with minimal sample processing, which can introduce impurities and/or isobaric interferences, and limited sample loss. In this study, we review an analytical protocol that was specifically designed to allow the determination of the abundances of first-row transition metals, Ga and Ge via LA-ICP-MS with maximum sensitivity and minimal matrix effects and/or laser-induced fractionation. The method established here relies on the use of medium-resolution mass discrimination ($m/\Delta m = 4000$), multiple matrix-matched external calibrants, namely NIST SRM610 and the USGS reference glasses BHVO-2G, BIR-1G and BCR-2G, and controlled ablation procedures, including: the minimization of oxide production; longer dwell times for less abundant isotope mass stations; measurements of multiple isotopes of the same element (when available) in order to monitor potential isobaric interferences; disablement of the guard electrode and use of a "hot" plasma; slow traverse speeds; large beam spot diameters; low to moderate laser light intensity; low repetition rates; linear ablation paths rather than spots; and, low depth-to-diameter laser pit ratios. The results of this study show that the analytical method presented here can be used to produce data that is statistically equivalent to compiled reference values acquired through other analytical protocols (*e.g.*, EPMA, INAA and XRF) but with improved

uncertainties on the order of ≤3% ($2\sigma_m$). This method may be directly applied to the analysis of geological materials, particularly oceanic basalts.

Chapter 3: Uncertainties in the composition of Earth, its core and silicate sphere[1,2]

[1] R. Arevalo Jr. and W.F. McDonough contributed to the interpretation of the data. The text, tables and figures were written/created by W.F. McDonough.

[2] This chapter has been published as:
McDonough, W.F. and Arevalo Jr., R., 2008. Uncertainties in the composition of Earth, its core and silicate sphere. *Journal of Physics: Conference Series* (136), 022006, doi:10.1088/1742-6596/136/2/022006.

3.1 Abstract

A self consistent model for the Earth has the heat producing elements, K, Th and U concentrated in the silicate Earth, with negligible quantities stored in the core. With uncertainties reported at the 2 sigma level, the silicate Earth has 80 ± 25 ng/g Th and 20 ± 8 ng/g U, with a Th/U of 3.9 ± 0.4; it also has a K/U of 1.38 ± 0.26 x 10^4 and a K content of 280 ± 120 μg/g. Thus, the radiogenic contribution to the Earth's thermal power is 21 ± 4 TW relative to a total output of 46 ± 6 TW.

3.2 Introduction

As geoneutrino data are accumulated, the particle physics community looks to the geological community for insight and guidance into the composition of the bulk Earth and its major reservoirs: the crust, mantle and core. A fundamental question is - how well do we know the composition of the Earth, including its core and mantle, as these regions not directly accessible? Establishing uncertainties on geochemical estimates depends critically on what are the known knowns, known unknowns, and worse yet, the unknown unknowns, to quote Don Rumsfeld. This paper examines the absolute

uncertainties in our Earth models and provides a reference frame for future geoneutrino tests.

Compositional models of the Earth must be consistent with geophysical and cosmochemical data. First order geophysical constraints on the Earth come from seismology and geodesy, whereas constraints from cosmology come from compositional comparisons between the solar photosphere and meteorites, gross features of planet in the solar system and astronomical observations on mineral phases in the interstellar medium and accretion disks of other systems. The Earth's shape is a function of its spin, mass distribution, and rotational flattening, which gives a coefficient of the moment of inertia for the Earth of 0.330 Ma^2 (Yoder, 1995), which is consistent with it having a metallic liquid core that is surrounded by a stiffer, less deformable, lower density mantle. The seismological profile of the Earth is a description of seismic wave speed velocities through the planet, which is a function of the distribution of density and the bulk and shear moduli. These data can be used to describe a radial density profile for the Earth that is perturbed to be consistent with the Earth's free oscillation frequencies. By combining this information with mineral physics data (*e.g.*, equation of state, or EOS, data for Earth materials at appropriate conditions), we can identify the mineralogical and chemical constituents of the core and mantle and compare these phases with candidate materials found in meteorites and terrestrial rocks.

As the building blocks of planets, chondritic meteorites are undifferentiated materials (possessing a mixture of metal and silicate components) upon which our planetary models are constructed. Of fundamental importance is the observation that

the solar photosphere and carbonaceous chondrites have a 1:1 match in composition for >5 orders of magnitude for most elements except the gases, when referenced to 10^6 atoms of Si. This stunning compositional match coupled with the fact that the Sun represents the mass of the solar system, empowers geochemists to use chondrites for modeling the composition of the planet. There is, however, a broad compositional spectrum of chondritic meteorites with different proportions of refractory inclusions, chondrules and matrix, the dominant components that make up chondrites. Also, chondrites formed under a broad range of oxidation-reduction conditions with some types (carbonaceous) being completely oxidized (*i.e.*, all Fe as Fe-oxides) and other types (enstatite) very reduced (*i.e.*, all Fe as metal or sulfide and other elements such as Si as both oxide and metal; Fig. 3.1). Nonetheless, as a first order cut, there is only a factor of 2 spread in their absolute U and Th contents, as is the case for other refractory elements across the different groups of chondrites. This observation translates to an upper bound of uncertainty for the Earth's U and Th content. Moreover, chondritic meteorites have a narrow range in Th/U ratios of 3.5 to 4.2, which is also confirmed by their limited range of $^{208}Pb/^{206}Pb$ isotopic compositions. In contrast, the only other significant heat producing element in terms of a planetary thermal budget, K, varies by more than a factor of 2 between different groups of chondritic meteorites, and there are reasons to believe that the Earth has an even lower K/U bulk value than that found in chondritic meteorites. Thus, estimating the abundance of K, and other non-refractory (volatile) elements requires further constraints to describe the Earth.

Astronomical observations find that gas-dust clouds in the interstellar medium and accretion disks contain a small fraction of minerals and that these minerals are dominated by olivine ($(Mg,Fe)_2SiO_4$), pyroxene ($(Mg,Fe)_2Si_2O_6$) and Fe-metal. These are also the common minerals in chondrites and non-chondritic meteorites, and thus are the dominant phases that contribute to planet building.

3.3 Earth model

A simple model for the Earth that describes 95% of its mass consists of a core, which is mostly an Fe-Ni alloy with a chondritic Fe/Ni ratio (17.5 ± 1.0, 2σ; McDonough, 2003), and a silicate shell (with ~6.5% of oxidized Fe, based on mantle samples) made up of a mixture of olivine and pyroxene. Compositional models for the Earth consider a range from a pyroxene- to olivine-rich mantle, or Mg/Si atomic proportions of >1.0 to <1.3, respectively, for the silicate Earth. A model composition (McDonough and Sun, 1995; McDonough, 2003) for the Earth, including its core and silicate shell, is presented in Table 3.1. This compositional model has a homogenous major element composition for the silicate portion of the Earth with an Mg/Si atomic proportion of 1.25.

There is good evidence that the mantle has been sufficiently overturned throughout Earth's history such that surface processes randomly and representatively sample the bulk of the mantle, and that there is a negligible bulk compositional gradient in the mantle. Support for this perspective comes from tomographic images of subducted plates of oceanic lithosphere penetrating the 660 km seismic

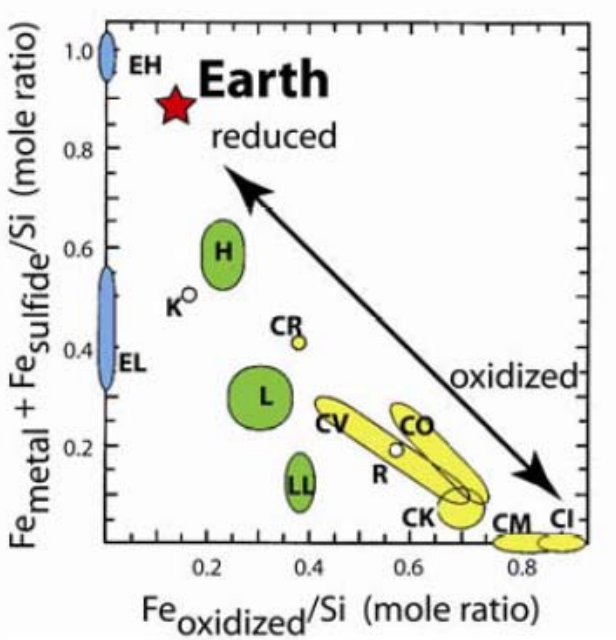

Fig. 3.1. Urey-Craig diagram showing the fields for different groups of chondritic meteorites with respect to their oxidation state of iron relative to silicon. Oxidized iron is incorporated into silicate minerals, whereas reduced iron is in metals and sulfides. Blue fields are for the enstatite chondrites (EH, EL), green the ordinary chondrites (H, L, LL), yellow the carbonaceous chondrites (CI, CM, CO, CV, CR), and unfilled are other. High iron content chondrites (EH and H) contrast with low iron ones (EL, L and LL). The K chondrites (Kakangari) and R chondrites (Rumuruiites) are the least populated groups. The Earth (star) has the vast majority of its iron (87% by mass) in the core.

discontinuity. Not all subducted plates directly penetrate this boundary layer in the mantle; some have been imaged translating laterally through the mantle transition zone (between the 410 km and 660 km seismic discontinuities) and appear to sink later, perhaps due to thermal densification effects.

Alternatively, there are geophysical models of the mantle based on EOS and seismological constraints that do not correspond with a compositionally homogeneous system, but rather require a chemically distinct upper and lower mantle. These models generally appeal to a lower mantle that is either SiO_2 or FeO enriched (Matas *et al.,* 2007; Khan *et al.,* 2008). These models are dependent on the quality of the input EOS data and the form of the equation used, as well as requiring that there are isolated mantle domains not sampled today. The tomographic seismic images and chondritic ratios plots for mantle samples are observations that are at odds with such alternative compositional models.

Based on the above observations, we can now use key element ratios in chondrites to further constrain models for the U, Th and K content of the silicate Earth. Importantly, the 5 most abundant elements in the Earth (O, Fe, Si, Mg, Ni), which make up 95% of the planet's composition (both atomic and by weight), can be determined by key ratios (*e.g.*, atomic Mg/Fe and Fe/Ni) in both chondrites and mantle samples. Aside from Mg and Th, however, other elements have been suggested to have been sequestered into the Earth's core. Therefore, constraints on the Th and U content of the silicate Earth come from the range (<30%) of Mg/Th 3.3 ± 0.9 (2σ) in average chondrite types (Kallemeyn and Wasson, 1981).

Table 3.1. Composition of the bulk Earth, core and silicate Earth (adapted from Sun and McDonough, 1995; McDonough, 2003; Arevalo et al., 2009).

Element	Earth	Core	silicate Earth	Element	Earth	Core	silicate Earth
H (µg/g)	300	600	100	Rh (µg/g)	0.2	0.7	0.001
Li	1.1	0	1.6	Pd	1	3	0.004
Be	0.046	0	0.068	Ag	0.1	0.2	0.008
B	0.2	0	0.3	Cd	0.1	0.2	0.04
C	730	2000	120	In	0.007	0	0.01
N	57	170	2	Sn	0.3	0.5	0.13
O	297,000	0	440,000	Sb	0.05	0.1	0.0055
F	10	0	15	Te	0.29	0.9	0.012
Na	1,800	0	2,670	I	0.05	0.1	0.01
Mg	153,900	0	228,000	Cs	0.04	0.07	0.021
Al	15,880	0	23,530	Ba	4.5	0	6.6
Si	163,000	64,000	210,000	La	0.44	0	0.65
P	1,100	3,200	90	Ce	1.1	0	1.7
S	6,300	19,000	250	Pr	0.17	0	0.25
Cl	76	200	17	Nd	0.84	0	1.2
K	190	0	280	Sm	0.27	0	0.41
Ca	17,080	0	25,300	Eu	0.1	0	0.15
Sc	11	0	16.2	Gd	0.37	0	0.54
Ti	815	0	1205	Tb	0.067	0	0.1
V	94	120	82	Dy	0.47	0	0.67
Cr	4,700	9,000	2,625	Ho	0.1	0	0.15
Mn	720	50	1,045	Er	0.3	0	0.44
Fe	319,000	850,000	62,600	Tm	0.046	0	0.07
Co	885	2,500	105	Yb	0.3	0	0.44
Ni	18,200	52,000	1,960	Lu	0.046	0	0.068
Cu	60	125	30	Hf	0.19	0	0.28
Zn	35	0	55	Ta	0.025	0	0.037
Ga	2.7	0	4	W	0.17	0.5	0.013
Ge	7.2	20	1.1	Re	0.075	0.23	0.00028
As	2	5	0.05	Os	0.9	2.8	0.003
Se	2.7	8	0.075	Ir	0.8	2.6	0.003
Br	0.3	0.7	0.05	Pt	1.9	5.7	0.007
Rb	0.4	0	0.6	Au	0.2	0.5	0.001
Sr	13.4	0	19.9	Hg	0.02	0.05	0.01
Y	2.9	0	4.3	Tl	0.01	0.03	0.0035
Zr	7.07	0	10.5	Pb	3.3	1.2	0.15
Nb	0.44	0	0.66	Bi	0.01	0.03	0.0025
Mo	2	5	0.05	Th	0.054	0	0.08
Ru	1	4	0.005	U	0.014	0	0.02

Compositional models for the silicate Earth estimate the abundances of the refractory lithophile elements at 2.2 to 2.8 times that in C1 carbonaceous chondrites, which translates into a 25% spread in the concentration of Th and U in the silicate Earth (63-83 ng/g Th and 17-22 ng/g U, respectively). Cosmochemical constraints, both

isotopic and chemical, and melting models add to this uncertainty, resulting in a silicate Earth with 80 ± 25 ng/g Th and 20 ± 8 ng/g U, with a Th/U of ~3.9 (with only 10% uncertainty; McDonough and Sun, 1995). The combination of Sr, Pb and U isotope systematics shows that the silicate Earth has a chondritic Th/U ratio within uncertainties, although these data do not preclude a negligible amount of U in the core. However, combined evidence from geochemical, cosmochemical and petrological studies demonstrate that there is negligible U and/or K in the core (Wheeler *et al.,* 2006; Corgne *et al.,* 2007). Therefore, based on the above and the silicate Earth's K/U value ($1.38 \pm 0.26 * 10^4$; Arevalo *et al.,* 2009), we estimate that the heat-producing elements (*i.e.*, U, Th and K) contribute 21 ± 4 (2σ) TW of power to the Earth.

The Earth's total thermal output, however, is not entirely derived from heat generated by radioactive decay; the remainder largely comes from secular cooling of the planet (see Jaupart *et al.,* 2007 and references therein). Figure 3.2 presents a simplified model for the relative contributions of the thermal emission from inside the planet. The "other" component in this figure includes contributions from differentiation, tidal forces, thermal contraction, etc. Also note, Davies (1999) has estimated up to 28 TW for the mantle radiogenic component (as cited in Jaupart *et al.,* 2007). Estimates of the planet's Urey ratio, defined as the ratio of total heat production to total heat loss (*i.e.*, surface heat flux), range from 0.4 to 1.0, depending on the assumed abundances for heat producing elements within the Earth and the total thermal output of the planet. An estimate for the mantle Urey ratio (*i.e.*, mantle heat production to total heat loss minus the continental contribution) vary from as low as

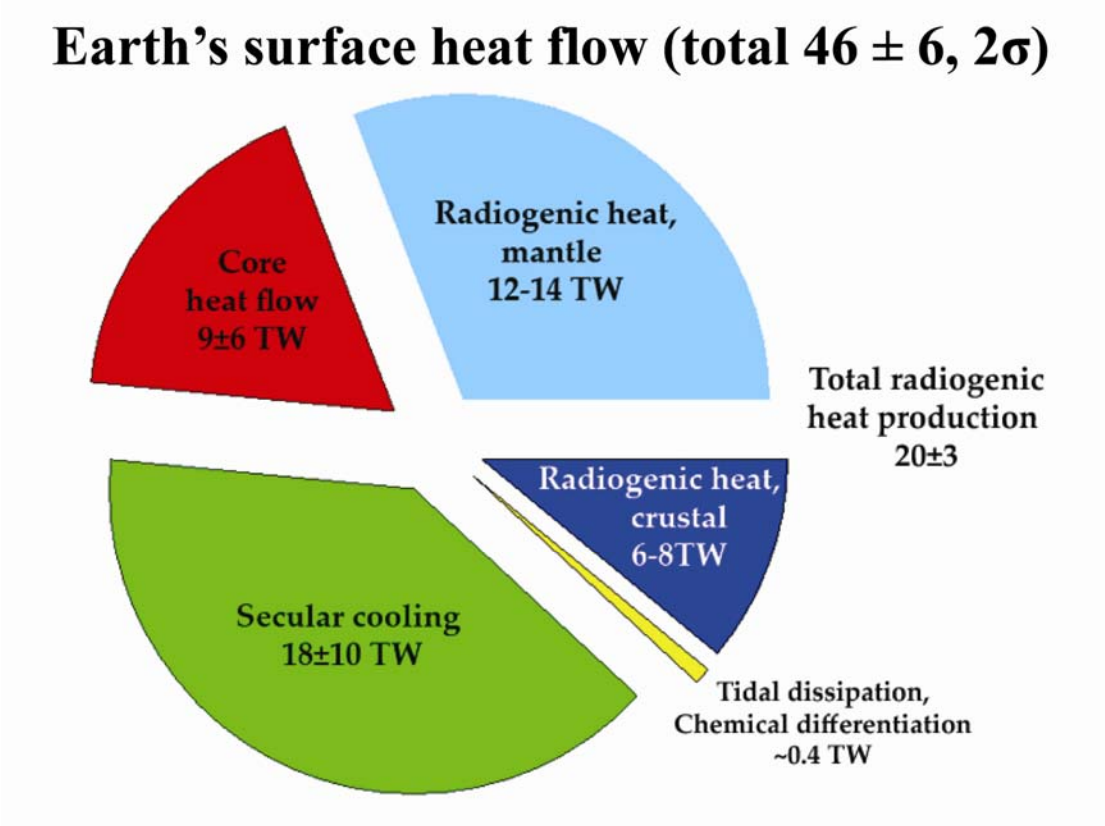

Fig. 3.2. Earth's thermal budget and its contributors, based on a model of 46 ± 6 TW (2σ) of total output power from Jaupart *et al.*, (2007) with modifications from Arevalo *et al.*, (2009). The radiogenic contribution is ~40% of the Earth total surface heat flow. The continental crust constitutes ~0.55% of the mass of the silicate Earth, with the remainder made up by the mantle. The continental crust is on average 40 km thick (base of the mantle is 2890 km) and has a factor of 10^2 more heat producing elements than the mantle.

0.2 to as high as 0.7 (Jaupart *et al.,* 2007; Korenaga, 2007; Labrosse and Jaupart, 2007 and references therein), reflecting that continents contain a significant portion (~33%) of the heat producing elements in the planet. A current value for the radiogenic heat contribution is 21 TW (14 TW from the mantle and 7 TW from the continents), which, in turn, would imply a mantle Urey ratio of 0.3. This mantle Urey ratio is low and outside the range of most geophysical models that attempt to parameterize convection in the mantle (*e.g.*, Turcotte *et al.,* 2001; Kellogg *et al.,* 1999; Grigné *et al.,* 2005, 2007).

Geophysical and geochemical interpretations of the systematics of mantle convection (including the distribution of radioactive elements and the mode of convective cycling) are currently incongruous. Geophysical models that describe the kinetics and dynamics of mantle convection are designed to be self-consistent and comprehensive, such that they integrate the entire history of convection in the Earth. In general, these models place numerical limits on the secular evolution in the heat flux out of the Earth. One form of a scaling law that can be used to describe the thermal evolution of the mantle is $Q \propto Ra^{\beta}$, which relates heat flux (Q) for a fluid (*e.g.*, convective mantle) to the Rayleigh number (Ra) of the fluid (Davies, 1980; Schubert *et al.,* 1980, 2001). Constraints on the exponent β, an amplifier for the force balance between viscosity and heat dissipation, in this analysis are crucial and not presently available; for an isoviscous fluid it is recognized that the exponent β has a value of $\approx 1/3$, a self-regulated state, which expresses a balance of forces between heat generation and dissipation. Such high values for β suggest slower cooling rates due to enhanced viscosity (as a result of lower internal heating) and thus the evolution of the

system depends more on the initial conditions. A considerable effort has been invested in understanding the relative balance of forces and thus what might be appropriate values of β (see summary in Grigné *et al.,* 2005). For a mantle Urey ratio of ~0.3, appropriate β values are low; Grigné *et al.,* (2005) and Labrosse and Jaupart (2007), however, believe that the size and distribution of plates and subduction zones and aspect ratios of convective cells may play a greater role in thermal dissipation than previously thought. Alternatively, Loyd *et al.,* (2007) and Korenaga (2007) conclude that changes in the oceanic heat flux and past sea-level variations have been limited, based on plate reconstruction and sea-level changes. However, all models depend on the core heat flux, as well as any potential heat generation in a D″ reservoir that sits on the core-mantle boundary, which may play a significant role in heat production. Recent estimates of the heat flux across this region (from the core and D″), based on the post-perovskite phase transition (Hernlund *et al.,* 2005; Lay *et al.,* 2006), imply fluxes in this region of 10 TW or more.

Further collaborations between physics and geology in the field of geoneutrino research should generate observations requiring inputs from both disciplines to interpret more precisely the terrestrial antineutrino spectral data. Our ultimate goal is to map out the Earth's internal distribution of radioactive elements in order to better define the nuclear engine that powers this planet.

Chapter 4: Tungsten geochemistry and implications for understanding the Earth's interior[1,2]

[1] R. Arevalo Jr. and W.F. McDonough contributed to the development of the analytical protocol established in this study, with preliminary experiments and all sample measurements performed by R. Arevalo Jr. Both authors contributed to the interpretation of the data. The text, tables and figures were written/created by R. Arevalo Jr.

[2] This chapter has been published as:
Arevalo Jr., R. and McDonough, W.F., 2008. Tungsten geochemistry and implications for understanding the Earth's interior. *Earth and Planetary Science Letters* (272), 656-665, doi:10.1016/j.epsl.2008.05.031.

4.1 Abstract

The concentration of tungsten (W) in basaltic melts provides a window into the behavior of this element during core-mantle separation, crust formation, silicate differentiation, and potentially core-mantle interaction. We have analyzed an extensive suite of modern basalts (n = 86) for their trace element chemistry via laser ablation ICP-MS, with barium (Ba), thorium (Th), uranium (U), and W concentrations typically determined to ≤5% (2σ) uncertainty. We find that the partitioning behavior of U mirrors that of W during basalt genesis, whereas Ba and Th both behave more incompatibly. The W/U ratio of our complete sample suite (0.65 ± 0.45, 2σ) is representative of the mean modern mantle, and is indistinguishable from that of mid-ocean ridge basalts (W/U_{MORB} = 0.65 ± 0.41, n = 52), ocean island basalts (W/U_{OIB} = 0.63 ± 0.07, n = 10), and back-arc basin basalts (W/U_{BABB} = 0.62 ± 0.09, n = 12). This ratio is also consistent with the W/U ratio of the continental crust, and thus represents the W/U ratio of the entire silicate portion of the Earth.

Assuming a concentration of 20 ± 8 (2σ) ng/g U in the bulk silicate Earth, the abundance of W in the silicate Earth is 13 ± 10 ng/g. Following mass balance, this implies a mean modern mantle and core composition of 8.3 ± 7.1 ng/g W and 510 ± 120 ng/g W, respectively. Additionally, the MORB source is modeled to contain approximately 3.0 ± 2.3 ng/g W, indicating a four-fold depletion of the highly incompatible elements in the MORB source relative to the silicate Earth.

Although both the isotopic composition of W and the constancy of the silicate Earth W/U ratio allow for potential insight into core-mantle exchange, both of these proxies are extremely dependent on the chemical composition of the source. A case study of three Hawaiian picrites with enrichments in ^{186}Os-^{187}Os but terrestrial ε_{182W} can be explained by: i) a lack of a core component in the Hawaiian "plume," ii) crustal contamination, or iii) a source composition enriched in incompatible trace elements relative to the bulk silicate Earth.

4.2 Introduction

The metallic core separated from the silicate portion of the Earth some 10 to 70 million years after the formation of the solar system (*e.g.*, Kleine *et al.,* 2004a; Jacobsen, 2005), during which >90% of the planet's budget of tungsten (W) was sequestered into the core (Jagoutz *et al.,* 1979; Sun, 1982; Newsom and Palme, 1984). The distribution of W, along with many other siderophile (iron-loving) elements, has been established by chemical differentiation processes that were controlled by a spectrum of pressure, temperature and oxygen fugacity conditions as the Earth has evolved (*e.g.*, Righter, 2003 and references therein). Following core formation,

however, the geochemical behavior of W in the silicate Earth has been dominantly lithophilic (silicate-loving) and highly incompatible during mantle melting and crust formation (Newsom *et al.,* 1996 and references therein); therefore, W provides insights into both core-mantle segregation and the differentiation of the silicate Earth.

Recently, the isotopic composition of W has been used as a short-term geochronometer for dating planetary and asteroidal core formation (*e.g.*, Kleine *et al.,* 2002, 2004a, 2005a; Schoenberg *et al.,* 2002; Yin *et al.,* 2002) and early silicate differentiation (*e.g.*, Righter and Shearer, 2003; Kleine *et al.,* 2004b, 2005b). Tungsten isotopic anomalies have also been implicated as a potentially robust geochemical tracer for core-mantle interactions (Scherstén *et al.,* 2004; Brandon and Walker, 2005). However, the geochemical behavior of W in the silicate portion of the Earth is not well-constrained, largely due to its highly incompatible behavior during mantle melting and the depleted composition of mantle-derived basalts. Estimates of the abundance of W in the silicate Earth range from as low as 7 ng/g to as high as 29 ng/g (Jagoutz *et al.,* 1979; Sun, 1982; Sims *et al.,* 1990; McDonough and Sun, 1995; Newsom *et al.,* 1996; Palme and O'Neill, 2003; Lyubetskaya and Korenaga, 2007). Defining the abundance and distribution of W within the Earth is imperative to: i) understand its geochemical behavior, ii) assess the usefulness of W as a tracer of geochemical processes, iii) quantitatively model the composition of the MORB (mid-ocean ridge basalt) source and any potential deep mantle reservoir, and iv) investigate putative core-mantle interactions through both W isotopes and concentration ratios. Here we report high-precision concentration data for Ba, Th, U, and W in an

extensive suite of oceanic basalts in order to define the abundance of W in the modern mantle, bulk silicate Earth and core.

4.3 The abundance of W in the silicate Earth

4.3.1 The geochemical behavior of W

As a refractory element, the initial abundance of W in the bulk Earth can be calculated from chondritic relative abundances without a volatility correction. Estimates of W in the silicate portion of the Earth, however, are poorly constrained. Difficulties in determining the abundance of W in the silicate Earth stem from the binary behavior of the element; whereas W acts as a moderately siderophile element under reducing conditions (*i.e.*, during core formation), it has behaved as an extremely incompatible lithophile element during the differentiation of the silicate Earth (Palme and Rammensee, 1981). Consequently, W is strongly enriched in the core and continental crust, respectively, leaving the modern mantle depleted.

In the silicate Earth, the abundances of siderophile elements that are compatible during mantle melting ($D^{sil \cdot crystal/sil \cdot liq} > 1$; *e.g.*, Ni and Co) are established from studies of massif peridotites and mantle xenoliths because these elements are largely retained in olivine during partial melting. However, in order to determine the silicate Earth abundances of siderophile elements that behave incompatibly during mantle melting, it is necessary to determine the abundances of these elements in both the modern mantle and continental crust. Knowledge of the composition and relative mass contributions of the mantle and crustal reservoirs allows a reconstruction of the

concentration of these elements in the silicate Earth to be calculated (Newsom *et al.,* 1990; Sims *et al.,* 1990).

4.3.2 Incompatible element concentration ratios

The concentration of incompatible elements in basaltic melts is controlled by the concentration of these elements in the source mantle as well as a variety of fractionation processes, including partial melting, fractional crystallization and crustal contamination. Concentration ratios of similarly incompatible trace elements provide a reliable estimate of the trace element composition of the source and can complement information derived from radiogenic isotopes (Hofmann, 2003 and references therein). Concentration ratios must be used with care, however, because unlike isotope ratios they may be fractionated during processes of magma genesis. A concentration ratio that is uniform in all types of oceanic basalts (*e.g.*, mid-ocean ridge basalts, MORB, oceanic island basalts, OIB, and back-arc basin basalts, BABB) and is independent of the absolute concentrations of the elements involved represents a mantle value that has been unfractionated by silicate differentiation. Such constant ratios (*e.g.*, Zr/Hf, Sm/Hf, Rb/Ba, Nb/Ta, etc.) reflect element pairs with nearly identical bulk partition coefficients during the genesis of basaltic partial melts and may be inferred to be representative of their source ratios (Hofmann *et al.,* 1986; Newsom *et al.,* 1986; Sun and McDonough, 1989). Constant concentration ratios of highly incompatible elements are particularly likely to represent the trace element ratios of their source regions, as these elements are quantitatively removed from their source after only a few percent of partial melting.

Because W is one of the most incompatible elements during mantle melting, a concentration ratio involving W and another similarly incompatible element (*e.g.*, W/Ba, W/Th or W/U) likely characterizes the ratio of the modern mantle if the ratio remains constant throughout a range of MORB, OIB and BABB samples. Although no other element behaves exactly like W in all geologic processes, previous work suggests that the geochemical behavior of W in silicate systems is most comparable to that of Ba, Th and U (Newsom and Palme, 1984; Newsom *et al.,* 1986, Sims *et al.,* 1990; Noll *et al.,* 1996; Newsom *et al.,* 1996).

4.3.3 Tungsten in the bulk continental crust

Newsom *et al.,* (1996) estimated the abundance of W in the silicate Earth by measuring relatively constant W/Th ratios in representative samples of both the continental crust and modern mantle. In order to characterize the abundance of W in the bulk crust, they examined a comprehensive collection of samples representative of the lower, middle and upper crustal reservoirs; over 145 crustal samples were analyzed, including 18 lower crustal xenoliths, 20 rocks from high-grade metamorphic terrains, 45 samples of continental sediments, 13 rocks from oceanic volcanic arcs, 35 rocks from continental volcanic arcs, 8 continental basalts, and 7 komatiites. Their study, which established the concentration of W in the continental crust as ~ 1000 ng/g, still serves as the standard for examining the abundance of W in the bulk continental crust (Rudnick and Gao, 2003).

4.3.4 Tungsten in the modern mantle

Newsom *et al.,* (1996) also estimated the abundance of W in the modern mantle, but they analyzed only a limited sample set of mantle-derived oceanic basalts (n = 20)

and altered mantle nodules (n = 7) with measured reproducibilities between 10-30% (2σ). As opposed to mantle xenoliths, examining a broad spectrum of MORB, OIB and BABB is instrumental to constraining the abundance of W in different mantle reservoirs because oceanic basalts represent the most significant volume of terrestrial magmatism (an average rate of ~30 km^3/yr of basalt has been produced over the past 180 Myr; Crisp, 1984) and carry the smallest risk of being contaminated during magma transport (Jochum *et al.,* 1989; Hofmann, 1997). In this study, 86 mantle-derived samples are analyzed, including 52 MORB, 16 intraplate basalts and 18 convergent margin samples. The reproducibility of our measurements (typically ≤ 5%, 2σ) are improved over previous studies, and the extensive compilation of mantle-derived materials considered here characterizes source regions from various depths of the mantle, a wide spatial distribution across the globe and every major tectonic setting.

4.4. Materials and methods

4.4.1 Sample descriptions

The mantle rocks analyzed in this study include both normal-type MORB (N-MORB, K/Ti ≤ 0.140) and enriched-type MORB (E-MORB, K/Ti > 0.140), as well as a multitude of intraplate basalts, island arc volcanics, and back-arc basin basalts. Most of the rocks are oceanic basaltic glasses or fine-grained scoria, ranging from 40 to 59 wt% SiO_2 and 3 to 10 wt% MgO; thus, a range of magma compositions, from primitive to differentiated, are represented by this sample set. More information

regarding the diversity of these samples, including a map showing their global distribution, is provided in Section 2.2.

4.4.2 Analytical method

Compared to rocks with coarser textures, glassy and/or fine-grained samples provide comparatively homogeneous surface compositions that can be analyzed via laser ablation mass spectrometry. This in-situ method of measuring trace element concentrations produces high-precision data and has been validated through numerous analytical studies (*e.g.*, Pearce *et al.,* 1997; Eggins *et al.,* 1998; Norman *et al.,* 1998; Eggins and Shelley, 2002; Jochum *et al.,* 2005, 2006, 2007). Laser ablation mass spectrometry also allows for: i) analyses of fresh, unaltered materials, ii) low blanks, iii) millimeter-scale sample specimens, iv) spatially resolved, ng/g-level chemical measurements, and v) surface and grain-boundary contamination to be avoided. All samples examined in this study were analyzed using a New Wave frequency-quintupled Nd:YAG laser (213 nm light) coupled to a Thermo Finnigan Element2 single-collector ICP-MS at the University of Maryland.

The laser and mass spectrometer parameters utilized for the measurements of this study are provided Table 4.1. Prior to sample analysis, the mass spectrometer was tuned to maximize signal (based on ^{43}Ca and ^{232}Th spectra) and minimize oxide production ($^{232}Th^{16}O/^{232}Th < 0.20\%$). The detection parameters included a dwell time of 10 ms for $^{135, 137}Ba$, 30 ms for ^{232}Th and ^{238}U, and 100 ms for $^{182, 183, 184, 186}W$ in order to accumulate adequate counting statistics to evaluate and constrain isobaric interferences, thus increasing analytical precision.

Table 4.1. LA-ICP-MS operating conditions employed for this study.

Laser Ablation Parameters	
Ablation Pattern	Line
Scan Speed	10 μm/s
Spot Size (Diameter)	45-250 μm
Repetition Rate	8-20 Hz
Energy Density*	2.0-3.0 J/cm^2
Mass Spectrometer Parameters	
Forward Power	1250W
HV	10 kV
Scan Optimization	Speed
Number of Pre-Scans	1
Active Dead Time	25 ns
Cool Gas Flow	16 L/min
Auxiliary Gas Flow	1.5 L/min
Sample Gas Flow	0.7 L/min
Carrier (He) Gas Flow	1.0 L/min
Cones	Ni-alloy

*Laser parameters were programmed to produce ideal photon fluences between 2-3 J/cm$^{2.}$

Spectral matrix effects (*i.e.*, isobaric interferences) were considered and monitored during analysis in order to prevent a compromise in accuracy. In this study, the only potential elemental isobaric interference is ^{186}Os at mass ^{186}W, but the concentration of Os in our basaltic melts was lower than our lower limit of detection. A potentially more problematic source of isobaric interferences is diatomic oxides. However, our analytical protocol measured the concentration of W by monitoring four isotope mass stations: ^{182}W, ^{183}W, ^{184}W, and ^{186}W. Any potential oxide interferences on these masses would yield discordant results between isotope ratios, but no systematic variances were detected (see Section 2.2). Further, we conducted an experiment in which we analyzed a synthetic basaltic glass doped with 500 μg/g of the heavy rare-earth elements (HREE). Employing the analytical parameters described above, HREE-oxide production rates (*i.e.*, YbO/Yb and TmO/Tm) were

measured to be ~$10^{-6.}$ Accordingly, HREE-oxides do not present significant isobaric interferences to even the most depleted W concentrations in our natural samples.

Non-spectral matrix effects in concentration measurements acquired through laser ablation ICP-MS can result from differences in chemical compositions between the analyte and the standard reference material. Although NIST SRM 612 (the standard reference material utilized for our measurements) has been well characterized and found to be homogeneous with respect to Ba, Th, U, and W, this glass represents a more enriched composition (with approximately 40 μg/g of each of these elements) than oceanic basalts, which can be far more depleted, particularly in regard to Th, U and W. In order to account for this discrepancy, which could potentially lead to analytical biases, we have externally calibrated our W, Th and U measurements to a suite of rocks analyzed via solution ICP-MS, including both isotope dilution and high-precision standard addition analyses. More details on the calibration of our trace element analyses are provided in Section 2.2.

4.5 Results

4.5.1 Data precision and accuracy

Concentrations and uncertainties of Ba, Th, U, and W for all 86 samples investigated in this study are reported in Table 4.2. Concentrations of W range from < 10 ng/g in the most depleted MORB to > 2000 ng/g in the most enriched intraplate basalt. Most sample concentrations were determined with ≤5% uncertainty ($2\sigma_m$; external reproducibility of 8-16 measurements for W, and 2-4 measurements for Ba, Th and

Table 4.2. Tungsten, U, Th, and Ba sample concentrations.

Sample/ID	Type[a]	Location[b]	W (ng/g)	±2σ_m[c]	U (ng/g)	±2σ_m[c]	Th (ng/g)	±2σ_m[c]	Ba (µg/g)	±2σ_m[c]	W/U	2RSD[d]	W/Th	2RSD[d]	W/Ba	2RSD[d]
OC180 D5-1	N-MORB	NMAR	13.84	0.51	19	5	51.2	6.7	2.18	0.02	0.732	29%	0.270	14%	0.00634	3.8%
VG 6930	N-MORB	NMAR	23.45	1.36	17.2	0.2	53.3	0.9	3.26	0.12	1.365	5.9%	0.440	6.0%	0.00720	6.8%
VG 6936	N-MORB	NMAR	20.99	0.69	16.9	0.2	58.9	0.5	3.36	0.08	1.246	3.5%	0.357	3.4%	0.00624	4.1%
VG 6937	N-MORB	NMAR	27.48	1.15	20.2	0.5	77.3	2.9	5.17	0.21	1.362	4.9%	0.356	5.6%	0.00532	5.8%
TK 5-1	N-MORB	NMAR	25.14	0.74	20.9	0.3	65.2	1.4	4.04	0.03	1.205	3.3%	0.386	3.7%	0.00622	3.0%
OCD180 D26-3	N-MORB	NMAR	21.1	0.2	53.9	1.0	190	8	10.4	0.0	0.390	2.0%	0.111	4.3%	0.00202	0.9%
TK 1-2	N-MORB	NMAR	34.21	0.69	36.8	0.9	130	7	5.57	0.03	0.930	3.2%	0.262	5.6%	0.00614	2.1%
TK 2-1	N-MORB	NMAR	12.7	0.3	41.8	0.6	151	9	6.82	0.03	0.304	2.4%	0.084	6.1%	0.00186	2.0%
OC180 D13-2	N-MORB	NMAR	28.9	0.4	53.9	1.9	200	3	12.6	0.13	0.537	3.8%	0.145	2.0%	0.00230	1.7%
VG 0738	N-MORB	NMAR	13.8	0.3	45.8	1.5	181	9	8.02	0.30	0.301	4.2%	0.076	5.7%	0.00172	4.5%
VG 0739	N-MORB	NMAR	13.2	0.7	50.6	0.7	164	2	7.94	0.40	0.262	5.2%	0.080	5.1%	0.00167	7%
TK 4-6	N-MORB	NMAR	15.7	0.2	48.2	0.9	137	5	8.43	0.03	0.326	2.3%	0.114	3.7%	0.00186	1.3%
VG 0741	N-MORB	NMAR	16.2	0.4	55.9	1.6	179	7	8.75	0.15	0.290	3.9%	0.091	4.9%	0.00185	3.2%
VG 0735	N-MORB	NMAR	22.2	0.4	65.1	0.7	234	7	11.6	0.38	0.342	1.9%	0.095	3.4%	0.00192	3.7%
Atlantica	E-MORB	MAR	109.7	1.6	160	4	713	11	64.3	1.6	0.685	3.0%	0.154	2.2%	0.00171	3.0%
MAR	N-MORB	MAR	39.74	0.61	31.0	0.6	109	2	5.93	0.05	1.283	2.6%	0.364	2.4%	0.00670	1.7%
VG 9055	N-MORB	SMAR	16.06	0.37	35.2	0.6	105	3	2.89	0.07	0.456	2.8%	0.152	3.3%	0.00555	3.4%
VG 9056	N-MORB	SMAR	16.08	0.83	35.7	2.5	114	2	2.94	0.13	0.451	8.6%	0.142	5.5%	0.00547	7%
VG 9052	N-MORB	SMAR	15.39	0.68	32.7	0.1	101	2	2.99	0.09	0.470	4.5%	0.152	4.7%	0.00514	5.3%
VG 3630	E-MORB	SMAR	47.3	0.6	165	2	508	31	29.9	1.6	0.287	1.9%	0.093	6.3%	0.00158	5%
R74-6	N-MORB	EPR	10.19	0.67	10.30	0.39	23.4	0.6	0.88	0.06	0.989	7.6%	0.435	7.1%	0.01157	9.6%
2384-9	N-MORB	EPR	8.7	0.3	15.2	0.5	33	1	1.42	0.09	0.571	5.0%	0.264	3.9%	0.00611	7%
2384-3	N-MORB	EPR	20.31	1.05	15.2	0.7	30.0	0.8	1.38	0.12	1.339	6.7%	0.676	5.8%	0.01467	10%
R30-30	N-MORB	EPR	29.7	4.6	32.5	1.6	80.9	3.6	1.80	0.15	0.914	16%	0.368	16%	0.01656	18%
R1-14	N-MORB	EPR	14.4	1.66	17.4	1.6	42.2	1.6	1.72	0.13	0.827	15%	0.340	12%	0.00834	14%
2387-2	N-MORB	EPR	13.2	0.2	35.2	0.6	105	2	7.34	0.21	0.376	2.2%	0.126	2.8%	0.00180	3.2%
R28-7	N-MORB	EPR	15.8	2.19	25.5	0.5	60.3	2.3	1.86	0.09	0.619	14%	0.261	14%	0.00848	15%
2706-7	N-MORB	EPR	34.00	0.98	37.2	0.4	84.4	1.0	4.91	0.12	0.913	3.1%	0.403	3.1%	0.00692	3.7%
R501-7	E-MORB	EPR	37.4	0.5	92.5	0.6	311	9	25.2	0.2	0.405	1.5%	0.120	3.3%	0.00148	1.6%
R494-5	E-MORB	EPR	35.4	0.4	87.1	3.0	269	5	24.7	0.7	0.407	3.6%	0.132	2.4%	0.00143	3.1%
R75-2	E-MORB	EPR	138	5	424	17	1.15E+03	3.7E+01	53.6	1.3	0.325	5.2%	0.120	4.7%	0.00257	4.2%
R501-2	E-MORB	EPR	43.5	0.5	103.7	2.1	336	6	27.1	0.4	0.420	2.3%	0.129	2.0%	0.00160	1.9%
R93-7	E-MORB	EPR	51.0	0.9	137	0	476	13	22.3	0.4	0.374	1.8%	0.107	3.2%	0.00228	2.5%
R15-2	E-MORB	EPR	555	8	990	41	3.58E+03	1.4E+02	306	7	0.560	4.4%	0.155	4.1%	0.00181	2.8%
R78-6	E-MORB	EPR	473	14	716	9	2.87E+03	1.1E+02	207	5	0.660	3.3%	0.165	5.0%	0.00229	3.8%
VE-32	E-MORB	EPR	56.8	0.6	122	3	353	12	51.5	0.4	0.465	2.7%	0.161	3.6%	0.00110	1.4%
2079-2	E-MORB	JdF Ridge	23.7	0.3	78.7	0.8	244	13	14.0	0.1	0.302	1.6%	0.097	5.3%	0.00169	1.5%
2082-6A	E-MORB	JdF Ridge	21.7	0.3	69.4	1.4	166	9	12.4	0.2	0.313	2.5%	0.131	5.6%	0.00175	2.1%
JdF MORB	E-MORB	JdF Ridge	31.2	0.3	104	1	249	5	15.7	0.9	0.300	1.6%	0.125	2.0%	0.00198	6%
VG-2	E-MORB	JdF Ridge	31.2	0.6	110.9	2.1	348	9	17.5	0.4	0.282	2.8%	0.090	3.4%	0.00178	2.9%
VG 5256	N-MORB	N Indian Ridge	9.59	0.39	10.37	0.49	42.5	3.6	2.02	0.04	0.925	6.2%	0.225	9.3%	0.00475	4.4%
VG 5253	N-MORB	N Indian Ridge	11.50	1.09	10.92	0.40	36.0	2.5	1.94	0.02	1.053	10%	0.319	12%	0.00593	9.5%
VG 5252	N-MORB	N Indian Ridge	11.81	0.92	11.3	0.5	35.6	1.0	2.06	0.10	1.049	8.8%	0.332	8.3%	0.00573	9%
VG 5259	N-MORB	N Indian Ridge	9.73	0.75	10.36	0.56	35.7	1.6	2.01	0.08	0.939	9.4%	0.272	9.0%	0.00485	9%
MD37-18 D2	E-MORB	SE Indian Ridge	149	5	185	11	858	9	55.0	1.5	0.805	6.9%	0.174	3.2%	0.00271	4.2%
AAD 10-10	E-MORB	SE Indian Ridge	25.2	0.4	55.5	0.9	241	5	14.8	0.3	0.454	2.3%	0.105	2.7%	0.00170	2.6%
AAD 7-3	E-MORB	SE Indian Ridge	64.4	0.4	133	1	557	9	33.5	0.7	0.485	1.0%	0.115	1.7%	0.00192	2.1%
AAD 8-8	E-MORB	SE Indian Ridge	130	2	191	5	592	20	68.2	1.4	0.678	3.0%	0.219	3.6%	0.00190	2.4%
MD 23-18 S3	N-MORB	C Indian Ridge	6.27	0.34	5.24	0.14	24.3	2.1	1.18	0.07	1.196	6.0%	0.258	10%	0.00534	8%
JC 2-17 D1(3)	E-MORB	C Indian Ridge	22.8	0.7	52.2	2.2	211	4	15.6	0.1	0.437	5.3%	0.108	3.8%	0.00146	3.3%
JC 3-02 D1	E-MORB	SW Indian Ridge	34.4	0.7	94.4	2.5	356	6	23.1	0.9	0.365	3.3%	0.097	2.6%	0.00149	4.3%
MD 34 D5	E-MORB	SW Indian Ridge	26.0	0.4	39.5	1.0	204	8	63.0	0.4	0.657	2.9%	0.127	4.2%	0.00041	1.6%

Table 4.2. Tungsten, U, Th, and Ba sample concentrations (continued).

Sample/ID			W (ng/g)	±2σm[c]	U (ng/g)	±2σm[c]	Th (ng/g)	±2σm[c]	Ba (µg/g)	±2σm[c]	W/U	RSD[d]	W/Th	RSD[d]	W/Ba	RSD[d]
Pu'u O'o 90	OIB	Kiluaea, HI	161	7	278	9	1.13E+03	4.5E+01	108	8	0.579	5.5%	0.143	6.0%	0.00149	9%
Pu'u O'o 93	OIB	Kiluaea, HI	177	4	310	0	8.93E+02	2.1E-01	110	2	0.572	2.0%	0.199	2.0%	0.00161	2.7%
VG A-99	OIB	Kiluaea, HI	248	4	500	13	1.97E+03	5.5E+01	184	6	0.495	3.1%	0.126	3.3%	0.00134	3.7%
NMNH 116111-22	OIB	Kilauea, HI	228	8	351	5	1.35E+03	1.5E+01	123	2	0.651	3.9%	0.170	3.8%	0.00186	4.1%
NMNH 113154-555	OIB	Galapagos	19.4	0.5	23.3	0.3	104	3	6.82	0.14	0.832	2.9%	0.186	4.1%	0.00284	3.3%
NMNH 113154-557	OIB	Galapagos	27.5	0.5	48.1	0.8	213	7	12.5	0.4	0.573	2.3%	0.129	3.7%	0.00221	3.5%
NMNH 113710-F709	OIB	Galapagos	218	4	400	11	1.64E+03	4.9E+01	114	13	0.545	3.3%	0.133	3.6%	0.00191	12%
NMNH 112048-2	OIB	Hekla, Iceland	766	31	1084	12	4.96E+03	4.8E+01	325	1	0.707	4.3%	0.154	4.2%	0.00236	4.1%
NMNH 112055	OIB	Hekla, Iceland	828	24	1.22E+03	2.1E+01	5.45E+03	1.5E+02	335	12	0.679	3.4%	0.152	3.9%	0.00247	4.5%
NMNH 112207-75	OIB	Heard Is., Australia	675	6	1033	14	4.80E+03	4.6E+02	545	3	0.653	1.6%	0.141	9.5%	0.00124	1.0%
NMNH 113057-3	ICV	Nyiragongo, Zaire	2144	30	7900	51	2.35E+04	2.0E+02	2259	22	0.271	1.5%	0.091	1.6%	0.00095	1.7%
NMNH 115693	ICV	Nyiragongo, Zaire	2408	105	7510	126	2.18E+04	1.2E+03	2157	152	0.321	4.7%	0.111	7.0%	0.00112	8.3%
NMNH 112514	ICV	Nyamuragira, Zaire	1457	30	2003	30	1.43E+04	3.4E+02	1021	54	0.727	2.5%	0.102	3.1%	0.00143	5.7%
NMNH 068376	ICV	Sunset Crater, AZ	316	13	927	53	3.72E+03	1.8E+02	453	25	0.341	7.0%	0.085	6.2%	0.00070	6.8%
42995-3C	ICV	Yucca Mtn., NV	487	19	2103	71	1.06E+04	7.2E+02	1511	90	0.232	5.1%	0.046	7.8%	0.00032	7.1%
NMNH 116605.0013	ICV	Tower Hill, Australia	943	40	1174	32	6.61E+03	1.5E+02	503	11	0.803	5.1%	0.143	4.9%	0.00187	4.8%
NMNH 108800	IAB	Oshima Is., Japan	258	4	141	2	3.03E+02	8.6E+00	206	8	1.828	2.1%	0.853	3.2%	0.00125	4.3%
NMNH 116701-2	IAB	Galunggung, Indonesia	397	31	246	6	1.50E+03	2.2E+02	115	21	1.613	8.1%	0.265	16.5%	0.00345	19.8%
NMNH 116141	CAB	Pacaya, Guatemala	329	8	930	45	3.17E+03	3.8E+02	684	18	0.354	5.4%	0.104	12.3%	0.00048	3.5%
NMNH 108135	CAB	Mexico	201	5	295	13	1.06E+03	1.1E+02	285	26	0.681	5.2%	0.190	10.2%	0.00070	9.6%
NMNH 116601-12	CAB	Durango, Mexico	1101	16	1352	39	6.54E+03	1.7E+02	516	12	0.814	3.2%	0.168	3.0%	0.00213	2.7%
NMNH 113559-1	CAB	Vesuvius, Italy	926	23	2893	223	1.12E+04	7.5E+02	739	61	0.320	8.1%	0.082	7.2%	0.00125	8.6%
VG 3636	BABB	Scotia Back-Arc	45	1	109	2	3.76E+02	2.9E+00	41	1	0.411	2.7%	0.119	1.6%	0.00109	1.9%
VG 3637	BABB	Scotia Back-Arc	49	1	112	1	4.04E+02	4.9E+00	43	0	0.434	1.7%	0.120	1.6%	0.00113	1.6%
VG 3635	BABB	Scotia Back-Arc	46	0	106	1	431	6	40	1	0.433	1.4%	0.107	1.7%	0.00116	1.9%
VG 3638	BABB	Scotia Back-Arc	53	1	107	2	3.71E+02	3.9E+00	54	2	0.491	1.9%	0.142	1%	0.00098	4%
VG 3634	BABB	Scotia Back-Arc	43.5	0.6	102.5	3.3	398	6	38.4	0.9	0.424	3.5%	0.109	2.0%	0.00113	2.6%
SLB 133 GA	BABB	Southern Lau Basin	68.9	0.5	198.5	1.7	463	3	110.0	3.1	0.347	1.2%	0.149	1.0%	0.00063	2.9%
SLB 58 GA-1	BABB	Southern Lau Basin	71.9	0.9	200.4	2.4	484	3	94.5	3.0	0.359	1.7%	0.148	1.4%	0.00076	3.4%
SLB 53 GC-1	BABB	Southern Lau Basin	53.3	0.6	151.8	1.0	347	11	79.7	3.7	0.351	1.3%	0.154	3.3%	0.00067	4.8%
SLB 127 KD	BABB	Southern Lau Basin	71.5	1.5	185.4	2.4	451	13	95.0	2.7	0.386	2.5%	0.159	3.7%	0.00075	3.5%
CLB 7GC	BABB	Central Lau Basin	38.1	1.7	22	0	79	4	6	0	1.762	4.6%	0.485	6.9%	0.00613	4.9%
CLB 42GC	BABB	Central Lau Basin	32.6	0.6	21	0	69	1	6	0	1.588	2.1%	0.471	2.0%	0.00506	3.0%
CLB 46GC	BABB	Central Lau Basin	14.0	0.1	31	1	105	1	8.0	0.2	0.449	1.9%	0.133	1.7%	0.00175	3.1%
Hawaiian Picrites																
Lo-02-02			265	4	337	11	1.14E+03	3.6E+01	147	4	0.786	3.5%	0.232	3.6%	0.00180	3.4%
Lo-02-04			313	6	365	7	1.27E+03	1.8E+01	156	5	0.857	2.7%	0.246	2.3%	0.00201	3.5%
H-11			113	2	159	4	533	13	56.0	1.7	0.710	2.9%	0.211	3.1%	0.00201	3.6%

[a] N-MORB, E-MORB, OIB, and BABB defined in text; ICV = intracontinental basalt, IAB = island arc basalt, CAB = continental arc basalt

[b] NMAR = North Mid-Atlantic Ridge, SMAR = South Mid-Atlantic Ridge, EPR = East Pacific Rise, JdF Ridge = Juan de Fuca Ridge

[c] $2\sigma_m$ uncertainties determined as external reproducibilities of 8-16 measurements for W, and 2-4 measurements of B, Th and U.

[d] Relative uncertainties (2σ) in W/X ratios were determined through error propagation according to equation 3.26 from Bevington and Robinson (2003).

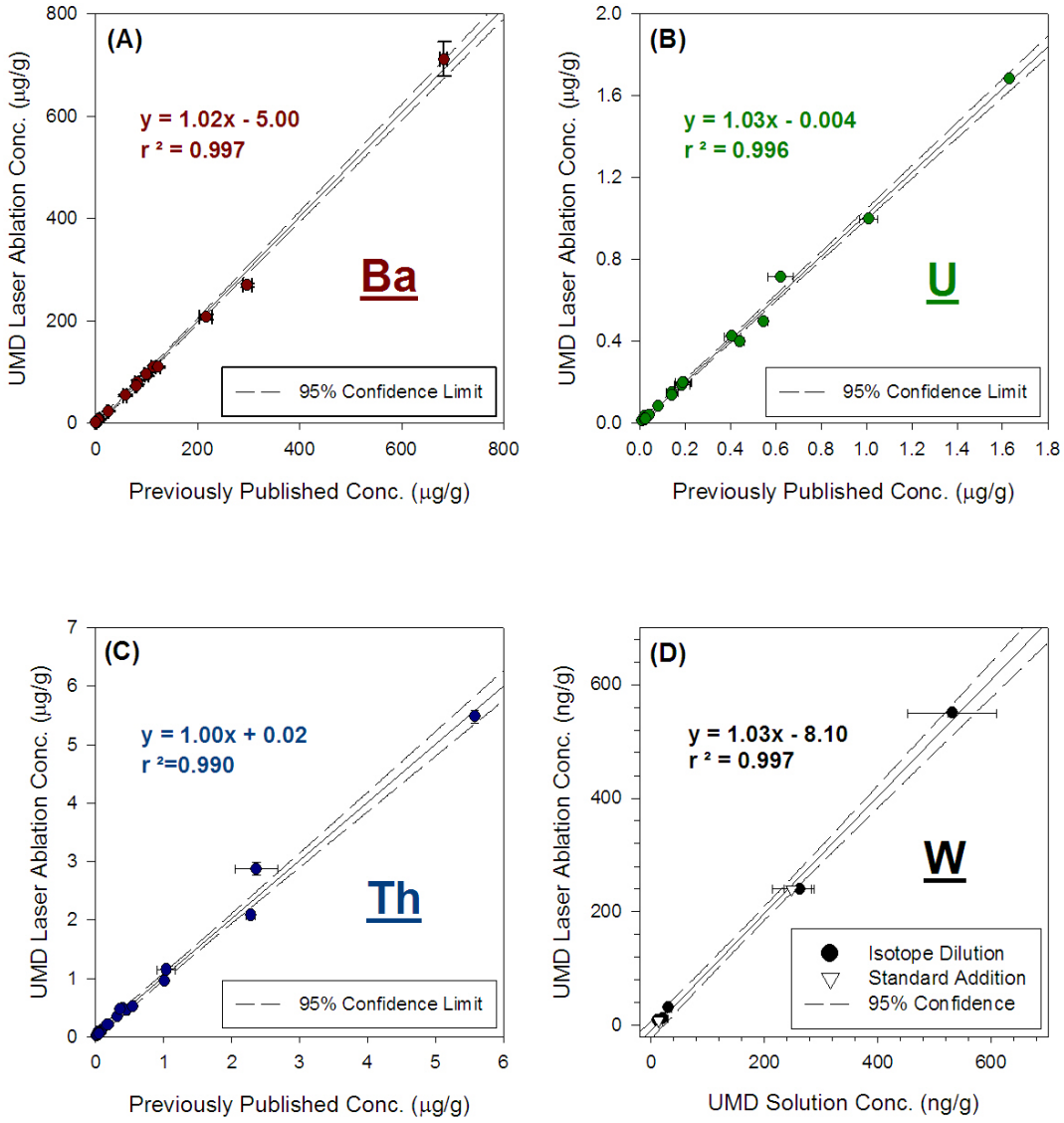

Fig. 4.1. Correlations between our LA-ICP-MS concentration data and those of previously published and/or recently acquired solution analyses of the same samples. Previously published values of Ba, Th and U include isotope dilution measurements from Loock *et al.*, (1990), solution ICP-MS measurements from Niu and Batiza (1997), and isotope dilution analyses of the homogeneous MPI-DING and USGS reference glasses by Jochum *et al.*, (2005, 2006). In regards to W, both natural samples (2384-9 and JdF MORB) and geologic reference glasses (BIR-1g, BHVO-2g, and BCR-2g) were analyzed by laser ablation and solution ICP-MS at the University of Maryland, including via both isotope dilution and high-precision standard addition methods. Details of these measurements are

provided in Section 2.2. In all cases, our laser measurements agree well with solution measurements (within ± 3%) over several orders of magnitude for each element. Deviations from a perfect correlation with slope (*m*) = 1.00 can be accounted for by the uncertainty in each of our measurements, which typically range from 2-5% ($2\sigma_m$).

U), though several analyses of phaneritic MORB glasses samples with low W concentrations resulted in uncertainties greater than 10%. The accuracy of our laser ablation method is demonstrated in Fig. 4.1, where our Ba, Th, U, and W measurements are compared with previously determined values from solution analyses, largely isotope dilution measurements.

4.5.2 The best geochemical analogue to W

Correlations between Ba, Th, U, and W concentrations in basaltic melts indicate that all four of these elements behave similarly during the evolution of basaltic magma. In order to establish which incompatible lithophile element most closely follows W in basaltic sources, and thus which W/X ratio best represents a constant concentration ratio representative of the modern mantle, we can examine the constancy of each W/X ratio across a wide range in W concentrations (Fig. 4.2). Sims and DePaolo (1997), however, noted that these types of diagrams have the distinct disadvantages that (a) the plotted variables are not statistically independent, and (b) variations in the y-variable of each curve (*i.e.,* W/X, spanning ~ 1 order of magnitude) are disproportionately small in comparison to variations in the x-variable (*i.e.,* W concentration, spanning > 2 orders of magnitude). Additionally, the slope of each linear regression in Fig. 4.2 is sensitive to the relative value of the mean W/X ratio, resulting in artificially high statistical deviations from a slope of 0 for W/Th and W/U. Nevertheless, this plot serves the qualitative purpose of illustrating that W/Ba, W/Th and W/U all remain relatively constant over a range of concentrations. In contrast, a ratio showing a systematic enrichment with increasing W concentration would indicate a lithophile element significantly less incompatible than W during

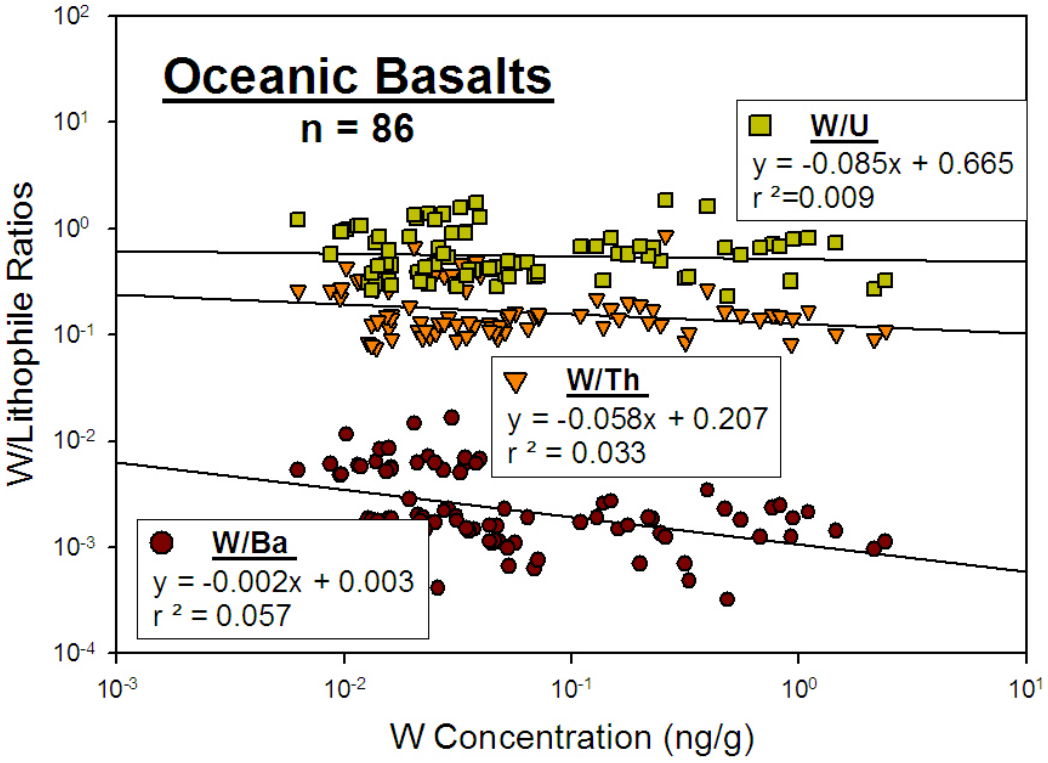

Fig. 4.2. W/Ba, W/Th and W/U ratios plotted against the W concentration (ng/g) of our samples. A perfectly constant element ratio would yield a slope of zero. The accompanying statistics suggest a systematic decrease in both W/Th and W/U as a function of increasing W concentration, but this represents an artificial bias due to the higher absolute value of the *y*-variables of these curves compared to W/Ba.

mantle melting, and a systematic depletion would designate a more incompatible lithophile element.

A more quantitative way to evaluate which lithophile element behaves most analogously to W during silicate differentiation is through a log-log co-variation plot (Sims and DePaolo, 1997; Hofmann, 2003). Fig. 4.3 illustrates such a diagram, with the concentrations of Ba, Th and U plotted against the concentration of W in our basaltic samples. Using this diagnostic approach, a constant concentration ratio will yield a slope of unity (m = 1.00). According to our sample data, the linear regression that is statistically closest to unity is that between W and U. Both Th and Ba yield slopes greater than unity when plotted against W, implying a higher incompatibility of these elements in basaltic melts. Additionally, the W/U ratio of the mantle does not appear to be affected by any differentiation processes, as the W/U ratios of our samples are independent of MgO content as well as tectonic setting (Fig. 4.4). Accordingly, we conclude that U is the incompatible lithophile element that behaves most similarly to W through silicate processing, despite the difference in mobility between these two elements in aqueous phases (Taylor and McLennan, 1985).

4.6 Discussion

4.6.1 W in the silicate Earth, modern mantle and core

Since U best mimics the geochemical behavior of W in our spectrum of basaltic samples, the average W/U ratio of our dataset likely has not been affected by silicate differentiation events, and thus represents the W/U ratio of the modern mantle. The average W/U ratio of our comprehensive sample suite, and thus of the mantle, is 0.65

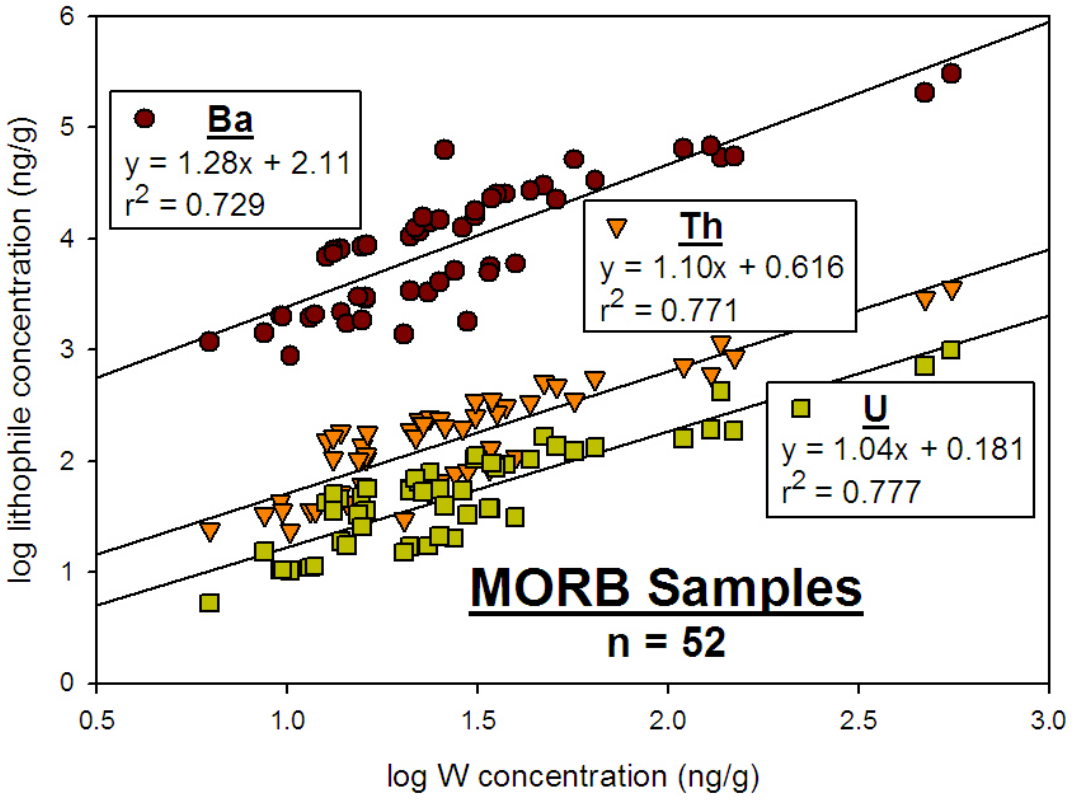

Fig. 4.3. Log-log co-variation diagram plotting the concentrations (ng/g) of Ba, Th and U versus the concentration of W in our MORB samples. On this type of plot, because the plotted samples share the same mantle source region (the Depleted MORB Mantle, or DMM), a regression line of slope 1.00 represents a perfectly constant element ratio, whereas a slope of >1.00 indicates a more incompatible lithophile element (*e.g.*, Ba, Th and U) during mantle melting. It can be seen that the linear regression between W and U yields the slope nearest unity (m = 1.04 ± 0.18, 95% confidence) and with the least statistical scatter (r^2 = 0.777). Although both Ba and Th yield slopes greater than unity, suggesting that they are more incompatible than W during mantle melting, the slope of log Th versus log W is within uncertainty of unity (m = 1.10 ± 0.20, 95% confidence).

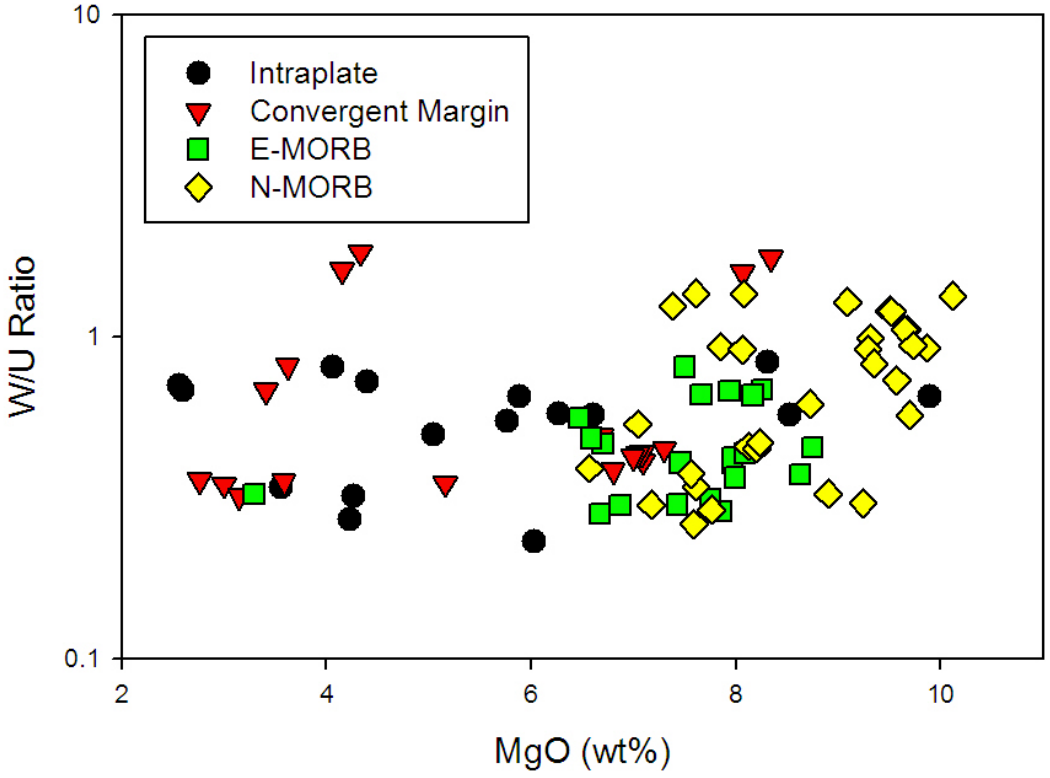

Fig. 4.4. The W/U ratio of our samples plotted against MgO (wt%) content. The W/U ratios of our modern basalts appear to be independent of the degree of silicate processing, and no systematic differences among the different sample populations (including N-MORB, E-MORB, convergent margin volcanics, and intraplate basalts) can be seen with regards to W/U.

± 0.45 (2σ; n = 86), which is statistically indistinguishable from the value obtained considering only MORB (W/U_{MORB} = 0.65 ± 0.41, n = 52), OIB (W/U_{OIB} = 0.63 ± 0.07, n = 10), or BABB (W/U_{BABB} = 0.62 ± 0.09, n = 12).

The W/U ratio of the modern mantle is also coincident with that of the continental crust (W/U = 0.77 ± 0.33, 2σ; Rudnick and Gao, 2003), which is largely based on upper-crustal sediments and loess deposits (median W/U ≈ 0.8) and high-grade metamorphic terrains representative of the lower crust (median W/U ≈ 0.8; data from Newsom *et al.,* 1996 and references cited therein). Therefore, the W/U ratio of the mantle may also be inferred to be representative of the entire silicate portion of the Earth, assuming the absence of a "hidden" repository with a W/U ratio outside the range displayed by sampled reservoirs (McDonough, 1991; Lassiter, 2004; Tolstikhin and Hofmann, 2005, 2006; Boyet and Carlson, 2005, 2006). Assuming a U concentration of 20 ± 8 (2σ) ng/g in the bulk silicate Earth (McDonough and Sun, 1995; Palme and O'Neill, 2003; Lyubetskaya and Korenaga, 2007) and a W/U ratio of 0.65 ± 0.45 (2σ), the concentration of W in the silicate portion of the Earth is 13 ± 10 ng/g.

Newsom *et al.,* (1996) and Rudnick and Gao (2003) reported that the bulk continental crust (~0.5% of the bulk silicate Earth, by mass) contains approximately 1000 ± 300 (2σ) ng/g W. Based on mass balance contributions and our preferred estimate of W in the silicate Earth, the mean concentration of W in the Earth's modern mantle reservoir is calculated to be 8.3 ± 7.1 ng/g (with MORB and OIB representing depleted and enriched source regions, respectively). Based on the unweighted mean W/Hf ratio of carbonaceous chondrites (W/Hf = 0.91 ± 0.06, $2\sigma_m$;

Kleine *et al.,* 2004b), a silicate Earth composition with 280 ± 60 (2σ) ng/g Hf, and negligible Hf in the core, the bulk Earth contains 172 ± 36 ng/g W. Accordingly, simple core-modeling and mass balance considerations predict that the core has 510 ± 120 ng/g W; this indicates a W metal/silicate partition coefficient ($D^{metal/silicate}$) of ~ 40 during the conditions of core formation, which is consistent with a deep (> 700km), potentially hydrous magma ocean early in Earth's history, according to high pressure-temperature metal/silicate partitioning experiments (Righter *et al.,* 1997; Righter and Drake, 1999; Righter, 2003).

4.6.2 Implications for the composition of the DMM and deep mantle

The MORB source, often referred to as the depleted MORB mantle (or DMM), is generally thought to have formed as the result of an ancient depletion (*i.e.*, continent formation). Although the source of MORB has been established to be compositionally heterogeneous (*e.g.*, van Keken *et al.,* 2002 and references therein), the relative depletion of this reservoir, as a whole, remains unsettled; this is largely due to difficulties in modeling the incompatible element budget of the DMM (Jagoutz *et al.,* 1979; Hofmann, 1988, 2003).

Several studies have attempted to model the composition of the MORB source by analyzing the trace element chemistry of abyssal peridotites, calculating parent-daughter ratios of radiogenic isotopes, and using constant elemental concentration ratios. Assuming a chondritic original composition and a two-stage evolution of the continental crust, Salters and Stracke (2004) estimated an average DMM composition with 4.7 ± 1.4 (2σ) ng/g U. This model represents a ~4x depletion of the highly incompatible elements in the MORB source relative to the unfractionated silicate

Earth, which is more depleted than the DMM composition of Boyet and Carlson (2006), which assumes a non-chondritic origin, but less depleted than the Workman and Hart (2005) model, which follows a gradual evolution of the continental crust. In order to further investigate the depletion of the DMM, we may also consider the incompatible trace element chemistry of global MORB in conjunction with simple partial melting dynamics. MORB from "typical" segments of mid-ocean ridges (those found far from known "plumes" or subduction zones) exhibit a mean composition of 16 ± 13 (2σ) μg/g Ba (Su, 2002), a highly incompatible element comparable to U. Assuming 8-12% partial melting of the MORB source (*e.g.*, Hofmann, 1988), this indicates that the DMM has approximately 1.6 ± 1.3 μg/g Ba, verifying a factor of ~4 depletion of highly incompatible elements in the MORB source compared to the bulk silicate Earth. According to the Salters and Stracke (2004) depletion model, the DMM is estimated to have 3.0 ± 2.3 (2σ) ng/g W.

Constraining the mean abundance of W in the modern mantle and the composition of the MORB source region allows us to make some inferences as to the composition of the deep mantle, which has been shown to be geochemically distinct from the DMM (*e.g.*, Hofmann, 1997). If we assume an upper and lower mantle separated by the 660 km discontinuity, this would necessitate ~10 ng/g W in the lower mantle, according to mass balance and a DMM composition of 3.0 ± 2.3 ng/g W. However, it has been widely demonstrated that the 660 km discontinuity cannot serve as a chemical boundary, as a significant mass flux across this depth has been established by tomographic studies (*e.g.*, Creager and Jordan, 1984; Davies and Richards, 1992; van der Hilst *et al.,* 1997; Grand *et al.,* 1997; Montelli *et al.,* 2004;

Nolet *et al.,* 2006). Recently, seismological, geochemical and geophysical observations have identified a potentially deeper boundary layer between the upper and a heterogeneous deep mantle (*e.g.*, Garnero, 2000 and references therein). A boundary layer at ~1600 km depth, as preferred by Kellogg *et al.,* (1999), would require an enriched deep mantle W abundance of ~25 ng/g, or roughly two times the W content of the unfractionated silicate Earth. Further, if we consider near-whole-mantle convection with the DMM constituting the entire mantle mass minus a 200-300 km thick boundary layer at the core-mantle boundary (which could serve as the early enriched reservoir invoked by Tolsikhin and Hofmann, 2005; Boyet and Carlson, 2005, 2006; and Tolstikhin *et al.,* 2006), this reservoir would contain ~190 ng/g W.

As an additional consideration, we can examine the constancy of the W/Th ratio in our basaltic dataset. Although the W/Th ratio in the mantle is more variable than W/U because it can be affected to some degree by partial melting (Fig. 4.4) and hydrothermal fluids (Noll *et al.,* 1996), the mean W/Th ratio of our oceanic basalts (W/Th = 0.19 ± 0.15, 2σ) is comparable to the MORB and OIB dataset of Newsom *et al.,* (1996; W/Th = 0.15 ± 0.11, 2σ). As such, if the W/Th ratio of the modern mantle is defined by our basaltic dataset, the mean mantle has a Th/U ratio of 3.3 ± 1.4 (2σ), which is higher than estimates of the MORB source (*e.g.*, 2.5; Turcotte *et al.,* 2001) but lower than the preferred value for the silicate Earth (*e.g.*, 3.9; McDonough and Sun, 1995) and chondritic meteorites (*e.g.*, 3.8; Rocholl and Jochum, 1993).

4.6.3 Detecting core-mantle interactions through W isotopes

Excesses of isotope ^{182}W are produced via beta-decay of the now-extinct ^{182}Hf nuclide, which has a half-life of 8.90 ± 0.09 Ma (Vockenhuber *et al.,* 2004). Both Hf and W are refractory elements, but differ in their geochemical affinities; under the reducing conditions of core formation, Hf acts as a lithophile element, and thus prefers to remain in silicate phases, whereas W behaves as a moderately siderophile element. Consequently, a metallic core will have a Hf/W ratio of ~ 0 and will therefore retain its original W isotopic composition. Because of the short-lived nature of this radiogenic system, any existing W isotopic heterogeneities within the Earth must have been inherited during the first ~50 Ma of solar system history, the functional lifetime of ^{182}Hf.

Studies of terrestrial samples and chondritic meteorites have established that the core of the Earth must be depleted by ~2 parts per 10,000 (or 2 ε-unit) in ^{182}W relative to the silicate Earth (Kleine *et al.,* 2002; Schoenberg *et al.,* 2002, Yin *et al.,* 2002). Because the concentration of W is significantly greater in the core compared to the mantle, small depletions in ^{182}W (relative to the silicate Earth) in "plume-derived" magmas that originate near the base of the mantle may result from core-mantle interactions. However, initial investigations into the W isotopic composition of several Hawaiian picrites that may record a core component in their source (on the basis of resolvable enrichments in ^{186}Os-^{187}Os; Brandon *et al.,* 1998, 1999) failed to resolve these rocks from terrestrial standards (Scherstén *et al.,* 2004).

The W content of the three Hawaiian picrites measured by Scherstén *et al.,* (2004) range from 113 ng/g (H-11) to 313 ng/g (Lo-02-04), as determined by this study. Assuming 5-15% partial melting, this indicates a Hawaiian source with anywhere from 5 to 45 ng/g W. Assuming a Hawaiian source with a concentration of 26 ng/g W, or approximately two times the W content of the undifferentiated silicate Earth (13 ng/g W), the three Hawaiian picrites may be accounted for by a two end-member mixing scenario between the outer core and an enriched deep mantle reservoir (Fig. 4.5). Such an enriched Hawaiian source is consistent with a lower mantle source defined below ~1600 km depth, as originally suggested by Kellogg *et al.,* (1999), and may result from pyroxenitic melting in the Hawaiian source region (Sobolev *et al.,* 2005, 2007). Additionally, as Brandon and Walker (2005) observed, even modest contamination by a crustal component could overprint any W core signature recorded in these rocks while having a negligible effect on their Os isotopic ratios. This is illustrated in the model source consisting of a silicate Earth component, with 13 ng/g W, mixed with 5 wt% continental crust in Figure 4.5. Although higher-precision measurements of the W isotopic compositions of these rocks might provide some clarity to these issues, an additional window into detecting core-mantle exchange may lie with the terrestrial W/U ratio.

4.6.4 Detecting core-mantle interactions through W concentration ratios

Whereas isotopic ratios can serve as geochemical tracers of either the physical admixture of or diffusive isotopic exchange between the core and mantle (Puchtel and Humayun, 2000), concentration ratios can only act as a proxy of the physical admixture of these two reservoirs, assuming the core and silicate Earth (including

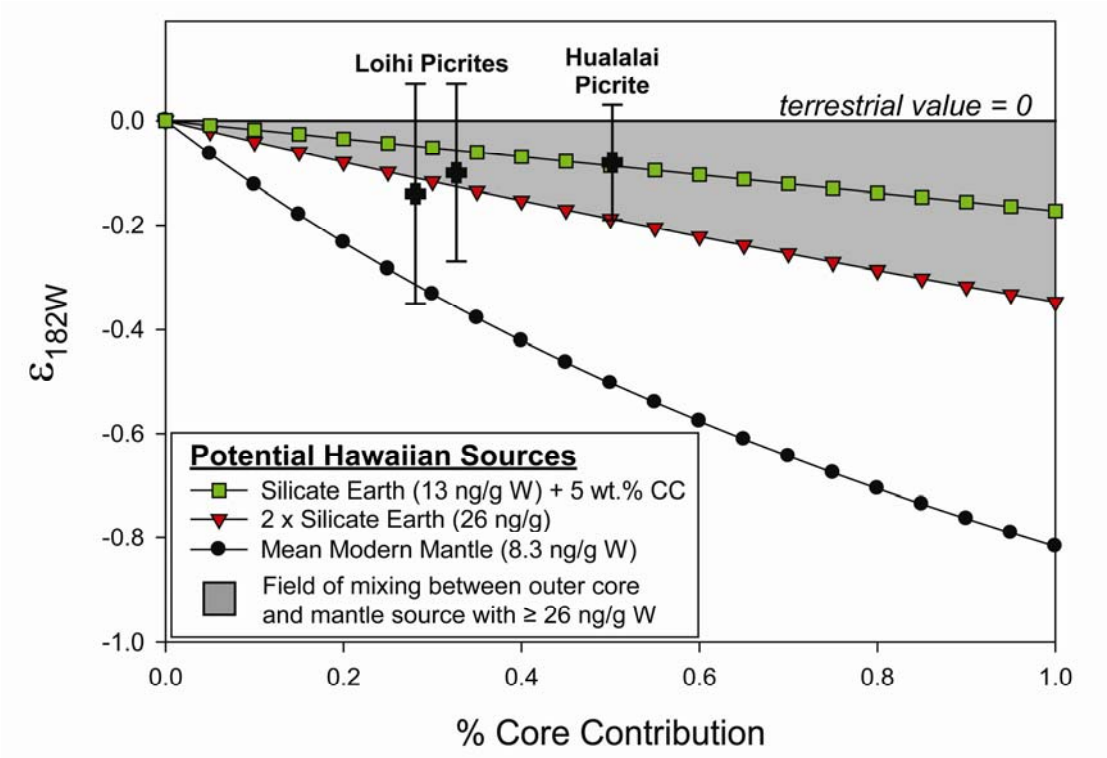

Fig. 4.5. Models of core-mantle exchange as detected by W isotopes (adapted from Brandon and Walker, 2005). Mixing between a model outer core (with 500 ng/g W, ε_{182W} = -2.1) and several potential Hawaiian sources. A Hawaiian source equal to the mean modern mantle (8.3 ng/g W) cannot account for the lack of ε_{182W} depletions in the Hawaiian picrites suggested by Brandon *et al.,* (1998, 1999) to record a core signature; this mixing trend mirrors the "preferred" core-mantle mixing curve of Scherstén *et al.,* (2004). However, a more enriched source equal to two times the silicate Earth (26 ng/g W), which is consistent with a deep mantle source defined below ~1600 km depth, could account for the W isotopic signatures of the Hawaiian picrites. A Hawaiian source comprised of a silicate Earth component (13 ng/g W) plus 5 wt% continental crust (CC) could also explain the picrite data. Parameters for the continental crustal component were taken from Scherstén *et al.,* (2004).

both the modern mantle and continental crustal reservoirs) each have a unique and constant value. Because core formation has depleted the silicate Earth in siderophile elements relative to the lithophile elements, siderophile-to-lithophile ratios provide the most sensitive type of tracers because such ratios are extremely high in the core and correspondingly low in the silicate Earth (Table 4.3). For example, Fe/Mn ratios, which have been implicated in the identification of a core signature in modern Hawaiian lavas (Humayun *et al.,* 2004), are enriched in the core relative to the mantle, but only by a factor of > 10. On the other hand, the W/U of the core is enriched by a factor > 10^5 relative to the modern mantle. As a result, W/U is potentially three-times more sensitive than Fe/Mn to a two end-member mixing scenario between the mantle and 1 wt% of core material, considering the reservoir compositions listed in Table 4.3.

Since the core contains approximately 95% of the bulk Earth's W budget and essentially no U (McDonough, 2003), it can be confidently established that the core has a W/U >> 1000. A two end-member mixing curve between a mantle reservoir with ≥8.3 ng/g W and W/U = 0.65 ± 0.45 (2σ) and an outer core reservoir with ~500 ng/g W and W/U = 1000 (as a lower limit), however, indicates that the physical entrainment of up to 1 wt% of outer core materials would fail to result in a resolvable increase in W/U; a more depleted source composition (*e.g.*, DMM with 3.0 ng/g W) or a higher degree of core contamination is required for core-mantle exchange to be identified through the use of this proxy (Fig. 4.6). An analysis of the three Hawaiian picrites examined by Brandon *et al.,* (1998, 1999) and Scherstén *et al.,* (2004) illustrates these limitations. Although all three of the picrites reside within the

Table 4.3. Siderophile/Lithophile element pairs.

Element	Silicate Earth (µg/g)[a]	Core (µg/g)[b]	Core/SE Enrichment Factor
P	90	2000	22
Ti	1200	0	0.0
Mn	1045	300	0.3
Fe	62600	855000	14
Mo	0.05	5	100
Pd	0.004	3.1	775
Ba	6.6	0	0.0
Ce	1.68	0	0.0
Nd	1.25	0	0.0
Yb	0.44	0	0.0
W	0.0131	0.504	38
Re	0.0003	0.23	767
Pb	0.15	0.4	2.7
Fe/Mn	60	2850	**> 10**
P/Nd	72	$>10^5$	**$> 10^3$**
Pb/Ce	0.089	$>10^3$	**$> 10^4$**
Mo/Ce	0.030	$>10^4$	**$> 10^5$**
W/Ba	0.0020	$>10^3$	**$> 10^5$**
Re/Yb	0.00068	$>10^3$	**$> 10^6$**
Pd/Ti	3.3E-06	$>10^4$	**$> 10^9$**

[a] From McDonough and Sun (1995), excepting W.
[b] From McDonough (2004), excepting W.

variability seen in our sample suite, this does not preclude a core component added to the source of these rocks. Brandon *et al.,* (1998, 1999) suggest that these three picrites carry only 0.3 – 0.5% core contribution; this amount of mass exchange is permitted with our mixing models assuming a Hawaiian source with an enriched mantle composition. Thus, although W/U serves as a potentially sensitive geochemical tracer of physical admixture between outer core and deep mantle materials, the variability seen in modern basaltic samples makes it difficult to unambiguously detect core contributions in materials derived from enriched source regions.

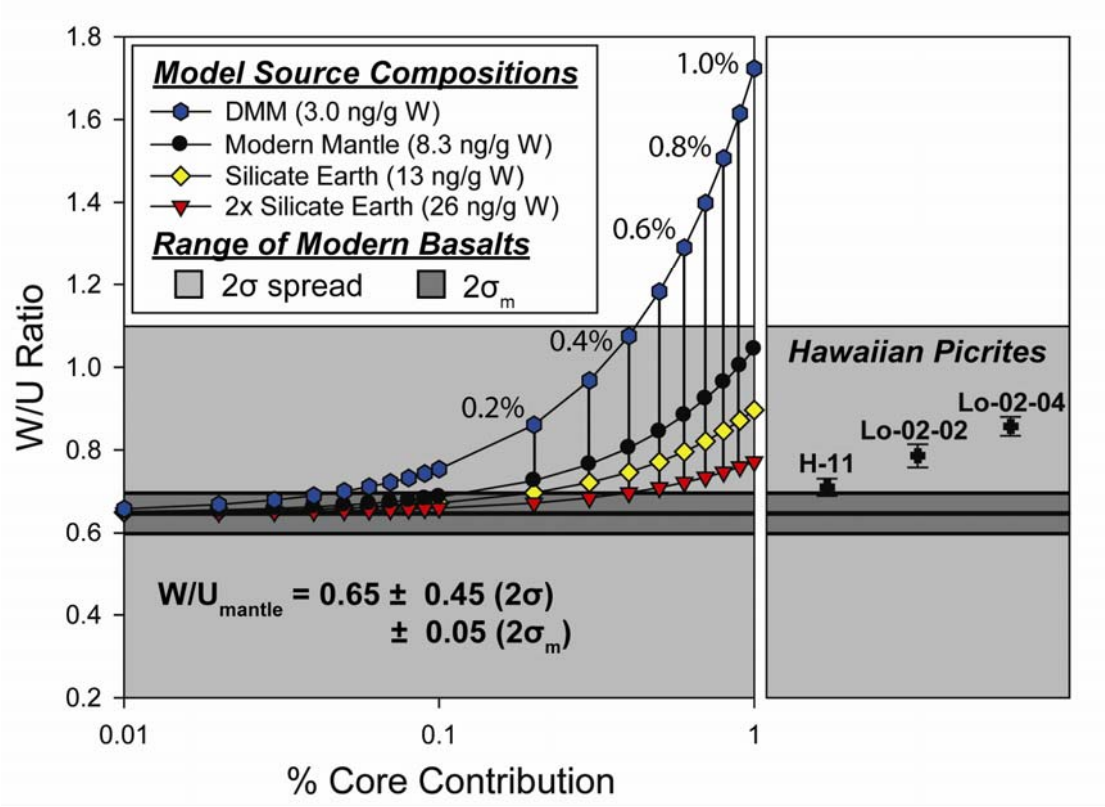

Fig. 4.6. Two end-member mixing between the outer core and model mantle sources. The light gray field represents the 2σ scatter seen in our mantle-derived samples; the dark gray region represents the $2\sigma_m$. The overall range of W/U seen in modern oceanic basalts makes assessing core-mantle exchange difficult for enriched sources and low degrees of core contribution. As seen in the figure, even up to 1 wt% of core material added to a mantle source with ≥8.3 ng/g W would not result in an enriched W/U outside of the spread seen in basaltic sources. However, a more depleted source, such as a source equal to the Depleted MORB Mantle (*i.e.,* DMM), would allow for the detection of < 1.0 wt% core contribution. Data for the Hawaiian picrites examined by Brandon *et al.,* (1998, 1999) and Scherstén *et al.,* (2004) lay above the mean and $2\sigma_m$ spread, but easily reside within the scatter seen in our basaltic samples. This does not preclude a core component added to the source of these samples, though, as the source of these picrites likely has >3.0 ng/g W.

4.7 Conclusions

Modern oceanic basalts, including both E-type and N-type MORB, intraplate and convergent margin volcanics, reveal that U behaves analogously to W during silicate differentiation. The average W/U ratio of these samples (0.65 ± 0.45, 2σ, n = 86) is representative of both the modern mantle and bulk silicate Earth, and suggests a bulk silicate Earth composition of 13 ± 10 ng/g W and a mean modern mantle composition of 8.3 ± 7.1 ng/g W. According to the model DMM composition of Salters and Stracke (2004), the MORB source likely contains 3.0 ± 2.3 ng/g W. Assuming a stratified mantle at ~~1600 km depth, this indicates a deep mantle with ~25 ng/g W. Alternatively, considering near whole-mantle convection with only a ~250 km thick D″ layer at the core-mantle boundary, this reservoir must be enriched up to ~190 ng/g W.

In theory, both W isotopes and W/U ratios can be used to identify core-mantle exchange. However, as with most geochemical tracers of internal processes within the Earth, these proxies are dependent on the model source composition of the sampled materials. Three Hawaiian picrites initially examined by Brandon *et al.,* (1998, 1999) have been suggested to record a core signature according to their ^{186}Os-^{187}Os isotopic compositions. However, no discernable core signature is seen via W isotopes or W/U ratios. This suggests either (1) the lack of a core component in the source of these rocks, (2) crustal contamination of the samples, or (3) a source with at least 26 ng/g W, which is consistent with a deep mantle source defined below ~1600 km. Accordingly, until further constraints can be placed on the source region of these samples, the issue of core-mantle exchange has yet to be resolved.

Chapter 5: The K/U ratio of the silicate Earth: Insights into mantle composition, structure and thermal evolution[1,2]

[1] R. Arevalo Jr., W.F. McDonough and M. Luong all contributed to the development of the medium-resolution LA-ICP-MS analytical method to measure K abundances in natural silicates. M. Luong conducted the majority (~75%) of the sample analyses, with R. Arevalo Jr. measuring the remainder (~25%). Both R. Arevalo Jr. and W.F. McDonough contributed to the interpretation of the data. The text, tables and figures were written/created by R. Arevalo Jr.

[2] This chapter has been published as:
Arevalo Jr., R., McDonough, W.F., and Luong, M., 2009. The K/U ratio of the silicate Earth: Insights into mantle composition, structure and thermal evolution. *Earth and Planetary Science Letters* (278), 361-369, doi:10.1016/j.epsl.2008.12.023.

5.1. Abstract

The abundance of K in the silicate Earth provides control on the composition of the Earth's interior, the dominant mode of mantle convection, the thermal evolution of the planet, and the concentration of Pb in the core. Because K acts as a volatile species during accretion, the K content of the silicate Earth is determined as a function of the terrestrial K/U ratio. A comprehensive examination of MORB from the Atlantic, Indian and Pacific oceans, including both normal- and enriched-type samples, reveals a composite MORB source K/U ratio of 19,000 ± 2600 (2σ). In comparison, ocean island basalts and average continental crust have average K/U values of 11,900 ± 2200 and 13,000 ± 3000, respectively. The fractional contributions of these reservoirs establishes the K/U ratio of the silicate Earth to be 13,800 ± 2600 (2σ), equating to 280 ± 120 μg/g K in the silicate Earth. As a result, the planet's convective Urey ratio is verified to be ~0.34, which indicates a current mantle cooling rate of 70-130 $KGyr^{-1}$ after taking into account potential heat flux across the core-

mantle boundary. Additionally, the Earth's balance of radiogenic heat flow and budget of ^{40}Ar necessitate a lower mantle reservoir enriched in radioactive elements. The bulk Earth Pb/U ratio, determined here to be ~85, suggests ~1200 ng/g Pb in the bulk Earth and ≥3300 ng/g Pb in the core.

5.2 Introduction

The dominant mode of convection in the modern mantle has been a hotly debated topic for decades. Whereas geophysical observations intimate significant material exchange across the entire mantle (*e.g.*, Creager and Jordan, 1984; Grand, 1994; van der Hilst, 1997; Zhao, 2001; Montelli, 2004), geochemical arguments based on chemical and isotopic differences between mid-ocean-ridge basalts (MORB) and ocean island basalts (OIB; *e.g.*, Morgan, 1971; Schilling, 1973; Hofmann and Hart, 1978; Langmuir and Hanson, 1980; Sun, 1980), rare gas systematics (Kurz *et al.,* 1982; O'Nions and Oxburgh, 1983, Allègre *et al.,* 1983, 1996), isotope variations between continental and oceanic crust (*e.g.*, DePaolo and Wasserburg, 1976; O'Nions *et al.,* 1979), and the Earth's radiogenic heat budget (Albarède and van der Hilst, 2002; van Keken *et al.,* 2002 and references cited therein) require a layered mantle structure consisting of at least two independent reservoirs: a depleted upper mantle and a chemically enriched lower mantle and/or D″ layer at the core-mantle boundary. Potassium (K) plays a pivotal role in geochemical models of mantle structure, as the rate of radiogenic heat production and budget of ^{40}Ar in the modern mantle and MORB source region are contingent on the abundance and distribution of K in the silicate Earth.

Although the budgets of thorium (Th) and uranium (U) in the planet are well-established, estimates of the abundance of K in the silicate Earth are disparate and range from 130 to 280 μg/g (Wasserburg *et al.,* 1964; Jochum *et al.,* 1983; Allègre *et al.,* 1987; Hofmann, 1988; McDonough *et al.,* 1992; McDonough and Sun, 1995; Albarède, 1998; Davies, 1999; Lassiter, 2004). In addition to modeling the dominant mode of convection in the mantle, constraining the quantity of K in the silicate Earth also provides insight into: the size of the of the OIB source region, the role of K during the thermal evolution of the Earth, the degree of volatile element depletion of the Earth, and the abundance of Pb in the core.

Because potassium is a moderately volatile element during accretion, determining the K content of the silicate Earth has traditionally hinged on establishing the relatively constant K/U ratio of continental crustal rocks and MORB. Based on the chemistry of a particular type of ocean island basalt (*i.e.*, HIMU-type) and the potential effects of eclogite in the mantle, Lassiter (2004) estimated the K/U ratio of the silicate Earth to be on the order of 7000 to 9000. This result, though consistent with several models of mantle degassing which suggest a silicate Earth K/U ratio on the order of 6000 – 7000 (Albarède, 1998; Davies, 1999), is significantly lower than traditional studies of terrestrial rocks (K/U ≥ 10,000; *e.g.*, Wasserburg *et al.,* 1964; Jochum *et al.,* 1983). Consequently, the terrestrial K/U ratio, and thus the abundance of K in the silicate Earth, remains a contentious issue.

In order to confidently establish the K/U ratio of the modern mantle, as well as critically test the constancy of this value among different mantle source regions, we have analyzed a comprehensive set of MORB from around the globe, including

both enriched and depleted samples from the Atlantic, Indian and Pacific oceans. We have also compiled literature data from the Max-Planck-Institut GEOROC database (http://georoc.mpch-mainz.gwdg.de/georoc/; see Appendices D – G) in order to more confidently estimate the K/U ratio of the OIB source region and bulk continental crust, as derivatives from these reservoirs generally have enough K (*i.e.*, $K_2O > 1$ wt%) to be confidently measured via common methods of major element analysis (*e.g.*, electron probe microanalysis, EPMA, or instrumental neutron activation analysis, INAA).

5.3 The K/U ratio of the DMM

Mid-ocean ridge basalts (MORB), which represent melt products of a mantle that has undergone a major depletion event (*i.e.*, crustal extraction), are typically depleted in incompatible elements ($D_i^{sol/liq} < 1$, where D is approximated by the concentration ratio of element *i* in the solid to the liquid). Thus, trace element determinations in MORB commonly require higher-precision analytical methods than OIB and crustal analyses. Here, we report the K/U ratio of a collection of "normal-type" MORB (N-MORB; La/Sm < 1.00) and "enriched-type" MORB (E-MORB; La/Sm ≥ 1.00), as well as a limited suite of back-arc basin basalts (BABB) and several ocean island basalts (OIB). Concentration measurements were determined by high-precision laser ablation (LA-) ICP-MS; U measurements were made in low-resolution detection mode ($m/\Delta m = 300$) following the protocol of Arevalo and McDonough (2008), but K measurements required medium-resolution detection ($m/\Delta m = 4000$) in order to discriminate the ^{39}K peak from isobaric interferences, namely $^{23}Na^{16}O$, ^{38}ArH and the

tail-end of ^{40}Ar. The typical uncertainty on our measurements was ≤3% ($2\sigma_m$, external reproducibility of 2-4 individual measurements). A subset of samples that were previously analyzed via isotope dilution mass spectrometry coincides within 1% of our laser ablation data (Fig. 5.1), thus validating the accuracy of our in-situ measurements; details regarding the method, calibration and accuracy of our K measurements are reviewed in more detail in Section 2.3.

A test as to the relative incompatibility of U versus K is illustrated in the log-log co-variation diagram shown in Fig. 5.2, where it is demonstrated that U behaves analogously to K in our spectrum of N-MORB (slope = 1.00 ± 0.10, 95% confidence), but Nb and La behave more and less incompatibly than K, respectively. Accordingly, K and U exhibit equally incompatible behavior during partial melting of upper mantle peridotite, and thus the K/U ratio of a mantle melt may provide a reliable proxy to the K/U ratio of the mantle source (*e.g.*, Hofmann, 1986; Newsom *et al.,* 1986). Accordingly, variations in the average K/U ratio of melts from different mantle reservoirs likely indicate distinct source compositions.

Because MORB are the products of passive upwelling, the MORB source represents the ambient upper mantle. As seen in Table 5.1 and Fig. 5.3, MORB can be divided into two distinct populations: N-MORB are characterized by a normal Gaussian distribution (skew = 0.0) with a mean K/U ratio of 20,000 ± 2300 (2σ), significantly higher than the N-MORB dataset reported by Jochum *et al.,* (1983; K/U = 12,700 ± 400, $2\sigma_m$), whereas E-MORB have an average K/U value of 15,700 ± 3100 (2σ) and a skewed Gaussian distribution (skew = 0.5). As a result, our N-MORB and E-MORB data define two statistically distinct populations at the 99.9%

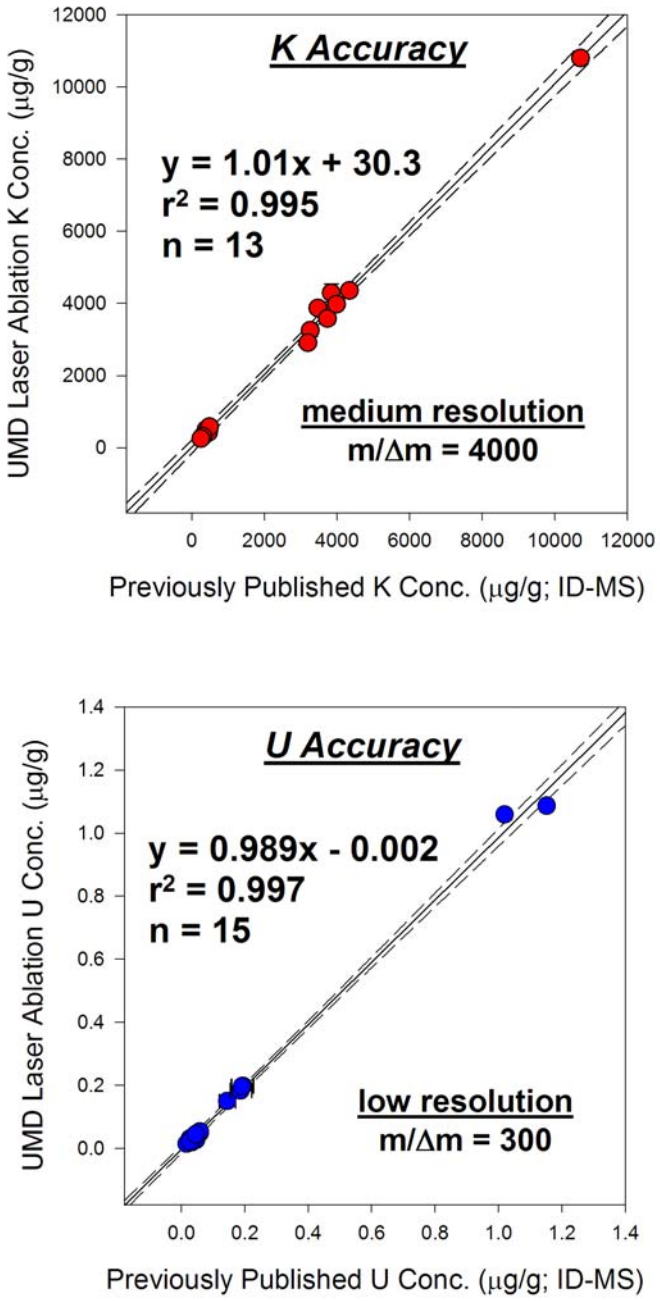

Fig. 5.1. Comparison of K and U concentration measurements of a subset of samples analyzed by both high-precision LA-ICP-MS (this study) and isotope dilution (various published works). Previously published data include: isotope dilution measurements of natural basaltic glasses from Loock *et al.*, (1990) and White (1993), and synthetic basaltic standards from Raczek *et al.*, (2001) and Jochum *et al.*, (2006). In this study, U measurements were made using low-resolution detection (m/Δm = 300) and external calibration techniques following

the protocol of Arevalo Jr. and McDonough (2008), whereas K measurements were made using medium resolution detection parameters ($m/\Delta m = 4000$) in order to discriminate the isobaric interferences from ^{38}ArH, $^{23}Na^{16}O$ and the tail of ^{40}Ar, and internal calibration with BIR-1G. For both K and U, typical uncertainties for our measurements are ≤3% (2σ), which are shown as error bars but are generally smaller than the size of the data points above. The dashed lines represent the 95% confidence limits of the data trends.

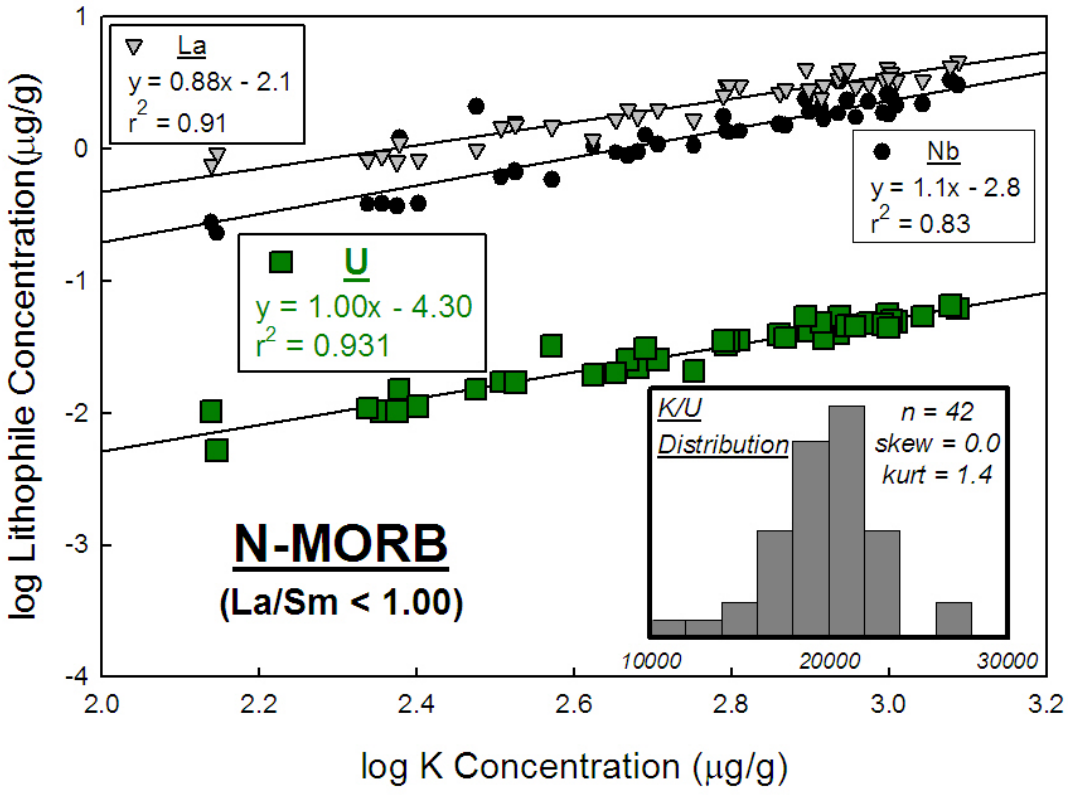

Fig. 5.2. Log-log co-variation diagram plotting the concentrations of Nb, La and U versus K (in µg/g) in "normal-type" MORB (N-MORB; La/Sm < 1.00). As the samples plotted here originate from the same source (upper mantle peridotite), this type of diagram reveals information regarding the effect of partial melting on the partitioning of K and U in mantle melts. A linear regression with a slope of 1.00 represents a perfectly constant element ratio. A slope of <1.00 indicates a more incompatible element along the abscissa, and vice-versa. Whereas Nb and La are shown to be more and less incompatible than K, respectively, U behaves analogously to K during mantle melting (slope = 1.00 ± 0.10, 95% confidence). Moreover, U shows a greater correlation with K (r^2 = 0.931) than either Nb (r^2 = 0.83) or La (r^2 = 0.91). A statistical evaluation of the K/U ratios of the N-MORB samples examined above reveal a normal Gaussian distribution with negligible skewness.

confidence-level. The E-MORB source, however, provides only a fractional contribution to the composite MORB source, or depleted MORB mantle (DMM); while segments of the East Pacific Rise have been documented to produce up to 10% E-MORB (Langmuir *et al.,* 1986), Donnelly *et al.,* (2004) suggest the E-MORB source comprises ≤3% (by mass) of the DMM based on a two-stage E-MORB generation model and the approximate frequency of E-MORB at the Mid-Atlantic Ridge south of the Kane Fracture Zone (the MARK area). Here we consider a 5% mass contribution of the E-MORB source and a 6x enrichment relative to the N-MORB source, as determined by the log-normal mean U concentration of each reservoir according to our data (following the protocol of Ahrens, 1954); this results in a DMM K/U ratio of 19,000 ± 2600 (2σ). Interestingly, this high K/U value is corroborated by MORB data from the Lamont-Doherty PetDB database, which suggest a DMM K/U ratio of >17,000 after low-precision measurements (*e.g.*, via EPMA and INAA methods) have been filtered out (data available for download from author or doi:10.1016/j.epsl.2008.12.023). It should also be noted that small-degree partial melts (as low as 1%) cannot reproduce the low K/U ratios and high K concentrations seen in the most enriched E-MORB, even if K is modeled as 5x more compatible than U during upper mantle melting.

Additional insight into the representative K/U ratio of the DMM is provided by oceanic flood basalts, which generate as much as >1.5 km^3 of basalt per year (Richards *et al.,* 1989) and have been suggested to represent plume heads that have entrained a significant fraction of ambient mantle on their journey to the surface (*e.g.*, Griffiths and Campbell, 1990). A compilation of published data from the GEOROC

database (http://georoc.mpch-mainz.gwdg.de/georoc/) illustrates a wide range in oceanic flood basalt compositions, but with an average K/U ratio of 19,500 ± 5100 ($2\sigma_m$; Fig. 5.4a), a value consistent with the high K/U ratio of the DMM as determined here.

Table 5.1. Representative K/U values of silicate Earth provenances.

Provenance	Avg. K/U[a]	±2σ[b]
Depleted MORB Mantle (DMM)	***19,000***	***2600***
Normal-type MORB[c] (n = 42)	20,000	2300
Enriched-type MORB[c] (n = 33)	15,700	3100
Back-arc basin basalts[c] (n = 12)	21,700	2000
Oceanic flood basalts	19,500	5100
Deep-source OIB (>1900 km depth)[d]	***11,900***	***2200***
Shallow-source OIB (<1900 km)[d]	12,100	2200
All OIB weighted by mass flux[e]	11,600	2000
Hawaii	13,300	400
Iceland	12,600	800
Continental Crust	***13,000***	***3000***
Rudnick and Gao (2003)	12,400	4900
Global andesites	13,900	500
Continental arcs	13,000	1000
Continental flood basalts	12,600	1400
BULK SILICATE EARTH[f]	***13,800***	***2600***

[a] Data can be accessed in Appendices B – G.
[b] $2\sigma_m$ reported for compiled GEOROC data.
[c] Original data reported in this study.
[d] Depth of origin from Montelli et al. (2004).
[e] Flux data from Sleep (1990).
[f] DMM-OIB source interface modeled at ~1900 km depth.

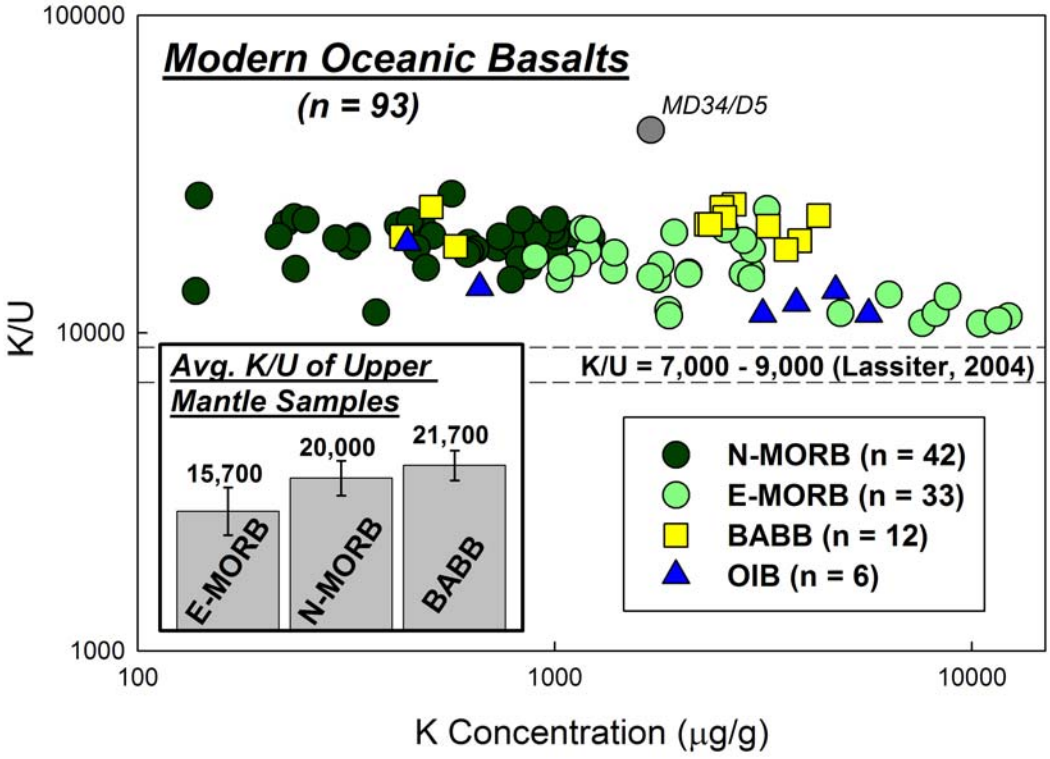

Fig. 5.3. K/U ratios of modern oceanic basalts examined here versus K concentration (in μg/g). Relative to a silicate Earth K/U ratio of 7,000 – 9,000, as preferred by Lassiter (2004), all of our oceanic basalts plot at higher K/U values. Amongst the mantle reservoirs examined here, back-arc basin basalts (BABB) have the highest average K/U ratio, whereas ocean island basalts (OIB) show the lowest values, though both sample sets are relatively small. Mid-ocean ridge basalts can be separated into two statistically distinct (at 99.9% confidence) populations; depleted N-MORB have an average K/U ratio of 20,000 ± 2300 (2σ), while "enriched-type" samples (E-MORB; La/Sm ≥ 1.00) display an average K/U ratio of 15,700 ± 3100 (2σ). The varying K/U ratios seen between different mantle reservoirs represent source differences rather than effects from partial melting, as K and U exhibit equally incompatible behavior during upper mantle melting (see Fig. 5.2). The anomalous MD34/D5 sample (K/U > 40,000) was not included in the calculations in this study.

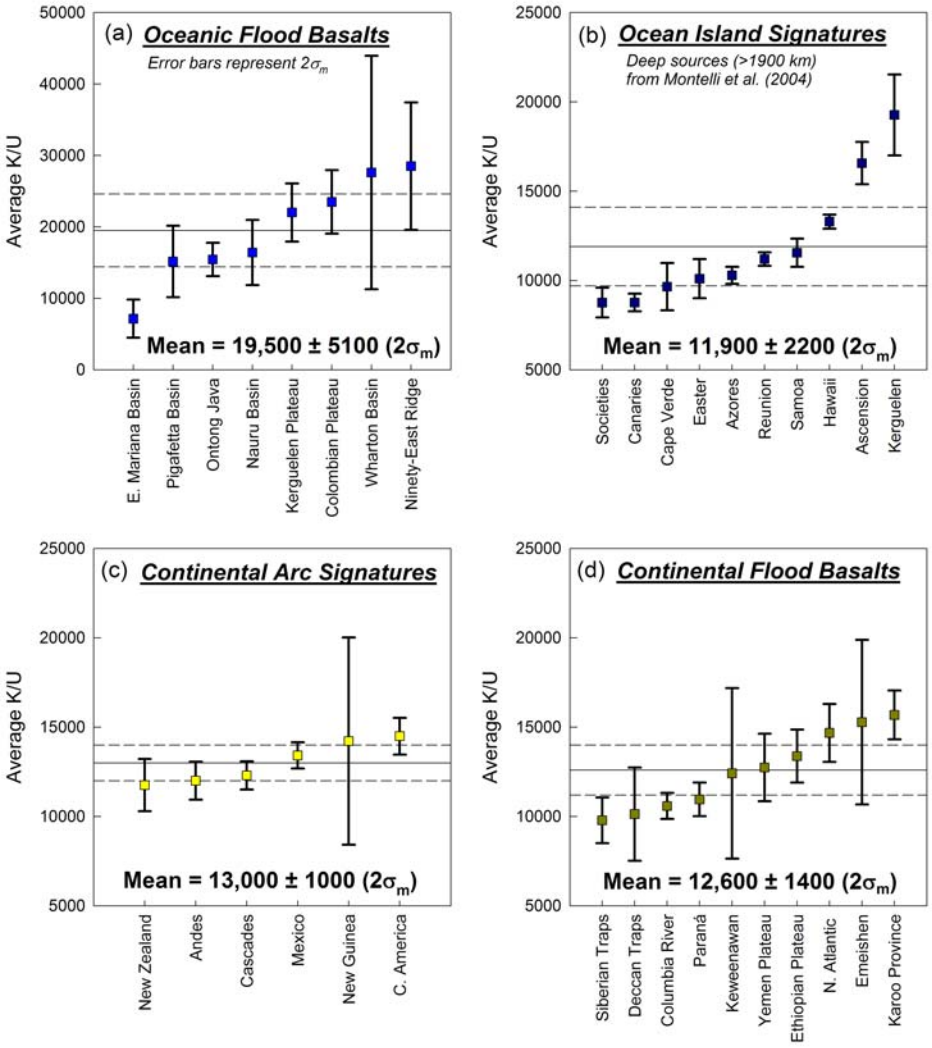

Fig. 5.4. Literature data for global oceanic and continental flood basalts, ocean island volcanics and continental arc rocks compiled from the GEOROC database (http://georoc.mpch-mainz.gwdg.de/georoc/). Sample data were filtered for major element totals >98.0 wt% and MgO contents between 4.0-16.0 wt%. The reported mean of the OIB source represents the average K/U ratio of ocean islands with evidence for a deep origin (>1900 km; Montelli *et al.,* 2004); this value is statistically indistinguishable from the average of OIB with shallower origins (K/U ≈ 12,100) as well as the average of all ocean islands weighted according to mass flux (K/U ≈ 11,600; flux data from Sleep, 1990). The compiled data files from GEOROC are available for download from the author or doi:10.1016/j.epsl.2008.12.023.

5.4 The K/U ratio of the OIB source region

Given the abundances of K, Th and U in the continental crust (models reviewed by Rudnick and Gao, 2003), >⅓ of the mantle was depleted by the extraction of the crust, and thus the DMM must extend below the 660 km discontinuity assuming a two-box model of mantle structure. However, the DMM and continental crust are not perfectly complimentary (*e.g.*, Sun and McDonough, 1989), and thus another distinct reservoir must exist somewhere in the mantle. Ocean island volcanics, which are generally characterized by super-primitive U/Pb, Th/Pb and U/Th and sub-primitive Rb/Sr and Nd/Sm ratios (*e.g.*, Zindler and Hart, 1986), and observed abundances of incompatible elements that are too enriched to be accounted for by conventional melting of a primitive source without requiring unrealistically small degrees of partial melting (*e.g.*, Hofmann and White, 1982), likely represent an enriched mantle source in the deep mantle. However, the exact depth of the compositional transition from the depleted upper mantle to the enriched lower mantle has not been well-constrained. Tomographic images of the mantle show that not all slabs that sink across the 660 km discontinuity reach the core-mantle boundary; many downwellings lose their characteristic planar geometry across a transitional interval from 1800-2300 km depth (*e.g.*, van der Hilst *et al.,* 1997). Additionally, seismological observations reveal compositional heterogeneities in the bottom 1000 km of the mantle (*e.g.*, van der Hilst and Karáson, 1999; Garnero, 2000; Trampert *et al.,* 2004), potentially suggesting a chemical stratification at deeper depths. Here, we model a variety of potential interface depths, each with specific implications as to the enrichment of the lower mantle and the bulk modern mantle K/U value.

Some intraplate ocean islands are thought to derive from the tails of deep-rooted mantle plumes (*e.g.*, Morgan, 1971), and studies of mantle tomography have revealed that a number of ocean island hotspots can be traced to the lowermost depths of the mantle (*e.g.*, Zhao, 2001; Montelli *et al.,* 2004); therefore, at least some OIB likely characterize the chemistry of the lower mantle. Compared to MORB, which typically have ≤ 0.5 wt% K_2O, OIB can have up to 5.0 wt% K_2O and thus can be readily measured via EPMA, INAA and/or other modes of traditional major element analyses. Although our sample set is small (n = 6), our laser ablation data suggest that ocean islands may be characterized by the lowest average K/U of the major mantle source regions.

The Hawaiian plume, which transfers a higher mass flux than any other ocean island hotspot (Sleep, 1990), has been demonstrated to originate in the deep portion of the mantle (*e.g.*, Russell *et al.,* 1998; Zhao, 2001; Montelli *et al.,* 2004), and thus provides a window into the lower mantle. A survey of the GEOROC database reveals that Hawaiian picrites and tholeiitic basalts are defined by an average K/U value of ~13,300. However, if we consider other ocean islands that are interpreted to have deep-mantle origins (>1900 km depth; Montelli *et al.,* 2004) in addition to Hawaii, the OIB source is approximated by a mean K/U ratio of 11,900 ± 2200 ($2\sigma_m$; Fig. 5.4b); it should be noted that this K/U value is statistically indistinguishable from the average K/U ratio of OIB without evidence for deep-rooted sources (K/U ≈ 12,100) as well as the average of *all* ocean islands weighted according to mass flux (K/U ≈ 11,600; flux data from Sleep, 1990), as shown in Table 5.1 (data available in Appendix B).

The ocean islands examined here show a significant spread in K/U values across relatively narrow ranges in $^{206}Pb/^{204}Pb$ (Fig. 5.5). These sub-parallel trends imply a diversity in K/U ratios (spanning a factor of 2-3) that is independent of radiogenic Pb and melt fraction, and thus likely not a coupled long-term source feature as argued by Lassiter (2004). Lassiter (2004) also asserts that eclogitic material in the mantle could significantly lower the K/U ratio of both the OIB source and silicate Earth. However, as suggested by primitive olivine compositions in Hawaiian lavas (Sobolev *et al.,* 2005, 2007), the Hawaiian source region may contain as much as 20-30% recycled ocean crust (present as eclogite), yet still exhibits an average K/U ratio >13,000. The Iceland source (K/U = 12,600, not shown in Fig. 5.4) and DMM (K/U = 19,000) also show evidence for an eclogitic component (Sobolev *et al.,* 2007), though both fail to produce low K/U ratios. Therefore, recycled eclogite in OIB sources does not appear to be responsible for low K/U values, and thus it is unlikely that the K/U ratio of the modern mantle, and therefore the K/U ratio of the silicate Earth, is significantly lowered by the role of eclogitic material.

5.5 The K/U ratio of the modern mantle

In order to establish the K/U ratio of the modern mantle, we need to consider the mass fraction of K and U in, and the relative sizes of, both the MORB and OIB source regions. In a comprehensive examination of global MORB ridge segments, Su (2002) established that typical MORB, located away from known hotspots, contain 1000 ± 100 ($2\sigma_m$) μg/g K; assuming average MORB represent 8-12% partial melting

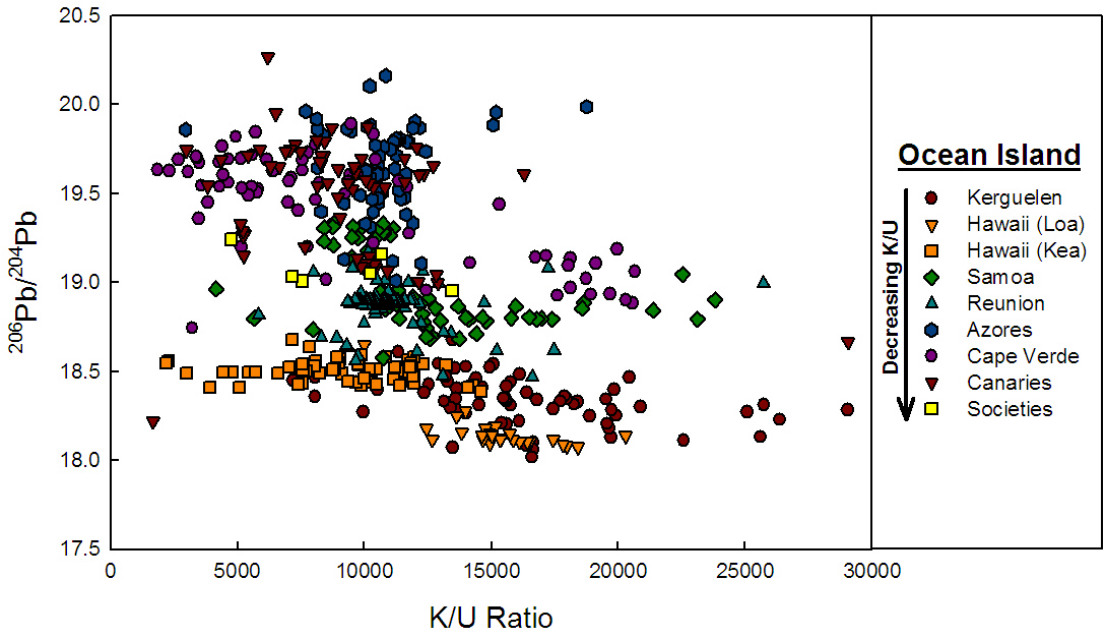

Fig. 5.5. $^{206}Pb/^{204}Pb$ versus K/U ratios in ocean island basalts with evidence for deep-rooted sources (Montelli *et al.*, 2004). Different volcanic centers appear to show sub-parallel, linear trends with large ranges in K/U (up to a factor of 2-3) over a relatively small range in $^{206}Pb/^{204}Pb$. This apparent decoupling between radiogenic Pb and K/U signatures suggests that a different process is responsible for the variable K/U values seen in OIB, as opposed to representing long-term source features or the effects of variable degrees of partial melting.

(*e.g.*, Hofmann, 1988) and a nominal K partition coefficient similar to that of U ($D_U^{sol/liq}$ = 0.001-0.0001; www.germ.com), the mean MORB source is predicted to have a composition with 100 ± 10 μg/g K. Thus, based on the K/U ratio of the DMM, defined here as 19,000 ± 2600 (2σ), the DMM has 5.4 ± 1.4 ng/g U, representing a ~4x depletion relative to the silicate Earth (20.3 ng/g U; McDonough and Sun, 1995). This MORB source composition is consistent with independent estimates of U in the DMM (Sun and McDonough, 1989) as well as chondritic and non-chondritic DMM models based on parent-daughter ratios of radiogenic isotopes (*e.g.*, Salters and Stracke, 2004; Boyet and Carlson, 2006).

Assuming the DMM represents the ambient upper mantle and deep-rooted mantle plumes represent a lower mantle reservoir, we can model the size of the lower mantle and the K/U ratio of the bulk modern mantle as a function of the enrichment of the OIB source region (Fig. 5.6). Modeling ~40 ng/g U in the OIB source (or 2x the concentration of the silicate Earth), as suggested by the maximum enrichment of U observed in our Hawaiian tholeiites and following 5-15% partial melting for Hawaiian lavas as suggested by picritic trace element signatures (Norman and Garcia, 1999) and tholeiite Th-U disequilibria (Sims *et al.,* 1999), the modern mantle is defined by a K/U ratio of 14,200 ± 2400 (2σ). Given this model composition, the OIB source must constitute ~20% of the mantle, which is in accord with the mass balance calculations of Workman and Hart (2005). Additionally, if the chemical distinction between the OIB and MORB source regions is preserved by a thermochemical boundary layer, the depth of this interface would need to have an average depth of ~1900 km, assuming an incompressible mantle. This proposed boundary, which

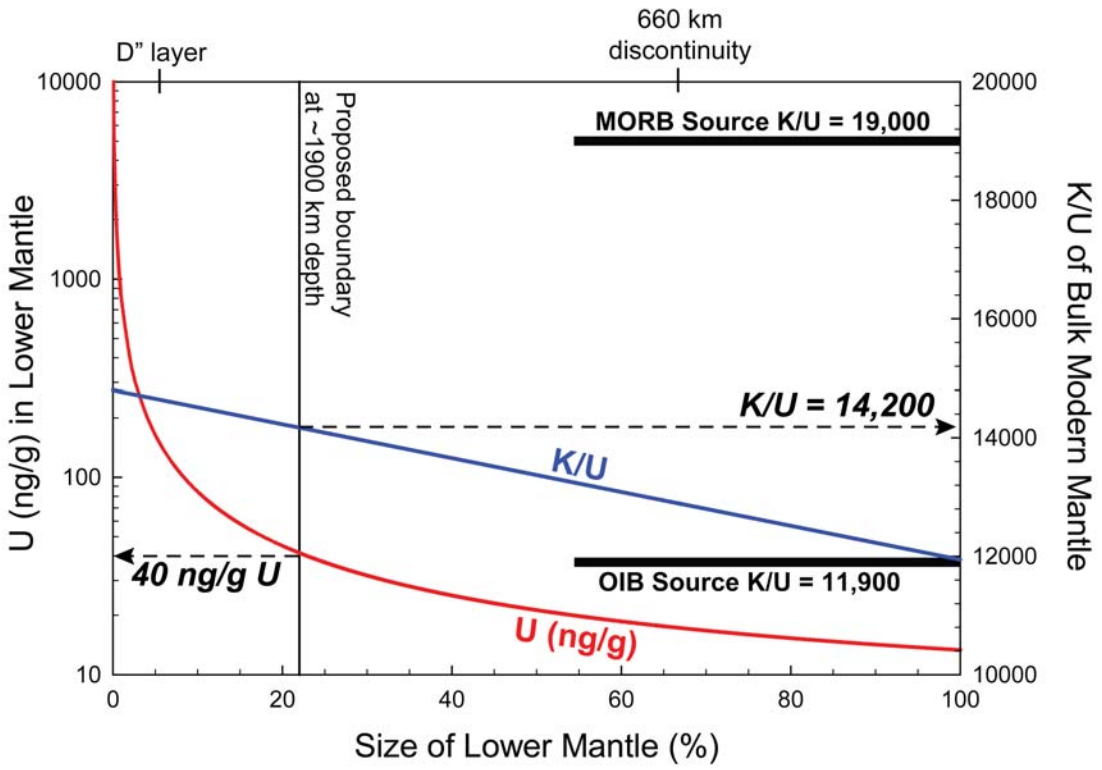

Fig. 5.6. Size of the lower mantle and K/U ratio of the bulk modern mantle modeled as a function of the enrichment of the lower mantle, as sampled by OIB. Assuming a composition with 40 ng/g U, as suggested by Hawaiian volcanics (see text), the lower mantle must constitute ~20% of the bulk modern mantle, resulting in a bulk mantle K/U ratio of 14,200 ± 2400 (2σ) and implicating a potential chemical layering at an average depth of ~1900 km in an incompressible mantle. Considering only a 300 km thick D″ layer, this reservoir would need to contain ≥160 ng/g U (≥8x the silicate Earth), which would be difficult to maintain convectively isolated due to radiogenic heat. Figure modified from Lassiter (2004).

provides support for the mid-mantle stratification proposed by Kellogg *et al.,* (1999), may correlate with the loss of resolution of downwelling material in tomographic studies (*e.g.*, van der Hilst *et al.,* 1997) as well as the identification of chemical heterogeneities in the lowermost 1000 km of the mantle (*e.g.*, van der Hilst and Karáson, 1999; Garnero, 2000; Trampert *et al.,* 2004). Alternatively, a less enriched OIB source region would necessitate a shallower chemical layering and a lower modern mantle K/U ratio, and a more enriched OIB source would require a deeper layering and higher mantle K/U.

We may further consider the effect of a chemically heterogeneous 200-300 km thick D″ layer at the core-mantle boundary, which has been suggested by seismological (*e.g.*, Lay *et al.,* 1998; Wen *et al.,* 2001), experimental (Murakami *et al.,* 2004), and geochemical observations (Boyet and Carlson, 2005, 2006; Tolstikhin and Hofmann, 2005). A 300 km thick enriched reservoir at the base of the mantle would indicate a modern mantle K/U value >14,700 and need to contain ≥160 ng/g U (or ≥8x the silicate Earth). However, such an enriched reservoir would be thermally unstable and difficult to isolate for several Ga, and the limited size of this reservoir likely could not serve as the source for deep-rooted OIB.

5.6 The K/U ratio of the continental crust and silicate Earth

Although the modern mantle comprises >99% of the silicate Earth by mass, ~35% of the highly incompatible element budget (*e.g.*, K, Th and U) of the silicate Earth resides in the continental crust (Rudnick and Gao, 2003). The composition of the bulk continental crust, though, is a significant variable; as an example, geochemical

estimates of K_2O in the crust vary by a factor >2 (Rudnick, 1995 and references cited therein). A comprehensive examination of the bulk continental crust by Rudnick and Gao (2003) suggests a mean crustal K/U ratio of ~12,400, but with an associated uncertainty of >40% (2σ). We attempt here to evaluate the bulk crustal K/U value by considering the role of continental arc rocks, global andesites and continental flood basalts.

Convergent margin tectonism has been linked to the formation of the continental crust through the recycling of crust back into the mantle and the production of arc magmatism. Trace element patterns of typical arc rocks, particularly continental arc lavas, are similar to those of continental crustal rocks (*e.g.*, high La/Nb and low Ce/Pb relative to the silicate Earth; Rudnick, 1995). Island arc basalts are typically characterized by high K/U ratios (Lassiter, 2004), comparable to our back-arc basin dataset (K/U ≈ 21,700; Table 5.1), and thus likely record an upper mantle signature. Continental arc rocks, on the other hand, are more commonly andesitic in composition, analogous to the composition of average continental crust (Rudnick, 1995). Published data for a number of continental arcs from the GEOROC database show a narrow variation with an average K/U ratio of 13,000 ± 1000 ($2\sigma_m$; Fig. 5.4c). This value is also broadly consistent with global andesitic lavas, which have a mean K/U value of ~13,900 (n > 1400; data available in from the author or doi:10.1016/j.epsl.2008.12.023).

Continental flood basalts may also provide a guide to the representative K/U ratio of the continental crust, as these massive lava flows travel through thick sequences of incompatible element-rich crust before they erupt at the surface,

resulting in chemical and isotopic overprinting by the continental crust (Carlson, 1984; McDonough, 1990). A compilation of flood basalt data from the most prominent large igneous provinces around the globe indicates that continental flood basalts have an average K/U ratio of 12,600 ± 1400 ($2\sigma_{m;}$ Fig. 5.4d).

Considering the crustal model of Rudnick and Gao (2003), as well as the average K/U ratio of continental arcs, global andesites and continental flood basalts, we propose a K/U value for the bulk continental crust of 13,000 ± 3000 (2σ; Table 5.1). As might be expected, the average K/U ratio of the continental crust is in between those of the enriched OIB and depleted MORB sources, indicating the complementary relationship of these three reservoirs and the bulk silicate Earth.

Taking into account the fractional contributions and K/U signatures of the modern mantle (modeled to included the DMM and OIB source regions stratified at an average depth of ~1900 km) and continental crust, as illustrated in Fig. 5.7, the silicate Earth is hereby defined by a K/U ratio of 13,800 ± 2600 (2σ), consistent with the original estimate of Jochum *et al.,* (1983; K/U ≈ 12,700), though for different reasons. All of the above observations are at odds with arguments for a lower K/U ratio in the silicate Earth, as advocated by Lassiter (2004) on the basis of eclogite in the mantle, as well as the degassing models of Albarède (1998) and Davies (1999). Further, a high K/U ratio for the silicate Earth: i) implies a greater role for K during the thermal evolution of the Earth, ii) exacerbates the need for a lower mantle reservoir enriched in radioactive elements and ^{40}Ar, and iii) suggests a less severe volatile element depletion in the bulk Earth, implying a significant fraction of Pb in the core.

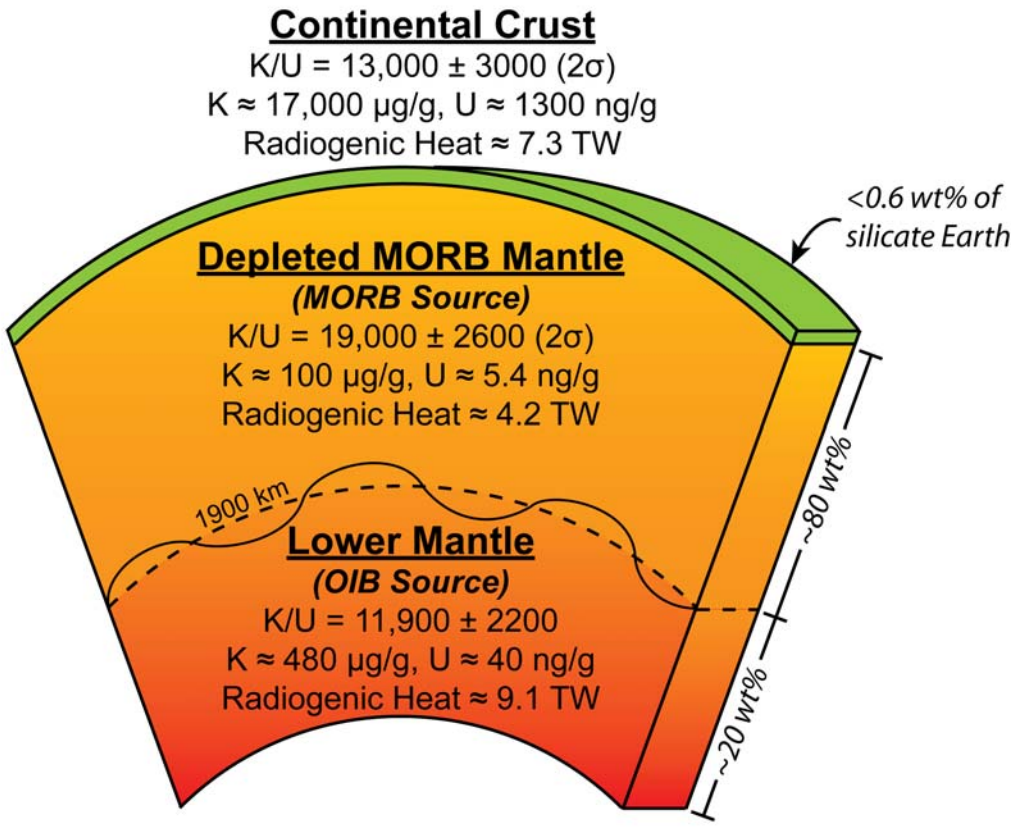

Fig. 5.7. Composition of and radiogenic heat flow from the continental crust, DMM and OIB source. The estimates of K and U in the continental crust do not take into account the role of the continental lithosphere, though its contribution is considered negligible. The continental crust is assumed to have 5.6 µg/g Th, following the model of Rudnick and Gao (2003), and the DMM 16 ng/g Th, following a mantle Th/U ratio of 3.0.

5.7 Discussion

5.7.1 Radiogenic heat and Earth's heat flux

The heat flow from the Earth's interior, which serves to drive mantle convection and global plate tectonics, derives primarily from two major components: energy from planetary accretion and differentiation (*e.g.*, gravitational collapse, core formation, inner core crystallization, and secular cooling), as well as radiogenic heat from the decay of long-lived radionuclides, namely ^{40}K, ^{232}Th and ^{235,238}U. Although primordial energy from secular cooling contributes a significant portion of the planet's current global heat loss, geochemical and geophysical models underline the role of radioactive isotopes in powering mantle convection, particularly early in the Earth's history when radiogenic heat generated more than 5x the energy than produced today (Fig. 5.8).

The Urey ratio (Ur), which serves to relate the radiogenic heat production within a body to its total heat output, can be defined in two distinct ways: geochemical studies often refer to a bulk Earth Ur, defined as the ratio of the planet's radiogenic heat production to total surface heat loss, whereas geophysical models focus on a convective Ur, or the ratio of radiogenic heat generation in the modern mantle to the total mantle heat flux (*e.g.*, Korenaga, 2008). The convective Ur can provide information regarding the thermal evolution of the planet and the driving forces behind a variety of global dynamic processes, including mantle convection, plate tectonics, secular cooling, the geodynamo, and inner core crystallization.

The value of the bulk Earth Urey ratio inherently depends on the terrestrial abundances of the long-lived radioactive isotopes of K, Th and U. Because the half-

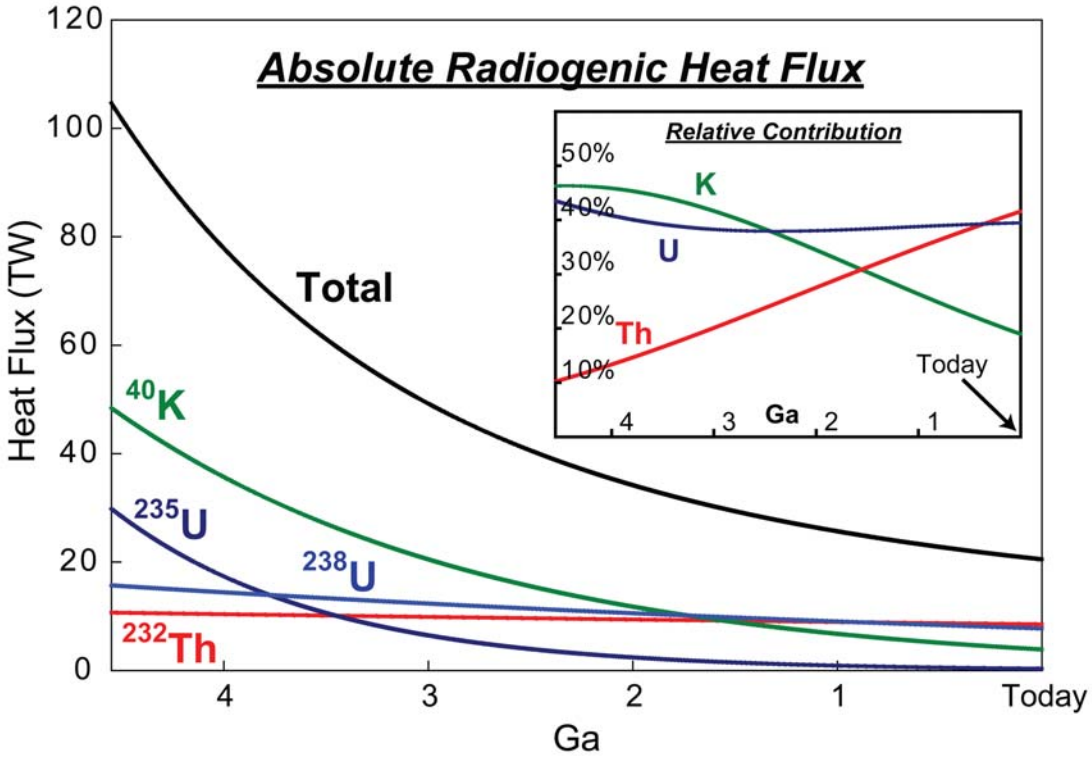

Fig. 5.8. Earth's radiogenic heat production from the decay of long-lived radionuclides through time. Prior to 2.5 Ga, K acted as the dominant radiogenic heat source within the planet. The exponential increase in radiogenic heat in the geologic past likely resulted in a higher convective Urey number in the ancient mantle.

life of ^{40}K ($t_{1/2}$ ~ 1.25 Gyr) is short relative to the age of the planet, the abundance of K in the silicate Earth is not only vital to the understanding of radiogenic heat production today, but even more so to evaluating the radiogenic heat budget of the early Earth, as more than 12 times more ^{40}K was extant ca. 4.5 Ga than today (Fig. 5.8). A silicate Earth composition with 20 ± 8 (2σ) ng/g U, which is consistent with both geochemical models (*e.g.*, McDonough and Sun, 1995) and measured geoneutrino fluxes (Araki *et al.,* 2005), implies 280 ± 120 (2σ) μg/g K in the silicate Earth, following a K/U value of 13,800 ± 2600 (2σ). Considering the silicate Earth also has 80 ± 25 (2σ) ng/g Th (McDonough and Sun, 1995) and assuming negligible K, Th or U in the core (*e.g.*, Chabot and Drake, 1999; Wheeler *et al.,* 2006; Corgne *et al.,* 2007), the Earth currently emits 21 ± 4 (2σ) TW of radiogenic heat. Relative to the Earth's total surface heat loss of 46 ± 6 TW (Jaupart *et al.,* 2007 and references therein), this represents a bulk Earth Ur of ~0.45.

More relevant to geophysical models is the convective Urey ratio, an essential variable for parameterized models of mantle convection that also provides a strong case for a stratified mantle structure. Subtracting the 7.3 ± 2.3 (2σ) TW of radiogenic heat produced within the continents today (Rudnick and Gao, 2003, with a crustal K/U = 13,000 ± 3000) from the total surface heat flow, we arrive at ~39 TW of heat currently being emitted by the modern mantle, with ~13 TW due to radiogenic heat. A DMM composition with 100 μg/g K, 5.4 ng/g U and ~16 ng/g Th (assuming a MORB Th/U ratio of 3.0), however, could only produce some ~5 TW of radiogenic heat assuming whole-mantle convection, leaving ~8 TW of radiogenic heat unaccounted for and suggesting a convective Ur of <0.15. Taking into account the

potential for a layered mantle structure with an enriched lower mantle reservoir, such as the source region of OIB, the budget of radioactive elements in the modern mantle can be reconciled to produce 13 TW of radiogenic heat, which is indicative of a more realistic convective Ur of 0.34, a value which is significantly lower than that preferred by parameterized convection models (Ur ≥ 0.65; *e.g.*, Davies *et al.,* 1980; Schubert *et al.,* 1980; Turcotte *et al.,* 2001; Schubert *et al.,* 2001), but consistent with the findings of Jaupart *et al.,* (2007) and Korenaga (2008), and suggestive of a current mantle cooling rate on the order of ~170 $KGyr^{-1}$ (assuming a constant mantle heat capacity of 1.2 $Jg^{-1}K^{-1}$). If we also consider the potential for 5-15 TW of heat flow across the core-mantle boundary (Lay *et al.,* 2008 and references cited therein), only 10-20 TW of the mantle's heat output represents secular cooling, implying a more probable modern mantle cooling rate somewhere between 70-130 $KGyr^{-1}$; this indicates a hotter ancient mantle than previous estimates based on wet Archean komatiite formation (*e.g.*, Grove and Parman, 2004 and references cited therein), studies of MORB-like Archean greenstones (Abbott *et al.,* 1994) and required conditions for subsolidus mantle convection (Jaupart *et al.,* 2007).

5.7.2 The terrestrial budget of ^{40}Ar and the bulk Earth Pb/U ratio

Noble gas systematics in mantle-derived materials have traditionally been interpreted as robust evidence for a chemically layered mantle. At the forefront of such arguments is the balance of ^{40}Ar in the planet, as originally described by Allègre *et al.,* (1996). Considering a silicate Earth composition with 280 ± 120 (2σ) μg/g K, 155 ± 70 (2σ) Eg (or 10^{18} g) of ^{40}Ar has been produced by the decay of ^{40}K over the past 4.5 Gyr (Fig. 5.9). Turekian (1959) determined that approximately ~66 Eg of

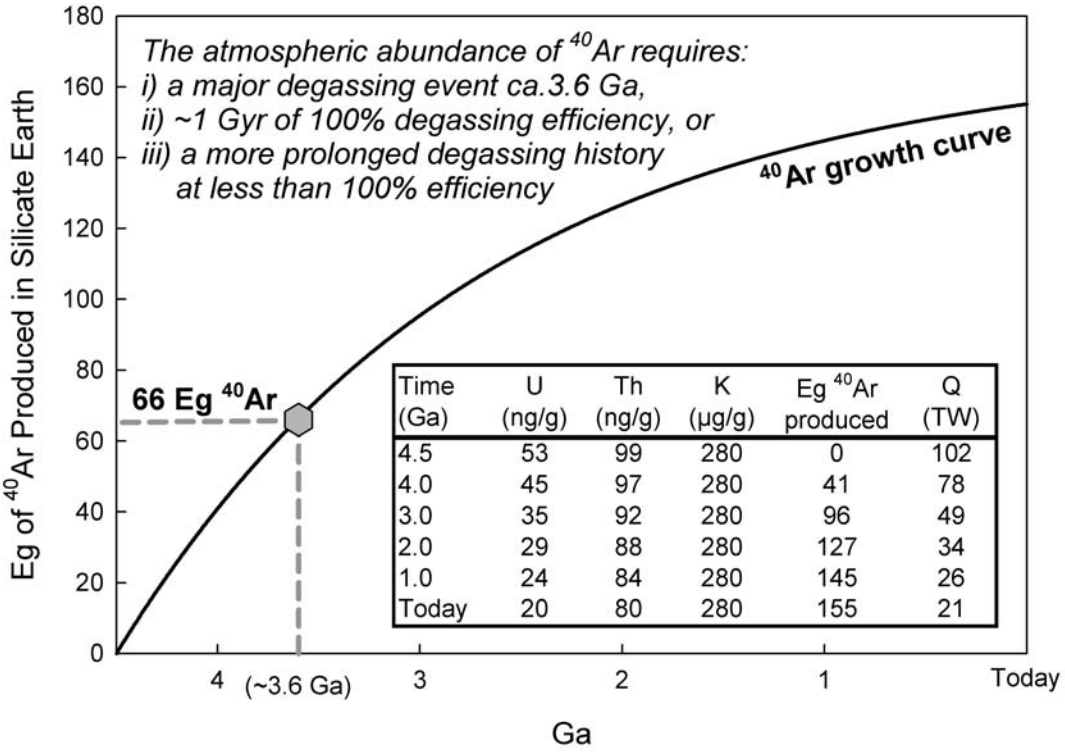

Fig. 5.9. Silicate Earth evolution and production of ^{40}Ar through time, and three different scenarios that could theoretically explain the abundance of ^{40}Ar in the atmosphere. Only the first two scenarios are compatible with recent measurements on the solubility and diffusivity of Ar in upper mantle minerals, which suggest that Ar behaves as a compatible element during modern mantle melting (Watson *et al.*, 2007). The abundance of ^{40}K, which comprises ~0.012% of K today, was more than 12x higher ca. 4.5 Ga, resulting in the higher production rates of ^{40}Ar in the geologic past.

^{40}Ar currently resides in the atmosphere, and an additional ~14 Eg of ^{40}Ar may reside in the continents, assuming no degassing and a bulk continental crustal composition with 1.3 μg/g U (Rudnick and Gao, 2003), a K/U ratio of 13,000 (and thus 17,000 μg/g K, or 2.0 wt% K_2O), and a mean crustal age of ~2.5 Ga. As such, ≥75 Eg of ^{40}Ar may reside in the mantle. However, considering whole-mantle convection with a DMM composition, ≤55 Eg of ^{40}Ar could be produced over 4.5 Ga. Therefore, a chemically enriched layer (*i.e.*, the OIB source) with excess ^{40}Ar likely resides somewhere in the deep mantle, providing further evidence for a stratified mantle structure.

As an additional observation, Pb/U and K/U ratios of carbonaceous chondrites are correlated (Allègre *et al.,* 1995) and suggest that the Pb/U ratio of the bulk Earth is on the order of ~85. Considering a bulk Earth composition with ~14 ng/g U, this ratio indicates ~1200 ng/g Pb in the bulk Earth. According to geochemical models which estimate between 150 and 180 ng/g Pb in the silicate portion of the Earth (*e.g.*, Hofmann, 1988; McDonough and Sun, 1995), the core must contain ≥3300 ng/g Pb, which is 10 times higher than previous estimates (*e.g.*, McDonough, 2003).

5.8 Conclusions

We have analyzed an extensive, global suite of MORB glasses, including both normal- and enriched-type samples, and determined the K/U ratio of the DMM to be 19,000 ± 2600 (2σ), consistent with the average K/U ratio of oceanic flood basalts and back-arc basin basalts. The lower mantle, as represented by deep-rooted OIB, and the continental crust, which is characterized by continental arc rocks, global andesites

and continental flood basalts, have mean K/U ratios of 11,900 ± 2200 and 13,000 ± 3000, respectively. Taking into account the mass fraction of K and U in each of theses reservoirs, the silicate Earth is modeled to have a K/U ratio of 13,800 ± 2600 (2σ).

Assuming a composition with 20 ± 8 (2σ) ng/g U, the silicate Earth has 280 ± 120 μg/g K. As a result: i) the planet's convective Urey ratio is confirmed to be ~0.34, which indicates a present-day mantle cooling rate on the order of 70-130 $KGyr^{-1}$ after taking into account potential heat flux across the core-mantle boundary; ii) the Earth's balance of radiogenic heat and budget of ^{40}Ar require a layered mantle structure; and iii) the Pb/U ratio of the bulk Earth, established here to be ~85, indicates ~1200 ng/g Pb in the bulk Earth and ≥3300 ng/g Pb in the core.

Chapter 6: Chemical variations and regional diversity observed in MORB[1,2]

[1] R. Arevalo Jr. measured the new trace element data reported in this study and compiled trace element data from other sources to augment the new data. Both R. Arevalo Jr. and W.F. McDonough contributed to the interpretation of the comprehensive dataset. The text, tables and figures were written/created by R. Arevalo Jr.

[2] This chapter has been published as:
Arevalo Jr., R., and McDonough, W.F., 2010. Chemical variations and regional diversity observed in MORB. *Chemical Geology* (271), 70-85, doi:10.1016/j.chemgeo.2009.12.013.

6.1 Abstract

An assemblage of MORB analyses (n = 792 samples), including a suite of new, high-precision LA-ICP-MS measurements (n = 79), has been critically compiled in order to provide a window into the chemical composition of these mantle-derived materials and their respective source region(s), commonly referred to as the depleted MORB mantle (DMM). This comprehensive MORB data set, which includes both "normal-type" (N-MORB, defined by $(La/Sm)_N < 1.00$) and "enriched-type" samples (E-MORB, $(La/Sm)_N \geq 1.00$), defines a global MORB composition that is more enriched in incompatible elements than previous models (*e.g.*, Hofmann, 1988; Sun and McDonough, 1989; Su, 2002). A statistical evaluation of the true constancy of "canonical" trace element ratios using this data set reveals that during MORB genesis Ti/Eu, Y/Ho and Ce/Pb remain constant at the 95% confidence-level; thus, the ratios recorded in MORB (Ti/Eu = 7060 ± 1270, 2σ; Y/Ho = 28.4 ± 3.6, 2σ; Ce/Pb = 22.2 ± 9.7, 2σ) may reflect the composition of the DMM, presuming the degree of source heterogeneity, component mixing and conditions of melting/crystallization of the

DMM are adequately recorded by global MORB (Stracke and Bourdon, 2009). Conversely, Ba/Th, Nb/U, Zr/Hf, Nb/Ta, Sr/Nd, and Th/U are shown to fractionate as a function of MORB genesis, and thus these ratios do not faithfully record the composition of the DMM.

Compared to samples from the Pacific and Indian Oceans, MORB derived from Atlantic ridge segments are characterized by statistically significant (≥95% confidence-level) enrichments in both highly incompatible elements (*e.g.*, light REE, TITAN group elements, Sr, Ba, Pb, Th, and U) as well as less incompatible elements (*e.g.*, heavy REE), indicating: i) a prominent recycled source component; ii) variable proportions of pyroxenite in the Atlantic source region; and/or, most likely iii) smaller degrees of melting and/or greater extents of fractional crystallization due to slower ridge spreading rates. Conversely, Pacific MORB have the most depleted regional signatures with regard to highly incompatible elements (*e.g.*, Ba, Pb, Th, and U), likely due to faster ridge spreading rates. Indian Ocean MORB exhibit limited variation in incompatible element enrichments/depletions but are generally the most depleted in more compatible elements (*e.g.*, Ti, Cr, Sc, and heavy REE), potentially due to distinct source characteristics or deep source melting in the garnet field. Atlantic, Pacific and Indian MORB can also be distinguished by trace element ratios, particularly Ce/Pb and Th/U, which is distinct at the >99% confidence-level. Global MORB, and by inference the DMM, are characterized by enrichments in Y/Ho and depletions in Th/U relative to the chondritic ratios, and are complementary to the continental crust. However, the median of global MORB and the bulk continental crust both have sub-chondritic Ti/Eu and Nb/Ta ratios, suggesting an under-

represented Ti- and Nb-rich reservoir in the Earth, potentially refractory, rutile-bearing eclogite at depth in the mantle.

6.2 Introduction

The chemical compositions of the individual components that constitute the silicate Earth (SE), including the largely depleted source of mid-ocean ridge basalts (MORB), the enriched mantle domain(s) frequently observed in ocean island basalts (OIB), and the incompatible element-rich continental crust, are important parameters for models of oceanic and continental crust generation, subduction and crustal recycling, mantle source mixing, intraplate volcanism, island arc processes, and the thermal evolution of the planet. As opposed to major element compositions, which exhibit limited diversity and primarily reflect the source lithology, trace element abundances span orders of magnitude and provide a perspective into mantle processes as well as source compositions because mantle phases incorporate and exclude trace elements with much greater selectivity than major elements. Thus, trace elements hold the key to understanding the evolution of the SE and its major source reservoirs.

The chemical and isotopic compositions of mantle derivatives, such as MORB, OIB and island arc volcanics, reflect the compositions of their respective source regions but also the extent of mixing between different source components, degree of melting and/or fractional crystallization (Stracke and Bourdon, 2009), in addition to the tectonic environment, crustal contamination and potential post-eruptive alteration. Mid-ocean ridge basalts, which are predominantly tholeiitic in composition (*e.g.*, Engel *et al.,* 1965; Melson *et al.,* 1976), provide an ideal case study

of the modern mantle as these melts represent adiabatic upwelling and decompression of the ambient upper mantle (*e.g.*, McKenzie and O'Nions, 1991), and therefore these samples exemplify a relatively simple melting history. Additionally, the average global rate of magma emplacement is between about 26 and 34 $km^3 \cdot yr^{-1}$, of which 75% is generated by mid-ocean ridge volcanism (Crisp, 1984); thus, MORB samples are generally fresh (<1 Ma), abundant and accessible. The MORB source region, or depleted MORB mantle (DMM), is largely depleted in incompatible trace elements ($D_i^{sol/liq} < 1$), those elements that preferentially partition into melt phases over residual solids, relative to more compatible trace elements. The depleted composition of the DMM has long been identified as a complementary geochemical signature compared with the incompatible-element enriched continental crust (*e.g.*, Hofmann, 1988; Sun and McDonough, 1989), with several notable exceptions (*e.g.*, Nb and Ta; McDonough, 1990).

Multiple studies have attempted to constrain the chemical composition of the DMM, including models based on upper mantle melts (*i.e.*, MORB; Salters and Stracke, 2004) and residues (*i.e.*, abyssal peridotites; Workman and Hart, 2005), as well as inferences based on cosmochemical arguments (*i.e.*, super-chondritic $^{142}Nd/^{144}Nd$ observed in terrestrial samples; Boyet and Carlson, 2006); however, the absolute depletion of this mantle volume remains unsettled due to difficulties in modeling the incompatible element budget of the DMM, which is a consequence of the wide variance in incompatible element concentrations observed in MORB and off-axis seamounts (*e.g.*, Zindler *et al.,* 1984; Graham *et al.,* 1988; Hofmann, 1988; Sun and McDonough, 1989; Graham *et al.,* 1996; Niu and Batiza, 1997; Hofmann,

2003), as well as upper mantle peridotites and xenoliths (*e.g.*, Jagoutz *et al.,* 1979; Nixon *et al.,* 1981; McDonough and Frey, 1989; McDonough and Sun, 1995; Niu, 2004).

Trace element concentrations in MORB provide one way to constrain the composition of the DMM, as these mantle derivatives generally represent mafic melts of their source. Highly incompatible elements, though, commonly show skewed frequency distributions in terrestrial samples (Ahrens, 1954; McDonough, 1990) and thus pose a challenge to interpreting the representative trace element chemistry of global MORB. In oceanic basalts, canonical trace element ratios such as Zr/Hf, Ce/Pb, Nb/Ta, and Th/U have also been used to characterize mantle sources (*e.g.*, Jochum *et al.,* 1983; Hofmann *et al.,* 1986, Newsom *et al.,* 1986; Hofmann, 1988; Sun and McDonough, 1989; Salters and Stracke, 2004; Workman and Hart, 2005; Boyet and Carlson, 2006). However, the utility of these ratios hinges on the presumption of equivalent partitioning behavior during MORB genesis and the assumption that source heterogeneity, component mixing and variations in melting/crystallization conditions are adequately represented by the melts (Stracke and Bourdon, 2009).

Here, we report new high-precision, externally calibrated trace element measurements of a global suite of MORB and incorporate these data into a critically compiled database that includes other high-quality analyses from several recently published, peer-reviewed data sets. With this comprehensive database we attempt to: i) establish a representative composition for global MORB; ii) investigate potential influences of mantle source mixing (which may affect the distribution of trace

elements in MORB); iii) statistically evaluate the effects of fractional melting and the preservation of canonical trace element ratios during MORB genesis; and, iv) identify prospective geochemical distinctions between MORB samples derived from the Atlantic, Pacific and Indian Ocean basins.

6.3 Global MORB database

Our new trace element concentration data were determined via high-precision laser ablation (LA-) ICP-MS methods and include analyses of both depleted and enriched MORB end-members. Following the protocol established by Arevalo and McDonough (2008), external calibration techniques were implemented in order to maximize precision and accuracy as well as account for any potential non-spectral matrix effects; two USGS basaltic glasses (BIR-1G and BCR-2G; *c.f.*, Jochum *et al.,* 2005a) and five MPI-DING silicate glasses (BM90/21-G, ML3B-G, StHs6/80-G, KL2-G, and T1-G; *c.f.*, Jochum *et al.,* 2000, 2005b), which together span between $10^{0.5}$-$10^{3.1}$ orders of magnitude in concentration for all elements measured here, were used as standard reference materials for external calibration. Spectral matrix effects, particularly isobaric interferences from potential diatomic oxides, were limited by implementing a standard tuning procedure that maximized the elemental signal (based on ^{43}Ca and ^{232}Th spectra) and minimized oxide production ($^{232}Th^{16}O/^{232}Th \leq 0.15\%$). The typical external reproducibility for our concentration measurements, which include new data for Sc, Cr, Sr, Y, Zr, Nb, Ba, the rare-earth elements (REE; from La to Lu), Hf, Ta, and Pb were determined to be ≤3% ($2\sigma_m$) for four replicate analyses of

each sample. The abundances of P, K, Ti, W, Th, and U were originally reported by Arevalo and McDonough (2008) and Arevalo *et al.,* (2009).

A comprehensive collection of trace element data for a more complete global set of MORB was manually compiled from a number of reliable references with established, high-precision and demonstrably accurate methods of analysis (*c.f.*, replicate measurements of standard reference materials, such as BCR-1, BHVO-1 and VG-2) in order to complement the new MORB data presented here. The inclusive data set (n = 792 samples), which encompasses a wide geographic distribution (Fig. 6.1) and includes samples from the Atlantic (n = 342), Pacific (n = 259) and Indian (n = 191) Oceans, also consists of: i) LA-ICP-MS trace element measurements for a global spectrum of MORB reported by Sun *et al.,* (2003, 2008); ii) the PetDB MORB data set from Salters and Stracke (2004), which was filtered to include only samples with <55 wt.% SiO_2, smooth REE patterns and eruption depths in excess of 2000 m; iii) ICP-MS, isotope dilution (ID-) thermal ionization mass spectrometry (TIMS) and ID-ICP-MS measurements of MORB samples from the Gorda Ridge (Davis *et al.,* 2008) and on-axis (Sims *et al.,* 2002; Hall *et al.,* 2006) and off-axis lavas from the East Pacific Rise (Sims *et al.,* 2003); and, iv) Indian MORB analyses from Mahoney *et al.,* (2002), Janney *et al.,* (2005) and Nauret *et al.,* (2006), which comprise measurements of dissolved sample solutions via ICP-MS and ID-ICP-MS. The compiled data set, including the new data reported here, can be downloaded from the author (by request) or online from doi:10.1016/j.chemgeo.2009.12.013.

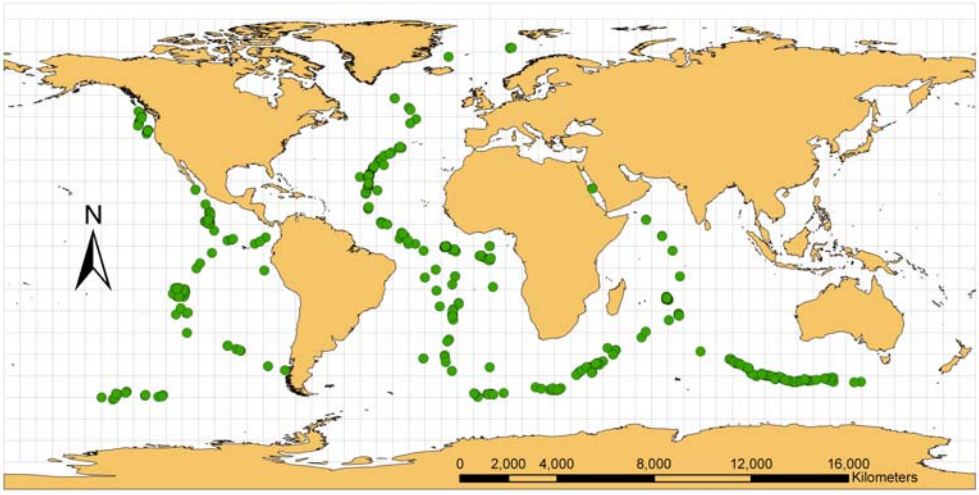

Fig. 6.1. Geographic distribution of the global MORB samples (n = 792) analyzed and/or manually compiled here.

6.4 The definition and chemical composition of prototypical MORB

6.4.1 Normal- versus enriched-type MORB

Mid-ocean ridge basalts, which represent mafic melts of a mantle reservoir that has largely been depleted due to the extraction of the continental crust early in Earth's history (*e.g.*, Hofmann, 1988; Sun and McDonough, 1989), are mostly unaffected by contamination by the continental crust and are highly variable in composition, particularly with regard to incompatible trace elements (those that concentrate in the liquid, *i.e.*, MORB, over the solid, *i.e.*, residual mantle peridotite). As far back as the work of Schilling (1973), MORB have often been subdivided into two distinct categories: "normal-type" and "enriched-type" samples. Normal-type MORB, or N-MORB, represent the majority of global MORB samples and are characterized by depletions in highly incompatible elements (*e.g.*, large-ion lithophile elements, LILE, and high-field strength elements, HFSE) relative to more compatible elements (*e.g.*, Engel *et al.,* 1965; Melson *et al.,* 1976; Hofmann, 1988; Sun and McDonough, 1989; Hofmann, 2003 and references therein), resulting in diagnostic trace element ratios (*e.g.*, $(La/Sm)_N < 1$) and isotopic compositions (*e.g.*, high εNd and low $^{87}Sr/^{86}Sr$). Alternatively, enriched-type MORB, or E-MORB, represent a subordinate component of global MORB and are anomalously enriched in highly incompatible elements, resulting in trace element ratios and isotopic compositions (*e.g.*, $(La/Sm)_N \geq 1$, low εNd and high $^{87}Sr/^{86}Sr$) distinct from more common N-MORB. Although segments of the East Pacific Rise have been documented to yield up to 5-10% E-MORB (Langmuir *et al.,* 1986; Lundstrom *et al.,* 1999), Donnelly *et al.,* (2004) estimate that ≤3% of MORB are chemically enriched based on: i) the frequency distribution of N-

and E-MORB sampled at the Mid-Atlantic Ridge south of the Kane zone (MARK area), a spreading region far from any known mantle hotspot; and, ii) a two-stage melting model of E-MORB genesis, involving metasomatism of ambient mantle peridotite by low-degree melts (*i.e.*, $F < 0.01$) of peridotite or eclogite, followed by typical MORB melting (*i.e.*, $F \approx 0.10$) of the newly enriched mantle source.

The origin of the enriched geochemical signatures observed in E-MORB relative to the depleted signatures characteristic of N-MORB has long been suspected to represent the infiltration of undepleted or enriched lower mantle materials into the ambient (depleted) upper mantle (*e.g.*, Schilling, 1973; Schilling *et al.,* 1983; Allègre *et al.,* 1984; le Roex *et al.,* 1985; Schilling, 1991; Taylor *et al.,* 1997), though metasomatism of ambient upper mantle peridotite by low degree partial melts (*e.g.*, Sun and Hanson, 1975; Wood, 1979; Allègre and Turcotte, 1986; Sun and McDonough, 1989; Niu *et al.,* 1996; Donnelly *et al.,* 2004) and/or melting of enriched eclogitic domains derived from subducted oceanic crust (*e.g.*, Hofmann and White, 1982; Allègre *et al.,* 1984; Zindler *et al.,* 1984; Niu and Batiza, 1997; Niu *et al.,* 1999) have also been suggested. Regardless of the exact origin of the source materials that contribute to the genesis of E-MORB, several filters (primarily La/Sm, $(La/Sm)_N$ and K/Ti ratios) can be and have been implemented to distinguish between N- and E-MORB.

Because collections of MORB do not represent a perfectly random sampling of the entire mid-ocean ridge system, the division of MORB samples into normal- and enriched-types has traditionally served as a way to avoid over-representing enriched samples when characterizing the global MORB reservoir, and by inference

geochemical models of the DMM and bulk SE. However, the global spectrum of MORB exhibits a continuous range in compositions, from highly depleted to enriched in incompatible element abundances (*e.g.*, Hofmann, 2003 and references therein), and thus dividing samples based upon an arbitrary chemical criterion also serves to bias models of global MORB. As a result, here we establish a representative composition of global MORB, as represented by both normal and enriched end-members. Anomalous samples with La/Sm ratios outside of the "outer fence," or 3× the interquartile range of values in this inclusive data set, are considered statistical outliers and are not considered here. For comparison, we also examine the composition of only N-MORB, defined here as samples with $(La/Sm)_N < 1.00$ (n = 597 out of 792 total MORB samples), in order to evaluate and quantify the effects of enriched mantle components in the DMM.

6.4.2 The chemical composition of global MORB and N-MORB

Frequency distributions of highly incompatible trace elements (*e.g.*, Ba, Th, U, and the light REE) in the MORB compilation examined here show ranges in concentrations that span nearly three orders of magnitude and are positively skewed rather than Gaussian, or "bell-shaped," in geometry (Fig. 6.2). As first recognized by Ahrens (1954), such skewed distributions may be anticipated for incompatible element abundances in terrestrial samples and can be converted into normal distributions by simply taking the logarithm of the variate, or the elemental concentration. Distributions of logarithmic concentrations are generally Gaussian in character (Fig. 6.2), and thus allow a statistical analysis of the mean concentration of both highly incompatible and moderately incompatible elements in MORB.

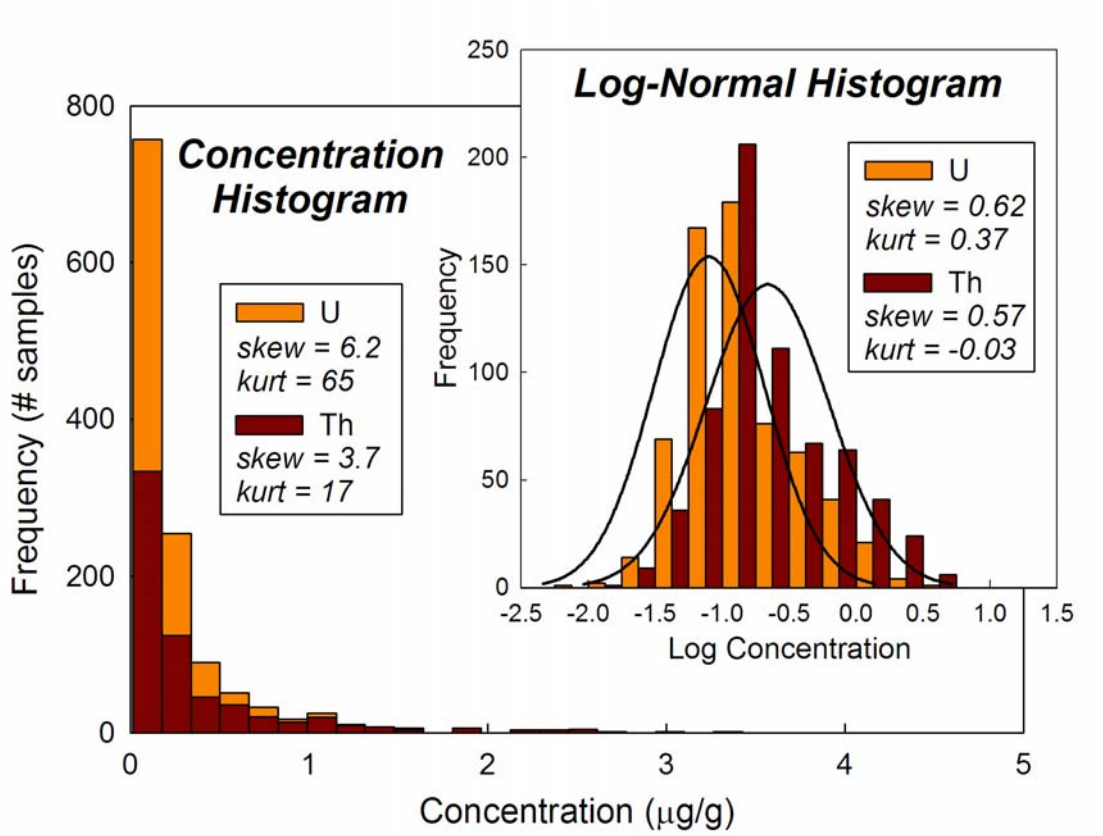

Fig. 6.2. Examples of frequency distributions of highly incompatible trace element abundances in global MORB. Both Th and U are highly incompatible during mantle melting and thus are characterized by skewed distributions; however, taking the logarithm of the sample abundances of these elements normalizes the data into distributions with a more Gaussian geometry (Ahrens, 1954).

Comparisons of the average and median values with the log-normal mean values for the chemical composition of global MORB and N-MORB are illustrated in Fig. 6.3; the log-normal mean values approximate the median (as expected for a skewed sample populations; *e.g.*, McDonough, 1990). The average, median and log-normal mean values all converge towards the less incompatible elements (*e.g.*, heavy REE). Table 6.1 defines the incompatible element budget of both global MORB and N-MORB as determined by the log-normal distribution of elements in the data set compiled here. Samples with anomalous trace element abundances that have been diagnosed as statistical outliers, defined by concentrations that reside outside of the "outer fence," or 3× the interquartile range, were not considered in our analytical investigations. The global MORB and N-MORB model compositions established here, which have 7.84 wt.% and 8.01 wt.% MgO respectively, are compared to previous characterizations of MORB based on trace element abundances measured in independent sample sets (Hofmann, 1988; Su, 2002) and an early survey of literature values (Sun and McDonough, 1989). Figure 6.3 illustrates the similarities and differences between the trace element patterns exhibited by each model composition. Whereas the model of Sun and McDonough (1989) delineates the most incompatible-element depleted model composition of MORB, the log-normal mean composition of global MORB, as determined here, represents the most enriched composition. The highest abundances of the heavy REE, however, are modeled by Hofmann (1988).

The complete chemical composition of global MORB, including major, minor and volatile elements, is expounded in Table 6.2, which compares the chemistry of MORB to CI carbonaceous chondrites, as surveyed by Palme and Jones (2003), and

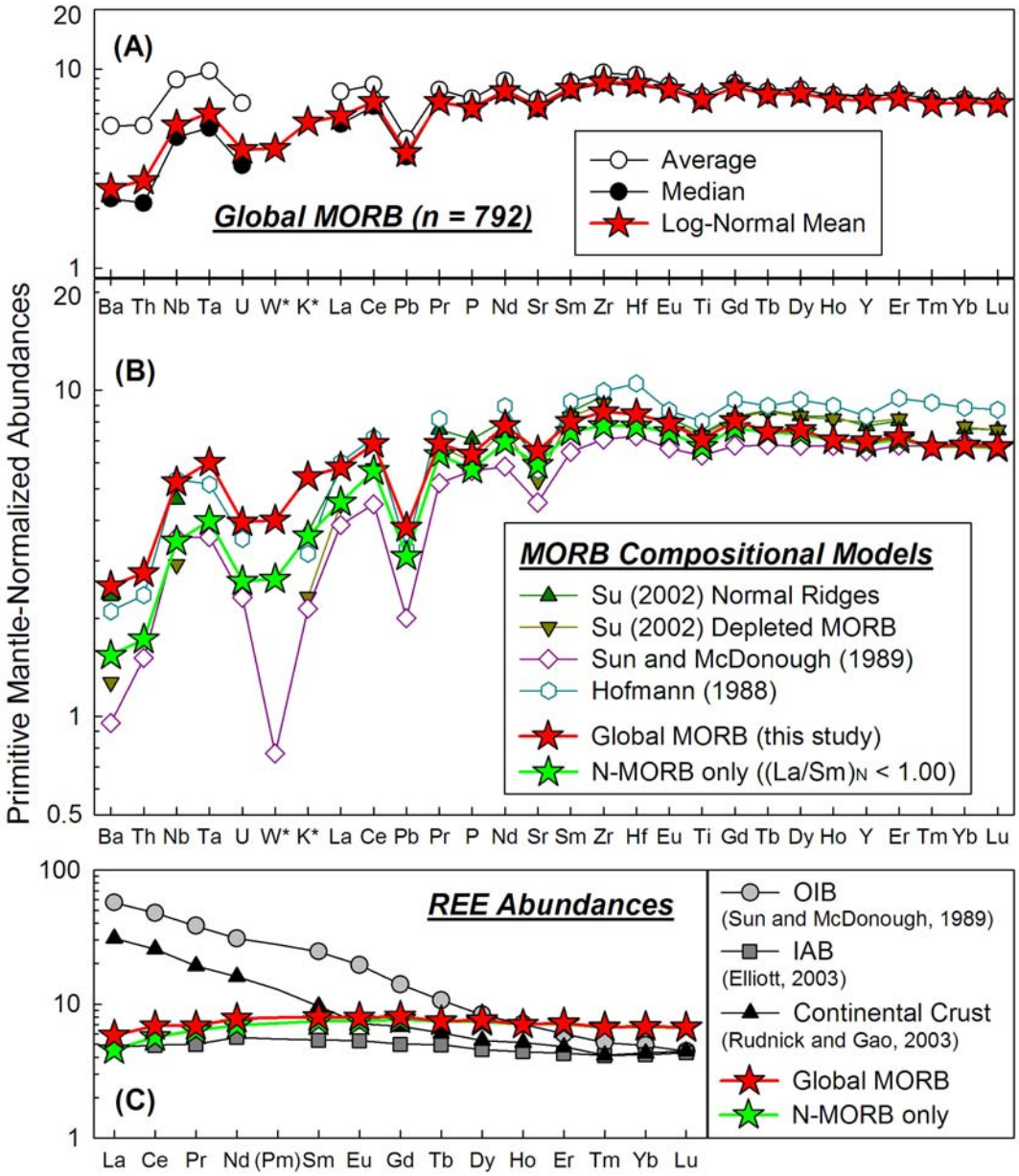

Fig. 6.3. Primitive-mantle normalized abundances of trace elements in various compositional models of MORB chemistry. The elements along the abscissa are ordered by relative incompatibilities observed in MORB, as determined in previous studies (*e.g.*, Hofmann, 1988; Sun and McDonough, 1989) and here. (A) The log-normal mean abundances of trace elements in our global MORB data set mimic the median rather than the statistical average due to the skewed

frequency distributions of highly incompatible elements observed in terrestrial samples (see Fig. 6.2). (B) Global MORB represent a more incompatible-element enriched composition compared to N-MORB and previous models of MORB composition, though the abundances of the less incompatible heavy REE merge with the values observed in N-MORB and predicted by Sun and McDonough (1989). (C) Although the abundances of light REE in global and N-MORB are depleted similar to typical IAB (as modeled by Elliott, 2003), the heavy REE observed in MORB are actually enriched relative to IAB, OIB and the bulk continental crust.

Table 6.1. Incompatible element budget (in µg/g) of global MORB compared to N-MORB and previous model compositions.

Element	Global MORB[a] Average	Standard Deviation	Skewness	n	Median	*Global MORB[a] Log-Normal Mean*	*N-MORB Only[b] Log-Normal Mean*	Su (2002) Normal Segments[c]	Su (2002) Depleted Samples[d]	Sun and McDonough (1989) N-MORB[e]	Hofmann (1988) N-MORB[f]
P[g]	641	371	2.7	695	567	***574***	***515***	637	546	510	
K[h]	-	-	-	-	-	***1520***	***1000***	1030	650	600	884
Sc	37.0	4.9	-0.9	502	37.2	***36.8***	***37.8***				41
Ti	8820	2520	1.4	679	8350	***8500***	***8100***	8930	8750	7600	9682
Cr	326	91	0.7	219	321	***326***	***330***				
Sr	140	59	3.3	674	125	***130***	***118***	122	105	90	113
Y	31.4	10.2	5.5	654	30.0	***30.0***	***29.6***	33.5	34.4	28.0	35.8
Zr	100	55	4.0	655	89.1	***90.1***	***81.6***	101	95.2	74.0	104
Nb	5.82	7.6	3.0	651	3.00	***3.44***	***2.27***	3.05	1.92	2.33	3.51
Ba	34.2	49.0	2.7	684	14.7	***16.6***	***10.2***	15.5	8.40	6.30	13.9
La	5.00	4.99	3.4	754	3.44	***3.77***	***2.94***	3.70	2.90	2.50	3.90
Ce	14.0	11.1	3.3	723	10.9	***11.5***	***9.49***	11.6	9.65	7.50	12.0
Pr	2.00	1.27	4.4	378	1.75	***1.74***	***1.62***	1.93	1.71	1.32	2.07
Nd	10.9	6.1	3.3	723	9.49	***9.8***	***8.67***	10.1	9.50	7.30	11.2
Sm	3.49	1.46	3.3	754	3.19	***3.25***	***3.03***	3.50	3.37	2.63	3.75
Eu	1.28	0.40	2.3	731	1.21	***1.22***	***1.15***	1.27	1.23	1.02	1.34
Gd	4.64	1.67	3.6	619	4.43	***4.40***	***4.17***	4.52	4.48	3.68	5.08
Tb	0.763	0.209	3.1	438	0.730	***0.738***	***0.733***	0.860	0.850	0.670	0.885
Dy	5.33	1.71	4.5	649	5.04	***5.11***	***4.97***	5.64	5.60	4.55	6.30
Ho	1.11	0.41	6.0	370	1.05	***1.05***	***1.05***	1.24	1.22	1.01	1.34
Er	3.29	1.09	6.0	647	3.16	***3.15***	***3.10***	3.53	3.58	2.97	4.14
Tm	0.481	0.196	6.3	309	0.460	***0.453***	***0.454***			0.456	0.621
Yb	3.12	1.05	7.1	728	3.00	***3.00***	***2.97***	3.36	3.41	3.05	3.90
Lu	0.471	0.158	6.9	706	0.45	***0.454***	***0.450***	0.510	0.510	0.455	0.589
Hf	2.64	1.38	4.5	673	2.35	***2.40***	***2.20***			2.05	2.97
Ta	0.364	0.449	2.7	562	0.189	***0.224***	***0.148***			0.132	0.192
W[i]	-	-	-	-	-	***0.052***	***0.034***			0.010	
Pb	0.668	0.467	3.2	603	0.544	***0.570***	***0.465***			0.300	0.489
Th	0.415	0.630	3.7	648	0.169	***0.219***	***0.137***			0.120	0.187
U	0.137	0.213	6.2	638	0.066	***0.080***	***0.053***			0.047	0.071

[a] Statistical outliers plotting outside of the "outer fence," defined by 3× the interquartile range, were not considered.

[b] Log-normal mean abundances in MORB with $(La/Sm)_N < 1.00$.

[c] Compositional model based on weighting MORB analyses according to 151 ridge segments located away from subduction zones or known hotspots.

[d] Compositional model based on weighting MORB analyses according to 62 normal ridge segments with average $K_2O/TiO_2 < 0.067$.

[e] Early survey of literature values of MORB characterized by depletions in light REE.

[f] Average composition of 26 MORB glasses characterized by depletions in light REE.

[g] P abundances converted from P_2O_5 major element analyses.

[h] Global MORB and N-MORB only K abundances calculated assuming a global MORB K/U = 19,000 and an N-MORB K/U = 20,000 after Arevalo et al. (2009).

[i] Global MORB and N-MORB only W abundances calculated assuming a silicate Earth W/U = 0.65 after Arevalo and McDonough (2008).

the unfractionated SE, as modeled primarily by McDonough and Sun (1995). The major element chemistry of global MORB has been derived from the median composition of the global data set presented here, whereas minor elements (*e.g.*, first-row transition metals), trace elements not reported here (*e.g.*, platinum-group elements) and volatile species (*e.g.*, halogens) have been derived through other analytical proxies defined in Table 6.2.

Table 6.2. Chemical composition of global MORB.

Element		CI[a]	SE[b]	MORB	Constraint	Reference(s)
H	µg/g	20200	120[c]	230	$H_2O/Ce = 180$	Michael (1995); Saal et al. (2002); le Roex et al. (2006)
He	mol/g	-	-	5.4×10^{-10}	molar C/He = 2.9×10^{4}	Javoy and Pineau (1991)
Li	µg/g	1.49	1.6	5.1	Li/Yb = 1.7	Ryan and Langmuir (1987)
Be	µg/g	0.025	0.068	0.49	Be/Nd = 0.05	Ryan and Langmuir (1988)
B	µg/g	0.69	0.3	1.5	B/K = 0.0010	Ryan and Langmuir (1993)
C	µg/g	32200	120	190	$CO_2/Nb = 200$	Saal et al. (2002); le Roex et al. (2006)
N	µg/g	3180	2	0.55	molar C/N = 400	Javoy and Pineau (1991); Marty and Zimmerman (1999)
F	µg/g	58.2	25	170	F/P = 0.3	Schilling et al. (1980); Saal et al. (2002)
Ne	mol/g	-	-	2.1×10^{-14}	molar He/Ne = 2.6×10^{4}	Sarda and Graham (1990)
Na	wt%	0.498	0.267	2.01	Median of global MORB	this study
Mg	wt%	9.61	22.8	4.73	Median of global MORB	this study
Al	wt%	0.849	2.35	8.19	Median of global MORB	this study
Si	wt%	10.68	21	23.6	Median of global MORB	this study
P	µg/g	926	90	574	Log-normal mean of global MORB	this study
S	µg/g	54100	250	1100	S/Dy = 220	Saal et al. (2002)
Cl	µg/g	698	17	140	Cl/K = 0.09	Jambon et al. (1995); Gannoun et al. (2007)
Ar	mol/g	-	-	4.2×10^{-10}	molar He/Ar = 1.3	Sarda and Graham (1990); Javoy and Pineau (1991)
K	µg/g	544	280[d]	1520	Log-normal mean of global MORB	Arevalo et al. (2009)
Ca	wt%	0.932	2.53	8.23	Median of global MORB	this study
Sc	µg/g	5.9	16.2	36.8	Log-normal mean of global MORB	this study
Ti	µg/g	458	1200	8500	Log-normal mean of global MORB	this study
V	µg/g	54.3	82	250	V/Sc = 6.7	Lee et al. (2005)
Cr	µg/g	2650	2620	326	Log-normal mean of global MORB	this study
Mn	µg/g	1930	1040	1320	Median of global MORB	this study
Fe	wt%	18.4	6.26	7.27	Median of global MORB	this study
Co	µg/g	506	105	56	Fe/Co = 1300	McDonough (1994)
Ni	µg/g	10800	1960	200	Ni/Cr = 0.6	McDonough (1994)
Cu	µg/g	131	30	70	Cu/Re = 8.4×10^{4}	Sun et al. (2003)
Zn	µg/g	323	55	80	molar Zn/Cd = 1000	Laul et al. (1972); Hertogen et al. (1980)
Ga	µg/g	9.71	4.0	21	molar Zn/Ga = 4.1	Hart (1976)
Ge	µg/g	32.6	1.1	1.6	molar Ge/Si = 2.6×10^{-6}	de Argollo and Schilling (1978)
As	µg/g	1.81	0.05	0.11	As/Ce = 9.6×10^{-3}	Sims et al. (1990)
Se	µg/g	21.4	0.075	0.21	Se/Re = 250	Hertogen et al. (1980); Morgan (1986)
Br	µg/g	3.50	0.050	0.32	Cl/Br = 430	Jambon et al. (1995)
Kr	mol/g	-	-	3.2×10^{-16}	molar He/Kr = 1.7×10^{6}	Sarda and Graham (1990)
Rb	µg/g	2.32	0.600	1.5	Ba/Rb = 11	Hofmann and White (1983)
Sr	µg/g	7.26	19.9	130	Log-normal mean of global MORB	this study
Y	µg/g	1.56	4.3	30.0	Log-normal mean of global MORB	this study
Zr	µg/g	3.86	10.5	90.1	Log-normal mean of global MORB	this study
Nb	ng/g	247	658	3440	Log-normal mean of global MORB	this study
Mo	ng/g	928	50	390	Mo/Ce = 0.034	Sun et al. (2003)
Ru	ng/g	683	5.0	0.041	Ru/Ir = 1.0	Bezos et al. (2005)
Rh	ng/g	140	0.9	0.029	Rh/Ir = 0.7	Tatsumi et al. (1999)
Pd	ng/g	556	3.9	0.69	Pd/Ir = 17	Bezos et al. (2005)
Ag	ng/g	197	8	27	Se/Ag = 7.7	Hertogen et al. (1980)
Cd	ng/g	680	40	140	Cd/Dy = 0.027	Yi et al. (2000)

Table 6.2. Chemical composition of global MORB (continued).

Element		CI[a]	SE[b]	MORB	Constraint	Reference(s)
In	ng/g	78	11	75	In/Y = 0.0025	Yi et al. (1995)
Sn	ng/g	1680	130	1000	Sn/Sm = 0.32	Jochum et al. (1993)
Sb	ng/g	133	5.5	14	Sb/Ce = 0.0012	Sims et al. (1990)
Te	ng/g	2270	12	4.9	$Te/Ni = 2.5 \times 10^{-5}$	Yi et al. (2000)
I	ng/g	433	10	21	$I/K = 1.4 \times 10^{-5}$	Deruelle et al. (1992)
Xe	mol/g	-	-	2.1×10^{-17}	molar $He/Xe = 2.6 \times 10^{7}$	Sarda and Graham (1990)
Cs	ng/g	188	21	19	Rb/Cs = 80	Hofmann and White (1983)
Ba	ng/g	2410	6600	16600	Log-normal mean of global MORB	this study
La	ng/g	245	648	3770	Log-normal mean of global MORB	this study
Ce	ng/g	638	1680	11500	Log-normal mean of global MORB	this study
Pr	ng/g	96.4	254	1740	Log-normal mean of global MORB	this study
Nd	ng/g	474	1250	9800	Log-normal mean of global MORB	this study
Sm	ng/g	154	406	3250	Log-normal mean of global MORB	this study
Eu	ng/g	58.0	154	1220	Log-normal mean of global MORB	this study
Gd	ng/g	204	544	4400	Log-normal mean of global MORB	this study
Tb	ng/g	37.5	99	738	Log-normal mean of global MORB	this study
Dy	ng/g	254	674	5110	Log-normal mean of global MORB	this study
Ho	ng/g	56.7	149	1050	Log-normal mean of global MORB	this study
Er	ng/g	166	438	3150	Log-normal mean of global MORB	this study
Tm	ng/g	25.6	68	453	Log-normal mean of global MORB	this study
Yb	ng/g	165	441	3000	Log-normal mean of global MORB	this study
Lu	ng/g	25.4	67.5	454	Log-normal mean of global MORB	this study
Hf	ng/g	107	283	2400	Log-normal mean of global MORB	this study
Ta	ng/g	14.2	37	224	Log-normal mean of global MORB	this study
W	ng/g	90.3	13[e]	52.0	Log-normal mean of global MORB	Arevalo and McDonough (2008)
Re	ng/g	39.5	0.28	0.83	$Yb/Re = 3.6 \times 10^{3}$	Sun et al. (2003)
Os	ng/g	506	3.4	0.003	Re/Os = 300	Gannoun et al. (2007)
Ir	ng/g	480	3.2	0.041	$Ni/Ir = 4.8 \times 10^{6}$	Bezos et al. (2005)
Pt	ng/g	982	7.1	0.45	Pt/Ir = 11	Bezos et al. (2005)
Au	ng/g	148	1.0	1.2	Au/Ir = 30	Hertogen et al. (1980); Tatsumi et al. (1999)
Hg	ng/g	310	10	12.6	$Hg/Mn = 9.6 \times 10^{-6}$	Salters and Stracke (2004)
Tl	ng/g	143	3.5	6.6	Rb/Tl = 230	Hertogen et al. (1980)
Pb	ng/g	2530	150	570	Log-normal mean of global MORB	this study
Bi	ng/g	111	2.5	9.5	Bi/Pb = 0.0167	Salters and Stracke (2004)
Th	ng/g	29.8	79.5	219	Log-normal mean of global MORB	this study
U	ng/g	7.80	20.3	80.0	Log-normal mean of global MORB	this study

[a]CI carbonaceous chondrite (CI) values taken from Palme and Jones (2003).
[b]Silicate Earth (SE) values taken from McDonough and Sun (1995), unless otherwise stated.
[c]H abundance in silicate Earth from Palme and O'Neill (2003).
[d]K abundance in silicate Earth from Arevalo et al. (2009).
[e]W abundance in silicate Earth from Arevalo and McDonough (2008).

6.5 Relative incompatibilities during MORB genesis

6.5.1 MORB melting models

The simplest model of upper mantle melting at mid-ocean ridges assumes passive upwelling and decompression-induced melting as approximated as a reversible, adiabatic process with isentropic productivity (*e.g.*, Asimow *et al.,* 1997 and references therein). If a mantle melt remains in contact with the residue during magma migration and emplacement, then the bulk composition of the system (melt + residue) is effectively held constant and the melting process may be approximated by equilibrium (or batch) melting (*e.g.*, Kinzler and Grove, 1992). However, realistic

models of melt generation and segregation implicate polybaric near-fractional melting rather than equilibrium melting at mid-ocean ridges (Langmuir *et al.,* 1977; Wood, 1979a,b; McKenzie, 1984; McKenzie and Bickle, 1988; Johnson *et al.,* 1990; Spiegelman and Kenyon, 1992; Hart, 1993; Iwamori, 1993; Sobolev & Shimizu 1993; Kelemen *et al.,* 1997). Additionally, U-series disequilibria in global MORB robustly demonstrate that the isotopic composition of most MORB can not be reproduced via equilibrium melting models without requiring unrealistically small degrees of melting, but require near-fractional melting and/or more complex melting mechanisms (*e.g.*, Condomines *et al.,* 1981; Newman *et al.,* 1983; McKenzie, 1985; Goldstein *et al.,* 1989, 1992; Rubin and McDougall, 1992; Goldstein *et al.,* 1993; Volpe and Goldstein, 1993; Sims, 1995).

Consequently, here we adapt a simplified model of (modal) accumulated fractional melting following Shaw (1970), where the concentration of element *i* in a mantle melt (C_i^{liq}), such as MORB, is related to the concentration in the source (C_i^0), such as the DMM, in addition to the degree of partial melting (F) and the partition coefficient ($D_i^{sol/liq}$):

$$C_i^{liq} = \frac{C_i^0}{F}\left(1-\left(1-F\right)^{1/D_i^{sol/liq}}\right) \qquad (6\text{-}1).$$

Here it may be seen that incompatible trace elements ($D_i^{sol/liq} < 1$) concentrate in the liquid, particularly at low degrees of melting (F). Following this model, the concentration ratio of two elements *i* and *j* in MORB is given by:

$$\frac{C_i^{MORB}}{C_j^{MORB}} = \left(\frac{C_i^{DMM}}{C_j^{DMM}}\right)\left(\frac{1-\left(1-F\right)^{1/D_i^{DMM/MORB}}}{1-\left(1-F\right)^{1/D_j^{DMM/MORB}}}\right) \qquad (6\text{-}2).$$

Accordingly, a concentration ratio between two trace elements may remain constant through MORB genesis under three conditions: i) if the two elements behave similarly during mantle melting (*i.e.*, $D_i^{sol/liq} \approx D_j^{sol/liq}$); ii) if the two elements are both highly incompatible ($D_{i,j}^{sol/liq} << 1$); and/or, iii) if the system experiences unrealistically high melt fractions (*i.e.*, $F \approx 1$). If any of these criteria is met, Eqn. 6-2 reduces to:

$$\frac{C_i^{MORB}}{C_j^{MORB}} \approx \left(\frac{C_i^{DMM}}{C_j^{DMM}} \right) \qquad (6\text{-}3)$$

and the ratio measured in MORB may be inferred to be representative of the source region, or local DMM, presuming the melt adequately represents the heterogeneity and contribution of all source components involved (Stracke and Bourdon, 2009).

6.5.2 Log-log concentration correlations

"Canonical" trace element ratios, such as Zr/Hf, Ce/Pb, Nb/Ta, and Th/U remain relatively constant over a large range in concentration and MgO content (Fig. 6.4) and have commonly been summoned by geochemical studies to constrain terrestrial source compositions, including the DMM (*e.g.*, Salters and Stracke, 2004; Workman and Hart, 2005; Boyet and Carlson, 2006), modern mantle (*i.e.*, DMM + OIB source region; *e.g.*, Hofmann *et al.,* 1986; Newsom *et al.,* 1986), continental crust (*e.g.*, McLennan *et al.,* 1980; Taylor and McLennan, 1985; Sims *et al.,* 1990; Plank and Langmuir, 1998; Rudnick and Gao, 2003), bulk SE (*e.g.*, Jochum *et al.,* 1983; Hofmann, 1988; Sun and McDonough, 1989; McDonough and Sun, 1995; Palme and O'Neill, 2003), and by inference the core (*e.g.*, McDonough, 2003). However, several studies have begun to systematically explore the true constancy and regional

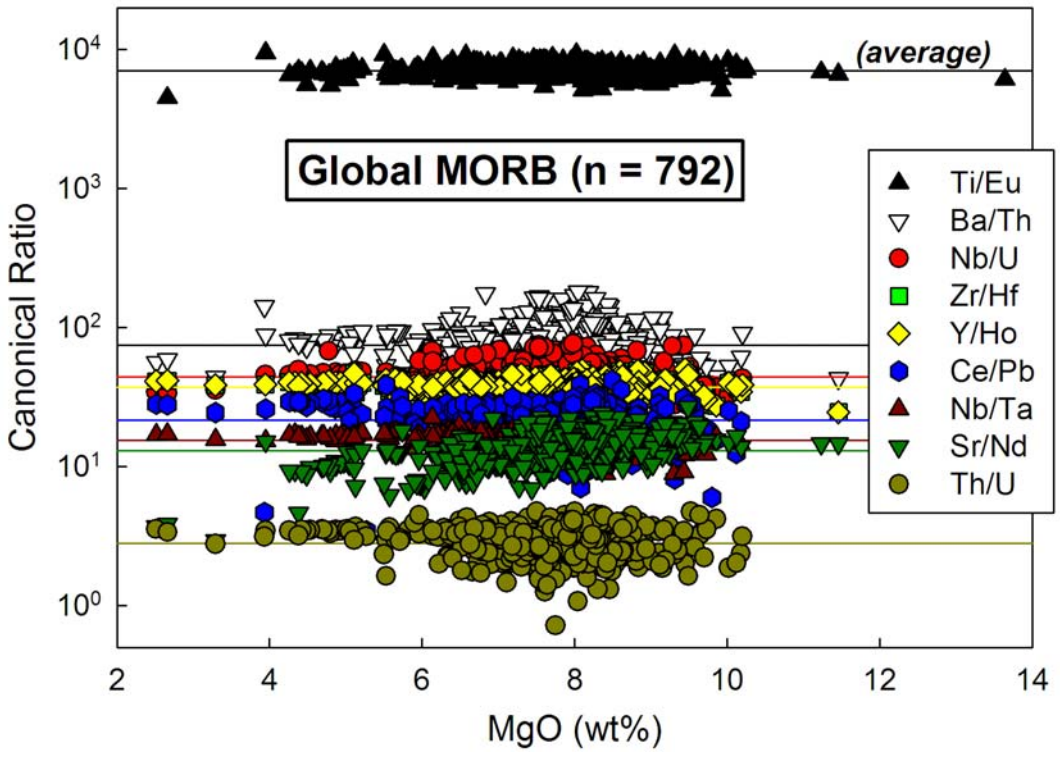

Fig. 6.4. Constancy of "canonical" trace element concentration ratios in global MORB as a function of magmatic processing. Constant trace element ratios are not expected to deviate when plotted versus MgO content, which commonly serves as a proxy for magmatic differentiation. However, log-log covariation diagrams provide a more robust method for determining the relative incompatibility of two elements that behave similarly during geochemical processes. Statistical outliers, defined as data points residing outside of the "outer fence," or 3× the interquartile range, have been excluded.

variability of some canonical ratios, particularly Nb/U and Ce/Pb (Sims and DePaolo, 1997; Niu *et al.,* 1999; Stracke *et al.,* 2003; Willbold and Stracke, 2006; Pfänder *et al.,* 2007; Sun *et al.,* 2008) and K/U (Arevalo *et al.,* 2009), and found that these ratios are in fact not uniform in the modern mantle and may deviate as a result of asymmetrical partitioning behavior during mantle melting and/or source heterogeneities due to regional differences in the proportion of recycled lithologies. As a result, the true constancy of other commonly cited canonical ratios, and systematic variations in these ratios between different mantle source regions, need to be quantitatively examined to confidently establish the legitimacy of using such proxies as a guide to determining mantle and crustal compositions.

Historically, the constancy of a canonical trace element ratio was demonstrated by a lack of correlation between the ratio itself (*e.g.*, *i*/*j*) and the concentration of the elements involved (Jochum *et al.,* 1983; Hofmann *et al.,* 1986; Newsom *et al.,* 1986). However, such comparisons are not statistically robust, as the two variables are not mathematically independent (Sims and DePaolo, 1997). Consequently, errors in the concentration measurement of *i* (or *j*) appear in both x- and y-variables. Additionally, variations in *i*/*j* are relatively small compared to those in *i* (or *j*) for any trace element pair with similar partitioning behavior, thus variations in the ratio (typically $<10^1$) pale in comparison to the significantly larger variations seen in concentration (typically 10^1-10^3).

An alternative representation that provides a more robust analysis of the relative incompatibilities of two or more trace elements is a log-log covariation diagram (Sims and DePaolo, 1997; Hofmann, 2003; Willbold and Stracke, 2006;

Pfänder *et al.,* 2007; Arevalo and McDonough, 2008; Sun *et al.,* 2008; Arevalo *et al.,* 2009). This type of representation plots statistically independent variables that are dispersed across a wider distribution and a similar order of magnitude along both axes. In this way, the data and their associated errors are weighted uniformly across the range of values.

Solving for *F*, the (modal) accumulated fractional melting equation (Eqn. 6-1) provides the following relationship between two trace elements in the DMM and a mantle melt such as MORB:

$$log\, C_i^{MORB} = log\, C_i^{DMM} - log\, F + log\left(1-(1-F)^{1/D_i^{DMM/MORB}}\right) \quad (6\text{-}4)$$

$$log\left(1-(1-F)^{1/D_i^{DMM/MORB}}\right) = log\, C_i^{MORB} - log\, C_i^{DMM} + log\, F \quad (6\text{-}5).$$

Therefore, for two elements *i* and *j* with equal partition coefficients ($D_i^{sol/liq} = D_j^{sol/liq}$), we arrive at:

$$log\, C_i^{MORB} - log\, C_i^{DMM} = log\, C_j^{MORB} - log\, C_j^{DMM} \quad (6\text{-}6)$$

$$log\, C_i^{MORB} = log\, C_j^{MORB} + log\frac{C_i^{DMM}}{C_j^{DMM}} \quad (6\text{-}7)$$

which mimics a linear equation in the form $y = mx + b$. Therefore, in the case where elements *i* and *j* are equally incompatible ($D_i^{sol/liq} = D_j^{sol/liq}$), the slope ($m$) is equal to unity and the y-intercept (b) equals the logarithm of the representative *i/j* ratio of the source.

6.5.3 Effects of mantle source mixing

Although log-log covariation diagrams can and have served as a reliable tool for determining the relative incompatibilities of trace elements during modern mantle

melting (Sims and DePaolo, 1997; Hofmann, 2003; Willbold and Stracke, 2006; Pfänder *et al.,* 2007; Arevalo and McDonough, 2008; Sun *et al.,* 2008; Arevalo *et al.,* 2009), they may also cloud potential source heterogeneities with distinct trace element ratios and/or melting trends. Figure 6.5 illustrates how the utility of log-log covariation plots may be compromised by potential mixing (chemical or mechanical) between two or more source components with distinct trace element ratios and partitioning characteristics during melting. As described above, the vast majority (likely >90%) of MORB samples are defined by depletions in highly incompatible elements, such as LILE (*e.g.*, Ba, Th and U), HFSE (*e.g.*, Ti, Zr and Nb) and the light REE (*e.g.*, La, Ce and Pr) compared to less incompatible elements, such as the heavy REE (*e.g.*, Tm, Yb and Lu). Mid-ocean ridge basalts that are characterized by enrichments in highly incompatible elements likely represent mixing between the ambient, depleted component of the DMM and undepleted or enriched mantle domains with distinct trace element attributes.

In an attempt to characterize the K/U ratio of the composite DMM, including both depleted and enriched source components, Arevalo *et al.,* (2009) discretized the K/U ratio measured in N-MORB samples with La/Sm < 1.00 (defined by K/U = 20,000 ± 2300, 2σ) and the K/U ratio in E-MORB samples with La/Sm ≥ 1.00 (K/U = 15,700 ± 3100, 2σ). Only considering N-MORB samples, Arevalo *et al.,* (2009) asserted that K and U behave analogously during N-MORB source melting, and thus interpreted that the K/U ratio of global MORB was representative of the composite DMM. Because E-MORB represent a subordinate component of global MORB but are significantly more enriched than N-MORB, these authors modeled a 5% mass

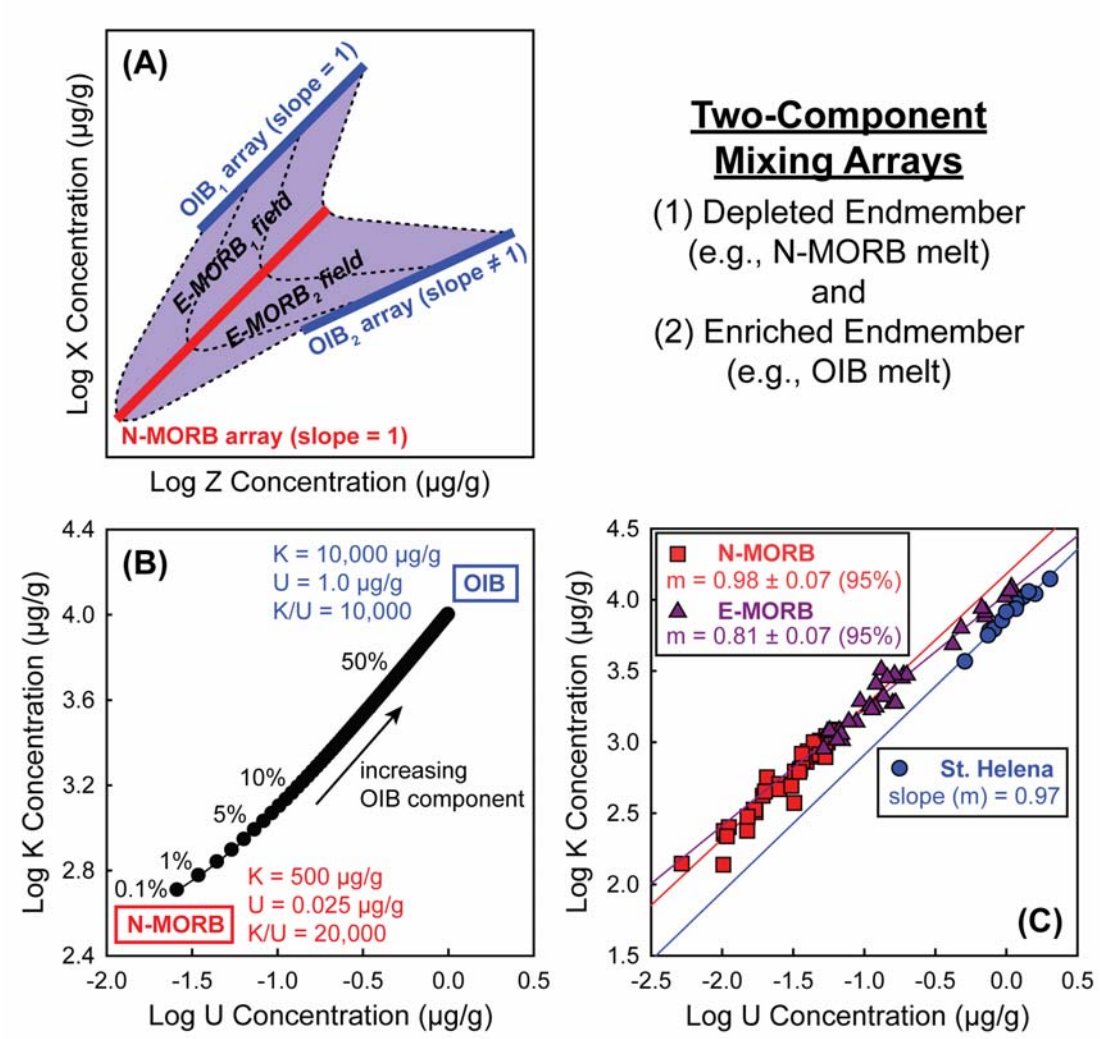

Fig. 6.5. Observable effects of two-component mixing on a log-log covariation diagram. (A) In a log-log covariation plot, an equally incompatible element pair is defined by a linear regression with a slope of unity (*m* = 1.00), whereas a more incompatible element along the abscissa would be revealed by a slope less than unity (*m* < 1.00) and a more incompatible element along the ordinate axis would yield a slope greater than unity (*m* > 1.00). Mixing between a depleted and enriched source component could be manifested as an apparent shift in geochemical behavior between two otherwise equally incompatible elements. (B) Two-component mixing between model N-MORB and OIB results in variable K/U ratios as well as K and U abundances. (C) E-MORB samples from Arevalo *et al.*, (2009), which were distinguished by La/Sm > 1.00, could represent two-component mixing between a depleted DMM domain and an enriched mantle

domain, such as that which feeds the St. Helena ocean islands (data from Willbold and Stracke, 2006), or a distinct lithology between the depleted component preferentially sampled by N-MORB and the enriched component observed in E-MORB. The samples from Arevalo *et al.,* (2009) suggest that K and U behave analogously during N-MORB genesis but unequally during the genesis of more enriched samples. Interestingly, the K and U abundances from St. Helena OIB hint at equal incompatibility between K and U during melting of this mantle source region.

contribution of E-MORB and a 6× enrichment relative to N-MORB, resulting in a global MORB and inferred composite DMM K/U ratio of 19,000 ± 2600 (2σ). Figure 6.5C, which plots the K and U log abundances of the N-MORB and E-MORB sample sets examined by Arevalo *et al.,* (2009), illustrates the unique slope (*m*) and y-intercept (*b*) of E-MORB relative to N-MORB. The deviation in partitioning behavior observed between E-MORB and N-MORB may correspond to distinct source lithologies, a reflection of extremely low degrees of melting (*e.g.*, $F < 0.01$) in the case of E-MORB, or mixing between a compositionally depleted and enriched DMM component, such as that which feeds the St. Helena ocean island chain (data from Willbold and Stracke, 2006). Regardless, the partitioning behaviors of K and U are not analogous when considering both N- and E-MORB samples together.

6.5.4 Constancy of canonical trace element ratios

The relative incompatibilities of the trace elements considered here are demonstrated by the log-log covariation diagrams seen in Figures 6.6 and 6.7. In these covariation plots, an equally incompatible pair of elements is distinguished by a linear regression with a slope of unity ($m = 1.00$); a slope of less than unity ($m < 1.00$) indicates a more highly incompatible element along the abscissa (x-axis), and a slope of greater than unity ($m > 1.00$) reveals a more incompatible element along the ordinate (y-axis). Table 6.3 summarizes the statistics of the linear regressions plotted in Figures 6.6 and 6.7, as well as linear regression statistics considering N-MORB only (samples with $(La/Sm)_N < 1.00$) for comparison.

Our global MORB data set shows that only Ti/Eu ($m = 0.97 \pm 0.07$, 95% confidence-level), Y/Ho ($m = 1.01 \pm 0.04$) and Ce/Pb ($m = 0.97 \pm 0.04$) yield slopes

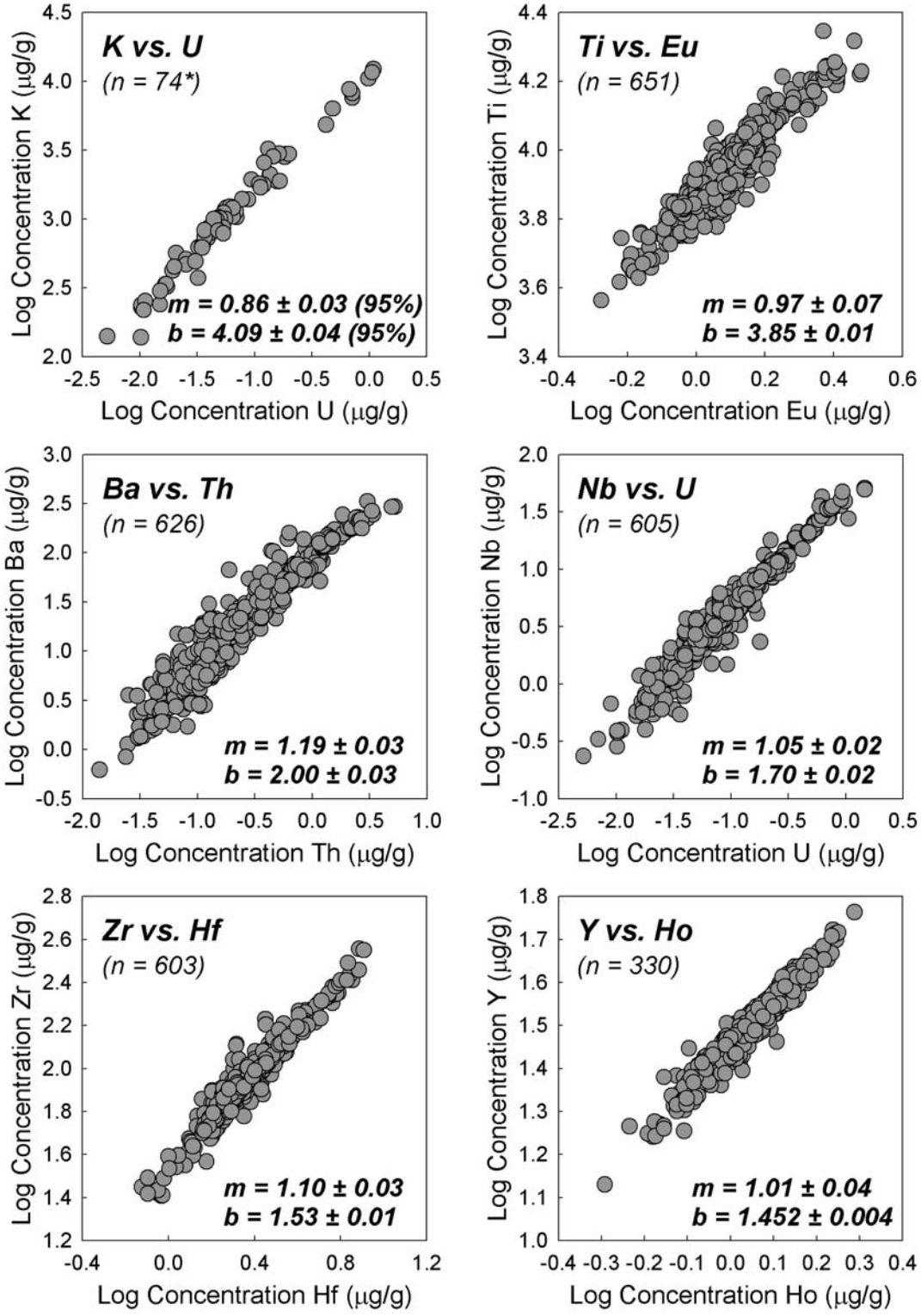
K vs. U
(n = 74*)
m = 0.86 ± 0.03 (95%)
b = 4.09 ± 0.04 (95%)
Log Concentration K (μg/g)
Log Concentration U (μg/g)
Ti vs. Eu
(n = 651)
m = 0.97 ± 0.07
b = 3.85 ± 0.01
Log Concentration Ti (μg/g)
Log Concentration Eu (μg/g)
Ba vs. Th
(n = 626)
m = 1.19 ± 0.03
b = 2.00 ± 0.03
Log Concentration Ba (μg/g)
Log Concentration Th (μg/g)
Nb vs. U
(n = 605)
m = 1.05 ± 0.02
b = 1.70 ± 0.02
Log Concentration Nb (μg/g)
Log Concentration U (μg/g)
Zr vs. Hf
(n = 603)
m = 1.10 ± 0.03
b = 1.53 ± 0.01
Log Concentration Zr (μg/g)
Log Concentration Hf (μg/g)
Y vs. Ho
(n = 330)
m = 1.01 ± 0.04
b = 1.452 ± 0.004
Log Concentration Y (μg/g)
Log Concentration Ho (μg/g)

Fig. 6.6. Log-log covariation plots of incompatible trace element pairs. Values for the slopes (*m*) and y-intercepts (*b*), which are given with 95% confidence-limits, are derived from a bivariate linear regression which accounts for uncertainties in both the x- and y-values unlike traditional univariate regressions (see Appendix C for a discussion of linear regression statistics). Slopes equal to unity ($m = 1.00$) indicate an equally incompatible pair of trace elements, whereas a slope greater than unity ($m > 1.00$) or less than unity ($m < 1.00$) indicates a more or less, respectively, incompatible element along the ordinate axis. Data for the K vs. U panel were extracted from Arevalo *et al.*, (2009). Statistical outliers, defined by data points residing outside of the "outer fence," or 3× the interquartile range, have been excluded.

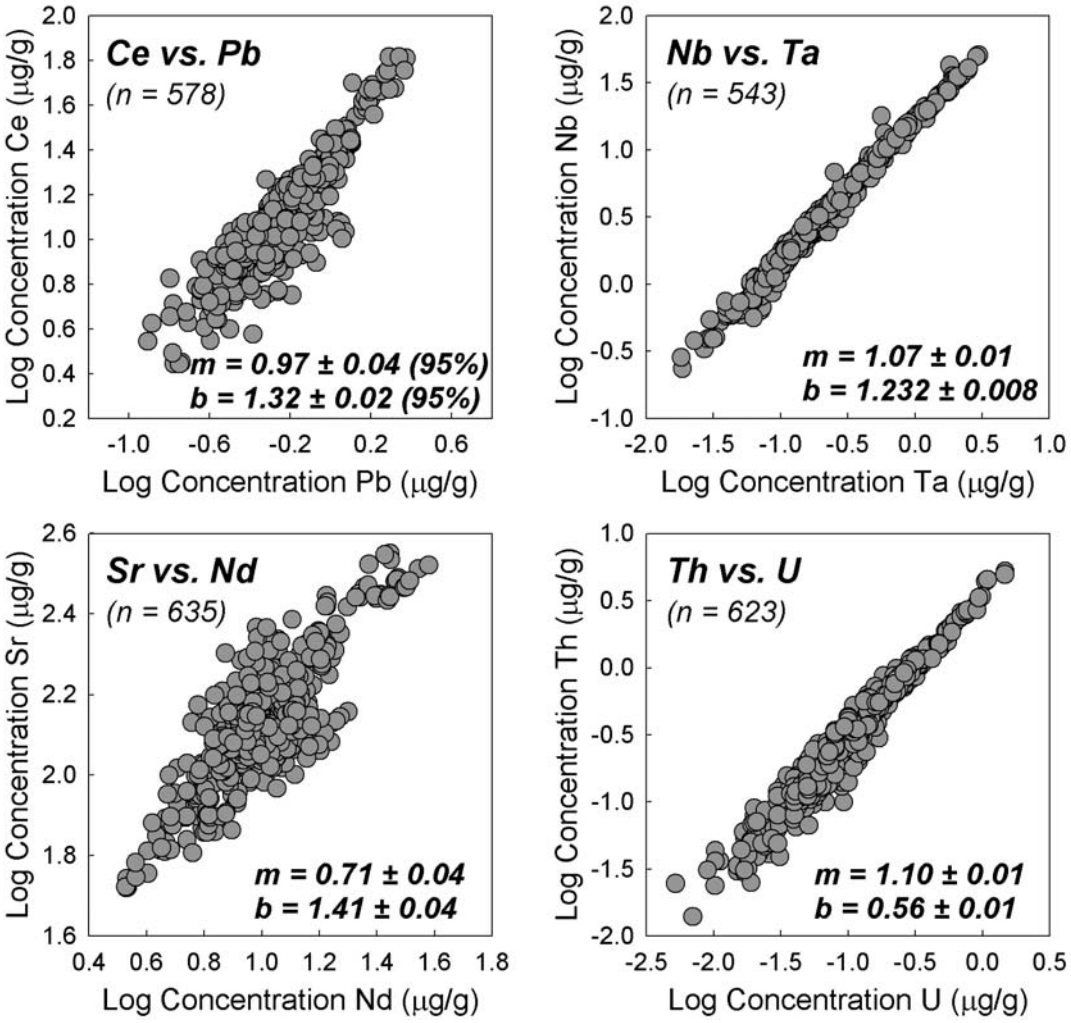

Fig. 6.7. Log-log covariation plots of incompatible trace element pairs (continued).

Table 6.3. Log-log bivariate linear regression statistics for canonical trace element pairs in global MORB and N-MORB.

	Ti vs. Eu	Ba vs. Th	Nb vs. U	Zr vs. Hf	Y vs. Ho	Ce vs. Pb	Nb vs. Ta	Sr vs. Nd	Th vs. U
Global MORB [a]									
slope[b]	0.97	1.19	1.05	1.10	1.01	0.97	1.07	0.71	1.10
± (95% conf)	0.07	0.03	0.02	0.03	0.04	0.04	0.01	0.04	0.01
y-intercept	3.849	2.00	1.70	1.53	1.452	1.32	1.232	1.41	0.56
± (95% conf)	0.009	0.03	0.02	0.01	0.004	0.02	0.008	0.04	0.01
MSWD[c]	0.15	14	8.4	0.73	0.56	15	3.0	2.0	8.2
n	651	626	605	603	330	578	543	635	623
N-MORB only									
slope[b]	0.99	1.31	1.15	1.10	1.00	0.84	1.08	0.59	1.14
± (95% conf)	0.10	0.06	0.05	0.03	0.05	0.06	0.02	0.05	0.04
y-intercept	3.849	2.11	1.82	1.53	1.453	1.26	1.243	1.51	0.60
± (95% conf)	0.010	0.05	0.06	0.01	0.004	0.02	0.015	0.05	0.04
MSWD[c]	0.16	16	9.6	0.83	0.58	16	2.9	1.8	7.0
n	529	473	452	463	280	431	405	504	469

[a] Statistical outliers plotting outside of the "outer fence," defined by 3× the interquartile range, were not considered.

[b] Regressions are derived by minimizing the sum of squares of the distances perpendicular to the best-fit line, following the protocol established in York (1966).

[c] MSWD calculated assuming a uniform uncertainty of ±5% (2σ) for both x- and y-values.

of unity within the uncertainties of the linear regression analyses, trends that are also observed when only considering N-MORB (with the exception of Ce/Pb; see discussion below); thus, these ratios do not statistically fractionate as a function of MORB source melting, mixing or subsequent emplacement and crystallization. Accordingly, the ratios observed in our global MORB database, specifically Ti/Eu = 7060 ± 1270 (2σ), Y/Ho = 28.4 ± 3.6 (2σ) and Ce/Pb = 22.2 ± 9.7 (2σ) may be inferred to represent the composition of the DMM, presuming global MORB adequately represent the compositional heterogeneity, variations in component mixing and melting/crystallization conditions of the DMM (Stracke and Bourdon, 2009). In contrast, Ba/Th, Nb/U, Zr/Hf, Nb/Ta, Sr/Nd, and Th/U yield slopes that are statistically distinct from unity in both global MORB and N-MORB, even within the uncertainties of the linear regression analyses; thus, these canonical trace element ratios fractionate (albeit only slightly for some) during MORB genesis. Interestingly, the behavior of Ce/Pb yields a statistically significant discrepancy when comparing global MORB, which include enriched samples, to N-MORB only. Our global MORB data set suggests that Ce behaves analogously to Pb during MORB genesis, but when considering only N-MORB, Pb behaves as a more incompatible element. This result suggests that the enriched component that is observed in global MORB may either: i) have a distinct lithology that partitions Ce and Pb differently than the lithology that dominates the source of depleted MORB samples; ii) be characterized by a distinct Ce/Pb ratio compared to the source of N-MORB, thus equating the discrepancy between global MORB versus N-MORB to different degrees of

component mixing; or, iii) represent a different melting or crystallization histories relative to the dominant source component that contributes N-MORB.

6.6 Variations in MORB compositions

6.6.1 Regional distinctions in log-normal mean abundances

Tables 6.1 and 6.2 summarize the representative composition of global MORB as determined primarily by the major and trace element chemistry of the comprehensive MORB data set presented here. However, regional geochemical signatures between samples derived from the Atlantic, Indian and Pacific Ocean basins may exist and potentially provide insight into the spatial and/or temporal scale and origin of heterogeneities in the DMM. Geochemical studies have previously established inter-oceanic distinctions based principally on isotopic differences (*e.g.*, Dupré and Allègre, 1983; Allègre *et al.,* 1984; Hart, 1984; Allègre *et al.,* 1987; Ito *et al.,* 1987; Mahoney *et al.,* 1989, 1992; White, 1993; Allègre *et al.,* 1995; Hofmann, 2003 and references therein).

Figure 6.8 illustrates the relative enrichment or depletion of MORB samples from each ocean basin with respect to the composition of *all* global MORB. This figure serves to qualitatively illustrate that Atlantic MORB are generally the most enriched in incompatible trace elements, whereas Pacific samples are generally the most depleted, potentially due to the prevalence of slow-spreading ridges in the Atlantic and fast-spreading ridges in the Pacific (*e.g.*, Niu and Hekinian, 1997). Overall, Indian Ocean MORB show the least variation in incompatible element

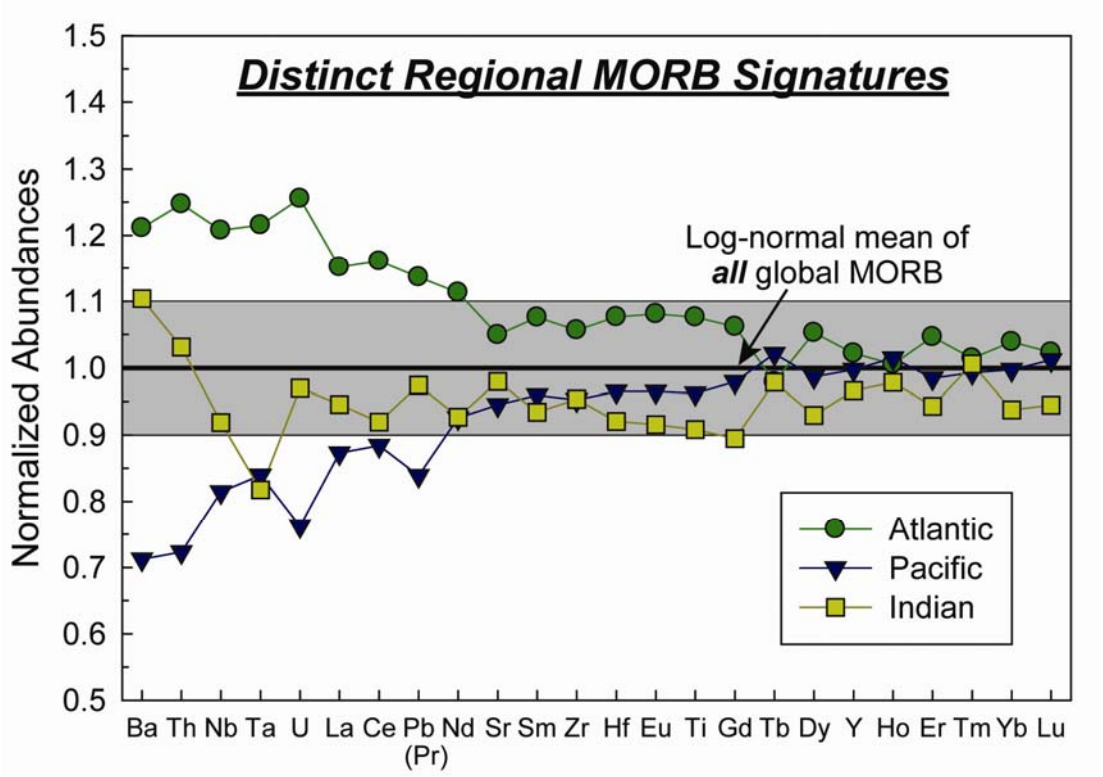

Fig. 6.8. Distinct regional geochemical signatures in trace element abundances of MORB samples derived from the Atlantic, Pacific and Indian Ocean basins. Log-normal mean abundances for MORB from each ocean basin have been normalized to the value measured in *all* global MORB. The shaded field, which represents ±10% deviations from the log-normal mean of the complete global data set, serves to highlight anomalous features, such as the enrichment of incompatible elements (*e.g.*, Ba, Th, U, and light REE) observed in Atlantic MORB compared to samples from the Pacific and Indian Oceans.

Table 6.4. Regional signatures in log-normal trace element abundances measured in MORB.

	MgO[a]	Sc	Ti	Cr	Sr	Y	Zr	Nb	Ba	La	Ce	Pr	Nd	Sm
Atlantic MORB	***7.53***	**35.9**	**9150**	**343**	**136**	**30.7**	**95.2**	**4.16**	**20.1**	**4.34**	**13.3**	**1.55**	**10.9**	**3.50**
n	310	289	310	53	304	292	304	289	286	315	301	33	299	315
Pacific MORB	***8.02***	**39.7**	**8180**	**332**	**123**	**30.0**	**85.8**	**2.81**	**11.8**	**3.29**	**10.2**	**1.75**	**9.03**	**3.12**
n	223	157	219	64	202	189	199	198	215	251	247	205	233	248
Indian MORB	***8.05***	**33.7**	**7720**	**312**	**127**	**29.0**	**85.9**	**3.16**	**18.3**	**3.56**	**10.6**	**1.78**	**9.04**	**3.04**
n	180	54	150	92	162	169	148	164	183	185	171	134	185	186
t-probabilities [b,c]														
Atlantic vs Pacific	0.0%	0.0%	0.0%	41%	0.0%	24%	0.4%	0.0%	0.0%	0.0%	0.0%	11%	0.0%	0.0%
Pacific vs Indian	91%	0.0%	1.9%	4.9%	24%	17%	98%	20%	0.0%	16%	41%	64%	97%	33%
Atlantic vs Indian	0.0%	0.3%	0.0%	2.2%	2.1%	1.0%	0.9%	0.3%	40%	0.1%	0.0%	6.9%	0.0%	0.0%

	Eu	Gd	Tb	Dy	Ho	Er	Tm	Yb	Lu	Hf	Ta	Pb	Th	U
Atlantic MORB	**1.32**	**4.67**	**0.722**	**5.38**	**1.06**	**3.30**	**0.460**	**3.11**	**0.464**	**2.58**	**0.272**	**0.647**	**0.273**	**0.100**
n	309	286	63	276	33	274	38	307	299	287	274	270	279	270
Pacific MORB	**1.18**	**4.31**	**0.754**	**5.04**	**1.07**	**3.10**	**0.450**	**2.99**	**0.459**	**2.31**	**0.188**	**0.478**	**0.158**	**0.061**
n	249	217	220	215	195	216	164	245	233	221	171	173	206	209
Indian MORB	**1.12**	**3.93**	**0.722**	**4.74**	**1.03**	**2.97**	**0.456**	**2.81**	**0.429**	**2.21**	**0.183**	**0.555**	**0.226**	**0.078**
n	171	113	154	154	139	154	104	172	170	160	117	160	163	159
t-probabilities [b,c]														
Atlantic vs Pacific	0.0%	0.1%	24%	0.2%	85%	0.3%	59%	2.4%	56%	0.0%	0.0%	0.0%	0.0%	0.0%
Pacific vs Indian	2.1%	0.3%	7.6%	1.1%	13%	5.7%	66%	0.3%	0.1%	16%	78%	0.8%	0.0%	0.7%
Atlantic vs Indian	0.0%	0.0%	100%	0.0%	57%	0.0%	84%	0.0%	0.0%	0.0%	0.0%	0.2%	6.0%	0.6%

[a] Concentrations are reported in µg/g and represent log-normal means with the exception of MgO, which represents the median and is reported in wt.%.

[b] Statistical outliers plotting outside of the "outer fence," defined by 3× the interquartile range, were not considered.

[c] Student t-test probabilities of ≤5% indicate compositions that are statistically distinct at the ≥95% confidence-level.

enrichments/depletions but appear to be depleted in the more compatible elements (*e.g.*, Sc, Ti, Cr, and heavy REE). Table 6.4 presents the log-normal mean composition of MORB derived from ridge segments from each of the three major ocean basins, as well as t-probabilities for each inter-oceanic comparison, representing the probability that MORB samples derived from two different oceanic basins originated from the same mantle source region.

Compared to MORB from the Indian and Pacific Oceans, Atlantic MORB are characterized by the lowest MgO abundances as well as statistically significant (at the ≥95% confidence-level) enrichments in most of the highly incompatible elements, including: Sr, the light REE (*i.e.*, La through Gd), Hf, Pb, Th, U, and the TITAN group elements (*i.e.*, Ti, Ta and Nb). However, the Atlantic samples also show enrichments in the more compatible heavy REE (*e.g.*, Dy, Er and Yb) compared to other MORB. Although these geochemical signatures could be indicative of a distinct Atlantic regional source with a prominent recycled component or different modal proportions of peridotitic minerals (*e.g.*, clinopyroxene due to variable proportions of a pyroxenitic source component; Stracke and Bourdon, 2009), the explanation that most easily accounts for the elevated abundances of both incompatible and compatible elements involves smaller degrees of melting or greater extents of fractional crystallization along the Mid-Atlantic Ridge, due to slow ridge spreading rates in the Atlantic (*e.g.*, Niu and Hekinian, 1997).

Opposite to Atlantic MORB, Pacific samples are distinguished by statistically relevant depletions in highly incompatible Ba, Pb, Th, and U, likely due to greater extents of melting beneath the fast-spreading centers diagnostic of Pacific ridges.

Indian samples, on the other hand, show depletions in the more compatible Sc, Ti, Cr, and heavy REE (*i.e.*, from Eu down to Lu); the origin of this geochemical signature may be attributed to a distinct source lithology in the Indian DMM and/or source melting in the garnet field.

6.6.2 Regional variations in canonical trace element ratios

Canonical trace element ratios may also be used to expose regional variations resulting from distinct source compositions, lithologies and mixing/melting/crystallization conditions. For example, Sims and DePaolo (1997) asserted that the average Ce/Pb ratio of Indian Ocean ridge segments was significantly lower than the ratio for Atlantic and Pacific ridges. Sun *et al.,* (2008), however, did not find such a deviation with regard to Ce/Pb, but instead found that the Nb/U ratio of Pacific MORB was distinct from that of Indian and Atlantic samples. As denoted by Sun *et al.,* (2008), such discrepancies between studies may be indicative of distinct DMM source compositions or simply represent sampling biases.

The average, standard deviation and median value of the canonical ratios considered here, which are by and large normally distributed, are given in Table 6.5 for global MORB as well as sample sets divided by ocean basin. Chondritic ratios and independent t-probabilities for each inter-oceanic comparison are also provided. As seen in Table 6.5, Atlantic MORB are characterized by anomalously low Ti/Eu, Ba/Th, Y/Ho, and Sr/Nd, in addition to distinct Ce/Pb and Th/U ratios relative to Pacific and Indian samples. Because Ti/Eu, Y/Ho and Ce/Pb are conserved during MORB genesis, the distinct ratios identified in Atlantic samples may be inferred to represent distinct source ratios relative to the Pacific and Indian DMM. Conversely,

Table 6.5. Regional signatures in canonical trace element ratios measured in MORB.

	Ti/Eu[a,b]	Ba/Th	Nb/U	Zr/Hf	Y/Ho[a,b]	Ce/Pb[b]	Nb/Ta	Sr/Nd	Th/U	Eu/Eu*[c]
Atlantic MORB										
Average	6950	75.0	43.8	36.9	27.4	22.2	15.8	12.7	2.88	1.000
Median	6950	76.5	43.7	36.9	27.3	22.1	15.8	12.3	2.92	0.998
2σ	1130	42.3	11.2	5.8	3.7	7.8	2.6	5.6	1.07	0.105
n	301	271	269	281	33	270	271	293	270	286
$2\sigma_m$	65	2.6	0.7	0.3	0.6	0.5	0.2	0.3	0.07	0.006
Pacific MORB										
Average	7170	81.8	47.4	37.2	28.5	23.5	15.1	13.9	2.64	0.979
Median	7140	78.0	46.6	36.9	29.3	24.8	15.4	13.9	2.54	0.973
2σ	1330	59.9	27.6	6.7	3.8	10.8	3.2	7.3	1.26	0.129
n	214	194	183	185	164	173	162	195	198	217
$2\sigma_m$	91	4.3	2.0	0.5	0.3	0.8	0.3	0.5	0.09	0.009
Indian MORB										
Average	7130	85.3	44.1	39.1	28.5	20.9	15.4	14.5	3.15	0.998
Median	7070	80.9	45.2	39.0	28.7	20.7	15.7	14.4	3.24	0.996
2σ	1380	59.0	17.1	7.5	3.0	10.6	3.9	6.0	1.63	0.085
n	136	156	154	136	138	145	107	163	158	112
$2\sigma_m$	118	4.7	1.4	0.6	0.3	0.9	0.4	0.5	0.13	0.008
Global MORB										
Average	7060	79.7	45.0	37.5	28.4	22.2	15.5	13.5	2.87	0.992
Median	7030	78.3	44.3	37.2	28.7	22.3	15.7	13.2	2.89	0.991
2σ	1270	53.3	19.2	6.8	3.6	9.7	3.2	6.5	1.35	0.112
n	651	621	606	602	335	588	540	651	626	615
$2\sigma_m$	50	2.1	0.8	0.3	0.2	0.4	0.1	0.3	0.05	0.005
CI Chondrites[d]	7900	80.8	31.7	36.1	27.5	11.2[e]	17.4	15.3	3.82	1.000
t-probabilities[f,g]										
Atlantic vs Pacific	0.0%	0.7%	0.1%	33%	0.4%	0.8%	0.0%	0.0%	0.0%	0.0%
Pacific vs Indian	57%	28%	0.8%	0.0%	88%	0.0%	29%	8.3%	0.0%	0.2%
Atlantic vs Indian	0.6%	0.0%	73%	0.0%	0.4%	1.2%	2.3%	0.0%	0.0%	72%

[a] Trace element ratios characterized by log-log covariation slopes of unity in global MORB.

[b] Trace element ratios characterized by log-log covariation slopes of unity in N-MORB with $(La/Sm)_N < 1.00$.

[c] $Eu/Eu^* = Eu_N/(Gd_N \times Sm_N)^{0.5}$.

[d] CI carbonaceous chondrite ratios taken from Palme and Jones (2003).

[e] Silicate Earth Ce/Pb ratio from McDonough and Sun (1995).

[f] Statistical outliers plotting outside of the "outer fence," defined by 3× the interquartile range, were not considered.

[g] Student t-test probabilities of ≤5% indicate compositions that are statistically distinct at the ≥95% confidence-level.

although Ba/Th, Nb/U, Zr/Hf, Nb/Ta, Sr/Nd, and Th/U show some level of statistical distinction between samples derived from Atlantic, Pacific and Indian Ocean ridge segments, these ratios are not preserved during MORB genesis (Figs. 6.6 and 6.7); thus, the mantle sources of these basalts cannot be characterized by their respective mantle derivatives, and the distinct ratios exhibited by these samples could reflect variations in mantle source heterogeneity, degrees of component mixing and/or melting/crystallization conditions.

As mentioned above, MORB samples derived from each of the three oceanic basins can be distinguished by their different Th/U ratios, which are statistically distinct at the >99% confidence-level. Statistically distinct Th/U ratios between the Atlantic, Pacific and Indian Ocean basins have been documented before (*e.g.*, Salters and Stracke, 2004) with results similar to those determined here: Indian MORB generally have the highest Th/U ratios (average Th/U = 3.15 ± 0.13, $2\sigma_m$) whereas Pacific samples represent the lowest (Th/U = 2.64 ± 0.09, $2\sigma_m$) despite similar median MgO contents, indicating a counterintuitive decoupling between MgO and Th/U in MORB. Because Th behaves more incompatibly than U, as determined by studies of MORB U-Th disequilibria (*e.g.*, Condomines *et al.,* 1981; Newman *et al.,* 1983; McKenzie, 1985; Goldstein *et al.,* 1989, 1992; Rubin and McDougall, 1992; Goldstein *et al.,* 1993; Volpe and Goldstein, 1993; Sims, 1995), the trace element chemistry of oceanic basalts (*e.g.*, Jochum *et al.,* 1983; Hofmann, 1988; Sun and McDonough, 1990) and the statistical analyses conducted here (Fig. 6.7), the Th/U ratio of the DMM must be lower than that of its derivatives. As global MORB are characterized by a mean Th/U ratio of 2.87, the global DMM must be characterized by Th/U <2.87, though we find it unlikely that the DMM is characterized by an average Th/U value of ≤2.5, as proposed by some U-Th disequilibria studies (*e.g.*, Condomines *et al.,* 1981; Newman *et al.,* 1983; Goldstein *et al.,* 1989) and models of mantle dynamics (*e.g.*, Jochum *et al.,* 1983; Turcotte *et al.,* 2001). An average DMM Th/U ratio close to 2.5 would provide further evidence for limited Th/U fractionation during crust-mantle differentiation, as both the continental crust (Th/U ≈ 4.3; Rudnick and Gao, 2003) and depleted mantle are only ≤35% different from the initial

chondritic value (Th/U = 3.82 ± 0.54; Palme and Jones, 2003). The log-normal mean abundances given in Table 6.4 reveal that the variation in Th/U is a reflection of the variability in both Th and U concentrations observed between MORB from the different oceanic basins.

Global MORB (Eu/Eu* = 0.992 ± 0.005, $2\sigma_m$) do not show a positive Eu anomaly, which would complement the negative Eu/Eu* value observed in the bulk continental crust (Rudnick and Gao, 2003), nor do the divided regional MORB data sets from the Atlantic, Pacific and Indian Oceans despite a range in median MgO values from 7.5 wt.% in the Atlantic (mean Eu/Eu* = 1.000) up to >8.0 wt.% in samples from the Pacific (mean Eu/Eu* = 0.979) and Indian (mean Eu/Eu* = 0.998). In fact, Pacific MORB exemplify a negative Eu/Eu* ratio, indicating a potential decoupling between MgO and Eu/Eu* (which are both associated with plagioclase fractionation) in global MORB. Additionally, the overall lack of a positive Eu anomaly in global MORB, despite a median MgO content of 7.84 wt.%, is counter to what has previously been postulated for relatively primitive MORB (defined by >7.6 wt.% MgO; Niu and O'Hara, 2009).

A complementary way to statistically examine distinct regional geochemical signatures as well as the relative homogenization of the DMM is through the dispersion of the data for each ocean basin. Box-and-whisker plots, such as those shown in Figure 6.9, provide a non-parametric, graphical depiction of the statistical scatter associated with a sample population; such representations may be diagnostic of the degree of source heterogeneity, component mixing and/or variation in melting/crystallization conditions of the DMM. Figure 6.9 illustrates the dispersion of

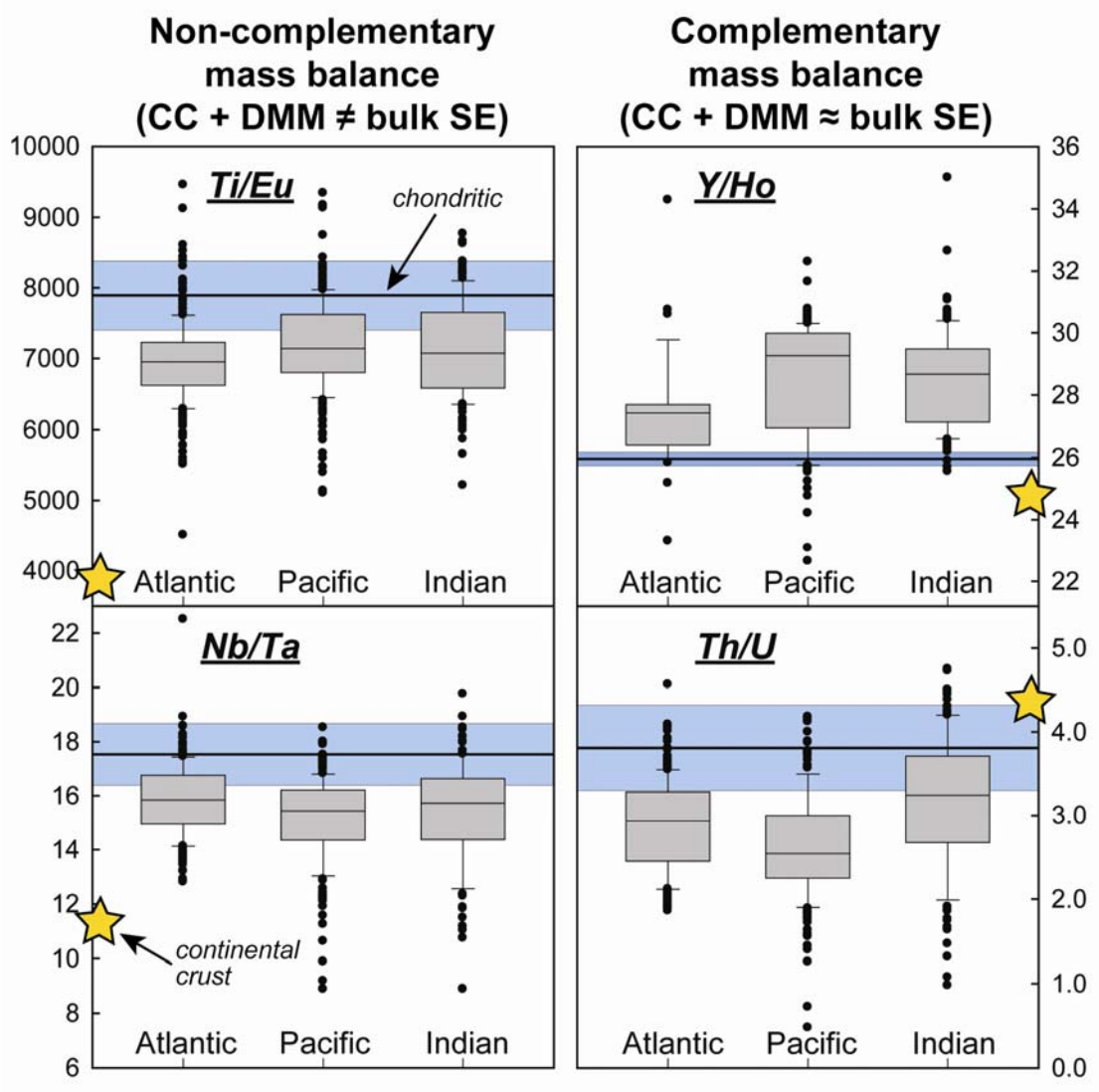

Fig. 6.9. Regional trends and box-and-whisker representations of the data dispersion for several canonical trace element ratios in Atlantic, Pacific and Indian MORB. Box-and-whisker plots provide a non-parametric way of illustrating the degree of statistical dispersion (spread) and skewness in a distribution of data. The lines located near the center of each box represent the median of the data distribution, thereby dividing the data into two equal parts. The edges of the box represent the first and third quartile of the data (also known as the interquartile range), and the whiskers represent the boundary within which 75% of the data reside. Average continental crust (Rudnick and Gao, 2003) is represented by a star (gold). A reference line for carbonaceous chondrites, as modeled by Palme and Jones (2003) for Ti/Eu, Th/U and Nb/Ta,

and Pack *et al.,* (2007) for Y/Ho, is represented by a solid line with a shaded (blue) uncertainty field. Global MORB, and by inference the DMM, are largely characterized by super-chondritic Y/Ho and sub-chondritic Th/U ratios; these geochemical signatures are balanced by the bulk continental crust, which is characterized by sub-chondritic Y/Ho and super-chondritic Th/U. However, the bulk continental crust and median global MORB are both characterized sub-chondritic Ti/Eu and Nb/Ta ratios, requiring an under-sampled terrestrial reservoir with a complementary enrichment of Ti/Eu and Nb/Ta, such as refractory, rutile-bearing eclogite (*e.g.*, McDonough, 1991; Rudnick *et al.,* 2000).

Ti/Eu, Y/Ho, Nb/Ta and Th/U observed in each of the major ocean basins. Because Ti/Eu and Y/Ho are not fractionated during MORB genesis (and Nb/Ta and Th/U are only fractionated slightly; Fig. 6.6), the ratios measured in MORB may be inferred to be representative of the DMM. As shown in Figure 6.9, Ti/Eu, Y/Ho, Nb/Ta, and Th/U are distinct in most MORB relative to the chondritic value. The enriched Y/Ho and depleted Th/U ratios observed in most global MORB, however, are balanced by the depleted Y/Ho and enriched Th/U ratios found in the continental crust, thus reconciling the silicate Earth (as modeled by the MORB source region + continental crust) with chondrites. Interestingly, Ti/Eu and Nb/Ta are found to be sub-chondritic in both the median of global MORB and the bulk continental crust, requiring an under-represented terrestrial reservoir with a complementary enrichment in Ti and Nb somewhere in the silicate Earth (*e.g.*, refractory, rutile-bearing eclogite at depth in the mantle; McDonough, 1991; Rudnick *et al.,* 2000) or core.

6.7 Conclusions

We have augmented a set of new, high-precision LA-ICP-MS measurements of a global spectrum of MORB samples with a critically compiled collection of analyses from several high-quality, peer-reviewed data sets. From the comprehensive MORB database assembled here, we have developed a compositional model for global MORB as well as N-MORB only (defined by $(La/Sm)_N < 1.00$) for comparison. Additionally, we have statistically evaluated the constancy of canonical trace element ratios through MORB genesis and investigated distinct regional geochemical

signatures between samples derived from the Atlantic, Pacific and Indian Ocean basins.

Global MORB represent a more incompatible-element enriched composition than previously suggested by earlier geochemical models (*c.f.*, Hofmann, 1988; Sun and McDonough, 1989; Su, 2002). Because Ti/Eu (global MORB mean = 7060 ± 1270, 2σ), Y/Ho (28.4 ± 3.6, 2σ) and Ce/Pb (22.2 ± 9.7, 2σ) do not significantly fractionate as a function of MORB genesis (at the 95% confidence-level), the ratios recorded in global (and regional) MORB likely represent the values of the DMM, presuming the source heterogeneity, degree of source component mixing and variations in melting/crystallization conditions of the DMM are adequately represented by the inclusive MORB database compiled here. Alternatively, Ba/Th, Nb/U, Zr/Hf, Nb/Ta, Sr/Nd, and Th/U are all significantly fractionated during MORB genesis and may not be inferred to represent the DMM.

Atlantic MORB are characterized by statistically significant enrichments in the incompatible trace elements, including Sr, the light REE, Hf, Pb, Th, U, and TITAN group elements, as well as enrichments in the more compatible heavy REE (*e.g.*, Dy, Er and Yb); these geochemical attributes, along with the low MgO content associated with Atlantic MORB (median MgO = 7.54 wt.%) compared to Pacific (8.03 wt.% MgO) and Indian MORB (8.05 wt.% MgO), are likely the result of smaller degrees of melting or greater extents of fractional crystallization due to slow ridge spreading rates along the Mid-Atlantic Ridge. Conversely, MORB derived from Pacific spreading centers are generally characterized by the lowest abundances of highly incompatible Ba, Pb, Th, and U, likely due to greater extents of melting

beneath the fast-spreading centers diagnostic of Pacific ridges. Indian MORB, on the other hand, exhibit depletions in the more compatible Sc, Ti, Cr, and heavy REE (*i.e.*, from Eu down to Lu), a geochemical signature that may be attributed to a distinct source lithology in the Indian DMM and/or deep source melting in the garnet field. Similar to the continental crust, global MORB and by inference the DMM are defined by sub-chondritic Ti/Eu and Nb/Ta ratios, requiring a complementary Ti- and Nb-rich reservoir somewhere in the silicate Earth (*e.g.*, rutile-bearing eclogite) or core.

Chapter 7: A Compositional Model for the Source(s) of Hawaiian Lavas and Other OIB[1,2,3]

[1] R. Arevalo Jr. measured the trace element data reported in Sections 7.1 through 7.7, with the assistance of T.J. Ireland. T.J. Ireland, R. Arevalo Jr., R.J. Walker, and W.F. McDonough all contributed to the interpretation of the data. The text, tables and figures were written/created by T.J. Ireland (~70%) and R. Arevalo Jr. (~30%).

[2] Sections 7.1 through 7.7 of this chapter have been published as:
Ireland, T.J., Arevalo Jr., R., Walker, R.J., and McDonough, W.F., 2009. Tungsten in Hawaiian picrites: A compositional model for the sources of Hawaiian lavas. *Geochimica Cosmochimica Acta* (73), 4517–4530, doi:10.1016/j.gca.2009.04.016.

[3] A. Stracke and M. Willbold measured the trace element data reported in Section 7.8. R. Arevalo Jr. and W.F. McDonough explored the data. The melting calculations, OIB model, text, table, and figures were written/created by R. Arevalo Jr.

7.1 Abstract

Concentrations of tungsten (W) and uranium (U), which represent two of the most highly incompatible elements during mantle melting, have been measured in a suite of Hawaiian picrites and primitive tholeiites from nine main-stage shield volcanoes. Tungsten abundances in the parental melts are estimated from correlations between sample W abundances and MgO contents, and/or by olivine correction calculations. From these parental melt determinations, along with independent estimates for the degree of partial melting at each volcanic center, we extrapolate the W content of the mantle sources for each shield volcano. The mantle sources of Hualalai, Mauna Loa, Kohala, Kilauea, Mauna Kea, Koolau and Loihi contain 9 ± 2 (2σ) ng/g, 11 ± 5 ng/g, 10 ± 4 ng/g, 12 ± 4 ng/g, 10 ± 5 ng/g, 8 ± 7 ng/g and 11 ± 5 ng/g respectively. When combined, the mean Hawaiian source has an average of 10 ± 3 ng/g W, which is three-times as enriched as the Depleted MORB Mantle (DMM; 3.0 ± 2.3 ng/g).

The relatively high abundances of W in the mantle sources that contribute to Hawaiian lavas may be explained as a consequence of the recycling of W-rich oceanic crust and sediment into a depleted mantle source, such as the depleted MORB mantle (DMM). However, this scenario requires varying proportions of recycled materials with different mean ages to account for the diversity of radiogenic isotope compositions observed between Kea- and Loa-trend volcanoes. Alternatively, the modeled W enrichments may also reflect a primary source component that is less depleted in incompatible trace elements than the DMM. Such a source would not necessarily require the addition of recycled materials, although the presence of some recycled crust is permitted within our model parameters and likely accounts for some of the isotopic variations between volcanic centers.

The physical admixture of ≤0.5 wt.% outer core material with the Hawaiian source region would not be resolvable via W source abundances or W/U ratios; however, W isotopes may provide a more sensitive to this mixing process. Recent W isotopic studies show no indication of core-mantle interaction, indicating that either such a process does not occur, or that mechanisms other than physical mixing may operate at the core-mantle boundary.

7.2 Introduction

The distinct geochemical behavior of tungsten (W) makes this element particularly suitable for addressing a range of geologic phenomena, including constraining the proportion of recycled crustal materials in mantle source regions and identifying potential core-mantle interactions in ocean island basalts (OIB). Tungsten behaves as

a moderately siderophile (iron-loving) element under reducing conditions, which has resulted in the sequestration of ≥90% of the terrestrial W budget into the core (Jagoutz *et al.,* 1979; Sun, 1982; Newsom and Palme, 1984; McDonough, 2003). Under the more oxidized conditions prevalent in the silicate portion of the Earth, however, W behaves as a highly incompatible element and strongly partitions into liquid phases during mantle melting. Consequently, core-mantle segregation and the production of oceanic and continental crust has depleted the mantle in W. Due to the large contrast in W abundances between the mantle and both the crust and core, W concentrations and elemental ratios may provide useful geochemical tracers of physical mixing between these reservoirs (Arevalo and McDonough, 2008).

The Hawaiian source, which represents the greatest mantle buoyancy flux (Sleep, 1990) and hottest potential temperature (*e.g.*, Putirka, 2008) of any modern intraplate ocean island, serves as an archetype of OIB volcanism. Consequently, primitive Hawaiian lavas may provide new insight to the utility of W as a geochemical tracer for both crustal recycling and core-mantle interactions. There is abundant geochemical support for the incorporation of recycled oceanic crustal materials into the mantle sources of the Hawaiian main-shield stage volcanoes (*e.g.*, Bennett *et al.,* 1996; Eiler *et al.,* 1996; Hauri, 1996; Hofmann and Jochum, 1996; Lassiter and Hauri, 1998; Blichert-Toft *et al.,* 1999; Sobolev *et al.,* 2000, 2005). The source region of the Hawaiian shield volcanoes has also been suggested to extend as deep as the core-mantle boundary, based on geophysical evidence (*e.g.*, Russell *et al.,* 1998; Zhao, 2001; Courtillot *et al.,* 2003; Montelli *et al.,* 2004), as well as geochemical evidence based on Os isotopes and Fe/Mn ratios (*e.g.*, Brandon *et al.,*

1999; Humayun *et al.,* 2004). Tungsten isotopes have been implicated as a useful proxy to assess a potential core contribution to the Hawaiian source (Scherstén *et al.,* 2004; Hawkesworth and Scherstén, 2007). Although W studies have not identified a core signature in Hawaiian lavas, an important aspect of W isotopic modeling is the accurate estimation of W abundances in the mantle sources.

Traditionally, the budget of W in mantle reservoirs (*e.g.*, Newsom and Palme, 1984; Newsom *et al.,* 1986; Sims *et al.,* 1990; Arevalo and McDonough, 2008) and the continental crust (*e.g.*, Rudnick and Gao, 2003; Hu and Gao, 2008) has hinged on relating well-established lithophile element abundances (*e.g.*, Ba, Th and U) to W via relatively constant concentration ratios in mid-ocean ridge basalts (MORB), mantle peridotites and crustal samples. Here, we report W and U concentrations for a suite of Hawaiian picritic lavas that represent primitive melts from the Hawaiian source region. As both W and U are highly incompatible elements, the relative abundances of these elements in a partial melt of the mantle reflect the composition of the source. The main objective of this study is to constrain the abundance of W in the mantle sources that feed the Hawaiian main-stage shield volcanoes by relating sample W concentrations to that of an estimated parental melt for each volcanic center. By establishing the mantle source abundances of W, we seek to evaluate the processes that may have contributed to these sources.

7.3 Samples and methods

The suite of picrites (≥13 wt% MgO; n = 22) and associated tholeiitic basalts (9-12 wt% MgO; n = 4) examined here include some of the most primitive melts from the

Hawaiian source region and spans a wide range in MgO, indicative of both olivine removal (low-MgO) and accumulation (high-MgO; Norman and Garcia, 1999). The picrites were derived from high density melts that erupted on the flanks of the main-stage shield volcanoes and bypassed the summit reservoirs (Garcia *et al.,* 1995). Hence, these lavas are less likely to have been affected by fractionation and/or assimilation processes that may operate in high-level magma chambers (Norman and Garcia, 1999), and thus are the best samples available to constrain the abundances of highly incompatible elements (*e.g.*, W and U) in the mantle sources of Hawaiian lavas. Samples were obtained from submersible dives and submarine dredge hauls that sampled the flanks of the Hawaiian volcanoes, as well as from subaerial collection (Table 7.1). Nine volcanic centers are represented here, including Mauna Kea, Mauna Loa, Hualalai, Loihi, Kilauea, Koolau, Kohala, Lanai and Molokai. Two high-MgO alkalic basalts (186-5 and 187-1) and a basanitoid (186-11) from Loihi were also analyzed in this study for comparison.

In order to obtain precise concentrations of W and U, glassy and/or microcrystalline sample sections were analyzed via laser ablation inductively-coupled plasma mass spectrometry (LA-ICP-MS) following the analytical procedures of Arevalo and McDonough (2008). The utility and reliability of in-situ laser ablation methods for measuring trace elements in geologic materials have been previously validated through numerous analytical studies (*e.g.*, Pearce *et al.,* 1997; Eggins *et al.,* 1998; Norman *et al.,* 1998; Jochum *et al.,* 2005, 2006, 2007). Additionally, LA-ICP-MS methods allow for: i) the identification and analysis of unaltered sample surfaces; ii) low analytical blanks; iii) minimal sample destruction; and, iv) spatially resolved

concentration measurements with typical lower limits of detection in the sub-ng/g range. The rocks examined in this study were analyzed using a New Wave frequency-quintupled Nd-YAG laser (213 nm light) coupled to a Thermo Finnigan Element2 single-collector ICP-MS at the University of Maryland.

Table 7.1. W and U abundance data for Hawaiian picrites.

Volcano	Sample Name	MgO_{wr} (wt%)[e]	W_{glass} (ng/g)	$2\sigma_m$	U_{glass} (ng/g)	$2\sigma_m$	W/U	%ol calc[g]	%ol point count	# points	W_{wr} (ng/g)[h]	$2\sigma_m$	U_{wr} (ng/g)	$2\sigma_m$
Mauna Kea														
	MK-1-6[a]	17.24	170	2	307	1	0.55	27	23	500	124	3	225	4
Mauna Loa														
	ML-2-50[a]	19.92	121	3	182	5	0.66	33			81	2	122	4
	ML KAH-1	21.66	171	10	297	26	0.57		34	500	113	10	196	21
	ML 1868-9	21.48	162	3	248	7	0.65		36	1000	103	5	159	8
Hualalai[a]														
	H-2	13.63	114	4	178	5	0.64	20	19	500	91	4	142	5
	H-7[b]	11.23	107	3	177	7	0.60	13	13	500	93	4	155	7
	H-9[b]	11.30	125	5	194	7	0.65	12	14	500	110	5	170	8
	H-11	13.67	113	2	161	4	0.70	18	18	500	92	3	132	4
	H-27	14.91	108	3	165	4	0.65	21			85	3	130	4
	H-P	23.19	102	3	161	5	0.63	40	44	1000	61	2	97	3
	average olivine[f]	47.73												
Loihi[a]														
	LO-02-02	24.21	265	4	337	11	0.79	40			158	4	202	7
	LO-02-04	26.58	313	6	365	7	0.86	56			139	3	162	4
	158-9	16.57	414	8	763	31	0.54	23			320	9	589	27
	186-5[c]	19.52	352	4	480	10	0.73		30	1000	247	12	336	18
	186-11[d]	13.76	572	11	739	13	0.77		21	1000	452	32	584	37
	187-1[c]	25.16	223	3	308	7	0.72	46			121	3	167	5
	average olivine[f]	46.80												
Kilauea														
	KIL-1-18[a]	13.80	165	5	361	9	0.46		15	1000	140	11	307	24
	KIL-2-3[a]	22.36	184	2	317	4	0.58		40	500	110	6	190	11
	KIL-2-4[a]	22.55	213	3	373	7	0.57	40			127	3	373	8
	KIL-3-1[a]	19.24	230	6	429	8	0.54	33			155	5	288	7
	KIL 1840-2	14.27	230	6	406	16	0.57		21	500	182	17	321	30
	average olivine[f]	48.15												
Koolau														
	K98-08	17.78	36	4	164	16	0.22		29	500	25	3	116	14
	S497-6[a]	21.55	198	24	306	22	0.65		42	500	115	15	177	16
	S500-5B[a]	21.22	109	2	170	1	0.64	39			67	2	104	2
Kohala[a]														
	KO-1-10	13.54	164	4	262	3	0.62		20	500	131	12	210	19
	KO-1-20[b]	9.60	199	10	316	16	0.63	10	10	500	180	11	286	17
	KOH-1-28	20.52	157	5	254	12	0.62	35			102	4	165	8
	average olivine[f]	47.53												
Lanai														
	LWAW-4	14.48	62	5	121	6	0.51		15	1000	53	6	103	9
	LWAW-7[b]	11.69	79	4	174	7	0.45		9	1000	72	8	158	17
Molokai[a]														
	S501-2	28.96	98	3	212	12	0.46	52	51	500	47	2	102	6

[a] Submarine sample.

[b] Tholeiitic basalt (MgO < 13 wt%).

[c] Alkali basalt.

[d] Basanitoid.

[e] MgO contents from Ireland et al. (2009) and references therein.

[f] Average olivine MgO content from Ireland et al. (2009).

[g] See table S1 for correction procedure.

[h] Example correction calculation: The matrix for MK-1-6 contains 170 ng/g W and olivine comprises 27% of this sample. The matrix concentration was converted to a whole rock concentration by accounting for the olivine present using the following formula: W(wr) =W(matrix) * (1 – ol%). Following this calculation, the whole rock W concentration for MK-1-6 is 124 ng/g.

Spectral matrix effects, particularly isobaric interferences from potential diatomic oxides, were limited by implementing a standard tuning procedure that maximized the elemental signal (based on ^{43}Ca and ^{232}Th spectra) and minimized oxide production ($^{232}Th^{16}O/^{232}Th < 0.15\%$). Our method monitored four W isotope mass stations (^{182}W, ^{183}W, ^{184}W, and ^{186}W) and the ratios of these isotopes in order to ensure that no isobaric interferences hindered our concentration measurements. Non-spectral matrix effects resulting from differences in chemical compositions between the analyte and a standard reference material were accounted for by externally calibrating our W measurements to multiple tholeiitic basalts and our U analyses to a suite of silicate reference glasses spanning a range in concentration. The basaltic standards were measured via solution ICP-MS, including both isotope dilution and high-precision standard addition analyses. Details on the calibration of our trace element analyses and the specific laser and mass spectrometer parameters utilized for the measurements of this study are reported in Arevalo and McDonough (2008).

Following determination of trace element abundances in the glassy and/or microcrystalline matrices, data were corrected to whole rock values by accounting for the dilutional effect of olivine, the only major phenocryst phase present. Olivine phenocrysts analyzed in this study had W and U concentrations at or below our analytical limits of detection (<1.0 ng/g). The modal fraction of olivine in each sample was independently determined by point counting of thin sections (between 500 and 1000 points each) and/or mass balance of MgO abundances in the matrix, olivine and whole rock. To test the robustness of these methods, both techniques were applied to several samples with consistent results (see Appendix D).

The precision of the matrix W and U concentrations were not limited by counting statistics and are typically reported with ≤5% uncertainty ($2\sigma_m$; external reproducibility), which translates to uncertainties of ≤6% and ≤10% in the whole rock calculations via mass balance and point counting respectively. Major element abundances, as well as average olivine compositions, were previously reported by Ireland *et al.,* (2009). The current study includes samples previously examined by Brandon *et al.,* (1999; ML 2-50, ML 1868-9, Lo-02-02, Lo-02-04, H-11, Kil 1-18, KOH 1-28) for which a core contribution was inferred based on coupled enrichments of ^{186}Os and ^{187}Os, as well as three samples analyzed by Scherstén *et al.,* (2004) for their W isotopic compositions.

7.4 Tungsten in Hawaiian picrites

Tungsten and U concentration data and W/U ratios for samples from nine Hawaiian shield volcanoes are presented in Table 7.1. The calculated whole-rock abundances of W in the Hawaiian picrites range from as low as 25 ng/g (Koolau sample K98-08) up to 458 ng/g (Loihi sample 186-11). The highest W (and U) concentrations were observed in the alkalic basalt (186-5 and 187-1), pre-shield picrite (158-9) and basanitoid (186-11) samples from Loihi, which are representative of the pre-shield stage of volcanism and likely represent different sources and lower degrees of melting than the later shield stage volcanics (Garcia *et al.,* 1995). Koolau sample S500-5B was reported to have been affected by Mn-crust alteration by Ireland *et al.,* (2009); however, the rock section analyzed in this present study was carefully selected to avoid the obvious alteration and no apparent effect was noticed. A duplicate

measurement of the matrix of sample H-11, which was previously analyzed by Arevalo and McDonough (2008), was found to be statistically indistinguishable from the previously reported value.

Although the calculated whole-rock W concentrations of the entire Hawaiian picrite suite appear to show no correlation with MgO (a proxy for crystal-liquid fractionation processes), data for several individual volcanic centers show linear trends (Figs. 7.1A and 7.2). In general, W abundances decrease with increasing MgO content at each main-stage shield volcano, reflecting the highly incompatible nature of W; Mauna Loa and Koolau appear to serve as exceptions, although each of these volcanoes are represented by only 3 samples that span a narrow range in MgO.

The W/U ratio of the silicate Earth (0.65 ± 0.45, 2σ) has been demonstrated to be invariant between mantle and crustal sources and is independent of bulk rock MgO, indicating analogous behavior of these elements during mantle melting and crystal-liquid fractionation (Arevalo and McDonough, 2008). The average W/U ratio of our suite of primitive Hawaiian lavas is 0.62 ± 0.19 (2σ; Fig. 7.1B), consistent with the terrestrial average. However, Koolau sample K98-08, which has the lowest W concentration (25 ng/g) of the samples analyzed here but a typical U content (115 ng/g), has an anomalously low W/U ratio (W/U = 0.22). This value is outside of the range of our picritic dataset, and is suggestive of a preferential loss of W, perhaps due to alteration effects. Hualalai lavas, in general, have the lowest W abundances (average of 90 ng/g; n=6), but possess normal W/U ratios (0.65 ± 0.06). Conversely, Loihi lavas are characterized by the highest W concentrations (up to 458 ng/g; n = 6)

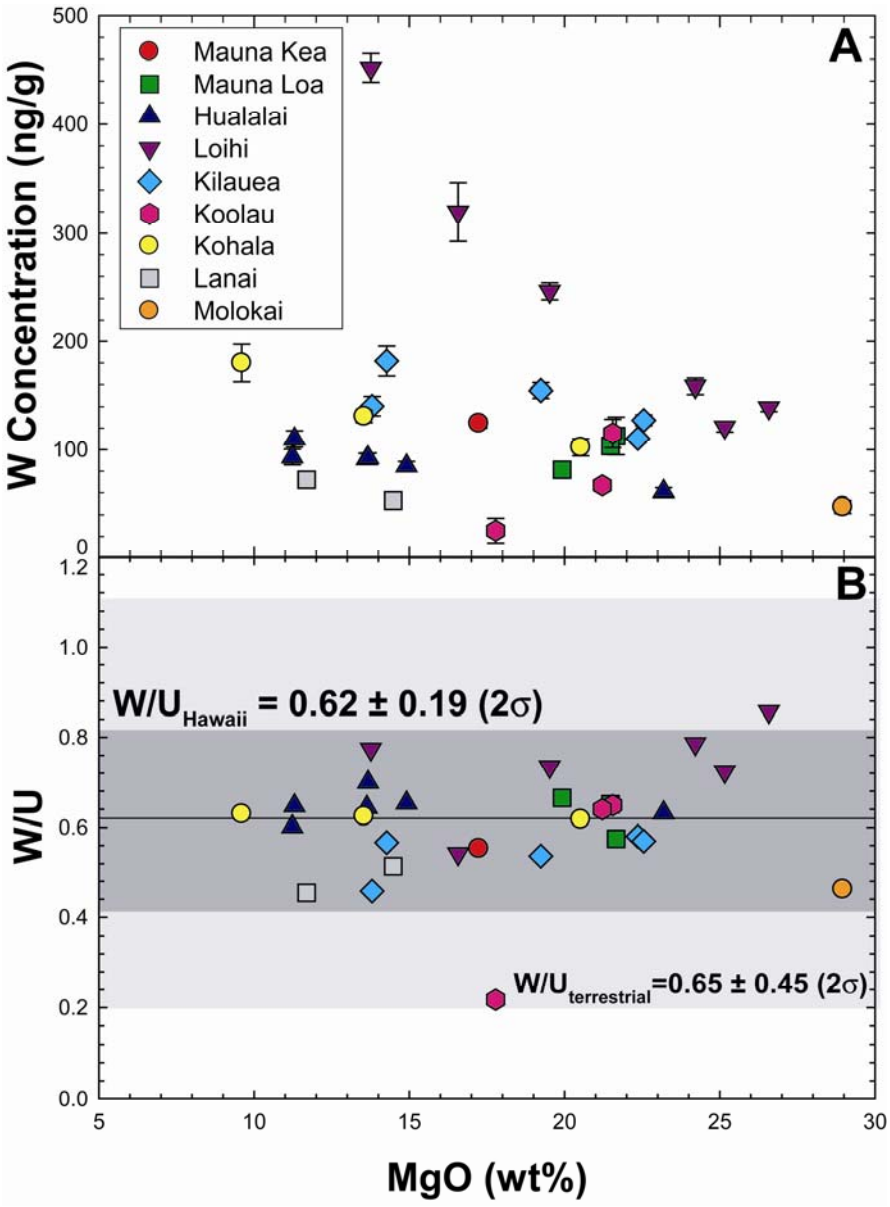

Fig. 7.1. (A) Tungsten versus MgO content for the primitive Hawaiian lavas analyzed in this study. Tungsten concentrations were determined by high-precision laser ablation ICP-MS following the analytical protocol of Arevalo and McDonough (2008). In general, W abundances decrease with increasing MgO content at each individual volcanic center with ≥3 samples (with the exception of Koolau). (B) The average W/U ratio of primitive Hawaiian melts (0.62 ± 0.19; dark shaded area) does not vary as a function of MgO and is identical to the terrestrial value established by Arevalo and McDonough (2008; 0.65 ± 0.45; lightly shaded area).

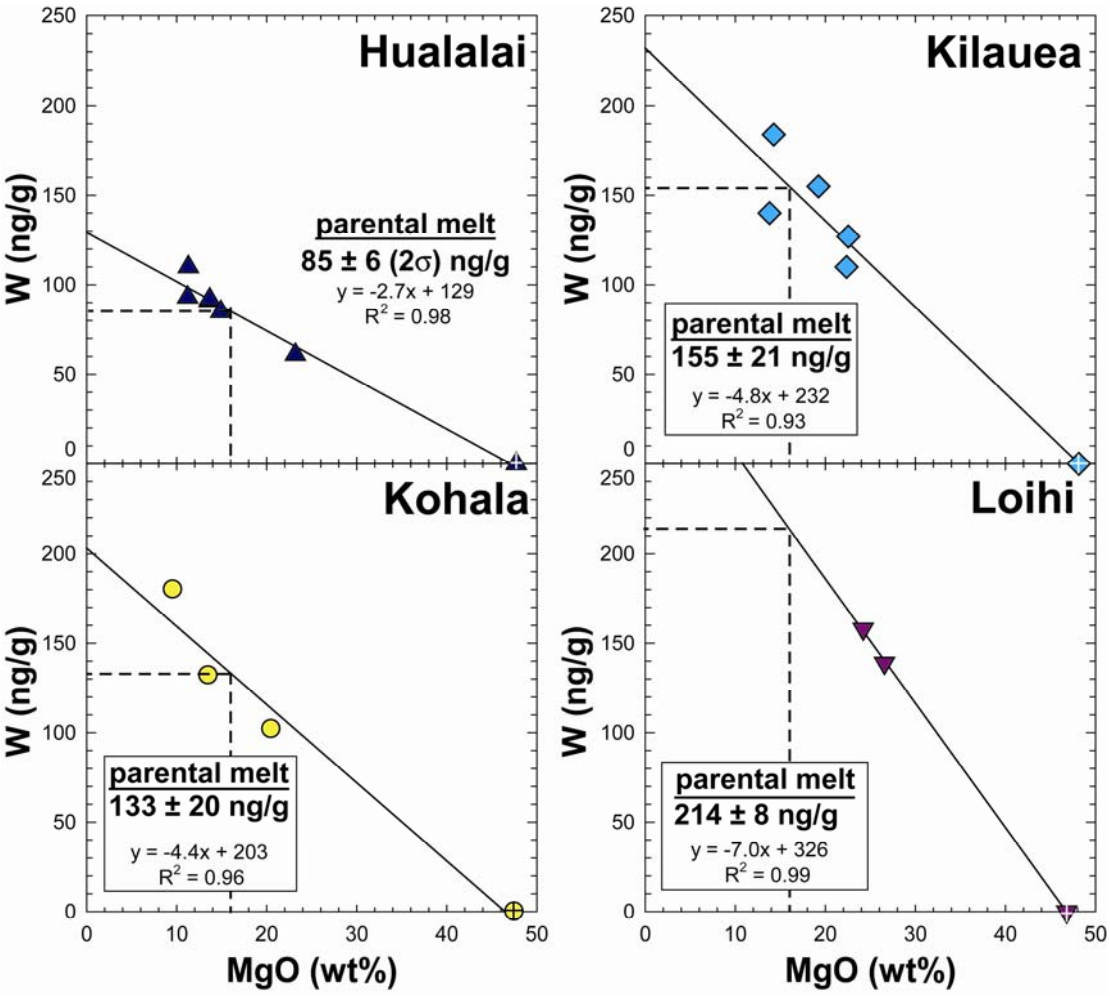

Fig. 7.2. Estimated concentrations of W (in ng/g) in parental melts from the Hualalai, Kilauea, Kohala and Loihi main-stage shield volcanoes. Tungsten abundances were determined from the intersection of the linear regressions of the data with 16 ± 1 wt% MgO, the parental melt MgO content as determined by Norman and Garcia (1999) and Ireland *et al.*, (2009). Co-existing olivine, which contains negligible W, is also plotted as part of the MgO-W trends and is denoted by the crossed symbols.

and W/U ratios (0.74 ± 0.21), although they reside within the range of variance defined by mantle-derived rocks.

Although visibly fresh rock chips were selected for analysis, several samples show evidence for alteration. Lanai samples LWAW-4 and LWAW-7, and Molokai sample S501-2 have high LOI values, as well as low alkali abundances (Ireland *et al.,* 2009), which are indicative of fluid-rock reactions involving the breakdown of igneous minerals (Crocket, 2000). These three samples also have low W concentrations and W/U ratios, suggesting that W may be affected by this alteration process to a slightly greater extent than U. Sample K98-08 may have been affected by a similar alteration process, although it is not reflected in the LOI or alkali abundances for this sample. Norman and Garcia (1999) noted high LOI contents for Lo-02-02 and Lo-02-04, but concluded that this feature was not due to alteration because Pb isotope, trace element and alkali characteristics were similar to other lavas from Loihi.

7.5 The W content of Hawaiian mantle sources

To model the mantle source W composition for each volcanic center considered here, various critical parameters must be estimated, including a suitable bulk crystal/melt partition coefficient (D) for W during mantle melting, the W content of the parental melts from each volcanic center and the degree of partial melting (F). As mentioned previously, W partitions in a similar manner to U during mantle melting, so a bulk crystal/melt partition coefficient of 0.001 is used. This estimate is similar to that determined for U in basaltic melts and partitioning experiments (0.001 to 0.0001; *e.g.*,

www.earthref.org/GERM). Sections 7.5.1 and 7.5.2 document our procedures for estimating the parental melt compositions for the Hawaiian shield volcanoes, and the degree of partial melting.

7.5.1 W content of Hawaiian parental melts

Parental melts are primary magmas produced from a mantle source region with minimal fractionation or contamination, and thus, can be used to place constraints on the composition of the source. Based on whole rock MgO and Al_2O_3 relationships of the samples analyzed in this study, in addition to olivine-melt equilibria, the parental melts for all of the Hawaiian shield volcanoes have been established to contain 16 ± 1 (2σ) wt% MgO (Norman and Garcia, 1999; Ireland *et al.,* 2009). Two different techniques were used to constrain the W content of the Hawaiian parental melts. The first method utilizes a linear regression of the MgO-W trends, as well as the average olivine composition for each volcanic center, to interpolate the W content at the primary MgO content of 16 ± 1 wt.%. The second approach is to individually correct each sample for olivine accumulation or removal to a MgO content of 16 wt.% and take an average of the samples at each volcanic center. The second technique is independent of the shape of the MgO-W trends and is more appropriate for those volcanic centers that do not show a linear correlation or are represented by few samples. For these estimations, it is essential that only those picritic and tholeiitic samples that are most likely to represent a parental melt of similar initial composition are used; therefore, the alkali basalts (186-5 and 187-1), pre-shield picrite (158-9) and the basanitoid (186-11) from Loihi that likely represent a different source from the

Loihi shield picrites, as well as samples that may have experienced alteration (*i.e.* LWAW-4, LWAW-7 and S501-2) are not considered in the following exercise.

Although the MgO content of Hawaiian picrites vary, primarily as a result of olivine accumulation and/or removal, the W content of the parental melts can be estimated by the intersection between the linear regressions of the MgO-W data and the determined parental melt MgO content of 16 ± 1 wt.% (Fig. 7.2). Since olivine is the only major phenocryst phase present, these regressions represent olivine control lines and the average composition of co-existing olivine for each volcanic center is also plotted as part of the trend (Fig. 7.2 and Table 7.1). As mentioned previously, olivine contains negligible concentrations of W (and U), so the linear regressions should intersect the MgO axis at an equivalent MgO content as the average olivine. This method was employed for four of the Hawaiian shield volcanoes, with the parental melts from Hualalai, Kohala, Kilauea and Loihi estimated to contain 85 ± 6 (2σ) ng/g, 133 ± 20 ng/g, 155 ± 21 ng/g and 214 ± 10 ng/g W, respectively (Table 7.2).

A second way to determine the W abundance of a Hawaiian parental melt is to individually correct each sample for olivine accumulation or removal to 16 wt.% MgO (*e.g.*, Garcia *et al.,* 1995; Hauri, 1996; Danyushevsky *et al.,* 2000; Huang and Frey, 2003). For samples that have lost olivine (MgO<16 wt.%), equilibrium olivine was mathematically added in 0.1% increments until the calculated whole rock MgO content reached 16 wt.% MgO following the procedure of Danyushevsky *et al.,* (2000). Likewise, for samples with accumulated olivine, Fo_{90} olivine (corresponding to the most magnesian olivine present in the sample suite) was subtracted from the

Table 7.2. Estimates of the source composition of Hawaii from various shield volcano parental melts.

Hawaiian Shield Volcano	Hualalai	Mauna Loa	Kohala	Kilauea	Mauna Kea	Koolau	Loihi
Method 1							
Parental Melt W (ng/g)	85 ± 6	-	133 ± 20	155 ± 21	-	-	214 ± 10
Degree of Partial Melting (F)	7.5-12.5	-	5-10	5-10	-	-	2.5-7.5
Mantle Source W (ng/g)	9 ± 2	-	10 ± 4	12 ± 4	-	-	11 ± 5
Linear Regression Results							
Slope	-2.7 ± 0.2	-	-4.4 ± 0.6	-4.8 ± 0.7	-	-	-7.0 ± 0.1
y-intercept	129 ± 4	-	203 ± 16	232 ± 18	-	-	326 ± 4
Parental Melt U (ng/g)	132 ± 10	-	212 ± 30	290 ± 30	-	-	263 ± 31
Degree of Partial Melting (F)	7.5-12.5	-	5-10	5-10	-	-	2.5-7.5
Mantle Source U (ng/g)	13 ± 3	-	16 ± 6	22 ± 8	-	-	13 ± 7
Linear Regression Results							
Slope	-4.3 ± 0.3	-	-6.9 ± 0.9	-9.2 ± 0.9	-	-	-8.6 ± 0.8
y-intercept	200 ± 7	-	324 ± 25	437 ± 24	-	-	400 ± 26
Method 2							
Parental Melt W (ng/g)	83 ± 18	111 ± 40	129 ± 39	149 ± 42	127 ± 46	104 ± 84	185 ± 20
Degree of Partial Melting (F)	7.5-12.5	7.5-12.5	5-10	5-10	5-10	5-10	2.5-7.5
Mantle Source W (ng/g)[a]	8 ± 3	11 ± 5	10 ± 4	11 ± 5	10 ± 5	8 ± 7	9 ± 5
Parental Melt U (ng/g)	129 ± 27	178 ± 40	206 ± 60	276 ± 77	231 ± 83	161 ± 127	225 ± 51
Degree of Partial Melting (F)	7.5-12.5	7.5-12.5	5-10	5-10	5-10	5-10	2.5-7.5
Mantle Source U (ng/g)[a]	13 ± 4	13 ± 4	15 ± 7	21 ± 9	17 ± 9	12 ± 10	13 ± 7
Averages							
Mantle Source W (ng/g)[b]	10 ± 3						
Mantle Source U (ng/g)[b]	15 ± 7						

[a] A bulk crystal/melt partition coefficient (D) of 0.001 was assumed for both W and U mantle source calculations.
[b] Averages calculated using *Method 1* for Hualalai, Kohala, Kilauea and Loihi, and *Method 2* for Mauna Loa, Mauna Kea and Koolau.

sample until the whole rock MgO content reached 16 wt.% MgO. In this manner, an average W content for each volcanic center is calculated at an MgO content of 16 wt.%, which is presumed to be representative of the parental melt (Table 7.2).

The main advantage of this calculation is that it is independent of the shape of the MgO-W trends, so it can be used for those volcanic centers with poor correlations between W and MgO (Mauna Loa, Koolau) and for those volcanic centers with small datasets (Mauna Kea). Following the olivine correction, the parental melts for Hualalai, Mauna Loa, Kohala, Kilauea, Mauna Kea, Koolau and Loihi are determined to contain 83 ± 18 (2σ) ng/g, 111 ± 40 ng/g, 129 ± 39 ng/g, 149 ± 42 ng/g, 127 ± 46

ng/g, 104 ± 84 ng/g and 185 ± 20 ng/g W, respectively. The parental melt for Mauna Kea, based upon one data point, is estimated to contain 127 ± 46, using the same relative error from Mauna Loa (40%).

Both parental melt estimation techniques were utilized for Hualalai, Kohala, Kilauea and Loihi, with the results of each method producing statistically indistinguishable estimates. Due to the smaller uncertainties on the W content from the MgO-W linear regression method, we use these values for the calculation of source composition.

7.5.2 Degree of partial melting

The degree of partial melting of the mantle source regions of the Hawaiian shield volcanoes is a key parameter for calculating the W contents of these sources; however, such estimations are far from straightforward and often require making significant assumptions about the initial source composition and/or mineralogy (Feigenson *et al.,* 2003). The assumptions inherent to melting models introduce a potentially large source of error into our calculations of source W contents, so an appropriate model must be carefully chosen. Several melting models have been suggested for Hawaii, based on different geochemical arguments, including incompatible element abundances (Norman and Garcia, 1999), rare earth element (REE) systematics (Feigenson *et al.,* 1996; 2003) and U-series disequilibria (Sims *et al.,* 1995, 1999; Pietruszka *et al.,* 2006).

Norman and Garcia (1999) used relationships between incompatible trace element ratios that are sensitive to the partial melting process, such as La/Yb, Sm/Nd and Lu/Hf, to infer that the degree of partial melting for the Hawaiian picrites was

between 4 to 10%. These authors also indicated that the average degree of partial melting increases in the sequence: Loihi < Koolau < Kilauea < Mauna Kea < Kohala ≤ Hualalai ≤ Mauna Loa. However, a significant assumption of their melting model involves a common source composition for all the picrites, which they modeled as a mixed spinel and garnet lherzolite source.

In a similar fashion, Feigenson *et al.,* (1996; 2003) used REE inverse modeling to estimate the degree of partial melting necessary to produce Mauna Kea basalts, ranging from alkalic to tholeiitic in composition, in the HSDP drill cores. The primary magmas at Mauna Kea were determined to result from 8 to 15% partial melting of the mantle source for alkalic and tholeiitic basalts respectively, based on equilibrium and accumulated fractional melting models of calculated primary magmas. Their primary magma for Mauna Kea was estimated to contain 19 to 21% wt.% MgO, which is higher than other estimates for Hawaiian primary magmas which suggest that Hawaiian primary magmas contain ~16 wt.% MgO (*e.g.* Hauri, 1996; Norman and Garcia, 1999).

Sims *et al.,* (1995; 1999) examined U-series disequilibria in Hawaiian basalts, ranging from basanitic to tholeiitic in composition, to determine melting zone porosity and mantle upwelling rates in the Hawaiian system. Their modeling indicates that total melt fractions range from 3% for alkali basalts up to 15% for tholeiitic basalts. In a similar study of U-series disequilibria, Pietruszka *et al.,* (2006) modeled Kilauean basalts as a result of an average of 10% partial melting. These melting models assume a constant melt productivity rate, and are reliant on the thickness of the melting zone. U-series disequilibria studies also require an accurate knowledge of

eruption age and suitable partition coefficients for U, Th, Ra and Pa in an presumed source mineralogy.

Despite different analytical and theoretical methods, the three melting models outlined above all provide similar estimates of the maximum degrees of partial melting (10 to 15%). For the purposes of our study, we use the relative degrees of partial melting outlined by Norman and Garcia (1999), coupled with conservative melting ranges (a 5% melting window) for each volcanic center (Table 7.2). The Norman and Garcia (1999) melting model best describes our picritic sample suite for several reasons: i) several samples from Norman and Garcia (1999) are included in our current work; ii) we estimate a similar parental melt MgO content of 16 wt.% (Ireland *et al.,* 2009); and, iii) La/Yb, Lu/Hf and Sm/Nd ratios for each volcanic center (our data; Norman and Garcia, 1999; Gurriet, 1998; see Appendix E) mirror the trends observed by Norman and Garcia (1999). Accordingly, we model Hualalai and Mauna Loa from 7.5 to 12.5% partial melting, Kohala, Kilauea, Mauna Kea and Koolau from 5 to 10% partial melting and Loihi from 2.5 to 7.5% partial melting.

7.5.3 W abundances of Hawaiian mantle sources

To infer the W content for the mantle source regions of the Hawaiian shield volcanoes, an equilibrium batch melting model is employed (*e.g.*, Shaw, 1970):

$$\left(\frac{C_i^{liq}}{C_i^0} = \frac{1}{D_i^{sol/liq} + (1 - D_i^{sol/liq})F} \right) \qquad (7\text{-}1)$$

with the parameters for the bulk partition coefficient of element *i* ($D_i^{sol/liq}$), parental melt concentration and degree of partial melting (F) outlined above, where C_i^{liq} and C_i^0 are the parental melt composition and mantle source composition with regard to

element *i*, respectively. Since W behaves incompatibly during mantle melting, aggregated fractional melting and equilibrium melting models yield essentially identical results. Following the equilibrium melting model described above, we generate estimates for the W content of the Hawaiian mantle source regions of 9 ± 2 (2σ) ng/g, 11 ± 5 ng/g, 10 ± 4 ng/g, 12 ± 4 ng/g, 10 ± 5 ng/g, 8 ± 7 ng/g and 11 ± 5 ng/g for Hualalai, Mauna Loa, Kohala, Kilauea, Mauna Kea, Koolau and Loihi respectively (Fig. 7.3; Table 7.2).

Overall, the mean W contents of the mantle sources for the Hawaiian shield volcanoes show a limited range of 8 to 12 ng/g with all calculated source compositions within statistical uncertainty of each other. The similar W concentrations in the mantle sources of each individual Hawaiian shield volcano suggest that the mantle components that contribute to each shield volcano have comparable absolute abundances of W, as well as analogous W/U ratios. Accordingly, the mean Hawaiian source region is determined to have 10 ± 3 (2σ) ng/g W, which is three-times more enriched than the Depleted MORB Mantle (DMM; 3.0 ± 2.3 ng/g W), but comparable to the Primitive Mantle (PM: 13 ± 10 ng/g W; Arevalo and McDonough, 2008). The mean W abundance of the Hawaiian source, as determined in this study, is also consistent with the approximation by Hawkesworth and Scherstén (2007), who estimated the Hawaiian source to contain between 8 to 12 ng/g W based on Th/W ratios of similar picritic samples.

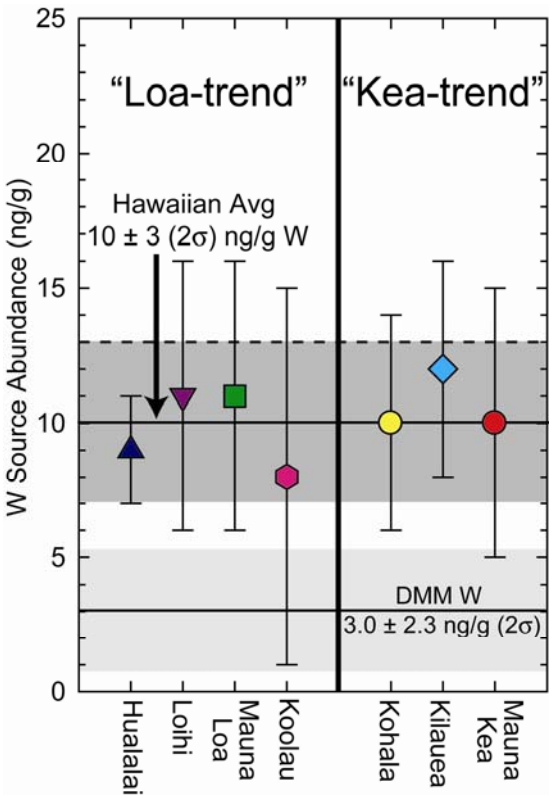

Fig. 7.3. The estimated W abundances for the mantle source regions of Hualalai, Mauna Loa, Kohala, Kilauea, Mauna Kea, Koolau and Loihi are estimated to be 9 ± 2 (2σ) ng/g, 11 ± 5 ng/g, 10 ± 4 ng/g, 12 ± 4 ng/g, 10 ± 5 ng/g, 8 ± 7 ng/g and 11 ± 5 ng/g W, respectively. The average W source abundance is 10 ± 3 ng/g (dark shaded area), which is similar to that of PM (13 ± 10 ng/g W, dashed line), but three-times greater than DMM (3.0 ± 2.3 ng/g W; lightly shaded area).

Similarly, the U abundances for the mantle sources of each volcanic center were calculated following the same modeling parameters as outlined above. This calculation not only provides an estimate for mantle source U abundance, but is also an independent test of the consistency of our W modeling. The estimated U abundances for the mantle source regions of Hualalai, Mauna Loa, Kohala, Kilauea, Mauna Kea, Koolau and Loihi are 13 ± 3 (2σ) ng/g, 13 ± 4 ng/g, 16 ± 6 ng/g, 22 ± 8 ng/g, 17 ± 9 ng/g, 12 ± 10 ng/g and 13 ± 7 ng/g U respectively, with a mean value of 15 ± 7 ng/g U. These results demonstrate excellent agreement with those derived from W abundances, with the mean Hawaiian mantle source having a W/U ratio of ≈0.65 and an U abundance three-times greater than DMM (4.7 ± 1.4 ng/g U; Salters and Stracke, 2004), but similar to PM (20 ± 8 ng/g U; McDonough and Sun, 1995).

7.6 Origin of W in the Hawaiian source region

7.6.1 Source components in the Hawaiian plume

Typically, three source components are invoked to explain the range of isotopic variations amongst the Hawaiian shield volcanoes (Staudigel *et al.,* 1984; West *et al.,* 1987; Kurz *et al.,* 1996; Eiler *et al.,* 1996). These three end-members are best expressed by lavas from Mauna Kea, Loihi and Koolau (Makapuu-stage lavas). The Kea component is characterized by relatively low $^{87}Sr/^{86}Sr$ and $^{187}Os/^{188}Os$, as well as high $^{143}Nd/^{144}Nd$, $^{176}Hf/^{177}Hf$ and Pb isotopic ratios (Lassiter *et al.,* 1996; Blichert-Toft *et al.,* 1999). Conversely, the Loihi component, which may represent a relatively undepleted deep mantle reservoir, is defined by more radiogenic Sr and Os, and less-radiogenic Nd, Hf and Pb isotopes relative to the Kea component. This end-member

is also distinguished by high $^{3}He/^{4}He$ ratios (Kurz *et al.,* 1983; Mukhopadhyay *et al.,* 2003). The Koolau (Makapuu) component, which is not characterized by any of the samples analyzed here, occupies the isotopic extreme with the highest $^{87}Sr/^{86}Sr$ and $^{187}Os/^{188}Os$, coupled with lowest $^{143}Nd/^{144}Nd$, $^{176}Hf/^{177}Hf$ and Pb isotopic ratios seen in Hawaiian lavas (West *et al.,* 1987; Roden *et al.,* 1994; Hauri, 1996; Lassiter and Hauri, 1998; Blichert-Toft *et al.,* 1999; Huang and Frey, 2005). A fourth component, which may not significantly contribute to the shield stage volcanoes analyzed here, may be required to explain Pb characteristics of some post-shield stage Hawaiian lavas (Abouchami *et al.,* 2000; Mukhopadhyay *et al.,* 2003).

The surface manifestation of the three dominant components of the Hawaiian source region is expressed as two geographically parallel, but geochemically distinct trends, commonly referred to as the Kea- and Loa-trends (*e.g.*, Frey and Rhodes, 1993; Hauri, 1996; Lassiter *et al.,* 1996; Ren *et al.,* 2005). Huang *et al.,* (2005) suggested that the Kea-trend volcanoes (Mauna Kea, Kilauea, Kohala) are dominated by the Kea and Loihi source components with negligible contribution from the Koolau component. The Loa-trend volcanoes (Mauna Loa, Loihi, Hualalai, Lanai, Koolau), on the other hand, are controlled by the Loihi and Koolau components with insignificant contribution from the Kea component. In the following sections, we model the origin of the apparent W enrichment observed in the composite Hawaiian source region.

7.6.2 Recycled oceanic crust and sediment in the Hawaiian mantle sources

To consider if recycled oceanic crust and sediment may influence the W content of the Hawaiian mantle source regions, the mobility of W during subduction must be

addressed. Although Kishida *et al.,* (2004) and Arnórrson and Óskarsson (2007) illustrate that W abundances are positively correlated with highly fluid-mobile elements (*e.g.*, B) and are enriched in hydrothermal fluids relative to ambient seawater, Noll *et al.,* (1996) found that W/Th ratios in a suite of subduction-related magmas: i) overlap with those of typical OIB and MORB; ii) do not decrease systematically with distance from the back-arc; and, iii) are independent of B/La ratios (a tracer of fluid flux), suggesting limited (if any) mobilization of W by hydrothermal fluids during subduction. Further, data from Noll (1994) indicate that W/Ba ratios in some arc lavas are actually depleted due to the preferential fluid-mobility of Ba compared to W in hydrothermal systems, and the continental crust is not enriched in W relative to Ba, Th or U, as would be expected if W was significantly more fluid-mobile (such as B, Pb, As and Sb).

König *et al.,* (2008) have recently asserted that W behaves as a fluid-mobile species in hydrothermal systems based on the significant scatter seen in W/Th ratios in a representative sample suite of subduction-related volcanic rocks from the Solomon Islands and Cyprus, but the average W/U ratio of these samples is statistically indistinguishable from typical MORB samples. Additionally, the Cyprus samples show a similar magnitude of scatter in Nb/U and Ba/Th ratios but constant Th/U ratios that are within the realm of typical MORB rocks, indicating variable fluid mobility between all high field strength elements, which are generally considered immobile in fluid systems. Thus, W/U may be selectively fractionated to some degree by fluid systems, but systematic variations have yet to be documented and, thus, the fluid mobility of W, particularly when compared to U, has yet to be resolved. For the

purposes of our modeling, it is assumed that W is conserved during the subduction process.

The recycling of oceanic crust, including associated pelagic sediment, into the deep mantle is one of the dominant paradigms for the introduction of chemical heterogeneities into the source region of OIB (*e.g.*, Hofmann and White, 1982; Hofmann, 1997, 2003 and references therein). For Hawaii, there is abundant geochemical support for the incorporation of recycled oceanic crustal materials in the Koolau component, as well as in the mantle sources of Loa-trend volcanoes (*e.g.*, Bennett *et al.,* 1996; Eiler *et al.,* 1996; Hauri, 1996; Hofmann and Jochum, 1996; Lassiter and Hauri, 1998; Blichert-Toft *et al.,* 1999; Sobolev *et al.,* 2000, 2005). The presence of variable proportions and types of recycled materials may explain the trace element and isotopic characteristics of the Hawaiian shields and the variations between individual volcanic centers. Crustal recycling is also consistent, to a first order, with the W (and U) enrichment of the Hawaiian sources relative to the DMM.

Typical oceanic crust contains on the order of ~30 ng/g W, consistent with 8 to 12% partial melting of a DMM source (3 ng/g W; Arevalo and McDonough, 2008). Sediment is generally more enriched in W than oceanic crust, reaching concentrations in excess of ~1400 ng/g W for upper crustal-derived sediments (Rudnick and Gao, 2003; Hu and Gao, 2008). Pelagic sediments contain even higher concentrations of W than upper continental crust, with an average of ~2700 ng/g W (Strekopytov, 1998). The recycled component in the Hawaiian source region may contain as much as 3% sediment derived from the upper crust without resulting in anomalous Nb/U ratios outside the variance seen in the Hawaiian lavas analyzed in this study. Here we model

a hypothetical recycled package containing 97% oceanic crust and 3% upper crustal sediment resulting in a subducted package with ~70 ng/g W, consistent with the crust-to-sediment proportions estimated in the Koolau mantle end-member based on O and Os isotopes (Bennett *et al.,* 1996; Lassiter and Hauri, 1998), presuming W is conserved during subduction (Fig. 7.4).

If the Hawaiian source region ultimately originates from a depleted end-member, modeled here to be DMM, that is variably contaminated by a recycled component similar to our model recycled package, two-component mixing calculations require the addition of between 3 and 20% recycled materials to the DMM to satisfy the estimated W concentration in the sources of the individual shield volcanoes, and between 5 to 20% recycled material to satisfy the mean W budget of the composite Hawaiian source region. The distinct isotopic signatures displayed by Kea-trend and Loa-trend volcanics, however, require either different proportions of recycled components, or incorporation of recycled components of different ages. Given the comparable W concentrations among the Hawaiian shield sources, the isotopic differences between volcanic centers may best be interpreted as the result of recycled materials with different mean ages. For example, the compositions of the Kea-trend volcanic centers can be satisfied by recycling 10 to 15% of young oceanic crust and sediment, whereas the Loa-trend trend volcanics would require similar proportions of an ancient (>1.8 Ga) crust + sediment package in order to account for the relatively high Sr and Os isotopic compositions, and the relatively low Nd, Hf and Pb isotopic ratios (Bennett *et al.,* 1996; Lassiter and Hauri, 1998).

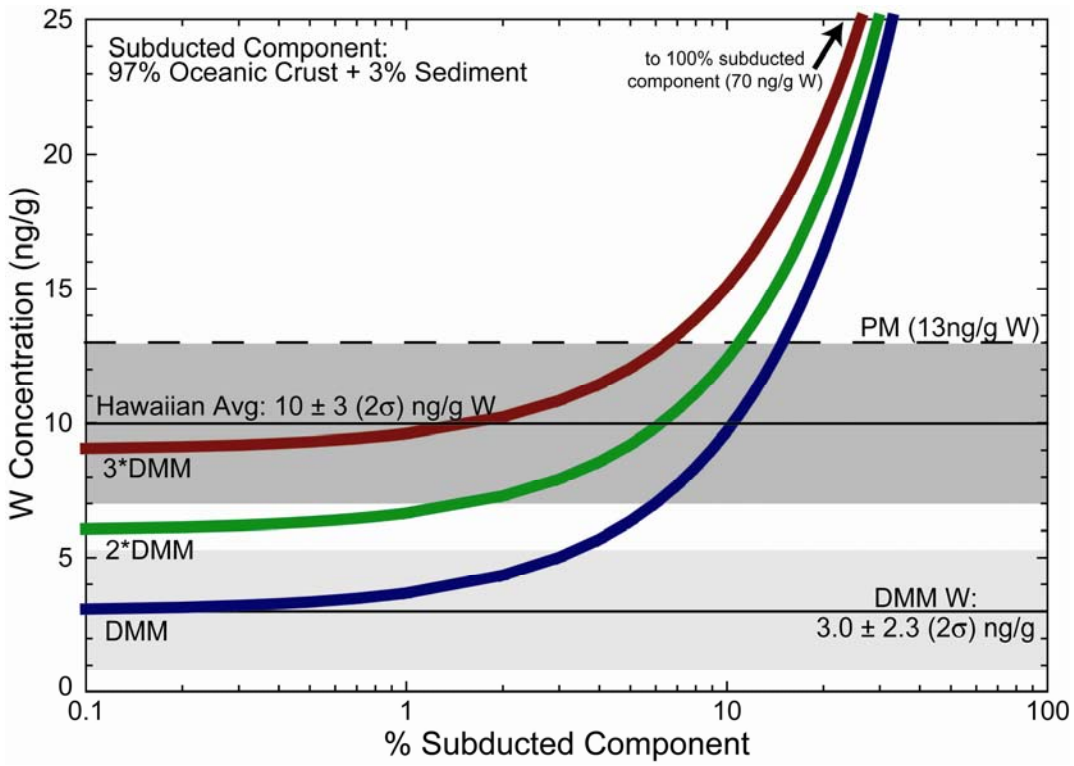

Fig. 7.4. Addition of a model subducted component to various mantle reservoirs. The subducted package consists of 97% oceanic crust (30 ng/g W) and 3% continental sediment (1400 ng/g W), resulting in a recycled package containing ~70 ng/g W. Adding such a recycled package to DMM (3 ng/g W) requires 5 to 20% of a subducted component to produce the average Hawaiian source W abundance. However, if a more enriched reservoir (*e.g.*, 3*DMM) is involved, no recycled material may be required to explain the estimated W source characteristics. With this second scenario, the addition of some recycled material is still permissible within the uncertainties of the model, which may explain the isotopic differences between Loa- and Kea-trend volcanoes. The dark shaded area represents the average W source abundance (10 ± 3 ng/g W), while the lightly shaded area shows the composition of DMM (3.0 ± 2.3 ng/g W).

An alternative explanation for the apparent W enrichment of the Hawaiian source region is that the Hawaiian source does not originate from a depleted end-member like DMM, but rather from an end-member that is less depleted in incompatible elements prior to crustal recycling. This scenario is consistent with some isotopic studies which have suggested that the DMM is not directly involved in producing Hawaiian magmas (Bennett *et al.,* 1996; Lassiter and Hauri, 1998; Blichert-Toft *et al.,* 1999). If the Hawaiian source samples a primary component that is less depleted in incompatible trace elements relative to DMM, then the incorporation of recycled material in the Hawaiian source is not necessary to account for the observed enrichment of W (Fig. 7.4). However, for this scenario, the addition of variable proportions of recycled crust (up to 10 to 12%) to account for the isotope characteristics associated with each volcanic center is permitted because this addition would not be resolvable within the W abundance uncertainties reported for the volcanic centers. For example, although the abundance of W in the sources of Mauna Loa and Loihi lavas (11 ± 5 ng/g) is within uncertainty of the rest of the shield volcanoes, the addition of as much as 11% recycled material to an undepleted source with ~9 ng/g W could be accommodated within the uncertainty of the estimated source composition. This scenario is consistent with the suggestion that Loa-trend volcanoes may involve some recycled material (*i.e.*, the Koolau component), while the Kea-trend volcanoes may have incorporated little to none (Huang *et al.,* 2005).

The ultimate origin of this hypothetical, less-depleted reservoir is uncertain. It would most likely represent a reservoir that has experienced little prior melt depletion, thereby preserving high incompatible element concentrations (McKenzie

and O'Nions, 1995). If such a reservoir exists, it would likely be located in the deep mantle in order to avoid mixing and/or processing in the upper mantle over geologic time and may be related to the FOZO mantle component (FOcused ZOne; Hart *et al.,* 1992; Hofmann, 2003). To account for the isotopic characteristics of Kea-trend volcanoes, this reservoir would have to be isotopically similar to the Kea end-member. Huang *et al.,* (2005) showed that the Loihi end-member component is similar to the Kea end-member in terms of $^{87}Sr/^{86}Sr$, $^{143}Nd/^{144}Nd$ and $^{176}Hf/^{177}Hf$, albeit slightly more enriched. If this hypothetical reservoir is related to the Loihi end-member, the isotopic constraints of both Kea- and Loa-trend volcanoes can be satisfied.

7.6.3 Core-mantle interactions?

A role for core-mantle interaction in the Hawaiian plume has been suggested based on observed coupled enrichments in ^{186}Os-^{187}Os isotopes in Hawaiian picrites (Brandon *et al.,* 1999), as well as elevated Fe/Mn ratios in Hawaiian basalts (Humayun *et al.,* 2004). These authors proposed that the enrichments may result from the incorporation of small amounts ($\leq$ 0.5 wt.%) of outer core material to the sources of some Hawaiian volcanoes. However, a lack of corresponding enrichments in the highly siderophile element abundances of the Hawaiian sources (Bennett *et al.,* 2000; Ireland *et al.,* 2009), recent thermal models for the core suggesting the relatively late inception of inner core crystallization (Buffett *et al.,* 1996; Labrosse *et al.,* 2001), and the discovery of other possible mechanisms to create coupled ^{186}Os-^{187}Os enrichments (Smith, 2003; Hawkesworth and Scherstén, 2007; Luguet *et al.,* 2008), have cast doubt on this hypothesis. Tungsten isotopes have been suggested as a more robust

tracer of core-mantle interactions (Scherstén *et al.,* 2004; Brandon and Walker, 2005; Hawkesworth and Scherstén, 2007; Takamasa *et al.,* 2009) because the silicate portion of the Earth is isotopically enriched in ^{182}W (the decay product of ^{182}Hf) relative to chondrites. Consequently, mass balance arguments suggest that Earth's core has approximately 2 parts in 10,000 (ε_w units) less ^{182}W than the silicate Earth (Kleine *et al.,* 2002).

The addition of core material to the Hawaiian source could, therefore, lead to a modest depletion in ^{182}W in lavas relative to the ambient upper mantle. Towards this end, Scherstén *et al.,* (2004) observed no difference in W isotopic compositions between a terrestrial standard and three Hawaiian samples (H-11, Lo-02-02 and Lo-02-04) that had previously been suggested to record a core component (Brandon *et al.,* 1999), leading these authors to conclude that no core material is involved in the Hawaiian source regions. The Scherstén *et al.,* (2004) model, however, was strongly dependent on the assumed concentration of W in the mantle source that would have been contaminated with W from the outer core.

Our current study suggests that the W content of the mean Hawaiian source region (10 ± 3 ng/g) is most consistent with the "preferred" model of Scherstén *et al.,* (2004) that assumed an initial W concentration of 8 ng/g. The addition of 0.5 wt.% of outer core material to the average Hawaiian source would raise the source W concentration by only ~2 ng/g, which is irresolvable within the uncertainty on the mantle source W estimates. Arevalo and McDonough (2008) also showed that the incorporation of 0.5 wt.% core material would not have a resolvable effect on the W/U ratios.

However, the physical addition of this amount of outer core material would result in a ε_w of -0.45, which should be resolvable by W isotopes. The lack of an outer core W signature in the Hawaiian rocks suggests that either core-mantle interaction does not occur, or that mechanisms other than physical mixing may operate at the core-mantle boundary (Puchtel and Humayun, 2000; 2005; Humayun *et al.,* 2004).

7.7 Conclusions

1) The concentration of W in Hawaiian picrites is highly variable, but within most individual shield volcanoes, linear trends are observed between W and MgO. The W/U ratios for Hawaiian picrites have an average of 0.62 ± 0.19 (2σ), which is indistinguishable from the W/U ratio for the sampled silicate Earth.

2) Estimates of the W content of the parental melts for the Hawaiian shield volcanoes were obtained by two different techniques, which yield statistically indistinguishable results. The parental melts for Hualalai, Mauna Loa, Kohala, Kilauea, Mauna Kea, Koolau and Loihi are determined to contain 85 ± 6 (2σ) ng/g, 111 ± 40 ng/g, 133 ± 20 ng/g, 155 ± 21 ng/g, 127 ± 46 ng/g, 104 ± 84 ng/g and 214 ± 8 ng/g W, respectively.

3) Correspondingly, the W abundances for the Hawaiian mantle sources are estimated to contain 9 ± 2 (2σ) ng/g, 11 ± 5 ng/g, 10 ± 4 ng/g, 12 ± 4 ng/g, 10 ± 5 ng/g, 8 ± 7 ng/g and 11 ± 5 ng/g for Hualalai, Mauna Loa, Kohala, Kilauea, Mauna Kea, Koolau and Loihi respectively. As a result, the mean Hawaiian source region contains 10 ± 3 (2σ) ng/g W, about three-times more than the DMM (3.0 ± 2.3 ng/g W), but comparable to the PM (13 ± 10 ng/g W). The estimated U abundances for the mantle

sources of the Hawaiian volcanic centers are consistent with those derived from W abundances.

4) Bulk addition of recycled oceanic material to the DMM alone can explain the enriched W composition of each individual Hawaiian shield volcano, but the mean age of the recycled material in Kea- and Loa-trend volcanoes would have to be fundamentally different to satisfy isotopic constraints. However, if the Hawaiian source regions originate from a less depleted mantle reservoir, crustal recycling is not necessary to produce the estimated source W abundances, although the addition of some recycled oceanic crust can be accommodated within the uncertainties of our model source compositions.

5) The incorporation of minor amounts (≤0.5 wt.%) of outer core material is irresolvable within the uncertainty of our W source modeling and W/U ratios, however, this addition should be detectable via W isotopes. The lack of a core W signature suggests that either core-mantle interaction does not occur, or that mechanisms other than physical mixing may operate at the core-mantle boundary.

7.8 A preliminary look into the source composition of the Austral-Cook Islands

At a gross scale, three dominant mantle components can be envisioned to account for the broad spectrum of isotopic composition observed in oceanic basalts (Fig. 7.5), including the MORB source region (or Depleted MORB Mantle, DMM), an enriched mantle component (Enriched-Mantle Type-I and Type-II, EM-I and EM-II) and a high-μ component ($\mu = (^{238}U/^{204}Pb)_{t=0}$, HIMU). Ocean island basalts are commonly classified as being EM-type or HIMU-type based on their characteristic isotopic

compositions. However, despite the expansive range of isotopic compositions observed in modern OIB, samples that represent the isotopic "extremes" commonly have similar trace element signatures to one another, indicating a potential common precursor or source component. As an example, lavas from both EM-type and HIMU-type sources have some compositional similarities, such as comparable Nb/U, La/Sm, La/Th, Sr/Nd, Ba/K, and Rb/K ratios, which suggest they share a common precursor or recycled source component (Willbold and Stracke, 2006). Thus, the shared elemental signatures of EM- and HIMU-type basalts may provide a relatively unadulterated look into a common OIB source region, despite their extreme isotopic compositions. In order to constrain the mass fraction of this common mantle source component, the relative enrichment of incompatible elements in this reservoir needs to be addressed.

Ireland *et al.,* (2009) took the first steps in developing a compositional model of the OIB source region based on Hawaiian volcanics, but these lavas do not encompass the most extreme isotopic signatures observed in modern OIB (Fig. 7.5). The range of isotopic compositions observed in Hawaiian volcanics, which extend from MORB-like signatures (*i.e.*, low $^{87}Sr/^{86}Sr$ and $^{206,207,208}Pb/^{204}Pb$, and high $^{143}Nd/^{144}Nd$) up to moderate EM-type signatures, suggest that the MORB source plays a significant role in the genesis of Hawaiian lavas, potentially serving to dilute the common, enriched component observed in extreme OIB.

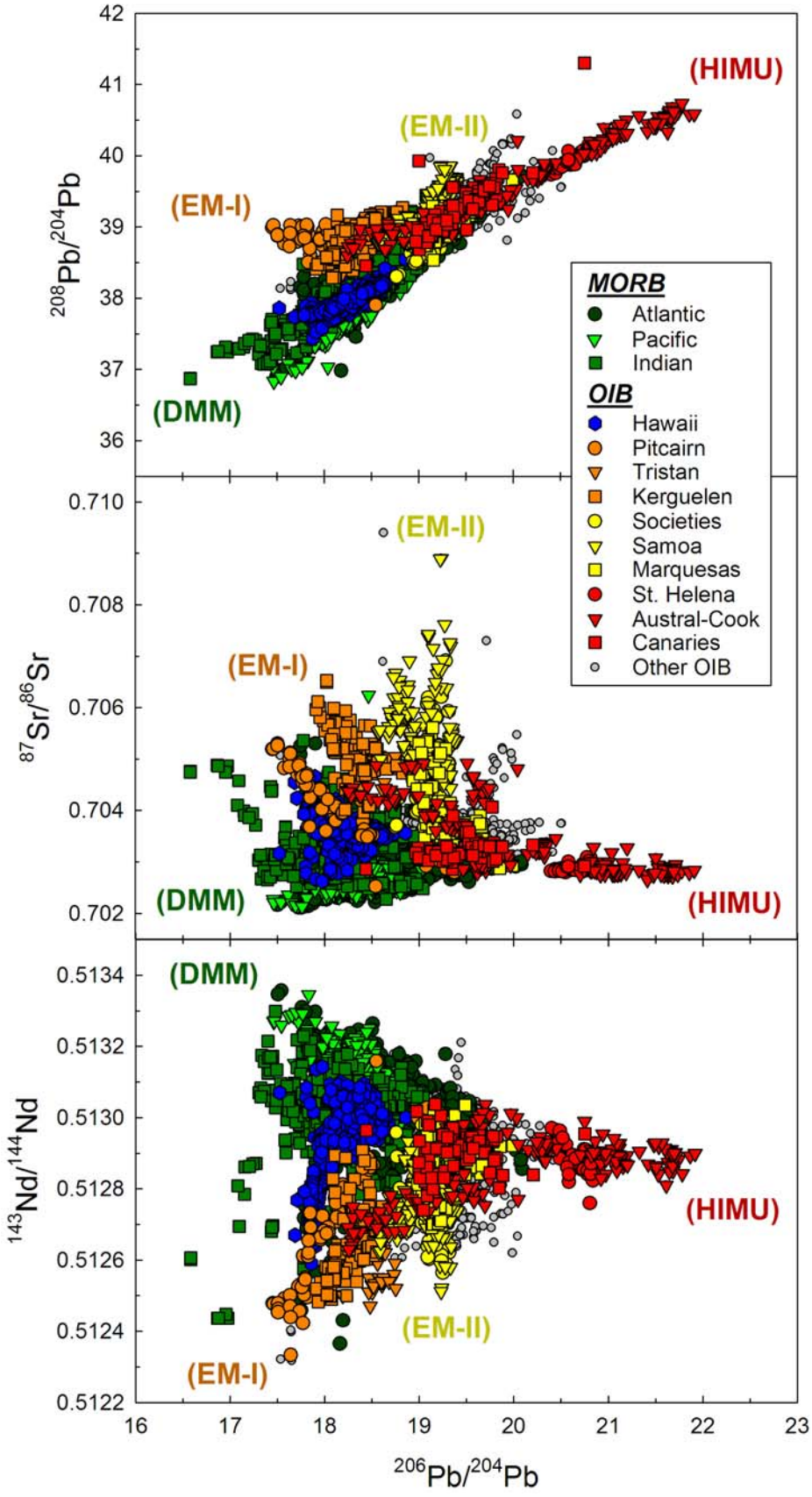
(HIMU)
(EM-II)
(EM-I)
(DMM)
MORB
Atlantic
Pacific
Indian
OIB
Hawaii
Pitcairn
Tristan
Kerguelen
Societies
Samoa
Marquesas
St. Helena
Austral-Cook
Canaries
Other OIB
208Pb/204Pb
87Sr/86Sr
143Nd/144Nd
206Pb/204Pb

Fig. 7.5. Isotopic variations observed in MORB and OIB. Note how Hawaiian volcanics show only a limited variation in isotopic signatures relative to the more "extreme" samples, which have historically been ascribed to defining a finite number of mantle end-members, or distinct mantle source components (Zindler and Hart, 1986). The Depleted MORB Mantle (DMM) represents the depleted source component observed in global MORB. High-μ lavas (HIMU; $\mu = (^{238}U/^{204}Pb)_{t=0}$), which are characterized by high U/Pb and Th/Pb ratios and low Rb/Sr relative to other OIB, are generally thought to represent a mantle source comprising ancient recycled oceanic crust (*e.g.*, White and Hofmann, 1982; Chauvel *et al.,* 1992). Enriched Mantle Type-I (EM-I) and Type-II (EM-II) volcanics, which are typically enriched in Rb/Sr and depleted in Sm/Nd compared to HIMU-type OIB, are generally thought to represent a combination of oceanic crust + pelagic sediments and oceanic crust + terrigenous sediments, respectively (for a review, see Hofmann, 1997, 2003 and Willbold and Stracke, 2006). Metasomatism from fluid-rock and/or low-degree melt-rock interactions has also been postulated as an alternative process that could account for the range of isotopic (and trace element) compositions observed in OIB (*e.g.*, Sun and McDonough, 1989; Niu and O'Hara, 2003; Workman *et al.,* 2004).

7.8.1 Estimating parental melt compositions

Because highly incompatible elements are effectively removed from residua during melting and excluded from early crystallizing phases during magma emplacement, linear correlations between highly incompatible element abundances (*e.g.*, W and Th) and the MgO contents of OIB indicate a systematic and predictable evolution of parental melts and their source compositions (Ireland *et al.,* 2009). A linear correlation is observed between the abundances of highly incompatible Th (which is less fluid-mobile than W but similarly incompatible) and the MgO contents of OIB derived from the Austral-Cook ocean island chain (Fig. 7.6); OIB from EM-type Tristan da Cunha and Gough Island and HIMU-type St. Helena show similar trends. Interestingly, basalts from all four of these localities show a similar enrichment in incompatible element abundances relative to the Hawaiian lavas examined by Ireland *et al.,* (2009). Even when considering individual volcanic centers within the Austral-Cook island chain, the linear correlation between Th and MgO is maintained and is not significantly affected by the age of the volcanic center. Table 7.3 summarizes the interpolated abundance of Th in the parental melts of the Austral-Cook samples, as well as the Tristan, Gough Island and St. Helena samples for comparison. A parental melt MgO content between 16 and 20 wt.% has been estimated for the Austral-Cook lavas based on reconstructing whole-rock major element chemistries to a model composition in equilibrium with Fo_{90} (Dasgupta *et al.,* 2010).

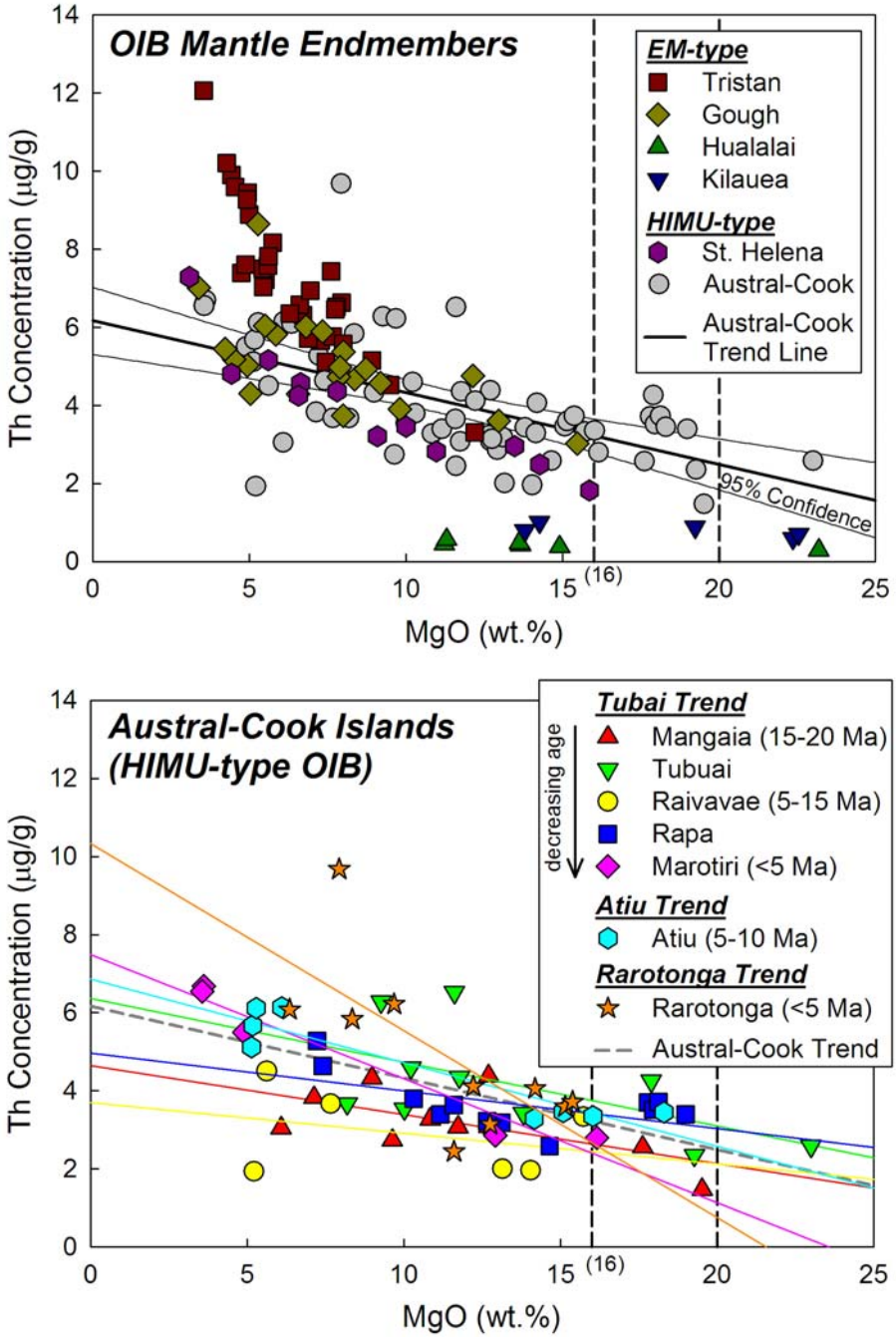

Fig. 7.6. Linear correlation between Th abundances and MgO content in EM- and HIMU-type OIB. Major and trace element data for samples from Tristan da Cunha, Gough Island and St. Helena are from Willbold and Stracke (2006); the Hawaiian data are from Ireland *et al.*, (2009). The major and trace element chemistry reported for samples from the Austral-Cook Islands represent unpublished data courtesy of Andreas Stracke and Matthias Willbold.

Table 7.3. Parental melt estimates and linear regression statistics for Th vs. MgO correlations of various OIB.

Ocean Island	slope (m)	95% Conf.	y-intercept (b)	95% Conf.	MgO_{16} Parental Th (ug/g)	95% Conf. (ug/g)	MgO_{20} Parental Th (ug/g)	95% Conf. (ug/g)
Hawaii								
Hualalai	-0.02	0.02	0.68	0.24	0.39	0.35	0.46	0.31
Kilauea	-0.03	0.05	1.36	0.89	0.85	1.17	0.98	1.05
Other EM-Type Locations								
Gough Island	-0.24	0.12	6.70	1.00	2.86	2.16	3.82	1.75
Tristan	-1.01	0.23	13.60	1.50	N/A	N/A	1.48	3.14
HIMU-type Locations								
St. Helena	-0.32	0.10	6.70	0.97	1.58	1.87	2.86	1.54
Austral-Cook Islands								
Mangaia	-0.15	0.11	4.70	1.40	2.30	2.25	1.70	2.61
Tubuai	-0.17	0.16	6.10	2.30	3.38	3.44	2.70	3.94
Raivavae	-0.03	0.25	2.70	2.90	2.22	4.94	2.10	5.78
Marotiri	-0.33	0.15	7.50	1.60	2.22	2.88	0.90	3.40
Rapa	-0.13	0.13	5.30	1.80	3.22	2.75	2.70	3.16
Atiu	-0.22	0.08	6.80	1.00	3.31	1.66	2.44	1.94
Rarotonga	-0.66	0.46	12.0	5.10	1.44	8.95	N/A	N/A
					average = 2.58 ± 0.64 ($2\sigma_m$)		***average = 1.62 ± 0.81 ($2\sigma_m$)***	

7.8.2 Melting models

Although realistic models of melt generation and segregation implicate near-fractional melting rather than equilibrium melting at mid-ocean ridges and intraplate volcanic centers (*e.g.*, McKenzie, 1984; Klein and Langmuir, 1987; McKenzie and Bickle, 1988), imperfect fractional melting produces liquids with incompatible trace element concentrations similar to those expected by equilibrium melting models (*e.g.*, Maaløe, 1982; Richter, 1986; Eggins, 1992; Planck and Langmuir, 1992; O'Hara, 1993; Maaløe, 1995), as long as the melting is accumulative. Consequently, here we adopt a modal batch melting model (Shaw, 1970) to simplify the melting process and describe it as a function of three definable parameters, namely the partition coefficient of element *i* ($D_i^{sol/liq}$) and the concentration of element *i* in the melt (C_i^{liq}) and source (C_i^0; Eqn. 7-1).

Two independent methods of estimating the degree of partial melting of mantle-derived materials, namely the source ratio method pioneered by Treuil and Joron (1975) and Minster and Allègre (1978) and the linear regression method of Maaløe and Pederson (2003), are based upon systematic variations in trace element ratios between two unequally incompatible, well-characterized trace elements, such as Th and Sm. Both melting models indicate that these OIB samples represent anywhere from 2 – 8% partial melting, assuming a range of experimentally derived and observed partition coefficients for garnet peridotite (*i.e.*, Salters *et al.,* 1999, 2002; Salters and Stracke, 2004); a pyroxenitic model source would require a significantly higher degree of melting (*i.e.*, Pertermann *et al.,* 2004). To constrain the lower limit of enrichment and thus the upper limit of the mass fraction of a common

OIB source component, for modeling purposes we can assume that the highest MgO content is representative of the Austral-Cook parental melt. Accordingly, the Austral-Cook parental melt has a model composition of 1.62 ± 0.81 μg/g Th ($2\sigma_m$; assuming an MgO content of 20 wt.%), which equates to a source composition with 83 ± 41 ng/g Th, following 5% batch melting.

7.8.3 Initial conclusions

The model source composition established here, which represents the lower limit of enrichment of the Austral-Cook source region and potentially the common enriched component observed in extreme OIB, is (≥)1.0x as enriched as the undifferentiated primitive mantle, and ≥3x as enriched as the mean MORB source region (following 10% partial melting of MORB; Arevalo and McDonough, 2010), similar to the OIB model proposed by Ireland *et al.,* (2009) based on Hawaiian volcanics. This result indicates that the common enriched component observed in OIB constitutes ≤50% of the mantle mass, following mass balance of the terrestrial inventory of Th (*i.e.*, continental crust + MORB source + OIB source; Fig. 1.9), and assuming a simplified two-box model of mantle structure consisting of the MORB source region and the OIB source component modeled here.

Chapter 8: Summary, conclusions and future work[1]

[1] The text in this chapter was written by R. Arevalo Jr.

8.1 Overall perspectives

Characterizing the chemical composition of distinct mantle source regions is of fundamental importance to understanding the structure and evolution of the modern mantle and bulk silicate Earth. Trace elements provide an important tool for investigating the composition of mantle-derived materials, because these elements are not buffered during mantle melting (unlike major elements), yet are sensitive to source chemistry and magma melting/crystallization conditions. Abundances of highly incompatible elements are of particular importance as these elements are effectively removed from a mantle source via only minor degrees of partial melting. The primary goal of this dissertation was to explore and quantify the heterogeneous characteristics of the modern mantle, as represented by the source regions of mid-ocean ridge basalts (MORB) and intraplate ocean island basalts (OIB), through trace element abundances and characteristic enrichments/depletions. The major, minor and trace element chemistry of a suite of MORB, OIB and other mantle-derived samples was analyzed via *in situ* laser ablation (LA-) ICP-MS methods. Moreover, a critical compilation of the available literature was amassed to characterize a broader spectrum of mantle derivatives. This comprehensive geochemical dataset is available for download, along with the new data reported here. The following sections in this chapter summarize the original motivation, results and implications for each of the research components included in this dissertation.

8.2 Uncertainties in the composition of Earth, its core and silicate sphere

Compositional models of the Earth must be consistent with both geophysical (*e.g.*, seismology + geodesy constraints) and cosmochemical (*e.g.*, solar photosphere + meteorite compositions) observations. The simplest model of the Earth considers ⅓ of the planet's mass as an Fe-Ni alloy core, and the remaining ⅔ as a thick silicate shell primarily composed of: olivine (*i.e.*, $(Mg,Fe)_2SiO_4$), pyroxene (*i.e.*, $XY(Si,Al)_2O_6$; X = Ca, Na, Fe^{2+}, Mg, etc.; Y = Cr, Al, Fe^{3+}, Mg, etc.) and an aluminous phase (*e.g.*, feldspars, spinel, garnet, etc.) at upper mantle depths (<660 km), and perovskite (*i.e.*, $((Mg,Ca,Fe)SiO_3$) and magnesiowüstite/ferropericlase (*i.e.*, (Mg,Fe)O) at lower mantle depths (>660 km). The most abundant elements in the Earth (*e.g.*, Fe, Mg, Ni), can be determined by key ratios (*e.g.*, atomic Mg/Fe and Fe/Ni) in both chondritic meteorites and mantle samples. The abundances of other elements, particularly minor and trace elements, may be derived from complementary relationships with these major element ratios; some elements, however, exhibit siderophile (iron-loving) and/or chalcophile (sulfur-loving) geochemical tendencies, and thus have been largely sequestered into the Earth's core.

Compositional models for the silicate Earth estimate the abundances of the refractory lithophile elements at 2.2 to 2.8 times that in CI carbonaceous chondrites, resulting in a 25% uncertainty in the concentrations of Th and U in the silicate Earth (63-83 ng/g Th and 17-22 ng/g U, respectively; *e.g.*, McDonough and Sun, 1995; Palme and O'Neill, 2003; Lyubetskaya and Korenaga, 2007). Cosmochemical constraints (both isotopic and chemical) and melting models add to this uncertainty, resulting in a silicate Earth compositional model with 80 ± 25 ng/g (2σ) Th and 20 ±

8 ng/g (2σ) U, with a Th/U of ~3.9 (McDonough and Sun, 1995). Coupled with a terrestrial K/U ratio of 13,800 ± 2600 (2σ), as established by Arevalo *et al.,* (2009), the three main heat-producing elements in the Earth (*i.e.*, U, Th and K) currently contribute 21 ± 4 (2σ) TW (~14 TW from the mantle, ~7 TW from the continental crust) to the planet's total surface heat flow of 46 ± 6 TW (2σ; see Jaupart *et al.,* 2007 and references therein). Further collaborations between physics and geology in the field of geoneutrino research will ultimately allow a more precise determination of the Earth's budget of heat-producing elements and the overall compositional make-up of the planet.

8.3 Tungsten geochemistry and implications for understanding the Earth's interior

Tungsten is a refractory element that exhibits binary behavior as a function of redox conditions. Under reducing conditions W behaves as a moderately siderophile element that preferentially partitions into metallic phases; conversely, under oxidizing conditions W behaves as a highly incompatible lithophile element that preferentially partitions into silicate melts. Consequently, >90% of the planetary budget of W has been sequestered in the core and the remaining <10% is distributed primarily in the continental crust, leaving the modern mantle largely depleted in W.

In this study, the trace element chemical composition of an extensive suite of modern oceanic basalts (n = 86) has been determined via *in situ* laser ablation (LA-) ICP-MS. The results indicate that the partitioning behavior of U mirrors that of W during basalt genesis, whereas both Ba and Th behave more incompatibly. The W/U

ratio of the collection of oceanic basalts analyzed here (W/U = 0.65 ± 0.45, 2σ) is representative of the mean modern mantle, and is indistinguishable from the average for MORB (W/U_{MORB} = 0.65 ± 0.41, n = 52), OIB (W/U_{OIB} = 0.63 ± 0.07, n = 10), back-arc basin basalts (W/U_{BABB} = 0.62 ± 0.09, n = 12), and continental crust (W/U_{CC} = 0.77 ± 0.33, 2σ; Rudnick and Gao, 2003); therefore, the ratio determined here is representative of the W/U ratio of the entire silicate portion of the Earth.

Assuming a concentration of 20 ± 8 (2σ) ng/g U in the bulk silicate Earth (McDonough and Sun, 1995), the abundance of W is 13 ± 10 ng/g. Following mass balance and accounting for a continental crust model with ~1000 ng/g W (Rudnick and Gao, 2003), this implies a mean modern mantle and core composition with 8.3 ± 7.1 ng/g W and 510 ± 120 ng/g W, respectively. Although both the isotopic contract between W in the core and mantle and the constancy of the silicate Earth W/U ratio allow for potential insights into putative core-mantle exchange, both proxies are dependent on the chemical composition of the mantle source region and have yet to unambiguously identify core-mantle interactions in Hawaiian picrites.

8.4 The K/U ratio of the silicate Earth: Insights into mantle composition, structure and thermal evolution

The terrestrial budget of K provides control on the composition and evolution of the silicate Earth, as well as the planet's volatile element depletion, radiogenic heat budget, degassing history, and dominant mode of mantle convection. However, because K acts as a volatile species during planetary accretion, the K content of the silicate Earth must be determined as a function of the terrestrial K/U ratio. In this

study, the trace element chemistry of a comprehensive collection of MORB, including both normal- (La/Sm < 1.00) and enriched-type (La/Sm ≥ 1.00) samples derived from the Atlantic, Pacific and Indian Ocean basins, was measured via LA-ICP-MS methods. Determining the abundance of K in these samples required the implementation of medium-resolution detection ($m/\Delta m = 4000$) in order to discriminate the ^{39}K peak from isobaric interferences, namely $^{23}Na^{16}O$, ^{38}ArH and the low-mass tail of ^{40}Ar. The MORB source, as represented by the samples analyzed here, is characterized by a K/U ratio of 19,000 ± 2600 (2σ). In comparison, OIB and the bulk continental crust have average K/U values of 11,900 ± 2200 and 13,000 ± 3000, respectively. The fractional contributions of these reservoirs, assuming the OIB source region encompasses approximately 20% of the modern mantle mass (equating to a stratified mantle depth at ~1900 km), establishes the K/U ratio of the silicate Earth to be 13,800 ± 2600 (2σ).

The terrestrial K/U value determined here indicates 280 ± 120 μg/g (2σ) K in the silicate Earth. As a result, of the 46 ± 6 TW (2σ) heat released by the planet, 21 ± 4 TW is produced from the decay of radioactive element, ~4 TW of which is derived from the decay of ^{40}K. The convective Urey ratio, which is determined to be ~0.34, suggests a current mantle cooling rate on the order of ~170 $K \cdot Gyr^{-1}$ (assuming a constant mantle heat capacity of 1.2 $Jg^{-1} \cdot K^{-1}$). However, if we also consider the potential for 5-15 TW of heat flow across the core-mantle boundary (Lay *et al.,* 2008 and references cited therein), only 10-20 TW of the mantle's heat output represents secular cooling, implying a more probable modern mantle cooling rate somewhere between 70-130 $K \cdot Gyr^{-1}$.

Considering the silicate Earth K content, 155 ± 70 Eg (or 10^{18} g) of ^{40}Ar has been produced by the decay of ^{40}K over the past 4.5 Gyr. Approximately ~66 Eg of ^{40}Ar currently resides in the atmosphere (Turekian, 1959), and an additional ~14 Eg of ^{40}Ar may reside in the continents, assuming no degassing and a bulk continental crustal composition with 1.3 μg/g U (Rudnick and Gao, 2003), a K/U ratio of 13,000 (and thus 17,000 μg/g K, or 2.0 wt% K_2O), and a mean crustal age of ~2.5 Ga. As such, as much as ~50% of the mantle may have been degassed, and/or ≥75 Eg of ^{40}Ar may still reside in the mantle. However, if the mantle were entirely represented by the MORB source region, only ≤55 Eg of ^{40}Ar could be produced over 4.5 Ga, indicating the need for another mantle component enriched in incompatible elements (including K) relative to the MORB source. Therefore, a chemically enriched layer (*i.e.*, the OIB source) with excess ^{40}Ar likely resides somewhere in the deep mantle, providing evidence for a stratified mantle structure. As an additional consideration, the K/U ratio of the silicate Earth serves as a control on the volatile element depletion of the bulk planet. Lead (Pb) and K are both volatile elements, and the Pb/U and K/U ratios of carbonaceous chondrites are correlated (Allègre *et al.,* 1995); assuming the Earth follows the chondritic trend and given the silicate (and bulk) Earth K/U ratio of ~13,800, the Pb/U ratio of the planet is determined to be on the order of ~85, indicating ~1200 ng/g Pb in the bulk Earth (of which ≥3300 ng/g Pb is in the core).

8.5 Chemical variations and regional diversity observed in MORB

Mid-ocean ridge basalts represent adiabatic upwelling and decompression melting (*e.g.*, McKenzie and O'Nions, 1991) of the ambient upper mantle (≤200 km depth;

e.g., Forsyth *et al.,* 1998), and thus exemplify a relatively simple melting history. Additionally, MORB samples are generally abundant, accessible and fresh (<1 Ma) near the ridge axis. Thus, in order to characterize and quantify the degree of heterogeneity in the upper mantle, a comprehensive compositional model of MORB needs to be established. Here, an extensive assemblage of MORB analyses (n = 792), including a suite of new, high-precision LA-ICP-MS measurements (n = 79), has been critically compiled in order to provide a window into the chemical composition of the MORB source region.

The comprehensive MORB data set presented here includes both normal- and enriched-type samples, and defines a global MORB composition that is more enriched in incompatible elements than previous models (*e.g.*, Hofmann, 1988; Sun and McDonough, 1989; Su, 2002). A statistical evaluation of the true constancy of "canonical" trace element ratios using this data set reveals that during MORB genesis Ti/Eu, Y/Ho and Ce/Pb remain constant at the 95% confidence-level; thus, the ratios recorded in MORB (Ti/Eu = 7060 ± 1270, 2σ; Y/Ho = 28.4 ± 3.6, 2σ; Ce/Pb = 22.2 ± 9.7, 2σ) may reflect the composition of the MORB source region, presuming the degree of source heterogeneity, component mixing and conditions of melting/crystallization are adequately represented by the global MORB data set presented here (Stracke and Bourdon, 2009). Conversely, Ba/Th, Nb/U, Zr/Hf, Nb/Ta, Sr/Nd, and Th/U fractionate as a function of MORB genesis, and thus these ratios do not faithfully record the composition of the MORB source.

Compared to samples from the Pacific and Indian Oceans, MORB derived from Atlantic ridge segments are characterized by statistically significant (≥95%

confidence-level) enrichments in both highly incompatible elements (*e.g.*, light REE, TITAN group elements, Sr, Ba, Pb, Th, and U) as well as less incompatible elements (*e.g.*, heavy REE), indicating: i) a prominent recycled source component; ii) variable proportions of pyroxenite in the Atlantic source region; and/or, most likely iii) smaller degrees of melting and/or greater extents of fractional crystallization due to slower ridge spreading rates. Conversely, Pacific MORB have the most depleted regional signatures with regard to highly incompatible elements (*e.g.*, Ba, Pb, Th, and U), likely due to faster ridge spreading rates. Indian Ocean MORB exhibit limited variation in incompatible element enrichments/depletions but are generally the most depleted in more compatible elements (*e.g.*, Ti, Cr, Sc, and heavy REE), potentially due to distinct source characteristics or deep source melting in the garnet field. Atlantic, Pacific and Indian MORB can also be distinguished by trace element ratios, particularly Ce/Pb and Th/U.

Global MORB, and by inference the nominal MORB source region, are characterized by enrichments in Y/Ho and depletions in Th/U relative to the chondritic meteorites, and are complementary to the continental crust. However, the median of global MORB and the bulk continental crust both have sub-chondritic Ti/Eu and Nb/Ta ratios, suggesting an under-represented Ti- and Nb-rich reservoir in the Earth, potentially refractory, rutile-bearing eclogite at depth in the mantle.

8.6 A compositional model for the source(s) of Hawaiian lavas and other OIB

Despite the wide range of isotopic compositions observed in modern OIB, samples that represent isotopic "extremes" commonly have similar trace element signatures,

indicating a potential common precursor or source component. A compositional model for this source component has been developed based on the trace element chemistry of primitive OIB from the Enriched Mantle-type (EM) Hawaii and the HIMU-type (high μ; $\mu = {}^{238}U/{}^{204}Pb$) Austral-Cook islands. Abundances of W and Th are found to correlate negatively with MgO in these rocks, revealing a systematic enrichment in highly incompatible elements as a function of magmatic evolution, which can be used to interpolate the composition of the parental melts of these lavas. The parental melts, in turn, define an array of compositions from which a source component may be modeled.

The Hawaiian volcanics analyzed here originated from parental melts with ~16 wt.% MgO, and the abundances of W that are interpolated by the negative linear regressions derived from each individual volcanic center range from 80 to 210 ng/g W. Combined with a simple model of batch melting, the W content of the mantle sources of the Hualalai, Mauna Loa, Kohala, Kilauea, Mauna Kea, Koolau and Loihi shield volcanoes are 9 ± 2 (2σ) ng/g, 11 ± 5 ng/g, 10 ± 4 ng/g, 12 ± 4 ng/g, 10 ± 5 ng/g, 8 ± 7 ng/g, and 11 ± 5 ng/g respectively. Accordingly, the mean Hawaiian source has an average of 10 ± 3 ng/g W (2σ), which is three-times as enriched as the MORB source region (3.0 ± 2.3 ng/g W; Arevalo and McDonough, 2008).

To constrain the lower limit of incompatible element enrichment, and thus the upper limit of the mass fraction of a common OIB source component from the Austral-Cook samples examined here, we assume that the highest MgO content is representative of the Austral-Cook parental melt. Due to present data constraints, the abundance of Th (which is less fluid-mobile but similarly incompatible to W) is

modeled for the Austral-Cook source region. Accordingly, the Austral-Cook parental melt is projected to have (≥)1.62 ± 0.81 μg/g Th ($2\sigma_m$; assuming an MgO content of 20 wt.%), which equates to a source composition of (≥)83 ± 41 ng/g Th (following ~5% batch melting). Similar to the model of Ireland *et al.,* (2009), this model source component is approximately is ~1.0x as enriched as the undifferentiated primitive mantle, and ≥3x as enriched as the mean MORB source region (following 10% partial melting of MORB; Arevalo and McDonough, 2010), suggesting that the common enriched component observed in OIB may constitute ≤50% of the mantle mass. However, further studies of the Austral-Cook samples are required to improve the modeling of the HIMU source region, including the implementation of a more realistic fractional melting model.

8.7 Future directions of research an closing remarks

The primary objective of this research project was to gain insight into the chemical composition, structure and evolution of both the modern mantle and bulk silicate Earth through the use of trace element abundances and systematics. Low- and medium-resolution laser ablation (LA-) ICP-MS analytical methods were used to collect the data for this study. New insights have been gained, particularly with regard to establishing the planet's budgets of highly incompatible elements (especially K, W, Th, and U) and the chemical variations observed in MORB. Nonetheless, this study also demonstrates the need to pursue further constraints on the source composition of mantle-derived materials. In particular, the isotopic composition of W in Hawaiian picrites, particularly samples that have previously been characterized by anomalously

elevated ^{186}Os-^{187}Os, needs to be investigated in order to clarify the existence of putative core-mantle interactions in plume-derived magmas. Additionally, the K/U ratio of ancient mantle derivatives, such as Archean komatiites, also needs to be examined in order to provide a dimension of time to the terrestrial K/U ratio and investigate secular variations in other key trace element ratios.

The advances made here in establishing a MORB compositional model emphasize the need to develop a comparable compositional model for the common OIB source region. The OIB source model developed here represents the first step in advancing a compositional model for the lower portion of the modern mantle. Future studies need to focus on the weaker aspects of this study, including the degree and mode (*i.e.*, fractional vs. equilibrium) of partial melting and the proportional contribution of a pyroxenitic component in the source region of OIB. The similar degrees of incompatible element enrichment observed in both EM- (*i.e.*, Hawaii) and HIMU-type (*i.e.*, the Austral-Cook Islands) sources point to common mantle source region or component. By continuing to define OIB parental melt compositions and improving our understanding of the melting process responsible for these magmas, we may finally be able to quantify (better) the mass fraction of the mantle that is common to many OIB. This geochemical information may be able to contribute to the boundary conditions of the next generation of geophysical experiments and computational models that will hopefully be able to address the fundamental questions of just how well-mixed the modern mantle is, and how exactly it got to be that way.

Appendices

Appendix A

Appendix A. Major and trace element chemistry of analyzed samples.

Sample/ID	Type[a]	Location[b]	Lat (°N)	Long (°E)	SiO_2 (wt%)	TiO_2	Al_2O_3	FeO_t	MnO	MgO	CaO	Na_2O	K_2O	P_2O_5	Total
OC180 D5-1	N-MORB	NMAR	27.0	315.5	48.78	0.94	16.82	8.72	0.16	9.57	12.01	2.23	0.03	0.08	99.34
VG 6930	N-MORB	NMAR	54.8	324.8	51.09	1.22	14.65	11.03	nd	7.61	12.16	2.08	0.04	0.12	100.00
VG 6936	N-MORB	NMAR	54.8	324.8	51.62	1.27	14.21	11.22	nd	7.38	12.24	2.08	0.04	0.13	100.19
VG 6937	N-MORB	NMAR	54.8	324.8	51.25	1.15	14.64	11.30	nd	8.08	11.72	1.96	0.05	0.11	100.26
TK 5-1	N-MORB	NMAR	25.7	314.9	50.06	1.04	15.70	8.50	0.16	9.50	11.80	2.43	0.05	0.09	99.33
OCD180 D26-3	N-MORB	NMAR	33.6	320.8	49.14	2.11	13.90	12.75	0.23	6.57	10.56	2.95	0.08	0.20	98.49
TK 1-2	N-MORB	NMAR	26.1	315.5	49.85	1.56	15.28	9.88	0.18	7.85	10.65	3.00	0.08	0.15	98.48
TK 2-1	N-MORB	NMAR	26.3	315.3	50.05	1.36	15.30	9.21	0.17	9.24	11.30	2.61	0.08	0.14	99.46
OC180 D13-2	N-MORB	NMAR	29.5	317.1	49.45	1.87	14.50	11.45	0.21	7.04	10.93	3.05	0.12	0.17	98.79
VG 0738	N-MORB	NMAR	25.4	314.7	51.35	1.51	15.37	9.76	nd	7.17	11.39	2.94	0.06	0.12	99.67
VG 0739	N-MORB	NMAR	25.4	314.7	51.45	1.57	16.10	9.26	nd	7.59	11.22	3.11	0.11	0.12	100.53
TK 4-6	N-MORB	NMAR	25.8	314.9	50.44	1.39	15.31	9.00	0.17	8.90	11.10	2.73	0.10	0.15	99.29
VG 0741	N-MORB	NMAR	25.4	314.7	50.51	1.64	16.43	9.31	nd	7.76	11.21	2.85	0.10	0.13	99.94
VG 0735	N-MORB	NMAR	25.4	314.7	51.72	1.56	16.32	9.37	nd	7.61	11.24	2.89	0.11	0.15	100.97
Atlantica	E-MORB	MAR	0.0	0.0	50.67	1.34	14.98	9.17	0.17	8.26	12.19	2.15	0.15	0.01	99.07
MAR	N-MORB	MAR	0.0	0.0	49.59	1.23	15.24	10.00	0.18	9.09	11.36	2.56	0.09	1.23	100.57
VG 9055	N-MORB	SMAR	-26.5	346.2	50.93	1.43	15.57	9.24	nd	8.12	11.75	2.48	0.07	0.11	99.70
VG 9056	N-MORB	SMAR	-26.5	346.2	50.78	1.41	15.74	9.26	nd	8.20	11.78	2.44	0.08	0.14	99.83
VG 9052	N-MORB	SMAR	-26.5	346.2	50.70	1.43	15.57	9.07	nd	8.23	11.79	2.42	0.07	0.12	99.40
VG 3630	E-MORB	SMAR	-1.7	335.5	50.19	1.36	16.74	9.10	nd	7.86	10.92	3.09	0.40	0.18	99.84
R74-6	N-MORB	EPR	10.6	256.2	50.32	0.94	15.14	8.81	0.19	9.31	12.83	2.03	0.03	0.13	99.73
2384-9	N-MORB	EPR	8.4	256.3	48.79	1.04	16.88	7.92	0.14	9.70	11.67	2.44	0.03	0.11	98.72
2384-3	N-MORB	EPR	8.4	256.3	48.95	0.95	17.35	7.98	0.17	10.12	12.09	2.33	0.03	0.06	100.03
R30-30	N-MORB	EPR	9.2	254.4	48.94	1.08	16.91	8.35	0.17	9.29	12.03	2.73	0.04	0.15	99.69
R1-14	N-MORB	EPR	5.8	257.8	49.18	1.01	16.42	8.43	0.15	9.35	12.76	2.29	0.04	0.13	99.76
2387-2	N-MORB	EPR	8.4	256.3	51.04	1.52	14.93	9.31	0.16	7.56	11.23	2.94	0.08	0.10	98.87
R28-7	N-MORB	EPR	8.8	256.1	49.85	1.15	15.94	8.88	0.19	8.72	12.41	2.41	0.06	0.16	99.77
2706-7	N-MORB	EPR	9.5	255.8	50.97	1.27	15.39	9.20	0.19	8.06	12.23	2.52	0.07	0.11	100.01
R501-7	E-MORB	EPR	9.8	255.7	50.46	1.47	14.44	10.15	0.18	7.97	12.24	2.76	0.11	0.12	99.90
R494-5	E-MORB	EPR	9.8	255.7	50.24	1.76	14.47	10.55	0.19	7.46	11.90	2.94	0.18	0.18	99.87
R75-2	E-MORB	EPR	10.7	256.1	54.89	2.62	12.81	13.34	0.26	3.29	7.50	3.97	0.48	0.55	99.71
R501-2	E-MORB	EPR	9.8	255.7	50.46	1.47	14.44	10.15	0.18	7.97	12.24	2.76	0.11	0.12	99.90
R93-7	E-MORB	EPR	12.3	256.4	49.48	1.36	16.84	8.29	0.17	8.63	11.77	2.77	0.21	0.19	99.71
R15-2	E-MORB	EPR	8.8	255.5	48.97	2.38	18.10	8.89	0.20	6.47	8.95	3.87	1.32	0.57	99.72
R78-6	E-MORB	EPR	11.2	256.4	50.25	1.52	17.17	7.99	0.16	7.66	10.48	3.33	0.80	0.30	99.66
VE-32	E-MORB	EPR	15.5	254.6	50.88	1.86	14.13	10.44	0.21	6.70	10.86	2.97	0.31	0.21	98.57
2079-2	E-MORB	JdF Ridge	45.0	229.8	49.93	1.56	14.50	11.03	nd	7.43	12.00	2.48	0.12	0.15	99.20
2082-6A	E-MORB	JdF Ridge	45.0	229.8	49.97	1.34	15.20	10.05	nd	7.75	12.27	2.34	0.12	0.13	99.17
JdF MORB	E-MORB	JdF Ridge	44.6	229.6	49.67	1.83	13.73	11.71	0.23	6.87	10.84	2.68	0.16	0.12	97.86
VG-2	E-MORB	JdF Ridge	0.0	0.0	50.81	1.89	14.00	11.84	0.21	6.67	11.06	2.62	0.19	0.20	99.49
VG 5256	N-MORB	I Indian Ridg	9.8	57.9	50.69	0.72	16.82	7.78	nd	9.86	13.22	1.71	0.04	0.08	100.92
VG 5253	N-MORB	I Indian Ridg	9.8	57.9	50.37	0.70	16.71	7.64	nd	9.67	13.17	1.69	0.04	0.09	100.08
VG 5252	N-MORB	I Indian Ridg	9.8	57.9	50.19	0.70	16.64	7.71	nd	9.65	13.05	1.76	0.05	0.08	99.83
VG 5259	N-MORB	I Indian Ridg	9.8	57.9	50.30	0.70	16.46	7.63	nd	9.73	13.03	1.73	0.06	0.08	99.72
MD37-18 D2	E-MORB	E Indian Rid	-39.0	78.1	50.73	1.83	15.12	9.22	0.11	7.50	11.10	2.54	0.21	0.03	98.39
AAD 10-10	E-MORB	E Indian Rid	-49.9	115.4	50.54	1.01	16.32	7.45	0.15	8.75	11.75	2.79	0.14	0.11	99.01
AAD 7-3	E-MORB	E Indian Rid	-49.0	124.0	51.50	1.52	17.20	7.26	0.14	6.59	10.54	3.67	0.40	0.22	99.04
AAD 8-8	E-MORB	E Indian Rid	-49.5	121.0	50.98	1.25	16.14	7.55	0.15	7.94	10.97	3.26	0.36	0.17	98.77
MD 23-18 S3	N-MORB	I Indian Ridg	-25.4	70.1	49.78	1.19	16.49	7.77	0.13	9.52	12.15	2.20	0.02	0.01	99.26
JC 2-17 D1(3)	E-MORB	I Indian Ridg	-25.7	70.1	50.74	1.74	15.67	8.40	0.15	8.09	11.08	2.91	0.09	0.03	98.91
JC 3-02 D1	E-MORB	W Indian Rid	-27.4	66.4	50.18	1.66	17.27	7.14	0.13	8.00	10.15	3.79	0.15	0.04	98.50
MD 34 D5	E-MORB	W Indian Rid	-43.9	40.7	51.74	1.18	15.52	7.96	0.16	8.17	11.38	2.55	0.13	0.00	98.78
Pu'u O'o 90	OIB	Kiluaea, HI	19.4	204.7	50.56	2.57	13.62	11.04	0.19	6.27	10.59	2.21	0.45	0.18	97.68
Pu'u O'o 93	OIB	Kiluaea, HI	19.4	204.7	50.39	3.40	13.50	11.01	0.16	6.61	10.71	2.30	0.34	0.10	98.50
VG A-99	OIB	Kiluaea, HI	0.0	0.0	51.06	3.95	12.44	13.15	0.19	5.04	9.04	2.72	0.82	0.43	98.84
NMNH 116111-22	OIB	Kilauea, HI	19.4	204.8	49.63	2.46	12.27	11.60	nd	9.90	11.35	2.04	0.45	0.17	99.87
NMNH 113154-555	OIB	Galapagos	2.4	264.4	50.05	0.95	16.54	9.02	nd	8.31	12.55	2.18	0.07	0.08	99.75
NMNH 113154-557	OIB	Galapagos	2.4	264.4	50.62	1.04	16.49	8.79	nd	8.53	12.34	2.24	0.04	0.06	100.15
NMNH 113710-F709	OIB	dina Is., Gal	-0.4	268.5	48.59	4.14	13.20	14.09	0.20	5.77	10.80	2.91	0.61	0.36	100.66
NMNH 112048-2	OIB	ekla, Icelan	64.0	340.3	56.39	1.90	15.44	11.93	0.27	2.56	6.26	3.39	1.39	0.71	100.26
NMNH 112055	OIB	ekla, Icelan	64.0	340.3	56.62	1.85	14.99	12.05	0.24	2.60	6.33	3.37	1.36	0.70	100.12
NMNH 112207-75	OIB	rd Is., Austr	-53.1	73.5	43.91	6.68	12.01	13.91	0.14	5.88	11.68	2.59	2.35	0.65	99.79
NMNH 113057-3	ICV	iragongo, Za	-1.5	29.3	39.75	2.51	14.94	13.10	0.28	4.23	12.16	5.50	5.37	1.25	99.09
NMNH 115693	ICV	iragongo, Za	-1.5	29.3	39.76	2.88	15.17	13.00	0.29	4.27	12.26	5.43	5.34	1.37	99.76
NMNH 112514	ICV	muragira, Z	-1.4	29.2	45.92	3.76	16.49	11.94	0.18	4.40	9.41	3.19	3.52	0.49	99.29
NMNH 068376	ICV	nset Crater,	35.4	248.5	50.07	3.08	13.97	14.34	0.22	3.56	8.31	3.38	2.18	1.02	100.14
42995-3C	ICV	Yucca Mou	36.6	243.6	49.15	1.89	16.74	10.37	0.17	6.03	8.64	3.26	1.68	1.19	99.12
NMNH 116605.0013	ICV	er Hill, Aust	-38.5	142.3	48.76	2.91	16.55	11.45	0.15	4.06	9.06	4.13	2.71	0.91	100.67
NMNH 108800	IAB	hima Is., Jap	34.8	139.3	54.67	1.52	12.49	15.99	0.21	4.33	8.85	1.85	0.55	0.01	100.46
NMNH 116701-2	IAB	ggung, Indo	-7.3	108.0	54.01	1.86	14.73	12.82	0.22	4.15	9.12	3.16	0.87	0.10	101.03
NMNH 116141	CAB	aya, Guaten	14.4	269.4	53.74	1.99	13.97	13.31	0.19	3.58	7.34	3.33	1.67	0.37	99.48
NMNH 108135	CAB	n-Guanajuat	19.5	257.8	59.44	1.67	15.24	9.47	0.15	3.41	5.86	3.50	1.49	0.26	100.49
NMNH 116601-12	CAB	rango, Mexi	24.2	255.6	48.91	3.92	16.60	11.32	0.17	3.62	8.03	3.81	3.53	0.86	100.78
NMNH 113559-1	CAB	esuvius, Ital	40.8	14.4	50.83	1.99	16.93	10.60	0.20	3.15	6.85	4.93	3.47	0.94	99.90
VG 3636	BABB	otia Back-A	-56.4	329.3	51.69	1.34	16.36	7.99	nd	7.09	11.24	3.09	0.23	0.16	99.19
VG 3637	BABB	otia Back-A	-56.4	329.3	51.58	1.37	16.39	8.22	nd	7.08	11.29	3.10	0.25	0.18	99.46
VG 3635	BABB	otia Back-A	-56.4	329.3	52.16	1.42	16.19	8.12	nd	7.04	11.21	3.07	0.26	0.17	99.64
VG 3638	BABB	otia Back-A	-60.1	330.1	51.34	1.54	15.99	8.91	nd	6.69	11.36	3.38	0.35	0.20	99.76
VG 3634	BABB	otia Back-A	-56.4	329.3	51.70	1.37	16.23	8.14	nd	6.99	11.14	3.11	0.25	0.20	99.13
SLB 133 GA	BABB	thern Lau B	-22.2	184.6	57.77	1.43	15.08	10.01	0.19	3.00	7.33	3.52	0.47	0.25	99.05
SLB 58 GA-1	BABB	thern Lau B	-22.0	184.6	58.80	1.34	14.79	9.52	0.18	2.76	6.85	3.67	0.44	0.23	98.58
SLB 53 GC-1	BABB	thern Lau B	-21.5	184.4	53.60	1.21	15.36	9.99	0.18	5.16	9.30	2.85	0.38	0.16	98.19
SLB 127 KD	BABB	thern Lau B	-22.7	184.7	51.90	0.75	15.86	9.49	0.19	6.80	10.55	1.81	0.37	0.12	97.84
CLB 7GC	BABB	ntral Lau Ba	-18.6	184.4	49.90	1.04	14.72	9.84	0.18	8.34	12.53	2.15	0.01	0.06	98.77
CLB 42GC	BABB	ntral Lau Ba	-18.6	184.4	49.69	1.05	14.83	10.01	0.14	8.06	12.15	2.38	0.04	0.12	98.48
CLB 46GC	BABB	ntral Lau Ba	-18.8	184.5	50.40	1.35	13.91	11.81	0.22	7.30	11.60	2.40	0.02	0.09	99.10

[a] N-MORB, E-MORB, OIB, and BABB defined in text; ICV = intracontinental basalt, IAB = island arc basalt, CAB = continental arc basalt.

[b] NMAR = North Mid-Atlantic Ridge, SMAR = South Mid-Atlantic Ridge, EPR = East Pacific Rise, JdF Ridge = Juan de Fuca Ridge.

Appendix A. Major and trace element chemistry of analyzed samples (continued).

La (µg/g)	Ce	Pr	Nd	Sm	Eu	Gd	Tb	Dy	Ho	Er	Tm	Yb	Lu
1.10	3.73	0.71	4.50	2.02	0.81	3.13	0.56		0.88			2.60	
1.51	4.97	1.04	6.79	2.82	0.98	4.04	0.75	5.58	1.20	3.68	0.51	3.64	0.54
1.60	5.15	1.07	7.19	2.96	1.08	4.49	0.83	6.14	1.34	4.04	0.59	3.95	0.60
1.66	5.07	1.03	6.62	2.74	0.97	4.05	0.75	5.50	1.21	3.64	0.54	3.60	0.53
1.64	5.20	0.94	5.75	2.19	0.85	3.25	0.59	4.38	0.90	2.85	0.40	2.56	0.40
3.97	13.51	2.45	14.38	5.28	1.77	7.50	1.30		2.02			5.84	
3.01	9.58	1.69	9.67	3.56	1.25	4.97	0.82	6.08	1.29	3.66	0.53	3.61	0.54
2.78	8.93	1.56	8.92	3.22	1.16	4.44	0.78	5.51	1.17	3.35	0.48	3.24	0.50
3.81	12.15	2.12	11.94	4.39	1.52	5.94	1.04		1.55			4.47	
3.96	10.61	2.04	12.76	4.57	1.58	6.66	1.11	7.85	1.66	4.78	0.70	4.55	0.69
3.72	10.31	1.91	11.54	4.11	1.43	5.65	0.93	6.73	1.44	4.13	0.60	3.88	0.58
3.06	9.46	1.61	9.11	3.15	1.17	4.17	0.75	5.34	1.10	3.15	0.47	3.04	0.44
4.05	11.29	2.10	12.60	4.32	1.56	5.98	1.01	7.18	1.49	4.39	0.62	4.06	0.60
4.19	10.92	1.99	12.11	4.36	1.45	5.69	1.00	7.18	1.51	4.39	0.63	4.26	0.64
5.38	11.04	1.53	7.72	2.46	0.86	3.04	0.54	3.74	0.82	2.36	0.35	2.44	0.33
			7.48										
3.01	8.56	1.59	9.74	3.47	1.19	4.86	0.86	6.19	1.33	3.88	0.56	3.69	0.56
2.99	8.66	1.63	9.69	3.42	1.21	4.73	0.82	5.95	1.26	3.73	0.53	3.52	0.49
3.00	8.75	1.62	9.72	3.42	1.22	4.51	0.80	5.72	1.18	3.56	0.51	3.47	0.50
6.51	13.05	2.13	11.60	3.58	1.30	4.44	0.74	5.22	1.07	3.17	0.45	3.01	0.43
0.75	2.68	0.53	3.55	1.55	0.62	2.30	0.41	3.01	0.64	1.83	0.26	1.78	0.24
1.18	3.96	0.84	5.68	2.31	0.89	3.17	0.54	3.89	0.81	2.38	0.33	2.24	0.32
1.10	3.50	0.79	5.33	2.28	0.84	3.06	0.55	3.90	0.82	2.38	0.34	2.32	0.32
1.48	4.99	1.02	6.65	2.69	0.97	3.72	0.63	4.46	0.93	2.75	0.39	2.61	0.38
1.44	4.77	0.94	5.87	2.23	0.91	3.22	0.58	4.14	0.86	2.54	0.36	2.46	0.35
2.54	7.50	1.49	9.50	3.73	1.26	5.12	0.91	6.61	1.40	4.16	0.60	3.98	0.60
1.98	6.35	1.20	7.28	2.75	1.04	3.84	0.66	4.72	0.97	2.93	0.42	2.79	0.39
2.80	7.50	1.43	8.79	3.25	1.16	4.48	0.80	5.84	1.21	3.58	0.51	3.52	0.50
4.90	11.11	1.92	11.14	3.79	1.32	5.18	0.87	6.28	1.32	3.99	0.56	3.59	0.57
4.69	11.12	1.87	10.52	3.62	1.25	4.56	0.78	5.62	1.18	3.43	0.51	3.34	0.49
19.23	50.31	8.48	47.52	15.20	3.97	19.67	3.26	22.83	4.80	14.07	2.04	13.50	2.02
4.95	11.92	1.97	10.97	3.55	1.29	4.64	0.78	5.53	1.17	3.42	0.49	3.33	0.48
6.10	14.73	2.20	11.36	3.39	1.25	4.14	0.67	4.76	0.98	2.75	0.39	2.68	0.37
30.05	60.56	7.77	33.93	7.29	2.33	6.56	0.89	5.51	1.03	2.81	0.38	2.51	0.35
19.62	33.51	3.97	17.17	3.85	1.26	4.20	0.67	4.56	0.94	2.70	0.38	2.45	0.38
			13.43										
4.20	10.43	1.89	11.21	4.04	1.35	5.32	0.92	6.59	1.39	4.13	0.60	3.96	0.60
3.33	8.68	1.53	8.88	3.18	1.13	4.09	0.71	5.16	1.08	3.21	0.47	3.17	0.45
4.81	13.10	2.19	12.57	4.28	1.41	5.62	0.98	7.00	1.48	4.35	0.64	4.30	0.63
5.87	13.84	2.57	14.99	5.12	1.60	6.70	1.14	8.08	1.73	5.00	0.74	4.87	0.74
0.80	2.44	0.53	3.53	1.57	0.66	2.49	0.43	3.33	0.73	2.15	0.31	2.14	0.31
0.82	2.45	0.52	3.57	1.70	0.67	2.47	0.44	3.40	0.73	2.17	0.32	2.14	0.31
0.82	2.48	0.54	3.54	1.63	0.65	2.47	0.45	3.32	0.73	2.15	0.32	2.08	0.30
0.88	2.74	0.57	3.82	1.70	0.67	2.41	0.44	3.32	0.71	2.08	0.30	2.08	0.30
6.67	13.72	2.08	10.79	3.19	1.14	3.88	0.64	4.52	0.91	2.65	0.38	2.63	0.36
3.60	9.82	1.52	8.35	2.74	1.01	3.72	0.64	4.54	0.94	2.75	0.40	2.68	0.41
7.48	20.10	2.96	15.06	4.42	1.48	5.47	0.92	6.53	1.35	3.87	0.55	3.63	0.58
6.91	16.98		10.79	3.29	1.21	3.95		4.49		2.75		2.46	0.39
0.92	3.12	0.70	4.83	2.00	0.79	2.89	0.53	3.79	0.82	2.45	0.34	2.34	0.33
3.66	9.92	1.81	10.54	3.50	1.26	4.56	0.78	5.55	1.15	3.48	0.49	3.20	0.45
5.55	13.59	2.21	11.40	3.27	1.20	3.98	0.64	4.38	0.92	2.69	0.38	2.48	0.36
3.53	7.16	1.15	6.26	2.07	0.93	2.48	0.40	2.72	0.54	1.54	0.21	1.40	0.20
12.37	29.61	4.23	21.23	5.92	2.04	5.82	0.87	5.45	0.97	2.65	0.33	2.25	0.29
12.67	29.81	4.36	22.15	5.85	1.99	5.91	0.87	5.67	1.04	2.65	0.37	2.27	0.30
23.75	47.17	7.36	37.81	9.65	2.93	9.37	1.36	8.16	1.47	3.85	0.50	3.08	0.42
15.23	32.00	4.69	23.48	5.93	1.87	6.04	0.88	5.38	0.98	2.55	0.33	2.12	0.28
2.00	5.20	1.02	6.44	2.49	0.89	3.54	0.63	4.63	1.01	3.09	0.44	3.08	0.45
2.71	7.41	1.29	7.77	2.90	1.07	4.09	0.74	5.53	1.20	3.51	0.51	3.46	0.51
18.93	37.59	5.69	28.75	7.41	2.27	7.42	1.10	7.36	1.41	3.80	0.51	3.29	0.48
58.57	101.13	15.11	74.03	17.96	4.89	18.04	2.75	17.82	3.45	9.47	1.32	8.43	1.23
55.63	104.53	14.84	71.63	16.69	4.86	16.93	2.52	15.78	3.06	8.76	1.22	7.67	1.11
46.86	88.04	11.93	55.66	11.85	3.59	10.27	1.35	7.33	1.25	2.94	0.35	1.99	0.26
195.31	320.80	34.90	125.18	18.69	4.86	11.83	1.42	7.91	1.37	3.60	0.46	2.89	0.43
190.82	307.73	33.62	122.46	17.79	4.62	12.32	1.40	8.12	1.53	3.74	0.50	2.85	0.42
87.38	142.75	17.43	70.16	11.36	2.95	8.67	1.14	6.77	1.21	3.46	0.44	2.92	0.42
31.46	51.85	6.86	31.64	6.70	1.89	5.81	0.85	5.15	0.95	2.51	0.35	2.25	0.30
121.47	191.81	24.09	99.26	15.98	3.68	11.53	1.44	7.97	1.44	3.77	0.50	3.06	0.46
52.12	85.32	11.49	51.31	10.61	3.20	9.13	1.18	6.69	1.09	2.61	0.32	1.89	0.24
2.31	6.13	1.11	6.67	2.47	0.82	3.41	0.61	4.54	0.99	2.97	0.45	3.03	0.47
6.78	12.77	1.99	11.48	3.33	1.06	4.30	0.68	4.83	0.97	2.87	0.45	2.71	0.43
20.34	39.28	6.17	31.38	8.14	2.07	7.93	1.21	7.84	1.56	4.39	0.65	4.32	0.62
13.97	24.57	3.82	18.60	4.57	1.18	4.24	0.60	3.97	0.79	2.06	0.30	2.06	0.29
45.91	79.10	10.93	49.60	10.78	3.23	9.07	1.25	7.56	1.39	3.56	0.46	2.95	0.41
91.23	137.07	17.20	72.13	13.77	3.29	10.99	1.42	8.44	1.57	4.27	0.57	3.52	0.49
5.57	13.02	2.22	12.27	3.80	1.35	4.58	0.75	5.25	1.09	3.21	0.45	2.97	0.43
5.87	13.55	2.28	12.64	3.96	1.37	4.61	0.78	5.46	1.10	3.24	0.47	3.05	0.44
5.40	12.63	2.06	11.28	3.52	1.21	4.42	0.74	5.07	1.06	3.08	0.44	2.85	0.42
6.13	13.61	2.36	12.87	4.00	1.42	4.80	0.82	5.68	1.15	3.33	0.49	3.23	0.46
4.93	12.15	1.93	10.31	3.18	1.13	3.70	0.63	4.27	0.87	2.57	0.36	2.47	0.35
5.24	12.49	2.17	12.78	4.27	1.42	5.30	0.91	6.45	1.35	4.08	0.60	3.99	0.59
5.53	13.60	2.35	13.77	4.59	1.50	5.73	0.99	7.00	1.47	4.31	0.64	4.33	0.63
4.30	10.47	1.80	10.19	3.33	1.16	4.21	0.70	5.12	1.05	3.12	0.46	3.10	0.45
3.59	7.70	1.25	6.88	2.16	0.78	2.77	0.45	3.19	0.68	1.96	0.29	2.00	0.30
1.57	4.54	0.92	6.10	2.38	0.90	3.69	0.67	4.94	1.05	3.21	0.46	3.07	0.46
1.56	4.77	0.93	5.95	2.44	0.94	3.36	0.62	4.55	0.97	2.90	0.42	2.94	0.42
2.24	6.40	1.28	8.30	3.25	1.20	5.07	0.92	6.89	1.48	4.34	0.64	4.35	0.65

Appendix B

Appendix B. K and U abundances of the oceanic basalts analyzed here.

Sample/ID	Rock Type	Location	Lat (°N)	Long (°E)	La (ppm)	Sm (ppm)	La/Sm	K (ppm)	2σm	RSD (%)	n (K)	U (ppm)	2σm	RSD (%)	n (U)
NMNH 116111-22	OIB	Kilauea, HI	19.42	204.75	15.23	5.93	2.57	4715	1	0.0	4	0.347	0.0050	1.4	4
VG A99	OIB	Kiluaea, HI			23.75	9.65	2.46	5659	145	2.6	4	0.495	0.0127	2.6	4
Pu'u O'o 93	OIB	Kiluaea, HI	19.40	204.70	12.82	6.09	2.10	3791	234	6.2	4	0.306	0.0052	1.7	4
Pu'u O'o 90	OIB	Kiluaea, HI	19.40	204.70	12.37	5.92	2.09	3151	143	4.5	4	0.275	0.0086	3.1	2
NMNH113154-557	OIB	Galapagos	2.44	264.38	2.71	2.90	0.93	661	13	1.9	2	0.048	0.0008	1.6	4
NMNH 113154-555	OIB	Galapagos	2.44	264.38	2.00	2.49	0.80	444	5	1.1	4	0.023	0.0003	1.2	4
SLB 127KD	BABB	Southern Lau Basin	-22.67	184.73	3.59	2.16	1.66	4294	247	5.8	3	0.184	0.0024	1.3	4
VG 3634	BABB	Scotia Back-Arc	-56.39	329.34	4.93	3.18	1.55	2516	59	2.3	4	0.101	0.0033	3.3	4
VG 3638	BABB	Scotia Back-Arc	-60.07	330.05	6.13	4.00	1.54	2692	80	3.0	4	0.106	0.0018	1.7	4
VG 3635	BABB	Scotia Back-Arc	-56.39	329.34	5.40	3.52	1.53	2311	18	0.8	4	0.105	0.0011	1.1	4
VG 3637	BABB	Scotia Back-Arc	-56.39	329.34	5.87	3.96	1.48	2553	45	1.8	4	0.111	0.0015	1.3	4
VG 3636	BABB	Scotia Back-Arc	-56.39	329.34	5.57	3.80	1.47	2360	114	4.8	4	0.108	0.0025	2.3	4
SLB 53GC1	BABB	Southern Lau Basin	-21.47	184.38	4.30	3.33	1.29	3249	170	5.2	3	0.150	0.0010	0.7	4
SLB 133GA	BABB	Southern Lau Basin	-22.18	184.62	5.24	4.27	1.23	3587	146	4.1	3	0.197	0.0017	0.9	4
SLB 58GA1	BABB	Southern Lau Basin	-21.99	184.56	5.53	4.59	1.20	3866	56	1.5	3	0.198	0.0024	1.2	4
CLB 46GC	BABB	Central Lau Basin	-18.75	184.52	2.24	3.25	0.69	578	20	3.5	3	0.031	0.0006	1.9	3
CLB 42GC	BABB	Central Lau Basin	-18.58	184.43	1.57	2.34	0.67	506	35	7.0	3	0.020	0.0003	1.4	3
CLB 7GC	BABB	Central Lau Basin	-18.58	184.42	1.57	2.38	0.66	430	26	6.0	3	0.021	0.0002	1.1	3
R78-6	E-MORB	N. Pacific	11.22	256.42	19.62	3.85	5.10	7601	431	5.7	3	0.709	0.0094	1.3	2
VG 4049	E-MORB	N. Atlantic	45.5088	-29.476	20.40	4.10	4.98	8189	79	1.0	4	0.711	0.0051	0.7	4
VG 4045	E-MORB	N. Atlantic	45.5088	-29.476	15.73	3.80	4.14	6326	245	3.9	4	0.479	0.0050	1.0	4
R15-2	E-MORB	N. Pacific	8.76	255.46	30.05	7.29	4.12	10456	461	4.4	3	0.980	0.0407	4.2	2
VG 11212	E-MORB	S. Pacific	-54.59	-138.53	20.88	5.92	3.53	8745	382	4.4	4	0.672	0.0128	1.9	3
Atlantica	E-MORB	MAR			5.38	2.46	2.19	1870	35	1.9	4	0.159	0.0041	2.6	4
VG 1223	E-MORB	N. Pacific	2.70	-95.24	28.47	13.50	2.11	12245	377	3.1	4	1.087	0.0117	1.1	4
AAD 8-8	E-MORB	Indian Ocean	-49.47	121.03	6.91	3.29	2.10	2955	71	2.4	3	0.189	0.0050	2.7	4
MD37-18(06/D2)	E-MORB	Indian Ocean	-38.98	78.14	6.67	3.19	2.09	2822	14	0.5	4	0.183	0.0114	6.2	4
VG 11216	E-MORB	S. Pacific	-54.84	-137.88	7.20	3.49	2.06	2957	19	0.6	4	0.199	0.0027	1.4	3
VG 1214	E-MORB	N. Pacific	2.70	-95.24	32.83	17.59	1.87	11567	811	7.0	4	1.058	0.0139	1.3	4
VG 3630	E-MORB	S. Atlantic	-1.69	335.46	6.51	3.58	1.82	2975	97	3.2	4	0.163	0.0023	1.4	4
R93-7	E-MORB	N. Pacific	12.29	256.36	6.10	3.39	1.80	2095	47	2.2	3	0.135	0.0004	0.3	4
JC03-02-01D1(4)	E-MORB	Indian Ocean	-27.40	66.43	5.55	3.27	1.70	1934	11	0.6	4	0.094	0.0025	2.7	4
AAD 7-3	E-MORB	Indian Ocean	-49.03	124.00	7.48	4.42	1.69	3224	180	5.6	4	0.131	0.0010	0.7	4
VG 7281	E-MORB	S. Atlantic	-35.278	-15.735	7.42	4.52	1.64	2834	30	1.1	4	0.145	0.0030	2.1	4
VG 11236	E-MORB	S. Pacific	-55.67	-121.44	5.52	4.08	1.35	2090	53	2.5	4	0.136	0.0055	4.0	3
AAD 10-10	E-MORB	Indian Ocean	-49.92	115.38	3.60	2.74	1.31	1166	33	2.8	6	0.055	0.0009	1.7	4
R75-2	E-MORB	N. Pacific	10.69	256.13	19.23	15.20	1.27	4835	159	3.3	3	0.420	0.0166	4.0	4
VG 11208	E-MORB	S. Pacific	-56.25	-138.88	6.70	5.39	1.24	1880	28	1.5	4	0.166	0.0045	2.7	3
VG 11232	E-MORB	S. Pacific	-55.76	-122.89	5.46	4.59	1.19	1765	135	7.6	4	0.120	0.0033	2.7	3
VG 2	E-MORB	N. Pacific			5.87	5.12	1.15	1794	18	1.0	4	0.110	0.0021	1.9	4
VG 11239	E-MORB	S. Pacific	-55.15	-121.14	5.19	4.57	1.14	1694	32	1.9	4	0.113	0.0043	3.8	3
VG 11220	E-MORB	S. Pacific	-54.27	-134.89	3.29	2.92	1.13	1383	20	1.4	4	0.088	0.0005	0.6	3
VG 5674	E-MORB	S. Atlantic	-55.833	-4.422	4.04	3.62	1.12	1202	16	1.3	4	0.067	0.0011	1.7	4
VG 11200	E-MORB	S. Pacific	-56.02	-143.87	3.48	3.15	1.11	1027	32	3.1	4	0.070	0.0004	0.6	3
2082-6A	E-MORB	N. Pacific	44.98	229.78	3.33	3.18	1.05	1136	15	1.3	4	0.069	0.0014	2.0	4
JC2-17D1(3)	E-MORB	Indian Ocean	-25.66	70.05	3.66	3.50	1.04	897	6	0.7	4	0.052	0.0022	4.2	4
2079-2	E-MORB	N. Pacific	44.97	229.77	4.20	4.04	1.04	1391	14	1.0	6	0.078	0.0008	1.1	4
VG 11224	E-MORB	S. Pacific	-53.92	-134.57	2.97	2.92	1.02	1201	13	1.1	4	0.057	0.0012	2.2	3
VG 5675	E-MORB	S. Atlantic	-55.833	-4.422	3.89	3.88	1.00	1036	38	3.7	4	0.065	0.0008	1.2	4
VE-32	E-MORB	N. Pacific	15.52	254.62				2558	106	4.1	3	0.121	0.0031	2.5	4

Appendix B. K and U abundances of the oceanic basalts analyzed here (continued).

Sample/ID	Rock Type	Location	Lat (°N)	Long (°E)	La (ppm)	Sm (ppm)	La/Sm	K (ppm)	2σm	RSD (%)	n (K)	U (ppm)	2σm	RSD (%)	n (U)
VG 7289	N-MORB	S. Atlantic	-34.553	-15.147	4.55	4.61	0.99	1225	6	0.5	4	0.061	0.0009	1.5	4
TK4-6	N-MORB	N. Atlantic	25.80	314.92	3.06	3.15	0.97	943	14	1.5	3	0.048	0.0009	1.9	4
VG 735	N-MORB	N. Atlantic	25.40	314.70	4.19	4.36	0.96	1197	28	2.4	4	0.064	0.0007	1.1	4
VG 5269	N-MORB	Indian Ocean	3.70	63.89	3.31	3.46	0.95	1104	27	2.4	4	0.054	0.0016	2.9	4
VG 741	N-MORB	N. Atlantic	25.40	314.70	4.05	4.32	0.94	995	3	0.3	3	0.055	0.0016	2.8	4
VG 296	N-MORB	N. Atlantic	22.24	-45.02	3.27	3.61	0.91	1024	11	1.1	4	0.049	0.0009	1.9	4
VG 739	N-MORB	N. Atlantic	25.40	314.70	3.72	4.11	0.91	1008	25	2.4	3	0.050	0.0007	1.4	3
VG 5262	N-MORB	Indian Ocean	3.78	63.87	3.39	3.75	0.90	983	9	0.9	4	0.047	0.0015	3.2	4
VG 708	N-MORB	S. Pacific	-9.0067	-83.53	3.36	3.73	0.90	862	8	0.9	4	0.040	0.0006	1.5	4
VG 11228	N-MORB	S. Pacific	-55.10	-127.61	2.65	3.00	0.88	726	7	0.9	4	0.039	0.0009	2.4	3
VG 9052	N-MORB	S. Atlantic	-26.49	346.25	3.00	3.42	0.88	621	8	1.2	4	0.032	0.0001	0.3	4
VG 9056	N-MORB	S. Atlantic	-26.49	346.25	2.99	3.42	0.87	646	8	1.2	4	0.035	0.0025	7.0	2
VG 9055	N-MORB	S. Atlantic	-26.49	346.25	3.01	3.47	0.87	627	14	2.2	4	0.035	0.0006	1.7	4
OC180 D13-2	N-MORB	N. Atlantic	29.50	317.10	3.81	4.39	0.87	866	51	5.9	3	0.053	0.0019	3.5	4
VG 738	N-MORB	N. Atlantic	25.40	314.70	3.96	4.57	0.87	886	13	1.5	3	0.045	0.0015	3.4	4
TK2-1	N-MORB	N. Atlantic	26.27	315.27	2.78	3.22	0.86	792	24	3.0	3	0.041	0.0006	1.4	4
2706-7	N-MORB	N. Pacific	9.54	255.76	2.80	3.25	0.86	740	17	2.3	4	0.037	0.0004	1.2	4
VG 11226	N-MORB	S. Pacific	-55.33	-127.76	2.95	3.43	0.86	907	6	0.7	4	0.045	0.0017	3.9	3
VG 5284	N-MORB	Indian Ocean	-1.65	67.77	3.42	3.99	0.86	999	19	1.9	3	0.044	0.0010	2.2	4
TK1-2	N-MORB	N. Atlantic	26.11	315.47	3.01	3.56	0.85	827	40	4.8	3	0.036	0.0009	2.5	4
VG 706	N-MORB	Indian Ocean	-11.1535	70.526	2.39	3.02	0.79	821	31	3.8	4	0.048	0.0013	2.7	4
OC180 D-26-3	N-MORB	N. Atlantic	33.59	320.85	3.97	5.28	0.75	785	31	3.9	3	0.053	0.0010	1.8	4
VG 968	N-MORB	N. Atlantic	28.90	-43.32	1.76	2.34	0.75	480	4	0.8	5	0.022	0.0015	7.0	4
TK5-1	N-MORB	N. Atlantic	25.73	314.89	1.64	2.19	0.75	566	13	2.2	6	0.021	0.0003	1.6	4
VG 11204	N-MORB	S. Pacific	-56.68	-139.67	1.98	2.69	0.74	509	7	1.5	4	0.025	0.0005	1.9	2
R28-7	N-MORB	N. Pacific	8.81	256.10	1.98	2.75	0.72	467	20	4.3	3	0.025	0.0005	2.0	3
VG 962	N-MORB	N. Atlantic	70.17	-15.28	1.18	1.68	0.70	421	9	2.1	4	0.019	0.0007	3.7	4
2387-2	N-MORB	N. Pacific	8.40	256.30	2.54	3.73	0.68	617	36	5.8	4	0.035	0.0006	1.7	4
R1-14	N-MORB	N. Pacific	5.77	257.82	1.44	2.23	0.65	322	6	2.0	3	0.017	0.0016	9.1	2
VG 6937	N-MORB	N. Atlantic	54.76	324.78	1.66	2.74	0.61	450	5	1.1	4	0.020	0.0005	2.6	3
R30-30	N-MORB	N. Pacific	9.18	254.40	1.48	2.69	0.55	373	7	1.9	3	0.032	0.0016	5.0	3
VG 6936	N-MORB	N. Atlantic	54.76	324.78	1.60	2.96	0.54	335	3	1.0	4	0.017	0.0002	1.2	4
VG 6930	N-MORB	N. Atlantic	54.76	324.78	1.51	2.82	0.54	336	13	3.9	4	0.017	0.0002	1.2	4
2384-3	N-MORB	N. Pacific	8.37	256.34	1.11	2.08	0.53	239	3	1.1	6	0.015	0.0007	4.8	4
VG 5259	N-MORB	Indian Ocean	9.83	57.95	0.88	1.70	0.52	227	7	3.1	4	0.010	0.0006	5.4	4
VG 5256	N-MORB	Indian Ocean	9.83	57.95	0.80	1.57	0.51	237	2	0.6	4	0.010	0.0005	4.7	4
2384-9	N-MORB	N. Pacific	8.38	256.33	0.98	1.95	0.50	299	3	1.1	4	0.015	0.0005	3.6	4
VG 5252	N-MORB	Indian Ocean	9.83	57.95	0.82	1.63	0.50	253	6	2.2	3	0.011	0.0005	4.1	4
R74-6	N-MORB	N. Pacific	10.62	256.16	0.75	1.55	0.48	138	9	6.6	3	0.010	0.0004	3.8	3
VG 5253	N-MORB	Indian Ocean	9.83	57.95	0.82	1.70	0.48	218	8	3.7	4	0.011	0.0004	3.7	4
MD23-18 S3/CIR	N-MORB	Indian Ocean	-25.39	70.06	0.92	2.00	0.46	140	6	3.9	4	0.005	0.0001	2.7	4
MAR	N-MORB	MAR						491	10	2.1	3	0.031	0.0006	2.1	4

Appendix C

Techniques for Deriving Best-Fit Linear Regressions

A linear regression approximates the relationship between two variables (*e.g.*, x and y) in the linear form:

$$y = mx + b$$

where m represents the slope of the best-fit line (namely the change in y that accompanies a change of one unit in x) and b is the y-intercept (the value of y at $x = 0$). An inherent assumption of this method is that the data are linear. In general, the goal of a linear regression is to find the linear equation that best predicts y from x. However, multiple statistical derivations of the "best-fit" linear regression exist and can provide different answers.

Conventional univariate least-squares method

Commercial software programs, such as Microsoft Excel and Systat SigmaPlot, utilize traditional linear regression methods, namely the *univariate method of least-squares* which relies on finding the line that **minimizes the sum of the squares of the vertical distances, or vertical residuals,** of the data points from the line. This procedure assumes that the errors/uncertainties (*e.g.*, standard deviations of each data point) in the y-values are substantially greater than the errors in the x-values. A second assumption is that the error/uncertainties in all the y-values are similar in magnitude and Gaussian, or normal, in character. Finally, this method also assumes that the statistical scatter about the best-fit linear regression is normally distributed:

thus, the *univariate least-squares* regression is based on minimizing the following expression:

$$\Sigma(y - y')^2 = \Sigma[y - (mx + b)]^2$$

where *y'* represents the expected value at any *x*-coordinate and *y* is the observed value.

The assumption of zero or negligible errors/uncertainties on the *x*-values is commonly not applicable to real data where both the *x*- and *y*-coordinates represent measurements of an unknown, and thus have inherent uncertainties in both *x* and *y*. For this reason, the *bivariate least-squares* and *robust regression* methods are superior for defining the trend of real scientific data.

Bivariate least-squares method

The most simple and straightforward linear regression method to account for a dataset with uncertainties in both *x*- and *y*-coordinates, termed the *bivariate least-squares* method, is based on **minimizing the sum of squares of the distances perpendicular to the best-fit line, or perpendicular residuals,** following the protocol established in York (1966). If the errors/uncertainties associated with each data point are non-uniform, each data point may be weighted inversely by its own variance; this allows data points with the smallest errors/uncertainties (and thus the highest degrees of confidence) to be given extra weight to the regression analysis. As with the conventional *univariate least-squares* method, however, the *bivariate least-squares* technique also relies on inherent assumptions, namely that the errors along both the x- and y-variables are Gaussian and that the statistical scatter of the dataset is normally

distributed. Both *least-squares* techniques are susceptible to the effects of outliers, which are given disproportional weight due to their locations at the extreme high or low end of the data spectrum. However, outliers can be statistically identified, and given that sample measurements are normally accompanied by analytical uncertainties, the bivariate least-squares regression analysis provides the preferred means to calculate a best-fit linear regression.

Robust Regression Method

An alternative means of fitting a linear equation to a dataset with two independent variables with associated uncertainties, commonly referred to as a *robust regression*, is based on a **distribution-free estimate of the best-fit linear slope** (Theil, 1950; Vugrinovich, 1981; Hoaglin *et al.,* 1983). This method calculates a slope from all possible pairs of data points (resulting in *n(n-1)/2* slope estimates) and then finds the median value of these slopes. This method assumes that all *x* are distinct, and defines:

$$m_{ij} = \frac{y_j - y_i}{x_j - x_i} \qquad \text{where} \quad 1 \le i < j \le n$$

with the best-fit slope is defined by:

$$m_T = med\{m_{ij}\}$$

Although this method can only describe data with uniform analytical errors, *robust regression* analysis makes no assumptions about the distribution of data scatter (unlike both *least-squares* methods, which assume a normal distribution of scatter) and weighs all data points equally, even outliers with extreme *x*- and *y*-coordinates (unlike both *least-squares* methods).

Appendix D

Apendix D. Olivine correction of matrix W concentrations to whole rock W concentrations.

Volcano	Sample Name	MgO_{wr} (wt%)[e]	MgO_{ol}[b]	MgO_{gl}[b]	%ol calc[c]	2σ calc[d]	%ol point count	#points	2σ point count[e]
Mauna Kea									
	MK-1-6[d]	17.24	46.63	6.47	26.8	0.5	23	500	2
Mauna Loa									
	ML-2-50	19.92	49.27	5.49	33.0	0.5			
	ML KAH-1	21.66	49.34				34	500	2
	ML 1868-9	21.48	48.31				36	1000	2
Hualalai									
	H-2	13.63	47.97	4.96	20.2	0.4	19	500	2
	H-7	11.23	47.76	5.91	12.7	0.4	13	500	2
	H-9	11.30	47.88	6.12	12.4	0.4	14	500	2
	H-11	13.67	47.29	6.35	17.9	0.4	18	500	2
	H-27	14.91	48.29	5.97	21.1	0.4			
	H-P	23.19	47.17	7.26	39.9	0.6	44	1000	2
Loihi									
	LO-02-02	24.21	47.31	8.69	40.2	0.7			
	LO-02-04	26.58	46.29	1.89	55.6	0.6			
	158-9	16.57	48.53	7.17	22.7	0.5			
	186-5	19.52	46.67				30	1000	1
	186-11	13.76	45.59				21	1000	1
	187-1	25.16	47.36	6.49	45.7	0.7			
Kilauea									
	KIL-1-18	13.80	48.35				15	1000	1
	KIL-2-3	22.36	48.11				40	500	2
	KIL-2-4	22.55	48.89	4.87	40.2	0.6			
	KIL-3-1	19.24	47.60	5.33	32.9	0.5			
	KIL 1840-2	14.27	47.80				21	500	2
Koolau									
	K98-08	17.78	45.74				29	500	2
	S497-6	21.55	47.78				42	500	2
	S500-5B	21.22	47.98	4.37	38.6	0.5			
Kohala									
	KO-1-10	13.54	46.95				20	500	2
	KO-1-20	9.60	47.26	5.56	9.7	0.3	10	500	1
	KOH-1-28	20.52	48.37	5.52	35.0	0.5			
Lanai									
	LWAW-4	14.48	44.87				15	1000	1
	LWAW-7	11.69	47.92				9	1000	1
Molokai									
	S501-2	28.96	48.05	8.39	51.9	0.8	51	500	2

[a] MgO contents from Ireland et al. (2009) and references therein.

[b] average olivine (n=8) and glass (n=5) MgO data collected on a JEOL JXA-8900 electron microprobe at the University of Maryland.

[c] % ol calc=$(MgO_{WR}-MgO_{gl})/(MgO_{ol}-MgO_{gl})*100$.

[d] 2σ calc was calculated assuming an external precision of 1% for MgO_{WR} and 0.2% for MgO_{gl} and $MgO_{ol.}$

[e] 2σ point count was calculated using the method from: van der Plas, L. and Tobi, A.C. (1965) A chart for judging the reliability of point counting results. American Journal of Science 263, 37-90.

Appendix E

Appendix E. La, Yb, Lu, Hf, Sm and Nd data for Hawaiian picrites.

Volcano	Sample Name	La (μg/g)	Yb	Lu	Hf	Sm	Nd
Mauna Kea							
	MK 1-6[a]	10.32	1.99	0.28	3.91	4.92	18.10
Mauna Loa							
	ML 2-50[a]	5.45	1.41	0.20	2.34	3.01	10.40
	ML KAH-1[a]	6.42	1.46	0.21	2.59	3.30	11.70
	ML 1868-9[a]	6.02	1.26	0.18	2.28	3.05	11.00
Hualalai							
	H-2[c]	6.80	1.51	0.20	2.15	3.68	12.92
	H-7[b]	7.41	1.76	0.22	2.74	3.84	14.30
	H-9[c]	9.24	2.10	0.29	3.09	4.91	17.33
	H-11[a]	7.19	1.65	0.23	2.61	3.52	12.60
	H-27[c]	7.08	1.76	0.25	2.56	3.81	13.11
	H-P[c]	5.01	1.36	0.18	1.99	3.00	10.00
Loihi							
	Lo-02-02[a]	7.73	1.03	0.14	2.16	2.69	11.10
	Lo-02-04[a]	8.43	1.08	0.15	2.26	2.94	11.90
Kilauea							
	KIL 1-18[a]	9.94	1.71	0.23	3.37	4.43	17.20
	KIL 2-3[c]	8.82	1.49	0.20	2.55	4.07	15.02
	KIL 2-4[c]	10.19	1.85	0.24	3.25	4.63	16.97
	KIL 3-1[c]	13.77	2.13	0.30	4.33	5.92	22.61
	KIL 1840-2[a]	9.68	1.71	0.24	3.37	4.52	17.00
Koolau							
	K 497-6[c]	8.70	1.57	0.23	2.95	4.35	15.77
	K 500-5B[c]	6.61	1.28	0.17	2.00	3.28	12.20
Kohala							
	Ko 1-10[c]	9.98	1.88	0.25	3.04	4.86	18.05
	Ko 1-20[c]	13.58	2.45	0.31	4.30	6.66	24.90
	Ko 1-28[a]	6.26	1.35	0.19	2.27	3.00	11.00

[a] Norman and Garcia (1999).

[b] Gurriet (1988).

[c] This study.

Bibliography

GeoReM Database. MPI für Chemie, Mainz, Germany, http://georem.mpch-mainz.gwdg.de/.

NIST Standard Reference Materials. National Institute of Standards and Technology, http://ts.nist.gov/measurementservices/referencematerials/index.cfm.

PetDB Petrological Database of the Ocean Floor. Geoinformatics for Geochemistry Program (LDEO-CIESIN), http://www.petdb.org/.

USGS Geochemical Reference Materials and Certificates. United States Geological Survey, http://minerals.cr.usgs.gov/geo_chem_stand/.

(2001)
CRC Handbook of Chemistry and Physics, 82nd Edition. CRC Press LLC.

(2005)
Excimer Laser Technology. Springer Science + Business Media, Inc., 433 pp.

(2006)
Handbook of Physics. Springer Science + Business Media, Inc. (Rensselaer, NY), 1181 pp.

D. Abbott, L. Burgess, J. Longhi and W.H.F. Smith (1994)
An empirical thermal history of the Earth's upper mantle. Journal of Geophysical Research: Solid Earth, 99, 13835-13850.

W. Abouchami, S.J.G. Galer and A.W. Hofmann (2000)
High precision lead isotope systematics of lavas from the Hawaiian Scientific Drilling Project. Chemical Geology, 169, 187-209.

L.H. Ahrens (1954)
The log-normal distribution of the elements (a fundamental law of geochemistry and its subsidiary). Geochimica Et Cosmochimica Acta, 5, 49-73.

F. Albarède (1998)
Time-dependent models of U-Th-He and K-Ar evolution and the layering of mantle convection. Chemical Geology, 145, 413-429.

F. Albarède and B. Beard (2004)
Analytical methods for non-traditional isotopes. In: C.M. Johnson, B.L. Beard and F. Albaréde (Eds.), Geochemistry of Non-Traditional Stable Isotopes, Reviews in Mineralogy and Geochemistry, 454.

F. Albarède and R.D. van der Hilst (2002)
Zoned mantle convection. Philosophical Transactions of the Royal Society of London Series A: Mathematical, Physical and Engineering Sciences, 360, 2569-2592.

C.J. Allègre (1969)
Behavior of U-Th-Pb systems in the upper mantle and a model of evolution of the upper mantle throughout geologic times. Geochemistry International USSR, 6, 1174.

C.J. Allègre, B. Hamelin and B. Dupré (1984)
Statistical analysis of isotopic ratios in MORB: The mantle blob cluster model and the convective regime of the mantle. Earth and Planetary Science Letters, 71, 71-84.

C.J. Allègre, B. Hamelin, A. Provost and B. Dupré (1987)
Topology in isotopic multispace and origin of mantle chemical heterogeneities. Earth and Planetary Science Letters, 81, 319-337.

C.J. Allègre, A. Hofmann and K. O'Nions (1996)
The argon constraints on mantle structure. Geophysical Research Letters, 23, 3555-3557.

C.J. Allègre, G. Manhes and C. Gopel (1995)
The age of the Earth. Geochimica Et Cosmochimica Acta, 59, 1445-1456.

C.J. Allègre, P. Schiano and E. Lewin (1995)
Differences between oceanic basalts by multitrace element ratio topology. Earth and Planetary Science Letters, 129, 1-12.

C.J. Allègre, T. Staudacher and P. Sarda (1987)
Rare-Gas Systematics - Formation of the Atmosphere, Evolution and Structure of the Earths Mantle. Earth and Planetary Science Letters, 81, 127-150.

C.J. Allègre, T. Staudacher, P. Sarda and M. Kurz (1983)
Constraints on evolution of Earth's mantle from rare gas systematics. Nature, 303, 762-766.

C.J. Allègre and D.L. Turcotte (1986)
Implications of a two-component marble cake mantle. Nature, 323, 123-127.

M.v. Allmen (1986)
Laser-Beam Interactions with Materials: Physical Principles and Applications. Springer-Verlag, 194 pp.

D.L. Anderson (1981)
Hotspots, basalts, and the evolution of the mantle. Science, 213, 82-89.

T. Araki, S. Enomoto, K. Furuno, Y. Gando, K. Ichimura, H. Ikeda, K. Inoue, Y. Kishimoto, M. Koga, Y. Koseki, T. Maeda, T. Mitsui, M. Motoki, K. Nakajima, H. Ogawa, M. Ogawa, K. Owada, J.S. Ricol, I. Shimizu, J. Shirai, F. Suekane, A. Suzuki, K. Tada, S. Takeuchi, K. Tamae, Y. Tsuda, H. Watanabe, J. Busenitz, T. Classen, Z. Djurcic, G. Keefer, D. Leonard, A. Piepke, E. Yakushev, B.E. Berger, Y.D. Chan, M.P. Decowski, D.A. Dwyer, S.J. Freedman, B.K. Fujikawa, J. Goldman, F. Gray, K.M. Heeger, L. Hsu, K.T. Lesko, K.B. Luk, H. Murayama, T. O'Donnell, A.W.P. Poon, H.M. Steiner, L.A. Winslow, C. Mauger, R.D. McKeown, P. Vogel, C.E. Lane, T. Miletic, G. Guillian, J.G. Learned, J. Maricic, S. Matsuno, S. Pakvasa, G.A. Horton-Smith, S. Dazeley, S. Hatakeyama, A. Rojas, R. Svoboda, B.D. Dieterle, J. Detwiler, G. Gratta, K. Ishii, N. Tolich, Y. Uchida, M. Batygov, W. Bugg, Y. Efremenko, Y. Kamyshkov, A. Kozlov, Y. Nakamura, H.J. Karwowski, D.M. Markoff, K. Nakamura, R.M. Rohm, W. Tornow, R. Wendell, M.J. Chen, Y.F. Wang and F. Piquemal (2005)
Experimental investigation of geologically produced antineutrinos with KamLAND. Nature, 436, 499-503.

R.J. Arculus and J.W. Delano (1981)
Siderophile element abundances in the upper mantle: Evidence for a sulfide signature and equilibrium with the core. Geochimica Et Cosmochimica Acta, 45, 1331-1343.

R. Arevalo Jr. and W.F. McDonough (2008)
Tungsten geochemistry and implications for understanding the Earth's interior. Earth and Planetary Science Letters, 272, 656-665.

R. Arevalo Jr. and W.F. McDonough (2010)
Chemical variations and regional diversity observed in MORB. Chemical Geology, 271, 70-85.

R. Arevalo Jr., W.F. McDonough and M. Luong (2009)
The K/U ratio of the silicate Earth: Insights into mantle composition, structure and thermal evolution. Earth and Planetary Science Letters, 278, 361–369.

P.D. Asimow, M.M. Hirschmann and E.M. Stolper (1997)
An analysis of variations in isentropic melt productivity. Philosophical Transactions of the Royal Society A: Mathematical Physical and Engineering Sciences, 355, 255-281.

C.M. Barshick, D.H. Smith, E. Johnson, F.L. King, T. Bastug and B. Fricke (1995)
Periodic nature of metal-noble gas adduct ions in glow-discharge mass spectrometry. Applied Spectroscopy, 49, 885-889.

D. Bäuerle (1996)
Laser Processing and Chemistry (2nd Edition). Springer-Verlag (Berlin), 649 pp.

J.S. Becker and H.J. Dietze (1995)
Cluster formation processes in laser and spark plasmas of rare-earth oxide-graphite mixtures. Journal of Analytical Atomic Spectrometry, 10, 637-641.

J.S. Becker and H.J. Dietze (1997)
Investigations on cluster and molecular ion formation by plasma mass spectrometry. Fresenius Journal of Analytical Chemistry, 359, 338-345.

J.S. Becker and H.J. Dietze (2000)
Oxide ion formation of long-lived radionuclides in double-focusing sector field inductively coupled plasma mass spectrometry and their analytical applications. International Journal of Mass Spectrometry, 202, 69-79.

J.S. Becker, G. Seifert, A.I. Saprykin and H.J. Dietze (1996)
Mass spectrometric and theoretical investigations into the formation of argon molecular ions in plasma mass spectrometry. Journal of Analytical Atomic Spectrometry, 11, 643-648.

F. Begemann, H.W. Weber and H. Hintenberger (1976)
Primordial abundance of ^{40}Ar. Astrophysical Journal, 203, L155-L157.

V.C. Bennett, T.M. Esat and M.D. Norman (1996)
Two mantle-plume components in Hawaiian picrites inferred from correlated Os–Pb isotopes. Nature, 381, 221-224.

P.R. Bevington and D.K. Robinson (2003)
Data Reduction and Error Analysis for the Physical Sciences. McGraw-Hill (New York, NY), 320 pp.

A. Bézos, J.P. Lorand, E. Humler and M. Gros (2005)
Platinum-group element systematics in mid-oceanic ridge basaltic glasses from the Pacific, Atlantic, and Indian Oceans. Geochimica Et Cosmochimica Acta, 69, 2613-2627.

J. Blichert-Toft and F. Albarède (1999)
Hf isotopic compositions of the Hawaii Scientific Drilling Project core and the source mineralogy of Hawaiian basalts. Geophysical Research Letters, 26, 935-938.

J. Blichert-Toft and F. Albarède (2009)
Mixing of isotopic heterogeneities in the Mauna Kea plume conduit. Earth and Planetary Science Letters, 282, 190-200.

J. Blichert-Toft, F.A. Frey and F. Albarède (1999)
Hf isotope evidence for pelagic sediments in the source of Hawaiian basalts. Science, 285, 879-882.

N. Bloembergen (1979)
Laser-Solid Interaction and Processing. American Institute of Physics (New York, NY).

A. Bogaerts and Z.Y. Chen (2005)
Effect of laser parameters on laser ablation and laser-induced plasma formation: A numerical modeling investigation. Spectrochimica Acta Part B: Atomic Spectroscopy, 60, 1280-1307.

A.M. Bond, T.A. Odonnell, A.B. Waugh and Mclaughl.Rj (1970)
Use of polarographic methods for determination of tin in geological samples. Analytical Chemistry, 42, 1168-1172.

H. Borchert, K. Dar´ee and M. Hugenschmidt (2005)
Plasma formation during the interaction of picosecond and nanosecond laser pulses with BK7 glass
Journal of Physics D: Applied Physics, 38, 300-305.

O.V. Borisov, X.L. Mao and R.E. Russo (2000)
Effects of crater development on fractionation and signal intensity during laser ablation inductively coupled plasma mass spectrometry. Spectrochimica Acta Part B: Atomic Spectroscopy, 55, 1693-1704.

M. Boyet and R.W. Carlson (2005)
^{142}Nd evidence for early (>4.53 Ga) global differentiation of the silicate Earth. Science, 309, 576-581.

M. Boyet and R.W. Carlson (2006)
A new geochemical model for the Earth's mantle inferred from ^{146}Sm-^{142}Nd systematics. Earth and Planetary Science Letters, 250, 254-268.

A.D. Brandon, M.D. Norman, R.J. Walker and J.W. Morgan (1999)
^{186}Os-^{187}Os systematics of Hawaiian picrites. Earth and Planetary Science Letters, 174, 25-42.

A.D. Brandon and R.J. Walker (2005)
The debate over core-mantle interaction. Earth and Planetary Science Letters, 232, 211-225.

A.D. Brandon, R.J. Walker, J.W. Morgan, M.D. Norman and H.M. Prichard (1998)
Coupled ^{186}Os and ^{187}Os evidence for core-mantle interaction. Science, 280, 1570-1573.

R. Brett (1984)
Chemical equilibration of the Earth's core and upper mantle. Geochimica Et Cosmochimica Acta, 48, 1183-1188.

R.W. Carlson (1984)
Isotopic constraints on Columbia River flood basalt genesis and the nature of the subcontinental mantle. Geochimica Et Cosmochimica Acta, 48, 2357-2372.

P. Carpenter, D. Counce, E. Kluk and C. Nabelek (2002)
Characterization of Corning EPMA standard glasses 95IRV, 95IRW, and 95IRX. Journal of Research of the National Institute of Standards and Technology, 107, 703–718.

N.L. Chabot and M.J. Drake (1999)
Potassium solubility in metal: The effects of composition at 15 kbar and 1900 degrees C on partitioning between iron alloys and silicate melts. Earth and Planetary Science Letters, 172, 323-335.

G.C.Y. Chan, W.T. Chan, X.L. Mao and R.E. Russo (2000)
Investigation of matrix effect on dry inductively coupled plasma conditions using laser ablation sampling. Spectrochimica Acta Part B-Atomic Spectroscopy, 55, 221-235.

Z.Y. Chen and A. Bogaerts (2005)
Laser ablation of Cu and plume expansion into 1 atm ambient gas. Journal of Applied Physics, 97, 063305 (2005).

R.Y. Chiao, E. Garmire and C.H. Townes (1964)
Self-Trapping of Optical Beams. Physics Review Letters, 13, 479–482.

M. Condomines, P. Morand and C.J. Allègre (1981)
^{230}Th-^{238}U radioactive disequilibria in tholeiites from the FAMOUS Zone (Mid-Atlantic Ridge, 36° 50'N): Th and Sr isotopic geochemistry. Earth and Planetary Science Letters, 55, 247-256.

A. Corgne, S. Keshav, Y.W. Fei and W.F. McDonough (2007)
How much potassium is in the Earth's core? New insights from partitioning experiments. Earth and Planetary Science Letters, 256, 567-576.

V. Courtillot, A. Davaille, J. Besse and J. Stock (2003)
Three distinct types of hotspots in the Earth's mantle. Earth and Planetary Science Letters, 205, 295-308.

K.C. Creager and T.H. Jordan (1984)
Slab penetration into the lower mantle. Journal of Geophysical Research, 89, 3031-3049.

J.A. Crisp (1984)
Rates of magma emplacement and volcanic output. Journal of Volcanology and Geothermal Research, 20, 177-211.

A. Davaille (1999a)
Simultaneous generation of hotspots and superswells by convection in a heterogenous planetary mantle. Nature, 402, 756-760.

A. Davaille (1999b)
Two-layer thermal convection in miscible viscous fluids. Journal of Fluid Mechanics, 379, 223-253.

A. Davaille, F. Girard and M.L. Bars (2002)
How to anchor hotspots in a convecting mantle? Earth and Planetary Science Letters, 203, 621-634.

G.F. Davies (1980)
Thermal histories of convective Earth models and constraints on radiogenic heat-production in the Earth. Journal of Geophysical Research, 85, 2517-2530.

G.F. Davies (1988)
Ocean bathymetry and mantle convection. 1. Large-scale flow and hotspots. Journal of Geophysical Research: Solid Earth and Planets, 93, 10467-10480.

G.F. Davies (1999)
Geophysically constrained mantle mass flows and the ^{40}Ar budget: A degassed lower mantle? Earth and Planetary Science Letters, 166, 149-162.

G.F. Davies and M.A. Richards (1992)
Mantle convection. Journal of Geology, 100, 151-206.

A.S. Davis, D.A. Clague, B.L. Cousens, R. Keaten and J.B. Paduan (2008)
Geochemistry of basalt from the North Gorda segment of the Gorda Ridge: Evolution toward ultraslow spreading ridge lavas due to decreasing magma supply. Geochemistry Geophysics Geosystems, 9, doi:10.1029/2007GC001775.

R. de Argollo and J.G. Schilling (1978)
Ge-Si and Ga-Al fractionation in Hawaiian volcanic rocks. Geochimica Et Cosmochimica Acta, 42, 623-630.

D.J. DePaolo and G.J. Wasserburg (1976)
Inferences about magma sources and mantle structure from variations of $^{143}Nd/^{144}Nd$. Geophysical Research Letters, 3, 743-746.

B. Deruelle, G. Dreibus and A. Jambon (1992)
Iodine abundances in oceanic basalts: Implications for Earth dynamics. Earth and Planetary Science Letters, 108, 217-227.

V. Detalle, M. Sabsabi, L. St-Onge, A. Hamel and R. He´on (2003)
Influence of Er:YAG and Nd:YAG wavelengths on laser-induced breakdown spectroscopy measurements under air or helium atmosphere. Applied Optics, 42, 5971-5977.

K.E. Donnelly, S.L. Goldstein, C.H. Langmuir and M. Spiegelman (2004)
Origin of enriched ocean ridge basalts and implications for mantle dynamics. Earth and Planetary Science Letters, 226, 347-366.

B. Dupré and C.J. Allègre (1983)
Pb-Sr isotope variation in Indian Ocean basalts and mixing phenomena. Nature, 303, 142-146.

S.F. Durrant (1999)
Laser ablation inductively coupled plasma mass spectrometry: Achievements, problems, prospects. Journal of Analytical Atomic Spectrometry, 14, 1385-1403.

S.M. Eggins, L.P.J. Kinsley and J.M.G. Shelley (1998b)
Deposition and element fractionation processes during atmospheric pressure laser sampling for analysis by ICP-MS. Applied Surface Science, 127, 278-286.

S.M. Eggins, R.L. Rudnick and W.F. McDonough (1998a)
The composition of peridotites and their minerals: A laser-ablation ICP-MS study. Earth and Planetary Science Letters, 154, 53-71.

S.M. Eggins and J.M.G. Shelley (2002)
Compositional heterogeneity in NIST SRM 610-617 glasses. Geostandards Newsletter: The Journal of Geostandards and Geoanalysis, 26, 269-286.

K. Ehlers, T.L. Grove, T.W. Sisson, S.I. Recca and D.A. Zervas (1992)
The effect of oxygen fugacity on the partitioning of nickel and cobalt between olivine, silicate melt, and metal. Geochimica Et Cosmochimica Acta, 56, 3733-3743.

J.M. Eiler, K.A. Farley and E.M. Stolper (1998)
Correlated helium and lead isotope variations in Hawaiian lavas. Geochimica Et Cosmochimica Acta, 62, 1977-1984.

J.M. Eiler, J.W. Valley and E.M. Stolper (1996)
Oxygen isotope ratios in olivine from the Hawaii Scientific Drilling Project. Journal of Geophysical Research: Solid Earth, 101, 11807-11813.

J. Eisele, W. Abouchami, S.J.G. Galer and A.W. Hofmann (2003)
The 320 kyr Pb isotope evolution of Mauna Kea lavas recorded in the HSDP-2 drill core. Geochemistry Geophysics Geosystems, 4, doi:10.1029/2002GC000339.

T. Elliott (2003)
Tracers of the Slab, In: Inside the Subduction Factory, Geophysical Monograph Series (ed. J.M. Eiler), Washington, DC, American Geophysical Union, 547-568.

A.E.J. Engel, C.G. Engel and R.G. Havens (1965)
Chemical characteristics of oceanic basalts and upper mantle. Geological Society of America Bulletin, 76, 719-734.

R. Fabbro, E. Fabre, F. Amiranoff, C. Garban-Labaune, J. Virmont and M. Weinfeld (1982)
Laser-wavelength dependence of mass-ablation rate and heat-flux inhibition in laser-produced plasmas. Physics Review A, 26, 2289–2292

A. Fernandez, X.L. Mao, W.T. Chan, M.A. Shannon and R.E. Russo (1995)
Correlation of spectral emission intensity in the inductively coupled plasma and laser-induced plasma during laser ablation of solid samples. Analytical Chemistry, 67, 2444-2450.

D. Figg and M.S. Kahr (1997)
Elemental fractionation of glass using laser ablation inductively-coupled plasma mass spectrometry. Applied Spectroscopy, 51, 1185-1192.

D.J. Figg, J.B. Cross and C. Brink (1998)
More investigations into elemental fractionation resulting from laser ablation inductively-coupled plasma mass spectrometry on glass samples. Applied Surface Science, 127, 287-291.

F.A. Frey, M.O. Garcia and M.F. Roden (1994)
Geochemical characteristics of Koolau volcano - Implications of intershield geochemical differences among Hawaiian volcanos. Geochimica Et Cosmochimica Acta, 58, 1441-1462.

F.A. Frey, S. Huang, J. Blichert-Toft, M. Regelous and M. Boyet (2005)
Origin of depleted components in basalt related to the Hawaiian hot spot: Evidence from isotopic and incompatible element ratios. Geochemistry Geophysics Geosystems, 6, doi:10.1029/2004GC000757.

F.A. Frey and J.M. Rhodes (1993)
Intershield geochemical differences among Hawaiian volcanos: Implications for source compositions, melting process and magma ascent paths. Philosophical Transactions of the Royal Society of London Series A: Mathematical, Physical and Engineering Sciences, 342, 121-136.

B.J. Fryer, S.E. Jackson and H.P. Longerich (1995)
The design, operation and role of the laser-ablation microprobe coupled with an inductively-coupled plasma mass spectrometer (LAM-ICP-MS) in the Earth sciences. Canadian Mineralogist, 33, 303-312.

M. Gaboardi and M. Humayun (2009)
Elemental fractionation during LA-ICP-MS analysis of silicate glasses: Implications for matrix-independent standardization. Journal of Analytical Atomic Spectrometry, 24, 1188-1197.

G.A. Gaetani and T.L. Grove (1997)
Partitioning of moderately siderophile elements among olivine, silicate melt, and sulfide melt: Constraints on core formation in the Earth and Mars. Geochimica Et Cosmochimica Acta, 61, 1829-1846.

A. Gannoun, K.W. Burton, I.J. Parkinson, O. Alard, P. Schiano and L.E. Thomas (2007)
The scale and origin of the osmium isotope variations in mid-ocean ridge basalts. Earth and Planetary Science Letters, 259, 541-556.

S. Gao, X.M. Liu, H.L. Yuan, B. Hattendorf, D. Gunther, L. Chen and S.H. Hu (2002)
Determination of forty two major and trace elements in USGS and NIST SRM glasses by laser ablation inductively-coupled plasma mass spectrometry. Geostandards Newsletter: The Journal of Geostandards and Geoanalysis, 26, 181-196.

E.J. Garnero (2000)
Heterogeneity of the lowermost mantle. Annual Review of Earth and Planetary Sciences, 28, 509-537.

S.J. Goldstein, M.T. Murrell and D.R. Janecky (1989)
Th and U isotopic systematics of basalts from the Juan De Fuca and Gorda Ridges by mass spectrometry. Earth and Planetary Science Letters, 96, 134-146.

S.J. Goldstein, M.T. Murrell, D.R. Janecky, J.R. Delaney and D.A. Clague (1992)
Geochronology and petrogenesis of MORB from the Juan De Fuca and Gorda Ridges by ^{238}U-^{230}Th disequilibrium. Earth and Planetary Science Letters, 109, 255-272.

S.J. Goldstein, M.T. Murrell and R.W. Williams (1993)
^{231}Pa and ^{230}Th chronology of mid-ocean ridge basalts. Earth and Planetary Science Letters, 115, 151-159.

D.W. Graham, P.R. Castillo, J.E. Lupton and R. Batiza (1996)
Correlated He and Sr isotope ratios in south Atlantic near-ridge seamounts and implications for mantle dynamics. Earth and Planetary Science Letters, 144, 491-503.

D.W. Graham, A. Zindler, M.D. Kurz, W.J. Jenkins, R. Batiza and H. Staudigel (1988)
He, Pb, Sr and Nd isotope constraints on magma genesis and mantle heterogeneity beneath young Pacific seamounts. Contributions to Mineralogy and Petrology, 99, 446-463.

S. Grand, R.D.v.d. Hilst and S. Widiyantoro (1997)
Global seismic tomography: A snapshot of convection in the Earth. GSA Today, 7, 1-7.

S.P. Grand (1994)
Mantle shear structure beneath the Americas and surrounding oceans. Journal of Geophysical Research: Solid Earth, 99, 11591-11621.

R.W. Griffiths and I.H. Campbell (1990)
Stirring and structure in mantle starting plumes. Earth and Planetary Science Letters, 99, 66-78.

T.L. Grove and S.W. Parman (2004)
Thermal evolution of the Earth as recorded by komatiites. Earth and Planetary Science Letters, 219, 173-187.

M. Guillong and D. Gunther (2002)
Effect of particle size distribution on ICP-induced elemental fractionation in laser ablation inductively-coupled plasma mass spectrometry. Journal of Analytical Atomic Spectrometry, 17, 831-837.

M. Guillong, I. Horn and D. Gunther (2002)
Capabilities of a homogenized 266 nm Nd:YAG laser ablation system for LA-ICP-MS. Journal of Analytical Atomic Spectrometry, 17, 8-14.

M. Guillong, I. Horn and D. Gunther (2003)
A comparison of 266 nm, 213 nm and 193 nm produced from a single solid state Nd:YAG laser for laser ablation ICP-MS. Journal of Analytical Atomic Spectrometry, 18, 1224-1230.

D. Günther and C.A. Heinrich (1999a)
Enhanced sensitivity in laser ablation ICP mass spectrometry using helium-argon mixtures as aerosol carrier (Plenary Lecture). Journal of Analytical Atomic Spectrometry, 14, 1363-1368.

D. Günther and C.A. Heinrich (1999b)
Comparison of the ablation behaviour of 266 nm Nd:YAG and 193 nm ArF excimer lasers for LA-ICP-MS analysis (Plenary Lecture). Journal of Analytical Atomic Spectrometry, 14, 1369-1374.

L.S. Hall, J.J. Mahoney, J.M. Sinton and R.A. Duncan (2006)
Spatial and temporal distribution of a C-like asthenospheric component in the Rano Rahi Seamount Field, East Pacific Rise, 15°-19°S. Geochemistry Geophysics Geosystems, 7, doi:10.1029/2005GC000994.

S.R. Hart (1976)
Chemical variance in deep ocean basalts. In: T.L. Vallier (Ed.), Initial Reports of the Deep Sea Drilling Project Vol. XXXIV, National Science Foundation, 301–335.

S.R. Hart (1984)
A large-scale isotope anomaly in the Southern Hemisphere mantle. Nature, 309, 753-757.

S.R. Hart (1993)
Equilibration during mantle melting: A fractal tree model. Proceedings of the National Academy of Sciences of the United States of America, 90, 11914-11918.

S.R. Hart and K.E. Davis (1978)
Nickel partitioning between olivine and silicate melt. Earth and Planetary Science Letters, 40, 203-219.

E.H. Hauri (1996)
Major element variability in the Hawaiian mantle plume. Nature, 382, 415-419.

C.A. Heinrich, D. Gunther, A. Audetat, T. Ulrich and R. Frischknecht (1999)
Metal fractionation between magmatic brine and vapor, determined by microanalysis of fluid inclusions. Geology, 27, 755-758.

C.A. Heinrich, T. Pettke, W.E. Halter, M. Aigner-Torres, A. Audetat, D. Gunther, B. Hattendorf, D. Bleiner, M. Guillong and I. Horn (2003)
Quantitative multi-element analysis of minerals, fluid and melt inclusions by laser ablation inductively-coupled plasma mass spectrometry. Geochimica Et Cosmochimica Acta, 67, 3473-3497.

J. Hertogen, M.J. Janssens and H. Palme (1980)
Trace elements in ocean ridge basalt glasses: Implications for fractionations during mantle evolution and petrogenesis. Geochimica Et Cosmochimica Acta, 44, 2125-2143.

T. Hirata and R.W. Nesbitt (1995)
U-Pb isotope geochronology of zircon: Evaluation of the laser probe inductively-coupled plasma mass spectrometry technique. Geochimica Et Cosmochimica Acta, 59, 2491-2500.

M.M. Hirschmann and M.S. Ghiorso (1994)
Activities of nickel, cobalt, and manganese silicates in magmatic liquids and applications to olivine liquid and to silicate metal partitioning. Geochimica Et Cosmochimica Acta, 58, 4109-4126.

D.C. Hoaglin, F. Mosteller and J.W. Tukey (1983)
Understanding Robust and Exploratory Data Analysis. John-Wiley and Sons, Inc. (New York, NY), 447 pp.

A.W. Hofmann (1988)
Chemical differentiation of the Earth: The relationship between mantle, continental crust and oceanic crust. Earth and Planetary Science Letters, 90, 297-314.

A.W. Hofmann (1997)
Mantle geochemistry: The message from oceanic volcanism. Nature, 385, 219-229.

A.W. Hofmann (2003)
Sampling mantle heterogeneity through oceanic basalts: Isotopes and trace elements. In: R.W. Carlson (Ed.), The Mantle and Core, Treatise on Geochemistry Vol. 2 (eds. H.D. Holland and K.K Turekian), Oxford, Elsevier-Pergamon, 61-101.

A.W. Hofmann and S.R. Hart (1978)
Assessment of local and regional isotopic equilibrium in mantle. Earth and Planetary Science Letters, 38, 44-62.

A.W. Hofmann, K.P. Jochum, M. Seufert and W.M. White (1986)
Nb and Pb in oceanic basalts: New constraints on mantle evolution. Earth and Planetary Science Letters, 79, 33-45.

A.W. Hofmann and W.M. White (1982)
Mantle plumes from ancient oceanic crust. Earth and Planetary Science Letters, 57, 421-436.

A.W. Hofmann and W.M. White (1983)
Ba, Rb and Cs in the Earth's mantle. Zeitschrift Fur Naturforschung Section A: A Journal of Physical Sciences, 38, 256-266.

M. Honda, I. Mcdougall, D.B. Patterson, A. Doulgeris and D.A. Clague (1991)
Possible solar noble-gas component in Hawaiian basalts. Nature, 349, 149-151.

I. Horn, D. Gunther and M. Guillong (2003)
Evaluation and design of a solid-state 193 nm OPO Nd:YAG laser ablation system. Spectrochimica Acta Part B: Atomic Spectroscopy, 58, 1837-1846.

I. Horn, R.L. Rudnick and W.F. McDonough (2000)
Precise elemental and isotope ratio determination by simultaneous solution nebulization and laser ablation ICP-MS: Application to U-Pb geochronology. Chemical Geology, 164, 281-301.

Z.C. Hu, S. Gao, Y.S. Liu, H.H. Chen and S.H. Hu (2008a)
Accurate determination of rare earth elements in USGS, NIST SRM, and MPI-DING glasses by excimer LA-ICP-MS at high spatial resolution. Spectroscopy Letters, 41, 228-236.

Z.C. Hu, S. Gao, Y.S. Liu, J. Xu, S.H. Hu and H.H. Chen (2008b)
Niobium and tantalum concentrations in NIST SRM 610 revisited. Geostandards and Geoanalytical Research, 32, 347-360.

S.C. Huang, F.A. Frey, J. Blichert-Toft, R.V. Fodor, G.R. Bauer and G.P. Xu (2005)
Enriched components in the Hawaiian plume: Evidence from Kahoolawe Volcano, Hawaii. Geochemistry Geophysics Geosystems, 6, doi:10.1029/2005GC001012.

S.C. Huang, M. Humayun and F.A. Frey (2007)
Iron/manganese ratio and manganese content in shield lavas from Ko'olau Volcano, Hawai'i. Geochimica Et Cosmochimica Acta, 71, 4557-4569.

M. Humayun, L.P. Qin and M.D. Norman (2004)
Geochemical evidence for excess iron in the mantle beneath Hawaii. Science, 306, 91-94.

E. Ito, W.M. White and C. Gopel (1987)
The O, Sr, Nd and Pb isotope geochemistry of MORB. Chemical Geology, 62, 157-176.

H. Iwamori (1993)
A model for disequilibrium mantle melting incorporating melt transport by porous and channel flows. Nature, 366, 734-737.

S. Jackson (2001)
The application of Nd:YAG lasers in LA-ICP-MS. In: P. Sylvester (Ed.), Laser ablation ICP-MS in the Earth sciences, St. John's, Newfoundland, Mineralogical Society of Canada, 243.

S.B. Jacobsen (2005)
The Hf-W isotopic system and the origin of the earth and moon. Annual Review of Earth and Planetary Sciences, 33, 531-570.

S.B. Jacobsen and Q.Z. Yin (1998)
W isotope variations and the time of formation of asteroidal cores and the Earth's core, Lunar and Planetary Science, LPI, Houston, 1852-1853.

E. Jagoutz, H. Palme, H. Baddenhausen, K. Blum, M. Cendales, G. Dreibus, B. Spettel, V. Lorenz and H. Wanke (1979)
The abundances of major, minor and trace elements in the earth's mantle as derived from primitive ultramafic nodules, 10th Proceedings of Lunar and Planetary Sciences, 2031-2050.

A. Jambon, B. Deruelle, G. Dreibus and F. Pineau (1995)
Chlorine and bromine abundance in MORB: The contrasting behaviour of the Mid-Atlantic Ridge and East Pacific Rise and implications for chlorine geodynamic cycle. Chemical Geology, 126, 101-117.

D. Jana and D. Walker (1997)
The impact of carbon on element distribution during core formation. Geochimica Et Cosmochimica Acta, 61, 2759-2763.

D. Jana and D. Walker (1997)
The influence of silicate melt composition on distribution of siderophile elements among metal and silicate liquids. Earth and Planetary Science Letters, 150, 463-472.

P.E. Janney, A.P. Le Roex and R.W. Carlson (2005)
Hafnium isotope and trace element constraints on the nature of mantle heterogeneity beneath the central Southwest Indian Ridge (13°E to 47°E). Journal of Petrology, 46, 2427-2464.

C. Jaupart, S. Labrosse and J.-C. Mareschal (2007)
Temperatures, heat and energy in the mantle of the Earth. In: G. Schubert (Ed.), Treatise of Geophysics, Elsevier.

M. Javoy and F. Pineau (1991)
The volatiles record of a "popping" rock from the Mid-Atlantic Ridge at 14°N: Chemical and isotopic composition of gas trapped in the vesicles. Earth and Planetary Science Letters, 107, 598-611.

T.E. Jeffries, S.E. Jackson and H.P. Longerich (1998)
Application of a frequency quintupled Nd:YAG source (213 nm) for laser ablation inductively-coupled plasma mass spectrometric analysis of minerals. Journal of Analytical Atomic Spectrometry, 13, 935–940.

T.E. Jeffries, W.T. Perkins and N.J.G. Pearce (1995a)
Measurements of trace elements in basalts and their phenocrysts by laser probe microanalysis inductively-coupled plasma mass spectrometry (LPMA-ICP-MS). Chemical Geology, 121, 131-144.

T.E. Jeffries, W.T. Perkins and N.J.G. Pearce (1995b)
Comparisons of infrared and ultraviolet laser probe microanalysis inductively-coupled plasma mass spectrometry in mineral analysis. Analyst, 120, 1365-1371.

A.M. Jellinek and M. Manga (2002)
The influence of a chemical boundary layer on the fixity, spacing and lifetime of mantle plumes. Nature, 418, 760-763.

A.M. Jellinek and M. Manga (2004)
Links between long-lived hot spots, mantle plumes, D ", and plate tectonics. Reviews of Geophysics, 42, -.

S.H. Jeong, O.V. Borisov, J.H. Yoo, X.L. Mao and R.E. Russo (1999)
Effects of particle size distribution on inductively-coupled plasma mass spectrometry signal intensity during laser ablation of glass samples. Analytical Chemistry, 71, 5123-5130.

K.P. Jochum, D.B. Dingwell, A. Rocholl, B. Stoll, A.W. Hofmann, S. Becker, A. Besmehn, D. Bessette, H.J. Dietze, P. Dulski, J. Erzinger, E. Hellebrand, P. Hoppe, I. Horn, K. Janssens, G.A. Jenner, M. Klein, W.F. McDonough, M. Maetz, K. Mezger, C. Munker, I.K. Nikogosian, C. Pickhardt, I. Raczek, D. Rhede, H.M. Seufert, S.G. Simakin, A.V. Sobolev, B. Spettel, S. Straub, L. Vincze, A. Wallianos, G. Weckwerth, S. Weyer, D. Wolf and M. Zimmer (2000)
The preparation and preliminary characterisation of eight geological MPI-DING reference glasses for *in situ* microanalysis. Geostandards Newsletter: The Journal of Geostandards and Geoanalysis, 24, 87-133.

K.P. Jochum, A.W. Hofmann, E. Ito, H.M. Seufert and W.M. White (1983)
K, U and Th in mid-ocean ridge basalt glasses and heat-production, K/U and K/Rb in the mantle. Nature, 306, 431-436.

K.P. Jochum, A.W. Hofmann and H.M. Seufert (1993)
Tin in mantle-derived rocks: Constraints on Earth evolution. Geochimica Et Cosmochimica Acta, 57, 3585-3595.

K.P. Jochum, W.F. McDonough, H. Palme and B. Spettel (1989)
Compositional constraints on the continental lithospheric mantle from trace elements in spinel peridotite xenoliths. Nature, 340, 548-550.

K.P. Jochum, J. Pfander, J.D. Woodhead, M. Willbold, B. Stoll, K. Herwig, M. Amini, W. Abouchami and A.W. Hofmann (2005b)
MPI-DING glasses: New geological reference materials for *in situ* Pb isotope analysis. Geochemistry Geophysics Geosystems, 6, doi:10.1029/2005GC000995.

K.P. Jochum, B. Stoll, K. Herwig and M. Willbold (2007)
Validation of LA-ICP-MS trace element analysis of geological glasses using a new solid-state 193 nm Nd:YAG laser and matrix-matched calibration. Journal of Analytical Atomic Spectrometry, 22, 112-121.

K.P. Jochum, B. Stoll, K. Herwig, M. Willbold, A.W. Hofmann, M. Amini, S. Aarburg, W. Abouchami, E. Hellebrand, B. Mocek, I. Raczek, A. Stracke, O. Alard, C. Bouman, S. Becker, M. Ducking, H. Bratz, R. Klemd, D. de Bruin, D. Canil, D. Cornell, C.J. de Hoog, C. Dalpe, L. Danyushevsky, A. Eisenhauer, Y.J. Gao, J.E. Snow, N. Goschopf, D. Gunther, C. Latkoczy, M. Guillong, E.H. Hauri, H.E. Hofer, Y. Lahaye, K. Horz, D.E. Jacob, S.A. Kassemann, A.J.R. Kent, T. Ludwig, T. Zack, P.R.D. Mason, A. Meixner, M. Rosner, K.J. Misawa, B.P. Nash, J. Pfander, W.R. Premo, W.D.D. Sun, M. Tiepolo, R. Vannucci, T. Vennemann, D. Wayne and J.D. Woodhead (2006)
MPI-DING reference glasses for *in situ* microanalysis: New reference values for element concentrations and isotope ratios. Geochemistry Geophysics Geosystems, 7, doi:10.1029/2005GC001060.

K.P. Jochum, M. Willbold, I. Raczek, B. Stoll and K. Herwig (2005a)
Chemical characterisation of the USGS reference glasses GSA-1G, GSC-1G, GSD-1G, GSE-1G, BCR-2G, BHVO-2G and BIR-1G using EPMA, ID-TIMS, ID-ICP-MS and LA-ICP-MS. Geostandards and Geoanalytical Research, 29, 285-302.

K.T.M. Johnson, H.J.B. Dick and N. Shimizu (1990)
Melting in the oceanic upper mantle: An ion microprobe study of diopsides in abyssal peridotites. Journal of Geophysical Research: Solid Earth and Planets, 95, 2661-2678.

J.S. Kane (1998)
A history of the development and certification of NIST glass SRMs 610-617. Geostandards Newsletter: The Journal of Geostandards and Geoanalysis, 22, 7-13.

P.B. Kelemen, H.J. Dick and J.E. Quick (1992)
Formation of harzburgite by pervasive melt/rock reaction in the upper mantle. Nature, 358, 635-641.

P.B. Kelemen, G. Hirth, N. Shimizu, M. Spiegelman and H.J.B. Dick (1997)
A review of melt migration processes in the adiabatically upwelling mantle beneath oceanic spreading ridges. Philosophical Transactions of the Royal Society A: Mathematical, Physical and Engineering Sciences, 355, 283-318.

P.L. Kelley (1965)
Self-Focusing of optical beams. Physics Review Letters, 15, 1005–1008.

L.H. Kellogg, B.H. Hager and R.D. van der Hilst (1999)
Compositional stratification in the deep mantle. Science, 283, 1881-1884.

A.J.R. Kent, B. Jacobsen, D.W. Peate, T.E. Waight and J.A. Baker (2004)
Isotope dilution MC-ICP-MS rare earth element analysis of geochemical reference materials NIST SRM 610, NIST SRM 612, NIST SRM 614, BHVO-2G, BHVO-2, BCR-2G, JB-2, WS-E, W-2, AGV-1 and AGV-2. Geostandards and Geoanalytical Research, 28, 417-429.

R.J. Kinzler and T.L. Grove (1992)
Primary magmas of mid-ocean ridge basalts: Applications. Journal of Geophysical Research: Solid Earth, 97, 6907-6926.

R.J. Kinzler, T.L. Grove and S.I. Recca (1990)
An experimental study on the effect of temperature and melt composition on the partitioning of nickel between olivine and silicate melt. Geochimica Et Cosmochimica Acta, 54, 1255-1265.

T. Kleine, K. Mezger, C. Munker, H. Palme and A. Bischoff (2004b)
^{182}Hf-^{182}W isotope systematics of chondrites, eucrites, and martian meteorites: Chronology of core formation and early mantle differentiation in Vesta and Mars. Geochimica Et Cosmochimica Acta, 68, 2935-2946.

T. Kleine, K. Mezger, H. Palme and C. Munker (2004a)
The W isotope evolution of the bulk silicate Earth: Constraints on the timing and mechanisms of core formation and accretion. Earth and Planetary Science Letters, 228, 109-123.

T. Kleine, K. Mezger, H. Palme, E. Scherer and C. Munker (2005a)
Early core formation in asteroids and late accretion of chondrite parent bodies: Evidence from ^{182}Hf-^{182}W in CAIs, metal-rich chondrites, and iron meteorites. Geochimica Et Cosmochimica Acta, 69, 5805-5818.

T. Kleine, C. Munker, K. Mezger and H. Palme (2002)
Rapid accretion and early core formation on asteroids and the terrestrial planets from Hf-W chronometry. Nature, 418, 952-955.

T. Kleine, H. Palme, M. Mezger and A.N. Halliday (2005b)
Hf-W chronometry of lunar metals and the age and early differentiation of the Moon. Science, 310, 1671-1674.

J. Korenaga (2008)
Urey ratio and the structure and evolution of Earth's mantle. Reviews of Geophysics, 46.

M.D. Kurz, W.J. Jenkins, J.G. Schilling and S.R. Hart (1982)
Helium isotopic variations in the mantle beneath the Central North Atlantic Ocean. Earth and Planetary Science Letters, 58, 1-14.

C.H. Langmuir, J.F. Bender and R. Batiza (1986)
Petrological and tectonic segmentation of the East Pacific Rise, 5° 30'-14° 30'N. Nature, 322, 422-429.

C.H. Langmuir, J.F. Bender, A.E. Bence, G.N. Hanson and S.R. Taylor (1977)
Petrogenesis of basalts from the FAMOUS Area: Mid-Atlantic Ridge. Earth and Planetary Science Letters, 36, 133-156.

C.H. Langmuir and G.N. Hanson (1980)
An evaluation of major element heterogeneity in the mantle sources of basalts. Philosophical Transactions of the Royal Society of London Series A: Mathematical, Physical and Engineering Sciences, 297, 383-407.

J.C. Lassiter (2004)
Role of recycled oceanic crust in the potassium and argon budget of the Earth: Toward a resolution of the "missing argon" problem. Geochemistry Geophysics Geosystems, 5, doi:10.1029/2004GC000711.

J.C. Lassiter and E.H. Hauri (1998)
Osmium-isotope variations in Hawaiian lavas: evidence for recycled oceanic lithosphere in the Hawaiian plume. Earth and Planetary Science Letters, 164, 483-496.

C. Latkoczy and D. Gunther (2002)
Enhanced sensitivity in inductively coupled plasma sector field mass spectrometry for direct solid analysis using laser ablation (LA-ICP-SFMS). Journal of Analytical Atomic Spectrometry, 17, 1264-1270.

J.C. Laul, E. Anders, J.W. Morgan, R.R. Keays and Ganapath.R (1972)
Chemical fractionations in meteorites V: Volatile and siderophile elements in achondrites and ccean ridge basalts. Geochimica Et Cosmochimica Acta, 36, 329-345.

T. Lay, J. Hernlund and B.A. Buffett (2008)
Core-mantle boundary heat flow. Nature Geoscience 1, 25 - 32 (2008), 1, 25-32.

T. Lay, Q. Williams and E.J. Garnero (1998)
The core-mantle boundary layer and deep Earth dynamics. Nature, 392, 461-468.

A.P. le Roex, H.J.B. Dick, A.M. Reid, F.A. Frey, A.J. Erlank and S.R. Hart (1985)
Petrology and geochemistry of basalts from the American-Antarctic Ridge, Southern Ocean: Implications for the westward influence of the Bouvet mantle plume. Contributions to Mineralogy and Petrology, 90, 367-380.

P.J. le Roux, S.B. Shirey, E.H. Hauri, M.R. Perfit and J.F. Bender (2006)
The effects of variable sources, processes and contaminants on the composition of northern EPR MORB (8-10°N and 12-14°N): Evidence from volatiles (H_2O, CO_2, S) and halogens (F, Cl). Earth and Planetary Science Letters, 251, 209-231.

C.T.A. Lee, W.P. Leeman, D. Canil and Z.X.A. Li (2005)
Similar V/Sc systematics in MORB and arc basalts: Implications for the oxygen fugacities of their mantle source regions. Journal of Petrology, 46, 2313-2336.

C. Li, E.M. Ripley and E.A. Mathez (2003)
The effect of S on the partitioning of Ni between olivine and silicate melt in MORB. Chemical Geology, 201, 295-306.

C. Li, R.D. van der Hilst, E.R. Engdahl and S. Burdick (2008)
A new global model for P wave speed variations in Earth's mantle. Geochemistry Geophysics Geosystems, 9, doi: 10.1029/2007GC001806.

F.E. Lichte, A.L. Meier and J.G. Crock (1987)
Determination of the rare-earth elements in geological materials by inductively-coupled plasma mass spectrometry. Analytical Chemistry, 59, 1150-1157.

J.J. Lichtin (1930)
Perchloric acid as oxidizing agent in the determination of chromium. Ind. Eng. Chem. Anal. Ed., 2, 126–127.

H.C. Liu, O.V. Borisov, X.L. Mao, S. Shuttleworth and R.E. Russo (2000)
Pb/U fractionation during Nd:YAG 213 nm and 266 nm laser ablation sampling with inductively-coupled plasma mass spectrometry. Applied Spectroscopy, 54, 1435-1442.

H.C. Liu, X.L. Mao, J.H. Yoo and R.E. Russo Early phase laser induced plasma diagnostics and mass removal during single-pulse laser ablation of silicon. Spectrochimica Acta Part B: Atomic Spectroscopy, 54, 1607-1624.

K. Lodders (2003)
Solar system abundances and condensation temperatures of the elements. Astrophysical Journal, 591, 1220-1247.

G. Loock, W.F. McDonough, S.L. Goldstein and A.W. Hofmann (1990)
Isotopic compositions of volcanic glasses from the Lau Basin. Marine Mining, 9, 235-245.

J.N. Ludden, R. Feng, G. Gauthier, J. Stix, L. Shi, D. Francis, N. Machado and G.P. Wu (1995)
Applications of LAM-ICP-MS analysis to minerals. Canadian Mineralogist, 33, 419-434.

C.C. Lundstrom, D.E. Sampson, M.R. Perfit, J. Gill and Q. Williams (1999)
Insights into mid-ocean ridge basalt petrogenesis: U-series disequilibria from the Siqueiros Transform, Lamont Seamounts, and East Pacific Rise. Journal of Geophysical Research: Solid Earth, 104, 13035-13048.

T. Lyubetskaya and J. Korenaga (2007)
Chemical composition of Earth's primitive mantle and its variance: 1. Method and results. Journal of Geophysical Research: Solid Earth, 112, B03212, doi:10.1029/2005JB004224.

J. Mahoney, A.P. Leroex, Z. Peng, R.L. Fisher and J.H. Natland (1992)
Southwestern limits of Indian Ocean ridge mantle and the origin of low ^{206}Pb-^{204}Pb mid-ocean ridge basalt: Isotope systematics of the central Southwest Indian Ridge (17°E-50°E). Journal of Geophysical Research: Solid Earth, 97, 19771-19790.

J.J. Mahoney, D.W. Graham, D.M. Christie, K.T.M. Johnson, L.S. Hall and D.L. Vonderhaar (2002)
Between a hotspot and a cold spot: Isotopic variation in the Southeast Indian Ridge asthenosphere, 86°E-118°E. Journal of Petrology, 43, 1155-1176.

J.J. Mahoney, J.H. Natland, W.M. White, R. Poreda, S.H. Bloomer, R.L. Fisher and A.N. Baxter (1989)
Isotopic and geochemical provinces of the western Indian Ocean spreading centers. Journal of Geophysical Research: Solid Earth and Planets, 94, 4033-4052.

A.J.G. Mank and P.R.D. Mason (1999)
A critical assessment of laser ablation ICP-MS as an analytical tool for depth analysis in silica-based glass samples. Journal of Analytical Atomic Spectrometry, 14, 1143-1153.

S.S. Mao, X. Mao, R. Greif and R.E. Russo (2000a)
Initiation of an early-stage plasma during picosecond laser ablation of solids. Applied Physics Letters, 77, 2464-2466.

S.S. Mao, X.L. Mao, R. Greif and R.E. Russo (2000b)
Dynamics of an air breakdown plasma on a solid surface during picosecond laser ablation. Applied Physics Letters, 76, 31-33.

S.S. Mao, X.L. Mao, R. Greif and R.E. Russo (2000c)
Simulation of a picosecond laser ablation plasma. Applied Physics Letters, 76, 3370-3372.

X.L. Mao, O.V. Borisov and R.E. Russo (1998a)
Enhancements in laser ablation inductively-coupled plasma atomic emission spectrometry based on laser properties and ambient environment. Spectrochimica Acta Part B: Atomic Spectroscopy, 53, 731-739.

X.L. Mao, W.T. Chan, M. Caetano, M.A. Shannon and R.E. Russo (1996)
Preferential vaporization and plasma shielding during nano-second laser ablation. Applied Surface Science, 96-98, 126-130.

X.L. Mao, A.C. Ciocan, O.V. Borisov and R.E. Russo (1998b)
Laser ablation processes investigated using inductively coupled plasma-atomic emission spectroscopy (ICP–AES). Applied Surface Science, 127–129, 262–268.

X.L.L. Mao, M.A. Shannon, A.J. Fernandez and R.E. Russo (1995)
Temperature and emission spatial profiles of laser-induced plasmas during ablation using time-integrated emission spectroscopy. Applied Spectroscopy, 49, 1054-1062.

B. Marty and L. Zimmermann (1999)
Volatiles (He, C, N, Ar) in mid-ocean ridge basalts: Assesment of shallow-level fractionation and characterization of source composition. Geochimica Et Cosmochimica Acta, 63, 3619-3633.

H. Matusiewicz, R.E. Sturgeon and S.S. Berman (1991)
Vapor-phase acid digestion of inorganic and organic matrices for trace element analysis using a microwave heated bomb. Journal of Analytical Atomic Spectrometry, 6, 283-287.

W.F. McDonough (1990)
Constraints on the composition of the continental lithospheric mantle. Earth and Planetary Science Letters, 101, 1-18.

W.F. McDonough (1991)
Partial melting of subducted oceanic crust and isolation of its residual eclogitic lithology. Philosophical Transactions of the Royal Society of London Series A: Mathematical, Physical and Engineering Sciences, 335, 407-418.

W.F. McDonough (1994)
Chemical and isotopic systematics of continental lithospheric mantle. In: H.O.A. Meyer and O. Leonardos (Eds.), Kimberlites, Related Rocks and Mantle Xenoliths, Proceedings of the 5th International Kimberlite conference Vol. 1, Brasilia, CPRM, 478-485.

W.F. McDonough (2003)
Compositional model for the Earth's core. In: R.W. Carlson (Ed.), The Mantle and Core, Treatise on Geochemistry Vol. 2 (eds. H.D. Holland and K.K Turekian), Oxford, Elsevier-Pergamon, 547-568.

W.F. McDonough and F.A. Frey (1989)
Rare earth elements in upper mantle rocks. In: B.R. Lipin and G.A. McKay (Eds.), Geochemistry and Mineralogy of Rare Earth Elements, Reviews in Mineralogy, 99-145.

W.F. McDonough and S.S. Sun (1995)
The composition of the Earth. Chemical Geology, 120, 223-253.

W.F. McDonough, S.S. Sun, A.E. Ringwood, E. Jagoutz and A.W. Hofmann (1992)
Potassium, rubidium, and cesium in the Earth and moon and the evolution of the mantle of the Earth. Geochimica Et Cosmochimica Acta, 56, 1001-1012.

D. McKenzie (1984)
The generation and compaction of partially molten rock. Journal of Petrology, 25, 713-765.

D. McKenzie (1985)
The extraction of magma from the crust and mantle. Earth and Planetary Science Letters, 74, 81-91.

D. McKenzie and M.J. Bickle (1988)
The volume and composition of melt generated by extension of the lithosphere. Journal of Petrology, 29, 625-679.

D. McKenzie and R.K. O'Nions (1991)
Partial melt distributions from inversion of rare-earth element concentrations. Journal of Petrology, 32, 1021-1091.

S.M. McLennan, W.B. Nance and S.R. Taylor (1980)
Rare earth element-thorium correlations in sedimentary rocks, and the composition of the continental crust. Geochimica Et Cosmochimica Acta, 44, 1833-1839.

W.G. Melson, T. Vallier, T.L. Wright, G. Byerly and J. Nelen (1976)
Chemical diversity of abyssal volcanic glass erupted along sea-floor spreading centers. Journal Geophysical Research Monograph, 19, 351-368.

P. Michael (1995)
Regionally distinctive sources of depleted MORB: Evidence from trace elements and H_2O. Earth and Planetary Science Letters, 131, 301-320.

E. Michiels and R. Gijbels (1984)
Cluster ion distributions and correlation with fragment valence in laser-induced mass spectra of oxides. Analytical Chemistry, 56, 1115-1121.

R. Montelli, G. Nolet, F.A. Dahlen, G. Masters, E.R. Engdahl and S.H. Hung (2004)
Finite-frequency tomography reveals a variety of plumes in the mantle. Science, 303, 338-343.

J.W. Morgan (1986)
Ultramafic xenoliths: Clues to Earth's late accretionary history. Journal of Geophysical Research: Solid Earth and Planets, 91, 2375-2387.

W.J. Morgan (1971)
Convection plumes in lower mantle. Nature, 230, 42-43.

T. Morishita, Y. Ishida and S. Arai (2005)
Simultaneous determination of multiple trace element compositions in thin (<30 um) layers of BCR-2G by 193 nm ArF excimer laser ablation-ICP-MS: Implications for matrix effect and elemental fractionation on quantitative analysis. Geochemical Journal, 39, 327-340.

M. Murakami, K. Hirose, K. Kawamura, N. Sata and Y. Ohishi (2004)
Post-perovskite phase transition in $MgSiO_3$. Science, 304, 855-858.

F. Nauret, W. Abouchami, S.J.G. Galer, A.W. Hofmann, C. Hemond, C. Chauvel and J. Dyment (2006)
Correlated trace element-Pb isotope enrichments in Indian MORB along 18-20°S, Central Indian Ridge. Earth and Planetary Science Letters, 245, 137-152.

S. Newman, R.C. Finkel and J.D. MacDougall (1983)
^{230}Th-^{238}U disequilibrium systematics in oceanic tholeiites from 21°N on the East Pacific Rise. Earth and Planetary Science Letters, 65, 17-33.

H.E. Newsom (1990)
Accretion and core formation in the Earth: Evidence from siderophile elements. In: H.E. Newsom and J.H. Jones (Eds.), Origin of Earth, Oxford Press, 273-288.

H.E. Newsom and H. Palme (1984)
The depletion of siderophile elements in the Earth's mantle: New evidence from molybdenum and tungsten. Earth and Planetary Science Letters, 69, 354-364.

H.E. Newsom, K.W.W. Sims, P.D. Noll, W.L. Jaeger, S.A. Maehr and T.B. Beserra (1996)
The depletion of tungsten in the bulk silicate Earth: Constraints on core formation. Geochimica Et Cosmochimica Acta, 60, 1155-1169.

H.E. Newsom, W.M. White, K.P. Jochum and A.W. Hofmann (1986)
Siderophile and chalcophile element abundances in oceanic basalts, Pb-isotope evolution and growth of the Earth's core. Earth and Planetary Science Letters, 80, 299-313.

Y.L. Niu (2004)
Bulk-rock major and trace element compositions of abyssal peridotites: Implications for mantle melting, melt extraction and post-melting processes beneath mid-ocean ridges. Journal of Petrology, 45, 2423-2458.

Y.L. Niu and R. Batiza (1997)
Trace element evidence from seamounts for recycled oceanic crust in the eastern Pacific mantle. Earth and Planetary Science Letters, 148, 471-483.

Y.L. Niu, K.D. Collerson, R. Batiza, J.I. Wendt and M. Regelous (1999)
Origin of enriched-type mid-ocean ridge basalt at ridges far from mantle plumes: The East Pacific Rise at 11° 20'N. Journal of Geophysical Research: Solid Earth, 104, 7067-7087.

Y.L. Niu and R. Hekinian (1997)
Spreading-rate dependence of the extent of mantle melting beneath ocean ridges. Nature, 385, 326-329.

Y.L. Niu and M.J. O'Hara (2003)
Origin of ocean island basalts: A new perspective from petrology, geochemistry, and mineral physics considerations. Journal of Geophysical Research: Solid Earth, 108, doi:10.1029/2002JB002048.

Y.L. Niu and M.J. O'Hara (2009)
MORB mantle hosts the missing Eu (Sr, Nb, Ta and Ti) in the continental crust: New perspectives on crustal growth, crust-mantle differentiation and chemical structure of oceanic upper mantle. Lithos, 112, 1-17.

Y.L. Niu, D.G. Waggoner, J.M. Sinton and J.J. Mahoney (1996)
Mantle source heterogeneity and melting processes beneath seafloor spreading centers: The East Pacific Rise, 18-19°S. Journal of Geophysical Research: Solid Earth, 101, 27711-27733.

P.H. Nixon, N.W. Rogers, I.L. Gibson and A. Grey (1981)
Depleted and fertile mantle xenoliths from southern African kimberlites. Annual Review of Earth and Planetary Sciences, 9, 285-309.

G. Nolet, S.I. Karato and R. Montelli (2006)
Plume fluxes from seismic tomography. Earth and Planetary Science Letters, 248, 685-699.

P.D. Noll, H.E. Newsom, W.P. Leeman and J.G. Ryan (1996)
The role of hydrothermal fluids in the production of subduction zone magmas: Evidence from siderophile and chalcophile trace elements and boron. Geochimica Et Cosmochimica Acta, 60, 587-611.

N.S. Nonose, N. Matsuda, N. Fudagawa and M. Kubota (1994)
Some characteristics of polyatomic ion spectra in inductively-coupled plasma-mass spectrometry. Spectrochimica Acta Part B: Atomic Spectroscopy, 49, 955-974.

M.D. Norman and M.O. Garcia (1999)
Primitive magmas and source characteristics of the Hawaiian plume: Petrology and geochemistry of shield picrites. Earth and Planetary Science Letters, 168, 27-44.

M.D. Norman, W.L. Griffin, N.J. Pearson, M.O. Garcia and S.Y. O'Reilly (1998)
Quantitative analysis of trace element abundances in glasses and minerals: A comparison of laser ablation inductively-coupled plasma mass spectrometry, solution inductively-coupled plasma mass spectrometry, proton microprobe and electron microprobe data. Journal of Analytical Atomic Spectrometry, 13, 477-482.

M.D. Norman, N.J. Pearson, A. Sharma and W.L. Griffin (1996)
Quantitative analysis of trace elements in geological materials by laser ablation ICP-MS: Instrumental operating conditions and calibration values of NIST glasses. Geostandards Newsletter, 20, 247-261.

H.S.C. O'Neill and S.M. Eggins (2002)
The effect of melt composition on trace element partitioning: An experimental investigation of the activity coefficients of FeO, NiO, CoO, MoO_2 and MoO_3 in silicate melts. Chemical Geology, 186, 151-181.

R.K. O'Nions (1987)
Relationships between chemical and convective layering in the Earth. Journal of the Geological Society, 144, 259-274.

R.K. O'Nions, N.M. Evensen and P.J. Hamilton (1979)
Geochemical modeling of mantle differentiation and crustal growth. Journal of Geophysical Research, 84, 6091-6101.

R.K. O'Nions and E.R. Oxburgh (1983)
Heat and helium in the Earth. Nature, 306, 429-431.

A. Pack, S.S. Russell, J.M.G. Shelley and M. van Zuilen (2007)
Geo- and cosmochemistry of the twin elements yttrium and holmium. Geochimica Et Cosmochimica Acta, 71, 4592-4608.

H. Palme and A. Jones (2003)
Solar system abundances of the elements. In: A.M. Davis (Ed.), Meteorites, Comets, and Planets, Treatise on Geochemistry Vol. 1 (eds. H.D. Holland and K.K Turekian), Oxford, Elsevier-Pergamon, 41-61.

H. Palme and H.S.C. O'Neill (2003)
Cosmochemical estimates of mantle composition. In: R.W. Carlson (Ed.), The Mantle and Core, Treatise on Geochemistry Vol. 2 (eds. H.D. Holland and K.K Turekian), Oxford, Elsevier-Pergamon, 1-38.

H. Palme and W. Rammensee (1981)
The significance of W in planetary differentiation processes: Evidence from new data on eucrites, 12th Lunar and Planetary Sciences Conference, 949-964.

N.J.G. Pearce, W.T. Perkins, J.A. Westgate, M.P. Gorton, S.E. Jackson, C.R. Neal and S.P. Chenery (1997)
A compilation of new and published major and trace element data for NIST SRM 610 and NIST SRM 612 glass reference materials. Geostandards Newsletter: The Journal of Geostandards and Geoanalysis, 21, 115-144.

W.T. Perkins, N.J.G. Pearce and J.A. Westgate (1997)
The development of laser ablation ICP-MS and calibration strategies: Examples from the analysis of trace elements in volcanic glass shards and sulfide minerals. Geostandards Newsletter: The Journal of Geostandards and Geoanalysis, 21, 175-190.

G.H. Pettit and M.N. Ediger (1996)
Corneal-tissue absorption coefficients for 193- and 213-nm ultraviolet radiation. Applied Optics, 35, 3386-3391.

J.A. Pfänder, C. Munker, A. Stracke and K. Mezger (2007)
Nb/Ta and Zr/Hf in ocean island basalts: Implications for crust-mantle differentiation and the fate of niobium. Earth and Planetary Science Letters, 254, 158-172.

C.R. Phipps and R.W. Dreyfuss (1993)
Laser ablation and plasma formation. In: A. Vertes, R. Gijbels and F. Adams (Eds.), Laser microprobe analysis, New York, NY, John Wiley, 369.

S. Pilet, M.B. Baker and E.M. Stolper (2008)
Metasomatized lithosphere and the origin of alkaline lavas. Science, 320, 916-919.

S. Pilet, J. Hernandez, P. Sylvester and M. Poujol (2005)
The metasomatic alternative for ocean island basalt chemical heterogeneity. Earth and Planetary Science Letters, 236, 148-166.

T. Plank and C.H. Langmuir (1998)
The chemical composition of subducting sediment and its consequences for the crust and mantle. Chemical Geology, 145, 325-394.

R.J. Poreda and K.A. Farley (1992)
Rare-gases in Samoan xenoliths. Earth and Planetary Science Letters, 113, 129-144.

J. Prytulak and T. Elliott (2007)
TiO_2 enrichment in ocean island basalts. Earth and Planetary Science Letters, 263, 388-403.

I. Puchtel and M. Humayun (2000)
Platinum group elements in Kostomuksha komatiites and basalts: Implications for oceanic crust recycling and core-mantle interaction. Geochimica Et Cosmochimica Acta, 64, 4227-4242.

K. Putirka (2008)
Excess temperatures at ocean islands: Implications for mantle layering and convection. Geology, 36, 283-286.

I. Raczek, B. Stoll, A.W. Hofmann and K.P. Jochum (2001)
High-precision trace element data for the USGS reference materials BCR-1, BCR-2, BHVO-1, BHVO-2, AGV-1, AGV-2, DTS-1, DTS-2, GSP-1 and GSP-2 by ID-TIMS and MIC-SSMS. Geostandards Newsletter: The Journal of Geostandards and Geoanalysis, 25, 77-86.

J.F. Ready (1965)
Effects due to absorption of laser radiation. Journal of Applied Physics, 36, 462-468.

J.F. Ready (1971)
Effects of High Power Laser Radiation. Academic Press (New York, NY), 433 pp.

Z.Y. Ren, S. Ingle, E. Takahashi, N. Hirano and T. Hirata (2005)
The chemical structure of the Hawaiian mantle plume. Nature, 436, 837-840.

M.A. Richards, R.A. Duncan and V.E. Courtillot (1989)
Flood basalts and hot-spot tracks: Plume heads and tails. Science, 246, 103-107.

G.W. Rieger, M. Taschuk, Y.Y. Tsui and R. Fedosejevs (2003)
Comparative study of laser-induced plasma emission from microjoule picosecond and nanosecond KrF-laser pulses. Spectrochimica Acta Part B: Atomic Spectroscopy, 58, 497–510.

K. Righter (2003)
Metal-silicate partitioning of siderophile elements and core formation in the early Earth. Annual Review of Earth and Planetary Sciences, 31, 135-174.

K. Righter and M.J. Drake (1999)
Effect of water on metal-silicate partitioning of siderophile elements: A high pressure and temperature terrestrial magma ocean and core formation. Earth and Planetary Science Letters, 171, 383-399.

K. Righter and M.J. Drake (2000)
Metal/silicate equilibrium in the early Earth: New constraints from the volatile moderately siderophile elements Ga, Cu, P, and Sn. Geochimica Et Cosmochimica Acta, 64, 3581-3597.

K. Righter, M.J. Drake and G. Yaxley (1997)
Prediction of siderophile element metal-silicate partition coefficients to 20 GPa and 2800°C: The effects of pressure, temperature, oxygen fugacity, and silicate and metallic melt compositions. Physics of the Earth and Planetary Interiors, 100, 115-134.

K. Righter and C.K. Shearer (2003)
Magmatic fractionation of Hf and W: Constraints on the timing of core formation and differentiation in the Moon and Mars. Geochimica Et Cosmochimica Acta, 67, 2497-2507.

A. Rocholl (1998)
Major and trace element composition and homogeneity of microbeam reference material: Basalt glass USGS BCR-2G. Geostandards Newsletter: The Journal of Geostandards and Geoanalysis, 22, 33-45.

A. Rocholl and K.P. Jochum (1993)
Th, U and other trace-elements in carbonaceous chondrites: Implications for the terrestrial and solar system Th/U ratios. Earth and Planetary Science Letters, 117, 265-278.

M.F. Roden, T. Trull, S.R. Hart and F.A. Frey (1994)
New He, Nd, Pb, and Sr isotopic constraints on the constitution of the Hawaiian plume: Results from Koolau volcano, Oahu, Hawaii, USA. Geochimica Et Cosmochimica Acta, 58, 1431-1440.

E.A. Rohlfing, D.M. Cox and A. Kaldor (1984)
Production and characterization of supersonic carbon cluster beams. Journal of Chemical Physics, 81, 3322-3330.

K.H. Rubin and J.D. MacDougall (1992)
Th-Sr isotopic relationships in MORB. Earth and Planetary Science Letters, 114, 149-157.

R.L. Rudnick (1995)
Making continental crust. Nature, 378, 571-578.

R.L. Rudnick, M. Barth, I. Horn and W.F. McDonough (2000)
Rutile-bearing refractory eclogites: Missing link between continents and depleted mantle. Science, 287, 278-281.

R.L. Rudnick and S. Gao (2003)
Composition of the continental crust. In: R.L. Rudnick (Ed.), The Crust, Treatise on Geochemistry Vol. 3 (eds. H.D. Holland and K.K Turekian), Oxford, Elsevier-Pergamon, 1-64.

A. Ruf, P. Berger, F. Dausinger and H. Hugel (2001)
Analytical investigations on geometrical influences on laser drilling. Journal of Physics D: Applied Physics, 34, 2918-2925.

S.A. Russell, T. Lay and E.J. Garnero (1998)
Seismic evidence for small-scale dynamics in the lowermost mantle at the root of the Hawaiian hotspot. Nature, 396, 255-258.

R.E. Russo (1995)
Laser ablation. Applied Spectroscopy, 49, 14A-28A.

R.E. Russo, X. Mao, H. Liu, J. Gonzalez and S.S. Mao (2002)
Laser ablation in analytical chemistry: A review. Talanta, 57, 425-451.

R.E. Russo, X.L. Mao, O.V. Borisov and H.C. Liu (2000)
Influence of wavelength on fractionation in laser ablation ICP-MS. Journal of Analytical Atomic Spectrometry, 15, 1115-1120.

R.E. Russo, X.L. Mao, H.C. Liu, J.H. Yoo and S.S. Mao (1999)
Time-resolved plasma diagnostics and mass removal during single-pulse laser ablation. Applied Physics A: Materials Science & Processing, 69, S887-S894.

J.G. Ryan and C.H. Langmuir (1987)
The systematics of lithium abundances in young volcanic rocks. Geochimica Et Cosmochimica Acta, 51, 1727-1741.

J.G. Ryan and C.H. Langmuir (1988)
Beryllium systematics in young volcanic rocks: Implications for ^{10}Be. Geochimica Et Cosmochimica Acta, 52, 237-244.

J.G. Ryan and C.H. Langmuir (1993)
The systematics of boron abundances in young volcanic rocks. Geochimica Et Cosmochimica Acta, 57, 1489-1498.

A.E. Saal, E.H. Hauri, C.H. Langmuir and M.R. Perfit (2002)
Vapour undersaturation in primitive mid-ocean ridge basalt and the volatile content of Earth's upper mantle. Nature, 419, 451-455.

K. Sakata and K. Kawabata (1994)
Reduction of fundamental polyatomic ions in inductively-coupled plasma mass spectrometry. Spectrochimica Acta Part B: Atomic Spectroscopy, 49, 1027-1038.

V.J.M. Salters and A. Stracke (2004)
Composition of the depleted mantle. Geochemistry Geophysics Geosystems, 5, doi:10.1029/2003GC000597.

P. Sarda and D. Graham (1990)
Mid-ocean ridge popping rocks: Implications for degassing at ridge crests. Earth and Planetary Science Letters, 97, 268-289.

A. Scherstén, T. Elliott, C. Hawkesworth and M. Norman (2004)
Tungsten isotope evidence that mantle plumes contain no contribution from the Earth's core. Nature, 427, 234-237.

J.-G. Schilling (1973)
Iceland mantle plume: Geochemical study of Reykjanes Ridge. Nature, 242, 565-571.

J.-G. Schilling (1991)
Fluxes and excess temperatures of mantle plumes inferred from their interaction with migrating mid-ocean ridges. Nature, 352, 397-403.

J.G. Schilling, M.B. Bergeron and R. Evans (1980)
Halogens in the mantle beneath the North-Atlantic. Philosophical Transactions of the Royal Society of London Series A: Mathematical, Physical and Engineering Sciences, 297, 147-178.

J.-G. Schilling, M. Zajac, R. Evans, T. Johnston, W. White, J.D. Devine and R. Kingsley (1983)
Petrologic and geochemical variations along the Mid-Atlantic Ridge from 29°N to 73°N. American Journal of Science, 283, 510-586.

R. Schoenberg, B.S. Kamber, K.D. Collerson and O. Eugster (2002)
New W-isotope evidence for rapid terrestrial accretion and very early core formation. Geochimica Et Cosmochimica Acta, 66, 3151-3160.

G. Schubert, D. Stevenson and P. Cassen (1980)
Whole planet cooling and the radiogenic heat source contents of the Earth and moon. Journal of Geophysical Research, 85, 2531-2538.

G. Schubert, D.L. Turcotte and P. Olson (2001)
Mantle Convection in the Earth and Planets. Cambridge University Press (Cambridge, UK), 956 pp.

M.A. Shannon, X.L.L. Mao, A. Fernandez, W.T. Chan and R.E. Russo (1995)
Laser ablation mass removal versus incident power density during solid sampling for inductively-coupled plasma atomic emission spectroscopy. Analytical Chemistry, 67, 4522-4529.

Y. Shao and G. Horlick (1991)
Recognition of mass spectral interferences in inductively coupled plasma mass spectrometry. Applied Spectroscopy, 45, 143-147.

D.M. Shaw (1970)
Trace element fractionation during anatexis. Geochimica Et Cosmochimica Acta, 34, 237-243.

D.M. Shaw (2006)
Trace Elements in Magmas: A Theoretical Treament. Cambridge University Press (Cambridge, UK), 243 pp.

K.W. Sims, H.E. Newsom and E.S. Gladney (1990)
Chemical fractionation during formation of the Earth's core and continental crust: Clues from As, Sb, W , and Mo. In: H.E. Newsom and J.H. Jones (Eds.), Origin of Earth, Oxford Press, 291-317.

K.W.W. Sims, J. Blichert-Toft, D.J. Fornari, M.R. Perfit, S.J. Goldstein, P. Johnson, D.J. DePaolo, S.R. Hart, P.J. Murrell, P.J. Michael, G.D. Layne and L.A. Ball (2003)
Aberrant youth: Chemical and isotopic constraints on the origin of off-axis lavas from the East Pacific Rise, 9°-10°N. Geochemistry Geophysics Geosystems, 4, doi:10.1029/2002GC000443.

K.W.W. Sims and D.J. DePaolo (1997)
Inferences about mantle magma sources from incompatible element concentration ratios in oceanic basalts. Geochimica Et Cosmochimica Acta, 61, 765-784.

K.W.W. Sims, D.J. DePaolo, M.T. Murrell, W.S. Baldridge, S. Goldstein, D. Clague and M. Jull (1999)
Porosity of the melting zone and variations in the solid mantle upwelling rate beneath Hawaii: Inferences from ^{238}U-^{230}Th-^{226}Ra and ^{235}U-^{231}Pa disequilibria. Geochimica Et Cosmochimica Acta, 63, 4119-4138.

K.W.W. Sims, D.J. Depaolo, M.T. Murrell, W.S. Baldridge, S.J. Goldstein and D.A. Clague (1995)
Mechanisms of magma generation beneath Hawaii and mid-ocean ridges: Uranium/thorium and samarium/neodymium isotopic evidence. Science, 267, 508-512.

K.W.W. Sims, S.J. Goldstein, J. Blichert-Toft, M.R. Perfit, P. Kelemen, D.J. Fornari, P. Michael, M.T. Murrell, S.R. Hart, D.J. DePaolo, G. Layne, L. Ball, M. Jull and J. Bender (2002)
Chemical and isotopic constraints on the generation and transport of magma beneath the East Pacific Rise. Geochimica Et Cosmochimica Acta, 66, 3481-3504.

K.W.W. Sims, H.E. Newsom and E.S. Gladney (1990)
Chemical fractionation during formation of the Earth's core and continental crust: Clues from As, Sb, W, and Mo. In: H.E. Newsom and J.H. Jones (Eds.), Origin of the Earth, New York, NY, Oxford University Press, 291-317.

N.H. Sleep (1990)
Hotspots and mantle plumes: Some phenomenology. Journal of Geophysical Research: Solid Earth and Planets, 95, 6715-6736.

A.V. Sobolev, A.W. Hofmann, D.V. Kuzmin, G.M. Yaxley, N.T. Arndt, S.L. Chung, L.V. Danyushevsky, T. Elliott, F.A. Frey, M.O. Garcia, A.A. Gurenko, V.S. Kamenetsky, A.C. Kerr, N.A. Krivolutskaya, V.V. Matvienkov, I.K. Nikogosian, A. Rocholl, I.A. Sigurdsson, N.M. Sushchevskaya and M. Teklay (2007)
The amount of recycled crust in sources of mantle-derived melts. Science, 316, 412-417.

A.V. Sobolev, A.W. Hofmann, S.V. Sobolev and I.K. Nikogosian (2005)
An olivine-free mantle source of Hawaiian shield basalts. Nature, 434, 590-597.

A.V. Sobolev and N. Shimizu (1993)
Ultra-depleted primary melt included in an olivine from the Mid-Atlantic Ridge. Nature, 363, 151-154.

M. Spiegelman and P. Kenyon (1992)
The requirements for chemical disequilibrium during magma migration. Earth and Planetary Science Letters, 109, 611-620.

J. Stix, G. Gauthier and J.N. Ludden (1995)
A critical look at quantitative laser ablation ICP-MS analysis of natural and synthetic glasses. Canadian Mineralogist, 33, 435-444.

A. Stracke and B. Bourdon (2009)
The importance of melt extraction for tracing mantle heterogeneity. Geochimica Et Cosmochimica Acta, 73, 218-238.

A. Stracke, A. Zindler, V.J.M. Salters, D. McKenzie, J. Blichert-Toft, F. Albarède and K. Gronvold (2003)
Theistareykir revisited. Geochemistry Geophysics Geosystems, 4, doi:10.1029/2001GC000201.

Y.J. Su (2002)
Mid-ocean ridge basalt trace element systematics: Constraints from database management, ICP-MS analyses, global data compilation, and petrologic modeling. Ph.D. thesis, Columbia University, 457 pp.

S.S. Sun (1980)
Lead isotopic study of young volcanic rocks from mid-ocean ridges, ocean islands and island arcs. Philosophical Transactions of the Royal Society of London Series A: Mathematical, Physical and Engineering Sciences, 297, 409-445.

S.S. Sun (1982)
Chemical composition and origin of the earth's primitive mantle. Geochimica Et Cosmochimica Acta, 46, 179-192.

S.-s. Sun and G.N. Hanson (1975)
Origin of Ross Island basanitoids and limitations upon heterogeneity of mantle sources for alkali basalts and nephelinites. Contributions to Mineralogy and Petrology, 52, 77-106.

S.-s. Sun and W.F. McDonough (1989)
Chemical and isotopic systematics of oceanic basalts: Implications for mantle composition and processes. In: A.D. Saunders and M.J. Norry (Eds.), Magmatism in the Ocean Basins, Geological Society Special Publication, 313-345.

W.D. Sun, V.C. Bennett, S.M. Eggins, R.J. Arculus and M.R. Perfit (2003)
Rhenium systematics in submarine MORB and back-arc basin glasses: Laser ablation ICP-MS results. Chemical Geology, 196, 259-281.

W.D. Sun, Y.H. Hu, V.S. Kamenetsky, S.M. Eggins, M. Chen and R.J. Arculus (2008)
Constancy of Nb/U in the mantle revisited. Geochimica Et Cosmochimica Acta, 72, 3542-3549.

Y. Tatsumi, K. Oguri and G. Shimoda (1999)
The behaviour of platinum-group elements during magmatic differentiation in Hawaiian tholeiites. Geochemical Journal, 33, 237-247.

H. Taura, H. Yurimoto, K. Kurita and S. Sueno (1998)
Pressure dependence on partition coefficients for trace elements between olivine and the coexisting melts. Physics and Chemistry of Minerals, 25, 469-484.

R.N. Taylor, M.F. Thirlwall, B.J. Murton, D.R. Hilton and M.A.M. Gee (1997)
Isotopic constraints on the influence of the Icelandic plume. Earth and Planetary Science Letters, 148, E1-E8.

S.R. Taylor and S.M. McLennan (1985)
The Continental Crust: Its Composition and Evolution. Blackwell Scientific Publications (Oxford), 312 pp.

H. Theil (1950)
A rank-invariant method of linear and polynomial regression analysis. Konink. Nederl. Akad. Wetensch., 53, 386-392.

M. Thompson and J.N. Walsh (1989)
A Handbook of Inductively-Coupled Plasma Spectrometry. Blackie (Glasgow), 310 pp.

M. Thompson and S.J. Wood (1982)
Atomic absorption methods in applied geochemistry. In: J.E. Cantle (Ed.), Techniques and Instrumentation in Analytical Chemistry: Atomic Absorption Spectrometry, Amsterdam, Elsevier Scientific Publishing Company Inc., 448.

I. Tolstikhin and A.W. Hofmann (2005)
Early crust on top of the Earth's core. Physics of the Earth and Planetary Interiors, 148, 109-130.

I.N. Tolstikhin, J.D. Kramers and A.W. Hofmann (2006)
A chemical Earth model with whole mantle convection: The importance of a core-mantle boundary layer (D") and its early formation. Chemical Geology, 226, 79-99.

J. Trampert, F. Deschamps, J. Resovsky and D. Yuen (2004)
Probabilistic tomography maps chemical heterogeneities throughout the lower mantle. Science, 306, 853-856.

D.L. Turcotte, D. Paul and W.M. White (2001)
Thorium-uranium systematics require layered mantle convection. Journal of Geophysical Research: Solid Earth, 106, 4265-4276.

K.K. Turekian (1959)
The terrestrial economy of helium and argon. Geochimica Et Cosmochimica Acta, 17, 37-43.

R.D. van der Hilst and H. Kárason (1999)
Compositional heterogeneity in the bottom 1000 kilometers of Earth's mantle: Toward a hybrid convection model. Science, 283, 1885-1888.

R.D. van der Hilst, S. Widiyantoro and E.R. Engdahl (1997)
Evidence for deep mantle circulation from global tomography. Nature, 386, 578-584.

P.E. van Keken, E.H. Hauri and C.J. Ballentine (2002)
Mantle mixing: The generation, preservation, and destruction of chemical heterogeneity. Annual Review of Earth and Planetary Sciences, 30, 493-525.

C. Vockenhuber, F. Oberli, M. Bichler, I. Ahmad, G. Quitte, M. Meier, A.N. Halliday, D.C. Lee, W. Kutschera, P. Steier, R.J. Gehrke and R.G. Helmer (2004)
New half-life measurement of ^{182}Hf: Improved chronometer for the early solar system. Physical Review Letters, 93, 1-4.

A.M. Volpe and S.J. Goldstein (1993)
^{226}Ra-^{230}Th disequilibrium in axial and off-axis mid-ocean ridge basalts. Geochimica Et Cosmochimica Acta, 57, 1233-1241.

R.G. Vugrinovich (1981)
A distribution-free alternative to least-squares regression and its application to Rb/Sr isochron calculations Mathematical Geology, 13, 443-454.

J. Wade and B.J. Wood (2001)
The Earth's 'missing' niobium may be in the core. Nature, 409, 75-78.

C.F. Wang, C.J. Chin, S.K. Luo and L.C. Men (1999)
Determination of chromium in airborne particulate matter by high resolution and laser ablation inductively coupled plasma mass spectrometry. Analytica Chimica Acta, 389, 257-266.

Z.R. Wang and G.A. Gaetani (2008)
Partitioning of Ni between olivine and siliceous eclogite partial melt: Experimental constraints on the mantle source of Hawaiian basalts. Contributions to Mineralogy and Petrology, 156, 661-678.

G.J. Wasserburg, W.A. Fowler, G.J.F. Macdonald and F. Hoyle (1964)
Relative contributions of uranium, thorium and potassium to heat production in Earth. Science, 143, 465-467.

J.T. Wasson and G.W. Kallemeyn (1988)
Compositions of chondrites. Philosophical Transactions of the Royal Society of London Series A: Mathematical, Physical and Engineering Sciences, 325, 535-544.

E.B. Watson, J.B. Thomas and D.J. Cherniak (2007)
^{40}Ar retention in the terrestrial planets. Nature, 449, 299-304.

L.X. Wen, P. Silver, D. James and R. Kuehnel (2001)
Seismic evidence for a thermo-chemical boundary at the base of the Earth's mantle. Earth and Planetary Science Letters, 189, 141-153.

K.T. Wheeler, D. Walker, Y.W. Fei, W.G. Minarik and W.F. McDonough (2006)
Experimental partitioning of uranium between liquid iron sulfide and liquid silicate: Implications for radioactivity in the Earth's core. Geochimica Et Cosmochimica Acta, 70, 1537-1547.

W.M. White (1993)
$^{238}U/^{204}Pb$ in MORB and open system evolution of the depleted mantle. Earth and Planetary Science Letters, 115, 211-226.

U. Wiechert and J. Hoefs (1995)
An excimer laser-based micro-analytical preparation technique for *in situ* oxygen isotope analysis of silicate and oxide minerals. Geochimica Et Cosmochimica Acta, 59, 4093-4101.

M. Willbold and K.P. Jochum (2005)
Multi-element isotope dilution sector field ICP-MS: A precise technique for the analysis of geological materials and its application to geological reference materials. Geostandards and Geoanalytical Research, 29, 63-82.

M. Willbold and A. Stracke (2006)
Trace element composition of mantle end-members: Implications for recycling of oceanic and upper and lower continental crust. Geochemistry Geophysics Geosystems, 7, doi:10.1029/2005GC001005.

D.A. Wood (1979b)
Variably veined suboceanic upper mantle: Genetic significance for mid-ocean ridge basalts from geochemical evidence. Geology, 7, 499-503.

D.A. Wood, J.L. Joron, M. Treuil, M. Norry and J. Tarney (1979a)
Elemental and Sr isotope variations in basic lavas from Iceland and the surrounding ocean floor: Nature of mantle source inhomogeneities. Contributions to Mineralogy and Petrology, 70, 319-339.

D.A. Wood, J. Tarney, J. Varet, A.D. Saunders, H. Bougault, J.L. Joron, M. Treuil and J.R. Cann (1979)
Geochemistry of basalts drilled in the North Atlantic by IPOD Leg-49: Implications for mantle heterogeneity. Earth and Planetary Science Letters, 42, 77-97.

R.K. Workman and S.R. Hart (2005)
Major and trace element composition of the depleted MORB mantle (DMM). Earth and Planetary Science Letters, 231, 53-72.

W. Yi, A.N. Halliday, J.C. Alt, D.C. Lee, M. Rehkamper, M.O. Garcia and Y.J. Su (2000)
Cadmium, indium, tin, tellurium, and sulfur in oceanic basalts: Implications for chalcophile element fractionation in the Earth. Journal of Geophysical Research: Solid Earth, 105, 18927-18948.

W. Yi, A.N. Halliday, D.C. Lee and J.N. Christensen (1995)
Indium and tin in basalts, sulfides, and the mantle. Geochimica Et Cosmochimica Acta, 59, 5081-5090.

Q.Z. Yin, S.B. Jacobsen, K. Yamashita, J. Blichert-Toft, P. Telouk and F. Albarède (2002)
A short timescale for terrestrial planet formation from Hf-W chronometry of meteorites. Nature, 418, 949-952.

T. Yokoyama, A. Makishima and E. Nakamura (1999)
Evaluation of the coprecipitation of incompatible trace elements with fluoride during silicate rock dissolution by acid digestion. Chemical Geology, 157, 175-187.

J.H. Yoo, S.H. Jeong, X.L. Mao, R. Greif and R.E. Russo (2000)
Evidence for phase-explosion and generation of large particles during high power nanosecond laser ablation of silicon. Applied Physics Letters, 76, 783-785.

D. York (1966)
Least-squares fitting of a straight line. Canadian Journal of Physics, 44, 1079-1086.

E.D. Young, D.W. Coutts and D. Kapitan (1998)
UV laser ablation and irm-GCMS microanalysis of $^{18}O/^{16}O$ and $^{17}O/^{16}O$ with application to a calcium-aluminium-rich inclusion from the Allende meteorite. Geochimica Et Cosmochimica Acta, 62, 3161–3168.

D. Zhao (2001)
Seismic structure and origin of hotspots and mantle plumes. Earth and Planetary Science Letters, 192, 251-265.

A. Zindler and S. Hart (1986)
Chemical geodynamics. Annual Review of Earth and Planetary Sciences, 14, 493-571.

A. Zindler, H. Staudigel and R. Batiza (1984)
Isotope and trace element geochemistry of young Pacific seamounts: Implications for the scale of upper mantle heterogeneity. Earth and Planetary Science Letters, 70, 175-195.